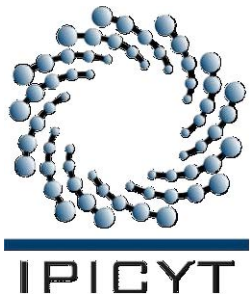

INSTITUTO POTOSINO DE INVESTIGACIÓN CIENTÍFICA Y TECNOLÓGICA, A.C.

POSGRADO EN CIENCIAS APLICADAS

Controlling Chemical and Physical Properties of Ordered Carbon Nanosystems

Tesis que presenta

Aarón Morelos Gómez

Para obtener el grado de

Doctor en Ciencias Aplicadas

En la opción de

Nanociencias y Nanotecnología

Codirectores de la Tesis:

Dr. Humberto Terrones Maldonado

Dr. Mauricio Terrones Maldonado

Dr. Emilio Muñoz Sandoval

San Luis Potosí, S.L.P., agosto de 2010

Constancia de aprobación de la tesis

La tesis "**Controlling Chemical and Physical Properties of Ordered Carbon Nanosystems**" presentada para obtener el Grado de de Doctor en Ciencias Aplicadas en la opción de Nanociencias y Nanotecnología fue elaborada por **Aarón Morelos Gómez** y aprobada el **20 de agosto de 2010** por los suscritos, designados por el Colegio de Profesores de la División de Materiales Avanzados del Instituto Potosino de Investigación Científica y Tecnológica, A.C.

_____
Dr. Humberto Terrones Maldonado
(Codirector de la tesis)

_____
Dr. Mauricio Terrones Maldonado
(Codirector de la tesis)

_____
Dr. Emilio Muñoz Sandoval
(Codirector de la tesis)

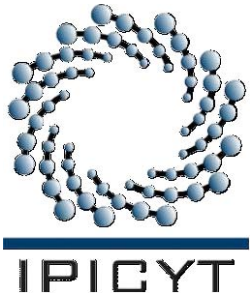

Créditos Institucionales

Esta tesis fue elaborada en las instalaciones y con la infraestructura de la División de Materiales Avanzados para la Tecnología Moderna del Instituto Potosino de Investigación Científica y Tecnológica, A.C., bajo la codirección del los doctores Humberto Terrones Maldonado, Mauricio Terrones Maldonado, Emilio Muñoz Sandoval.

Durante la realización del trabajo el autor recibió una beca académica del Consejo Nacional de Ciencia y Tecnología (No. de 202257) y del Instituto Potosino de Investigación Científica y Tecnológica, A. C.

IPICYT

Acta de Examen de Grado

Núm. 032

Nombre del Sustentante:
AARÓN MORELOS GÓMEZ

Firma

En la ciudad de San Luis Potosí, a los 20 días, del mes de agosto del año 2010, se reunió a las 17:00 horas, en las instalaciones del Instituto Potosino de Investigación Científica y Tecnológica, A.C., el Jurado integrado por:

Dr. Armando Encinas Oropesa	PRESIDENTE
Dr. José René Rangel Méndez	SECRETARIO
Dr. Anvar Abdulkhadovich Zakhidov	SINODAL
Dr. Facundo Ruiz	SINODAL

a fin de efectuar el examen, que para obtener el Grado de Doctor (a) en Ciencias Aplicadas en la opción de Nanociencias y Nanotecnología, sustentó el (la)

C. AARÓN MORELOS GÓMEZ

sobre la Tesis intitulada: Controlling Chemical and Physical Properties of Ordered Carbon Nanosystems

que se desarrolló bajo la dirección de: Dr. Humberto Terrones Maldonado y el Dr. Mauricio Terrones Maldonado, ambos hasta el 17 de diciembre de 2009 y bajo su dirección externa a partir del 18 de diciembre de 2009

El Jurado, después de deliberar, determinó: Y DR. Emilio Muñoz Sandoval APROBARLO.

Dándose por terminado el acto a las 18:30 horas, procediendo a la firma del Acta los integrantes del Jurado. Dando fé el Secretario Académico del Instituto.

Presidente

Secretario

Sinodal

Sinodal

Sinodal

INSTITUTO POTOSINO DE INVESTIGACIÓN CIENTÍFICA Y TECNOLÓGICA, A.C.
IPICYT
SECRETARIA ACADEMICA

Secretario Académico

Acknowledgments

I am grateful to Humberto Terrones, Mauricio Terrones and Emilio Muñoz Sandoval for guiding me throughout my research, for the fruitful discussions and recomendations. All my research was made under the co-direction of Humberto Terrones and Mauricio Terrones since August of 2007, further on in January of 2010 Emilio Muñoz Sandoval was integrated as co-director.

Additionally, I am also thankful for all of the support from my colleague students, professors and technicians who are (or have been) at IPICYT in the Nanoscience and Nanotechnology group*. Their ideas, support, recommendations and friendship have aided me throughout my journey as a PhD student.

My visit Gaithersburg with Robert D. Shull, National Institute of Standards and Technology at Gaithersburg, was enriching and introduced me to the area of magnetic materials an important contribution to my thesis reasearch. Therefore, I am thankful to Robert D. Shull, Cindi L. Dennis, Virgil Provenziano and the Magnetic Materials Group.

My work with carbon inverse opal was greatly improved with my visit with Anvar A. Zakhidov, Nanotech Institute at the University of Texas at Dallas, here I learned more about the production and interesting properties of opal and inverse opal. I would also like to thank the students, professors and technicians from Nanotech Institute** whom helped and shared great moments with me during my visit.

Also, I appreciate the help provided by Alberto Herrera Gómez and Pierre Giovanni Mani Gonzalez for their aid in the x-ray photoelectron spectroscopy of my samples.

I am also thankful to my mother (Leticia Gómez Rico), father (Antonio Morelos Pineda) and my sister (Nora Morelos Gómez) for always supporting and looking for my best interests, as well as my girlfriend (Elda Zoraida Piña Salazar).

* Nanoscience and Nanotechnology Group members
Dr. Humberto Terrones Maldonado, Dr. Mauricio Terrones Maldonado, Dr. Emilio Muñoz Sandoval, Dr. Yadira Itzel Vega Cantú, Dr. Fernando Jaime Rodríguez Macías

En. Daniel Ramírez González, M. Sc. Grisel Ramírez Manzanares, Dr. Hugo Martínez Gutiérrez, Dr. Ferdinando Tristán López, M. Sc. Beatriz Adriana Rivera Escoto, M. Sc. Gladis Judith Labrada Delgado, Gabriela Pérez Assaf, Karla Gómez Serrato

Dr. Sofia Magdalena Vega Diaz, Dr. Néstor Peréa López, Dr. Bernabe Rebollo Plata
Dr. Alicia Rodríguez Pulido

Dr. Ana Laura Elías Arriaga, Dr. José Manuel Romo Herrera, Dr. Eduardo Cruz Silva,

Dr. David Meneses Rodríguez, Dr. Jessica Rosaura Campos Delgado, Dr. Andrés Rafael Botello Méndez

M. Sc. Xavier Norberto Lepró Chávez, M. Sc. Claudia Guadalupe Espinosa González
M. Sc. Abraham Guadalupe Cano Márquez, M. Sc. Eduardo Gracia Espino, M. Sc. Antonio Esaú del Río Castillo, En. Viviana Jehová González Velázquez, B. Sc. Blanca Azucena Gómez Rodríguez, M. Sc. Juan Antonio Briones León, B. Sc. Alicia Elizabeth Chávez Guajardo, B. Sc. Cristal Martínez Ibañez, B. Sc. Isaac Aarón Morales Frías, B. Sc. José Jarib Alcaraz Espinosa, B. Sc. Josué Ortiz Medina, B. Sc. Julio César Chacón Torres, M. Sc. Juan Carlos García Gallegos, B. Sc. Juan Carlos Medina Llamas, M. Sc. Marcia Vianey Bojórquez Avitia, B. Sc. Miguel Angel Pelagio Flores, B. Sc. Rafael Martínez Gordillo, M. Sc. Rodolfo Lima Juárez, M. Sc. Yesmin Panecatl Bernal

** Nanotech Institute members
Dr. Anvar A. Zakhidov, Dr. Ali Aliev, B. Sc. Winston Layne, Dr. Mikhail Kozlov, Natalya Zakharova, Enedina Rodriguez, Ben Williams, Dr. Raquel Ovalle Robles, Dr. Javier Carretero Gonzalez , Dr. Marcio Lima, M. Sc. Gautam Hemani, Dr. Elizabeth Castillo Dr. Alexander Kuznetsov, M. Sc. Kamil Mielczareck, B. Sc. Josef Aaron Velten , B. Sc. Chao Chen Yuan, B. Sc. Brian Wang, M. Sc. Dean Hsu

Contents

Controlando Propiedades Químicas y Físicas de Nanosistemas Ordenados de Carbono

Resumen

La nanociencia y nanotecnología se dedica a la creación de nuevos materiales con propiedades interesantes como dureza, conductividad, propiedades magnéticas. Ahora también, se está estudiando el uso de estos nanomateriales como bloques de construcción para crear nuevos materiales. En este trabajo se estudiaron arreglos ordenados y desordenados: 1) ópalo inverso de carbono y 2) bosques de nanotubos de carbono.

Respecto al ópalo inverso de carbono, utilizamos un ópalo con nanopartículas de SiO_2 (300 nm) ordenadas de manera FCC como molde para la fabricación de ópalo inverso de carbono. Este ópalo inverso de carbono fue sintetizado mediante la infiltración de una solución conteniendo sacarosa como fuente de carbono; además, en esta misma solución se agrego pirazina como fuente de nitrógeno para así obtener ópalo inverso de carbono dopado con nitrógeno. Por otro lado, utilizamos nanopartículas de SiO_2 (10 y 100 nm) desordenadas como molde para sintetizar ópalo inverso de carbono dopado con nitrógeno. Estas muestras se caracterizaron mediante SEM, TEM, espectroscopía Raman, análisis termogravimétrico, adsorción de nitrógeno, difracción de rayos-X y espectroscopía de reflexión óptica. En los resultados obtenidos observamos ligeros cambios en la estructura de las muestras dependiendo de la concentración del dopaje, también observamos el corrimiento del pico de reflexión óptica dependiente a la concentración nitrógeno en la muestra; el corrimiento hacia el azul del pico de reflexión óptica dependiente a la concentración nitrógeno en la muestra.

Posteriormente, realizamos el estudio de las propiedades físicas de ópalo inverso dopado con diferente contenido de nitrógeno y tamaño de poro. En general, variando la concentración de nitrógeno y el tamaño de poro se puede variar controladamente sus propiedades físicas como la resistencia, emisión de campo, magnetoresistencia y magnetización. La resistencia se variar desde 0.30 hasta 0.02 Ω cm y dependiendo de su nivel de dopaje el mecanismo de transporte electrónico puede variar. En magnetoresistencia (MR) hay una transición de MR positivo a MR negativo, al variar de bajas hacia altas temperaturas. Así también, la magnetización de las muestras exhiben una transición de paramagnético a diamagnético al incrementar la temperatura; la temperatura de transición es más alta para poros más pequeños. Finalmente, se utilizó el ópalo inverso dopado con nitrógeno como sensor de acetona, etanol y cloroformo, mostrando que el dopaje con nitrógeno efectivamente aumenta la señal de respuesta del sensor.

Por otro lado, realizamos un estudio teórico y experimental de nanoalambres de Fe encapsulados en nanotubos de carbono. Observamos que las dimensiones (diámetro y longitud) determinan la coercividad, aunque el diámetro tiene una

mayor influencia; también el grado de alineación, pureza y composición química del sistema puede alterar las propiedades magnéticas. Estos conceptos se estudiaron para nanoalambres de Fe encapsulados en nanotubos de carbono de pared múltiple (MWNT), MWNT dopados con nitrógeno (CN_x) y MWNT funcionalizados con grupos oxigenados (CO_x), de igual manera se estudiaron nanoalambres de FeCo encapsulados en MWNT y CN_x.

PALABRAS CLAVE. ópalo inverso de carbono, carbono dopado con nitrógeno, nanotubos de carbono, nanoalambres magnéticos

Controlling Chemical and Physical Properties of Ordered Carbon Nanosystems

Abstract

Nanoscience and nanotechnology are dedicated to the creation of new materials with interesting properties like hardness, conductivity, magnetic properties, among others. Now, there is also interest in the use of these materials as building blocks to create new materials. In this work ordered and disordered arrays were studied: 1) carbon inverse opal and 2) carbon nanotube forests.

Regarding the carbon inverse opal, we used an opal with SiO_2 nanoparticles (300 nm) ordered in a FCC manner as a template for the fabrication of carbon inverse opal. This carbon inverse opal was synthesized by the infiltration of a solution containing sucrose as a carbon source; also, in this same solution we added pyrazine as a nitrogen source to obtain nitrogen doped carbon inverse opal. On another hand, we used disordered SiO_2 nanoparticles as a template to synthesize nitrogen doped carbon inverse opal. These samples were characterized by SEM, TEM, Raman spectroscopy, thermogravimetric analysis, nitrogen adsorption, X-ray diffraction and optical reflection spectroscopy. In the obtained results we observed slight changes in the structure depending on the doping concentration, also we observed the shift of the optical reflection peak depending upon the nitrogen concentration in the sample; observed a blue shift of the optical reflection peak dependent on the nitrogen concentration in the sample.

Furthermore, we realized the study of the physical properties of the carbon inverse opal with different contents of nitrogen and pore size. In general, varying the nitrogen concentration and pore size it is possible to vary in a controlled manner the physical properties such as resistance, field emission, magnetoresistance and magnetization. The resistance was varied between 0.30 down to 0.02 Ω cm and depending upon the degree of doping the transport mechanism of electrons may vary. In magnetoresistance (MR) there is a transition from positive MR to negative MR, when varying from low to high temperatures. Also, the magnetization of the samples exhibits a transition from paramagnetic to diamagnetic when increasing the temperature; the transition temperature is higher for smaller pore size. Finally, the carbon inverse opal doped with nitrogen was used as an acetone, ethanol and chloroform sensor, showing that doping with nitrogen effectively increases the sensing response signal.

On the other hand, we realized an experimental y theoretical study of Fe nanowires encapsulated inside carbon nanotubes. We observed that the dimensions (diameter and length) determine the coercivity, although the diameter has a greater influence; also the degree of alignment, purity and chemical composition of the system may alter the magnetic properties. These concepts were studied for Fe nanowires encapsulated in multiwall carbon nanotubes (MWNT), MWNT doped

with nitrogen (CN_x) and MWNT functionalized with oxygen groups (CO_x), in a similar manner FeCo nanowires encapsulated in MWNT and CN_x were studied.

KEY WORDS. carbon inverse opal, nitrogen doped carbon, carbon nanotubes, magnetic nanowires

1. General Introduction

1.1 Ordered Carbon Nanostructures

Since the beginning of nanoscience and nanotechnology scientists have been interested in being capable of creating new materials, and furthermore, ways to apply them in new innovative devices. There are two approaches to fabricate these nanomaterials: top-down and bottom-up. The top-down method starts by using a bulk material that is carved or patterned down to the nanoscale, this is generally aided by lithography techniques such as photolithography or beam (electron or ion) lithography. Now, the bottom-up approach uses the assembly of single molecules by self-assembly or positional assembly. Furthermore, one of the struggles is to create ordered arrays of nanostructures in one, two or three dimensions in order to create new materials at larger scales, in order to achieve this, methods like chemical synthesis, positional assembly, self-assembly, among others may be used; this is one of the objectives of the bottom-up approach, to use nanostructures as building blocks to construct new materials and devices.

Many natural systems consist of the arrangement of elements, due to the interaction between them and an interaction with the surrounding medium. This can be observed in the lamellar structure of shells, the formation of solar systems, etc. This phenomenon is known as self-assembly, it is defined as a reversible process where the precursor pieces or components are disordered in a pre-existing system capable to form more complex structures. It may be classified in static which is achieved when the system is at equilibrium and does not dissipate energy; dynamic self-assembly needs to absorb energy in order to form an organized system [1]. Some specific methods or phenomena for self assembly are evaporation [2], electrostatic force [3; 4], magnetic forces [5], biomolecule template [6], physical template [7], chemical template [4; 8] and Langmuir Blodgett [9], among others that may be related.

Templating methods can be very simple; this uses a mold which may give the predetermined form to the infiltrated material, in the end of the process the mold is removed leaving the negative structure. A specific example of this is porous anodic aluminum oxide (Figure 1.1 a), here it may be infiltrated with metals [10; 11], semiconductors (Figure 1.1 b) [12] or insulators [13], once the pores are infiltrated and the template is removed it is possible to obtain nanowires or even nanotubes. New materials with interconnected pores may also be used in order to create other porous materials with communicating pores, for example G. Meng et al. created multiply connected and hierarchically branched nanopores inside

anodic aluminum oxide templates, this was done by varying the anodization voltage used for the alumina oxide, afterward the branched alumina oxide was exposed to a chemical vapor deposition to cover the walls with carbon, later the alumina oxide was removed leaving Y branched carbon nanotubes (Figure 1.1 c-f) [14]. On another hand, soft lithography may also be helpful for templating, this was introduced in 1998 by Younan Xia and George M. Whitesides [15; 16], here a polysiloxane reproduces the relief of a certain mold, then this “stamp” is held in contact with a surface and a viscous material or solution is infiltrated by capillarity, later the material may harden or the solution will evaporate leaving behind an inverse pattern of the stamp (Figure 1.2).

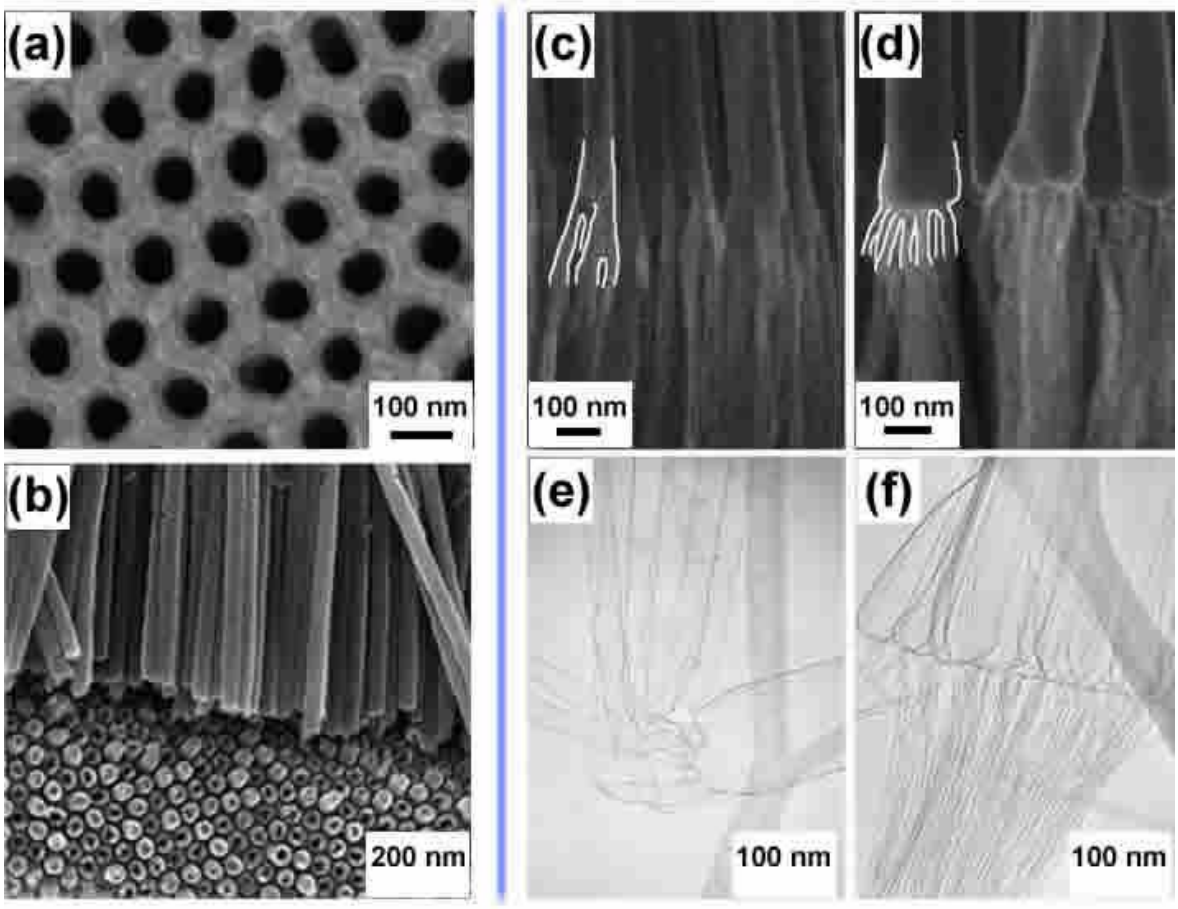

Figure 1.1: (a) Scanning electron microscopy (SEM) image of an ordered porous anodic alumina membranes (AAM). **(b)** ZnO rods produced using the AAM from image (a) (images from ref. **[12]**). **(c and d)** SEM and **(e and f)** transmission electron images of branched carbon nanotubes fabricated with a branched porous anodic aluminum oxide (images from ref. **[14]**).

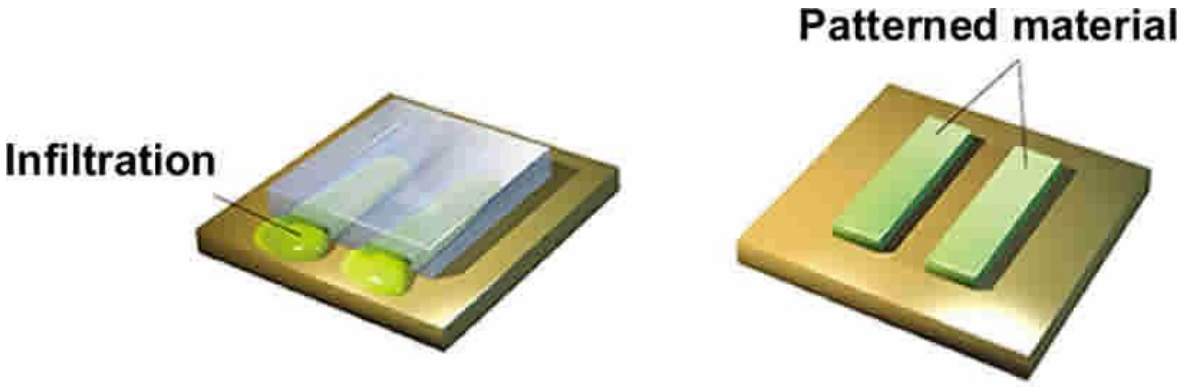

Figure 1.2: Micromolding in capillaries by soft lithography infiltration of the precursor inside a polysiloxane “stamp” further on the precursor is hardened or evaporated leaving the inverse pattern of the “stamp” (images from ref. **[16]**).

1.2 Carbon Allotropes and Doping

There are different forms of carbon that can be found in nature or manmade, they may be classified in ordered and disordered depending upon the crystal structure. Ordered carbon may be found commonly as graphite or diamond. Graphite is composed of several layers, where each layer is composed of a hexagonal lattice (Figure 1.3 a), due to the delocalization of electrons it is a conducting semimetal. Diamond has a crystal structure resembling two interpenetrated face centered cubic lattices displaced ¼ along the x, y and z direction (Figure 1.3 b), it is known as the hardest natural material and it exhibits a wide bandgap making it a good electrical insulator. Now, fullerenes may also be found in nature, but only in small quantities, they were only formally discovered until 1985 [17]. The most stable C_{60}, has a structure that resembles a truncated icosahedron with twenty hexagons and twelve pentagons (Figure 1.3 c). However, in 1976 carbon nanotubes were first observed and reported by Oberlin and Endo [18], its structure may be seen as a tube formed by the rolling of a single hexagonal lattice in a determined direction (Figure 1.3 b).

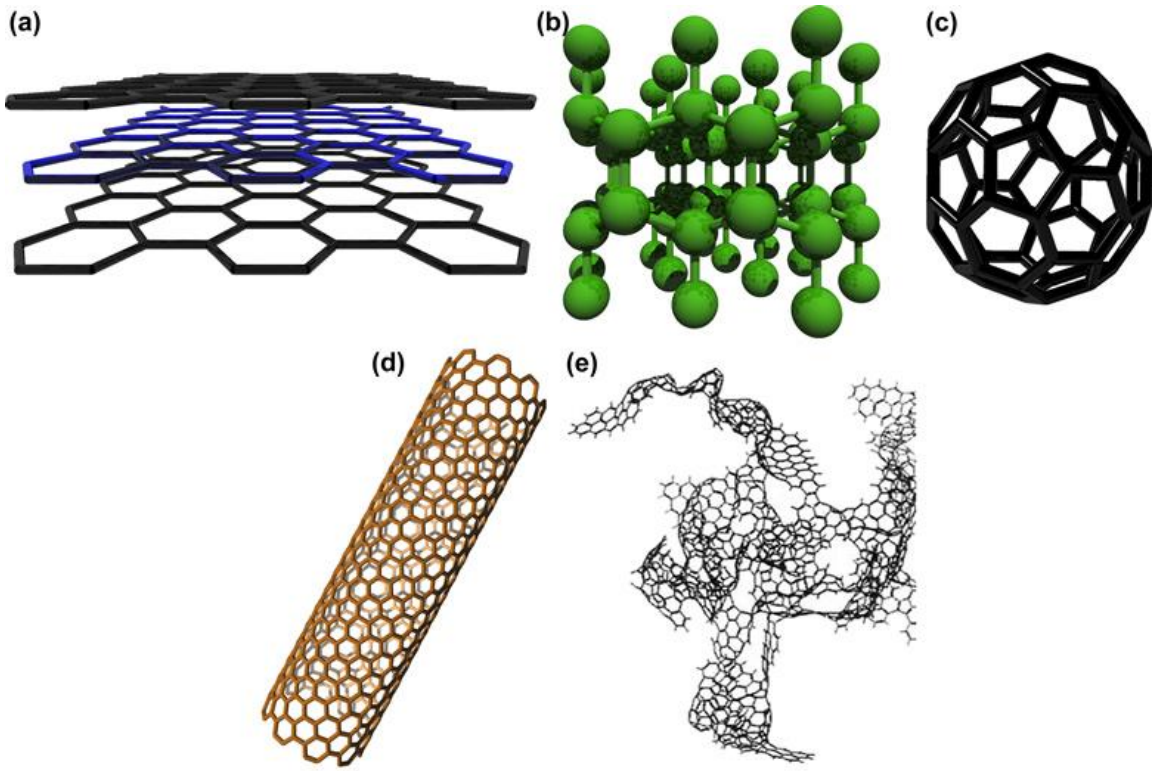

Figure 1.3: Carbon allotropes: **(a)** graphite, **(b)** diamond, **(c)** buckminsterfullerene, **(d)** carbon nanotube and **(e)** representation of amorphous carbon (image from ref. **[19]**).

On another hand, carbon materials may be doped with different elements in a endohedral, exohedral o even substitutional manner. Endohedral doped nanostructures may encapsulate a foreign molecule, ion/ions or crystalline materials inside of its structure, for example a single wall carbon nanotube (SWCNT) may contain fullerenes which is known as a “peapod” (Figure 1.4 a) [20], on another hand many metals such as Re, Pd, Ag, Au, Pb, Ni, Cr, Ge, Fe, Co, Cu, FeCo, FePt and FeNi [21; 22; 23; 24; 25; 26; 27; 28; 29; 30] [31] have been encapsulated. When atoms are intercalated in the voids of the structure it is known as exohedral doping, an example of this is the intercalation of alkali metals (Figure 1.4 b) such as K [32; 33], Na [34] and Li [35; 36], Cs [37], here the alkali metals are capable of elongating the interlayer distance in a carbon structure such as graphite, on the other hand for SWCNT the separation between nanotubes increases [34; 32]. Specifically when Li is intercalated along with NH_3 the interlayer separation may reach a point where it has been used to “unzip” carbon nanotubes [38]. On another hand, foreign atoms may replace carbon atoms in the lattice in a substitutional manner (Figure 1.4 c), commonly nitrogen [39; 40; 41; 42; 43] and boron [44; 45; 46] doping have been studied theoretically and experimentally, however Si [47] and S [48] also have some studies. Now, two foreign atoms may

also be located in the structure, this is called hetero-doping such as B-N [49] and N-P [50].

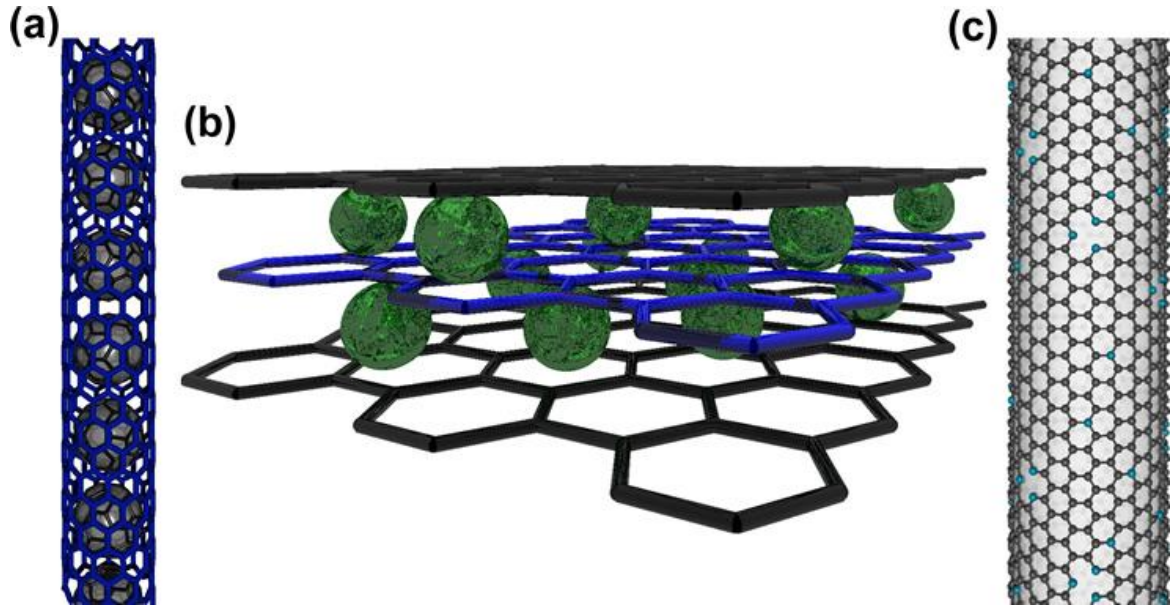

Figure 1.4: Schematic representations of **(a)** endohedral (fullerene inside a carbon nanotube), **(b)** exohedral (intercalation of an alkali metal in graphite) and **(c)** substitutional (nitrogen doped carbon nanotube, nitrogen atoms are shown in light blue) doping in carbon materials.

1.3 Porous Carbon

In 1997 Kyotani et al. infiltrated a zeolite with carbon, here carbon was deposited by a polymerization of acrylonitrile and furfuryl alcohol followed by a carbonization, and alternatively they used chemical vapor deposition (CVD) with propylene to infiltrate carbon in the zeolite (Figure 1.5 a). The carbon/zeolite complex was immersed in hydrofluoric acid in order to remove the zeolite template and maintain the carbon structure which was capable of creating the inverse structure, having a high surface area c. a. 2000 m^2/g [51]. Further on, in 1998 A. Zakhidov et al. infiltrated carbon in a synthetic opal by a phenolic route (Figure 1.5 b) and by CVD, here they successfully obtained the inverse structure of the opal with particular optical properties of a photonic crystal [52].

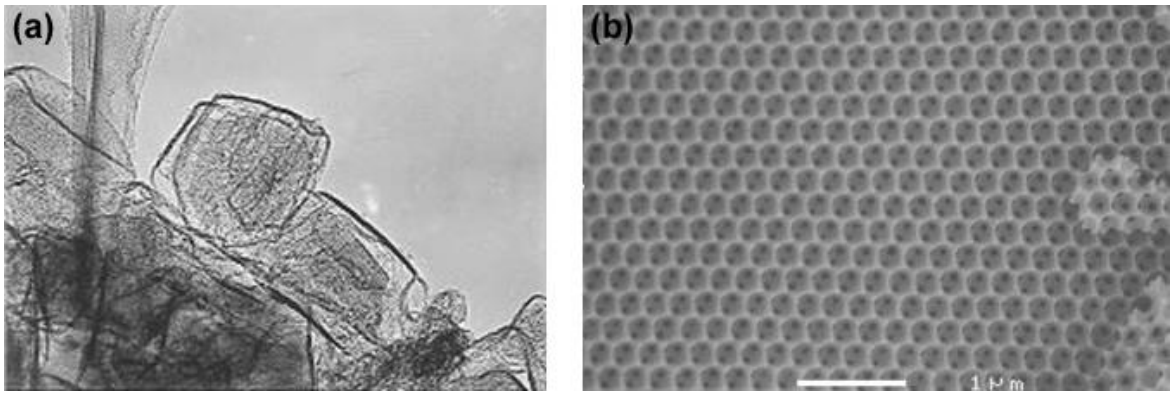

Figure 1.5: (a) Porous carbon produced from a chemical vapor deposition of carbon in a zeolite (image from ref. **[51]**). **(b)** Carbon inverse opal produced by the infiltration of a resin (image from ref. **[52]**).

Porous carbon materials are of interest because of their capability to store molecules being used as filters [53; 54]; if nanoparticles (i. e. Pt) are supported in these materials they may also be used for catalysis [55]. Now, if these materials exhibit a photonic crystal structure they may be used as oil sensors [56]. In chapter 2, the properties and possible applications of porous carbon materials will be discussed in more detail. Further on, if these porous carbon structures are doped their physical and chemical properties may change, regarding this, little work has been done and the majority of them have been only focused on the synthesis [57; 58; 59], leaving more work to be done to study their properties.

1.4 Carbon Nanotubes

Depending upon the direction of the folding the tip may be seen as zig-zag (n,0), armchair (n,n) or chiral (n,m) (Figure 1.6), these are known as single wall carbon nanotubes (CNTs). Armchair and certain zig-zag SWNTs are metallic and the rest are semiconductors with different band gaps. Now, if these carbon nanotubes exhibit several layers of tubes they are known as multiwall carbon nanotubes (MWNTs).

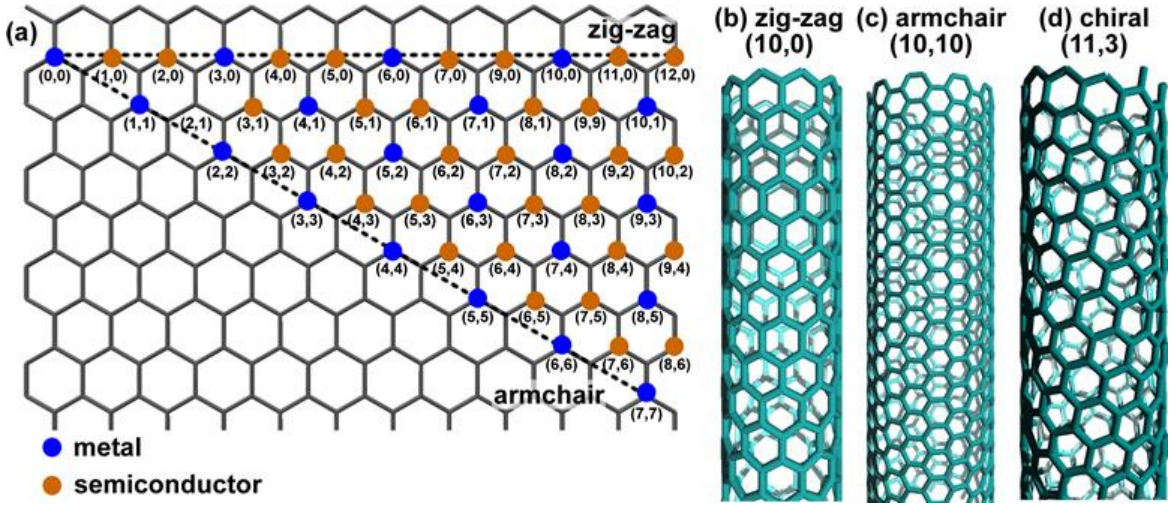

Figure 1.6: (a) Unrolled hezagonal lattice of a nanotube. Symmetry classification of nanotubes, **(b)** armchair, **(c)** zigzag and **(d)** chiral nanotube

Carbon nanotubes are of great interest mainly due to their electronic and mechanical properties. Experimental measurements of the conductivity of SWNT and MWNT have shown thermal activation energies in the range of 13-290 meV [60; 61], along with this, the resistivity of individual MWNT can reach values between $1.2x10^{-4}$ to $5.1x10^{-6}$ Ω cm [62; 63]. Amazingly, MWNT may exhibit superconductivity with a transition temperature of 12 K [64]. Also, carbon nanotubes have the ability to bend to some extent without fracturing [65]. The CNT stiffness is also governed by the chirality, just as the electronic properties, it has been reported that zig-zag SWNT are less stiff than the armchair SWNT [66]. A reported value for the Young's Modulus of MWNT is 1.28 TPa without any diameter dependence [67].

The encapsulation of foreign materials such as gases, fullerenes even nanoparticles in carbon nanotubes is very interesting, since the carbon walls may act as a shield preventing any degradation or reaction of the encapsulated material. Specifically, if they are encapsulated with magnetic nanowires, these nanowires may preserve their magnetic properties over time without any composition transformation such as oxidation [24]; we studied this kind of system in order to have a better understanding of the magnetic properties depending upon the nanowire dimmensions.

1.5 Organization of the Thesis

The work done during the PhD studies is divided in four chapters. In chapter two the fabrication and properties of synthetic opal is described, along with the synthesis of carbon inverse opal by a water based solution and on the other

hand by chemical vapor deposition. After the synthesis optimization of carbon inverse opal, in chapter three the synthesis and characterization of nitrogen doped carbon inverse opal is realized based on the procedure described in chapter two. Following the synthesis of nitrogen doped carbon inverse opal, in chapter four the physical properties such as resistivity, field emission, magnetoresistance and magnetization were measured, along with this the vapor sensing properties were assessed.

Due to the capability of carbon nanotubes to encapsulate foreign materials in chapter five the study of ferromagnetic (Fe and FeCo) nanowires encapsulated in multiwall carbon nanotubes, nitrogen doped multiwall carbon nanotubes and oxygen functionalized carbon nanotubes are studied. Here the dimensions of the encapsulated nanowires are analyzed in order to correlate them with the magnetic properties.

1.6 References

1. **Wikipedia contributors. Self-assembly. Wikipedia, The Free Encyclopedia (2010) at http://en.wikipedia.org/wiki/Self-assembly, Retrieved on July 13, 2010.**

2. *Self-assembly of gold nanorods.* **B. Nikoobakht, Z. L. Wang, M. A. El-Sayed.** 2000, J. Phys. Chem. B (2000), 104, 8635-8640, Vol. 104, pp. 8635-8640.

3. *Dynamic self-assembly and patterns in electrostatically driven granular media.* **M.V. Sapozhnikov, Y.V. Tolmachev, I. S. Aranson.** 2003, Phys. Rev. Lett., Vol. 90, pp. 114301.

4. *Guided molecular self-assembly: a review of recent efforts.* **Huie, J. C.** 2003, Smart Mater. Struct., Vol. 12, pp. 264–271.

5. *Programmable assembly of colloidal particles using magnetic microwell templates.* **B. B. Yellen, G. Friedman.** 2004, Langmuir, Vol. 20, pp. 2553–2559.

6. *Casting metal nanowires within discrete self-assembled peptide nanotubes.* **M. Reches, E. Gazit.** 2003, Science, Vol. 300, pp. 625-627.

7. *Self-organized Fe nanowire arrays prepared by shadow deposition on NaCl(110) templates.* **A. Sugawara, T. Coyle, G. G. Hembree, M. R. Scheinfein.** 1997, Appl. Phys. Lett., Vol. 70, pp. 1043.

8. *New approaches to nanofabrication: Molding, printing, and other techniques.* **B. D. Gates, Q. Xu, M. Stewart, D. Ryan, C. G. Willson, G. M. Whitesides.** 2005, Chem. Rev., Vol. 105, pp. 1171-1196.

9. *Langmuir−Blodgett silver nanowire monolayers for molecular sensing using surface-enhanced raman spectroscopy.* **A. Tao, F. Kim, C. Hess, J. Goldberger, R. He, Y. Sun, Y. Xia, P. Yang.** 2003, Nano Lett., Vol. 3, pp. 1229-1233.

10. *Self-organized Fe nanowire arrays prepared by shadow deposition on NaCl(110) templates.* **A. Sugawara, T. Coyle, G. G. Hembree, M. R. Scheinfein.** 1997, Appl. Phys. Lett., Vol. 70, pp. 1043.

11. *Magnetic properties and magnetization reversal of -Fe nanowires deposited in alumina film.* **Y. Peng, H.-L. Zhang, S.-L. Pan, Hu-L. Li.** 2000, J. Appl. Phys. , Vol. 87, pp. 7405.

12. *Direct electrodeposition of ZnO nanotube arrays in anodic alumina membranes.* **L. Li, S. Pan, X. Dou, Y. Zhu, X. Huang, Y. Yang, L. Zhang.** 2007, J. Phys. Chem. C, Vol. 111, págs. 7288-7291.

13. *Integration of large-area polymer nanopillar arrays into microfluidic devices using in situ polymerization cast molding.* **G. Chen, G. T. McCandless, R. L. McCarley, S. A. Soper.** 2007, Lab Chip, Vol. 7, pp. 1424–1427.

14. *Controlled fabrication of hierarchically branched nanopores, nanotubes, and nanowires.* **G. Meng, Y. J. Jung, A. Cao, R. Vajtai, P. M. Ajayan.** 2005, PNAS, Vol. 102, pp. 7074–7078.

15. *Soft lithography.* **Y. Xia, G. M. Whitesides.** 1998, Angew. Chem. Int. Ed., Vol. 37, pp. 550-575.

16. *The art of building small.* **G. M. Whitesides, J. C. Love.** 2001, Scientific American, pp. 38-47.

17. *C_{60}: Buckminsterfullerene.* **H. W. Kroto, J. R. Heath, S. C. O'Brian, R. F. Curl, R. E. Smalley.** 1985, Nature, Vol. 318, pp. 162-163.

18. *Simulation of nanoporous carbons: A chemically constrained structure.* **M. Acharya, M. S. Strano, J. P. Mathews, J. L. Billinge, V. Petkov, S. Subramoney, H. C. Foley.** 1999, Phil. Mag., Vol. B79, pp. 1499.

19. *Encapsulated C_{60} in carbon nanotubes.* **B. W. Smith, M. Monthioux, D. E. Luzzi.** 1998, Nature, Vol. 396, pp. 323-324.

20. *Synthesis of carbon nanotubes containing metal oxides and metals of the d-block and f-block transition metals and related studies.* **Y. K. Chen, A. Chu, J. Cook, M. L. H. Green, P. J. F. Harris, R. Heesom, M. Humphries, J. Sloan, S. C. Tsang, J. F. C. Turner.** 1997, J. Mater. Chem. , Vol. 7, pp. 545.

21. *Opening carbon nanotubes with oxygen and implications for filling.* **P. M. Ajayan, T. W. Ebbesen, . Ichihashi, S. Ijima, K. Tanigaki, H. Hiura.** 1993, Nature, Vol. 362, pp. 522.

22. *Nickel nanowires of 4 nm diameter in the cavity of carbon nanotubes.* **B. K. Pradhan, T. Kyotani, A. Tomita.** 1999, Chem. Commun., pp. 1317-1318.

23. *Enhanced magnetic coercivities in Fe nanowires.* **N. Grobert, W. K. Hsu, Y. Q. Zhu, J. P. Hare, H. W. Kroto, D. R. M. Walton, M. Terrones H. Terrones, Ph. Redlich, M. Rühle, R. Escudero, F. Morales.** 1999, Appl. Phys. Lett., Vol. 75, pp. 3363.

24. *Magnetic properties of aligned Fe-filled carbon nanotubes.* **T. Mül, D. Elefant, A. Graff, R. Kozhuharova, A. Leonhardt, I. Mönch, M. Ritschel, P. Simon, S. Groudeva-Zotova, C. M. Schneider.** 2003, J. Appl. Phys. 93, pp. 7894.

25. *Preparation and characteristics of carbon nanotubes filled with cobalt.* **S. Liu, J. Zhu, Y. Mastai, I. Felner, A. Gedanken.** 2000, Chem. Mater., Vol. 12, pp. 2205.

26. *Cu-filled carbon nanotubes by simultaneous plasma-assisted copper incorporation.* **G. Y. Zhang, E. G. Wang.** 2003, Appl. Phys. Lett., Vol. 82, pp. 1926.

27. *Production and characterization of single-crystal FeCo nanowires inside carbon nanotubes.* **A. L. Elías, J. A. Rodríguez-Manzo, M. R. McCartney, D. Golberg, A. Zamudio, S. E.Baltazar, F. López-**

Urías, E. Muñoz-Sandoval, L. Gu, C. C. Tang, D. J. Smith, Y. Bando, H. Terrones, M. Terrones. 2005, Nano Lett., Vol. 5, pp. 467.

28. *Carbon nanotube synthesis in supercritical toluene.* **D. C. Lee, F. V. Mikulec, B. A. Korgel.** 2004, J. Am. Chem. Soc., Vol. 126, pp. 4951.

29. *Alloy nanowires: Invar inside carbon nanotubes.* **N. Grobert, M. Mayne, M. Terrones, J. Sloan, R.E. Dunin-Borkowski, R. Kamalakaran, T. Seeger, H. Terrones, M. Rühle, D.R.M. Walton, H.W. Kroto, J.L. Hutchison.** 2001, Chem. Commun., Vol. 5, pp. 471.

30. *Thinning and opening of carbon nanotubes by oxidation using carbon dioxide .* **S. C. Tsang, P. J. F. Harris, M. L. H. Green.** 1993, Nature, Vol. 362, pp. 520.

31. *Formation of graphite-potassium intercalation compounds during activation of MCMB with KOH.* **R. Xue, Z. Shen.** 2003, Carbon, Vol. 41, pp. 1851 –1864.

32. *Purification of carbon single-wall nanotubes by potassium intercalation and exfoliation.* **A. Dailly, J. W. L. Yim, C. C. Ahn, E. Miura, R. Yazami, B. Fultz.** 2005, Appl. Phys. A, Vol. 80, pp. 717–722.

33. *Degradation of carbon materials by intercalation.* **O. Tanaike, M. Inagaki.** 1999, Carbon, Vol. 37, pp. 1759–1769.

34. *New alkali doped pillared carbon materials designed to achieve practical reversible.* **W. -Q. Deng, X. Xu, W. A. Goddard.** 2004, Phys. Rev. Lett., Vol. 92, pp. 166103.

35. *New alkali doped pillared carbon materials designed to achieve practical reversible hydrogen storage for transportation.* **W.-Q. Deng, X. Xu, W. A. Goddard.** 2004, Phys. Rev. Lett., Vol. 92, pp. 166103.

36. *Intercalation and exfoliation routes to graphite nanoplatelets.* **L. M. Viculis, J. J. Mack, O. M. Mayer, H. T. Hahn, R. B. Kaner.** 2005, J. Mater. Chem., Vol. 15, pp. 974–978.

37. *Ex-MWNTs: Graphene sheets and ribbons produced by lithium intercalation and exfoliation of carbon nanotubes.* **A. G. Cano-Márquez, F. J. Rodríguez-Macías, J. Campos-Delgado, C. G. Espinosa-González, F. Tristán-López, D. Ramírez-González, D. A. Cullen, D. J. Smith, M. Terrones, Y. I. Vega-Cantú.** 2009, Nano Lett., Vol. 9, pp. 1527-1533.

38. *Nitrogen-containing carbon nanotubes.* **R. Sen, B. C. Satishkumar, A. Govindaraj, K. R. Harikumar, M. K. Renganathan, C. N. R. Rao.** 1997, J. Mater. Chem., Vol. 7, pp. 2335–2337.

39. *Efficient route to large arrays of CNx nanofibers by pyrolysis of ferrocene/melamine mixtures.* **M. Terrones, H. Terrones, N. Grobert, W. K. Hsu, Y. Q. Zhu, J. P. Hare, H. W. Kroto, D. R. M. Walton, Ph. Kohler-Redlich, M. Ruhle, J. P. Zhang, A. K. Cheetham.** 1999, Appl. Phys. Lett., Vol. 75, pp. 3932-3934.

40. *Novel nanoscale gas containers: encapsulation of N_2 in CN_x nanotubes.* **M. Terrones, R. Kamalakaran,a T. Seegera, M. Rühlea.** 2000, Chem. Commun., pp. 2335–2336.

41. *N-doping and coalescence of carbon nanotubes: synthesis and electronic properties.* **M. Terrones, P.M. Ajayan, F. Banhart, X. Blase, D.L.Carroll, J.C. Charlier, R. Czerw, B. Foley, N. Grobert, R. Kamalakaran, P. Kohler-Redlich, M. Rühle, T. Seeger, H. Terrones.** 2002, Appl. Phys. A, Vol. 74, pp. 355–361.

42. *Synthesis of highly nitrogen-doped multi-walled carbon nanotubes.* **M. Glerup, M. Castignolles, M. Holzinger, G. Hug, A. Loiseau, P. Bernier.** 2003, Chem. Commun., pp. 2542-2543.

43. *Doping graphitic and carbon nanotube structures with boron and nitrogen.* **O. Stephan, P. M. Ajayan, C. Colliex, Ph. Redlich, J. M. Lambert, P. Bernier, P. Lefin.** 1994, Science, Vol. 266, pp. 1683-1685.

44. *Boron-doping effects in carbon nanotubes.* **W. K. Hsu, S. Firth, P. Redlich, M. Terrones, H. Terrones, Y. Q. Zhu, N. Grobert, A. Schilder, R. J. H. Clark, H. W. Kroto, D. R. M. Walton.** 2000, J. Mater. Chem., Vol. 10, pp. 1425-1429.

45. *Boron-doped carbon nanotubes prepared through a substitution reaction.* **W. Han, Y. Bando, K. Kurashima, T. Sato.** 1999, Chem. Phys. Lett., Vol. 299, pp. 368–373.

46. *Substitutional Si doping in deformed carbon nanotubes.* **S. B. Fagan, R. Mota, Antonio J. R. da Silva, A. Fazzio.** 2004, Nano Lett., Vol. 4, pp. 975-977.

47. *An atomistic branching mechanism for carbon nanotubes: sulfur as the triggering agent.* **J. M. Romo-Herrera, B. G. Sumpter, D. A. Cullen, H. Terrones, E. Cruz-Silva, D. J. Smith, V. Meunier, M. Terrones.** 2008, Angew. Chem. Int. Ed., Vol. 47, pp. 2948 –2953.

48. *Synthetic routes to nanoscale B C N architectures.* **M. Terrones, N. Grobert, H. Terrones.** 2002, Carbon, Vol. 40, pp. 1665–1684.

49. *Heterodoped nanotubes: theory, synthesis, and characterization of phosphorus nitrogen doped multiwalled carbon nanotubes.* **E. Cruz-Silva, D. A. Cullen, L. Gu, J. M. Romo-Herrera, E. Muñoz-Sandoval, F. López-Urías, B. G. Sumpter, V. Meunier, J.-C. Charlier, D. J. Smith, H. Terrones, M. Terrones.** 2008, ACS Nano, Vol. 2, pp. 441–448.

50. *Formation of new type of porous carbon by carbonization in zeolite nanochannels.* **T. Kyotani, T. Nagai, S. Inoue, A. Tomita.** 1997, Chem. Mater., Vol. 9, pp. 609-615.

51. *Carbon structures with three-dimensional periodicity at optical wavelengths.* **A. A. Zakhidov, R. H. Baughman, Z. Iqbal, C. Cui, I. Khayrullin, S. O. Dantas, J. Marti, V. G. Ralchenko.** 1998, Science, Vol. 282, pp. 897-901.

52. *Waste materials for activated carbon preparation and its use in aqueous-phase treatment: A review.* **J. M. Diasa, M. C.M. Alvim-Ferraza, M. F. Almeidaa, J. Rivera-Utrillab, M. Sánchez-Polo.** 2007, J. Env. Man., Vol. 85, pp. 833–846.

53. *Removal of arsenic(III) from aqueous solution by activated carbons prepared from solvent extracted olive pulp and olive stones.* **T. Budinova, N. Petrov, M. Razvigorova, J. Parra, P. Galiatsatou.** 2006, Ind. Eng. Chem. Res., Vol. 45, pp. 1896-1901.

54. *Ordered nanoporous arrays of carbon supporting high dispersions of platinum nanoparticles.* **S. H. Joo, S. J. Choi, I. Oh, J. Kwak, Z. Liu, O. Terasaki, R. Ryoo.** 2001, Nature, Vol. 412, pp. 169-172.

55. *Superoleophilic and superhydrophobic inverse opals for oil sensors.* **H. Li, J. Wang, L. Yang, Y. Song.** 2008, Adv. Funct. Mater., Vol. 18, pp. 1-7.

56. *Adsorption properties of nitrogen-alloyed activated carbon fiber.* **C.-M. Yang, K. Kaneko.** 2001, Carbon, Vol. 39, pp. 1075-1082.

57. *Structural and electrochemical characterisation of nitrogen enriched carbons produced by the co-pyrolysis of coal-tar pitch with polyacrylonitrile.* **J. Machnikowski, B. Grzyb, J.V. Weber, E. Frackowiak, J.N. Rouzaud d, F.Béguin.** 2004, Electrochim. Acta, Vol. 49, pp. 423-432.

58. *Porous structure and surface chemistry of nitrogen containing carbons from polymers.* **J. Lahaye, G. Nanséa, A. Bagreev, V. Strelko.** 1999, Carbon, Vol. 37, pp. 585-590.

59. *Electrical transport in pure and boron-doped carbon nanotubes.* **B. Wei, R. Spolenak, P. Kohler-Redlich, M. Ruhle, E. Arzt.** 1999, Appl. Phys. Lett., Vol. 74, pp. 3149-3151.

60. *Water-vapor effect on the electrical conductivity of a single-walled carbon nanotube mat.* **A. Zahab, L. Spina, P. Poncharal, C. Marliere.** 2000, Phys. Rev. B, Vol. 62, pp. 10000-10003.

61. *Probing electrical transport in nanomaterials: conductivity of individual carbon nanotubes .* **H. Dai, E. W. Wong, C. M. Lieber.** 1996, Science, Vol. 272, pp. 523–526.

62. *Electrical conductivity of individual carbon nanotubes .* **T. W. Ebbesen, H. J. Lezec, H. Hiura, J. W. Bennett, H. F. Ghaemi, T. Thio.** 1996, Nature, 1996, 382, 54–56, Vol. 382, pp. 54–56.

63. *Superconductivity in entirely end-bonded multiwalled carbon nanotubes.* **I. Takesue, J. Haruyama, N. Kobayashi, S. Chiashi, S. Maruyama, T. Sugai, H. Shinohara.** 2006, Phys. Rev. Lett., Vol. 96, pp. 057001.

64. *Structural flexibility of carbon nanotubes.* **S. Iijima, C. Brabec, A. Maiti, J. Bernholc.** 1996, J. Chem Phys., Vol. 104, pp. 2089–2092.

65. *Energetics of nanoscale graphitic tubules.* **D. H. Robertson, D. W. Brener and J. W.Minmire.** 1992, Phys. Rev. B., Vol. 4, pp. 12592–12595.

66. *Nanobeam mechanics: elasticity, strength, and toughness of nanorods and nanotubes.* **E. W. Wong, P. E. Sheehan, C. M. Lieber.** 1997, Science, Vol. 277, pp. 1971-1975.

67. *Guided molecular self-assembly; a review of recent efforts.* **Huie, J. C.** 2003, Smart Mater. Struct., Vol. 12, pp. 264-271.

2. Opal and Porous Carbon Inverse Opal

2.1 Opal

2.1.1 Introduction

Minerals such as opals exhibit a photonic crystal structure (Figure 2.1 a), meaning that they consist of silica spheres arranged in a periodic fashion (150 – 400 nm), with a water content between three and twenty percent. An opal is an amorphous mineral, found as a natural gemstone, which consists of closed packed silica particles (Figure 2.1 b). This material is used in jewelry and is considered as Australia's national gemstone and it is also available in Mexico, Peru, Brazil, Canada and Honduras. Some natural opals show an ordered array of particles, these arrays could have three different close-packed layer stacking: fcc structure (i.e., ABCABCABC), hexagonally closed-packed (hcp) structure (i.e., ABABAB) or randomly hexagonal closed-packed (rhcp) structure (i.e., ABABCAB). In other cases these opals may not be highly ordered.

The observed colors in opals are due to the interference and diffraction of light through its microstructure, the diffraction is caused by the grating of the stacking planes of the array of spheres. The color observed depends upon the sphere size; for small size (i. e. 150 nm) a blue color is evident and for larger spheres the color will shift to higher wavelengths towards red. Opals could be classified according to the colors shown in the presence of white light; precious opals exhibit uniform silica spheres within a three dimensional ordered array; common opals show a single solid color, here the spheres are relatively large and are not well ordered. The atomic structure of these opals can be classified in non-crystalline and others that may show some signs of crystalline order known as cryptocrystalline or microcrystalline opals. Microcrystalline opal has spheres that consist of microcrystalline blade of cristobalite and trydimite, these are polymorphs of quartz. Regarding non-crystalline opal, this may be classified in two groups. One of them is known as opal-AG, which consists of aggregates of silica spheres with water filling the voids, and the other kind is called opal-AN which corresponds to amorphous silica glass containing water.

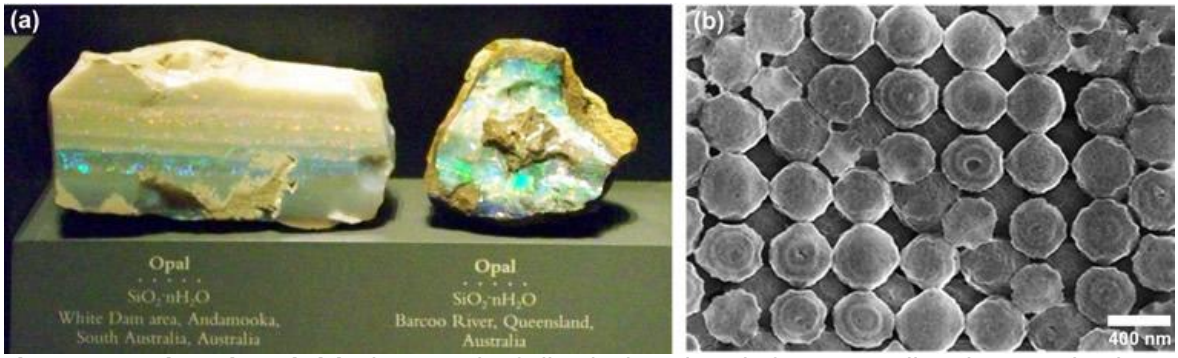

Figure 2.1: Mineral opal. (a) Photograph of sliced mineral opals from Australia. Photograph taken from Smithsonian Natural History Museum in Washington, D.C. **(b)** Scanning electron microscopy image of a Coober Pedy precious opal showing the ordered stacking of monodispersed silica spheres of c.a. 400 nm (image from Ref. **[1]**).

However, it is possible to produce a synthetic opal and this is made by the self assembly of silica spheres in an ordered or semi-ordered lattice. The methods of fabrication mainly use a colloidal suspension; in this chapter these fabrication methods will be discussed. Depending upon the properties of the opal such as particle size (150 – 400 nm), lattice defects (i.e. stacking and dislocations), medium of observation, observation angle, among other factors; their optical properties may vary; these will also be discussed in the present chapter.

2.1.2 Fabrication methods

The discovery of the structure of opal dates from 1974 by Pierre Gilson [2]. Later, Stöber introduced a sol-gel based method to synthesize SiO_2 (silica) particles, which is commonly used at present [3]. Once the silica particles are produced, they may be handled by different methods in order to produce an ordered array. These methods include sedimentation, mold infiltration, and dip coating, among others.

The simplest method for the production of synthetic opal is by sedimentation where the driving force is gravitation coupled with an evaporation of solvents which accommodates the particles. Unfortunately, this process requires weeks or even months if the sphere diameter is less than 300 nm [4; 5]. However, this process is capable of creating opal samples of relatively large dimensions in the order of dm^3 (Figure 2.2 a). According to A. E. Aliev et al. [5] the velocity of sedimentation (Eq. 2.1) is given by the balance of gravitational ($F_g = (1/6)\pi\rho_s g d^3$), Archimedes ($F_A = (1/6)\pi\rho_w g d^3$) and frictional forces ($F_f = 3\pi\eta v d$), where ρ_s and ρ_w are the sphere and water mass densities, g is the gravity acceleration, η is the viscosity of liquid, D is the sphere diameter, and V is their velocity.

Eq. 2.1
$$V = \frac{D^2(\rho_s - \rho_w)g}{18\eta}$$

Theory predicts that the fcc structure is the most energetically stable for a colloidal crystal [6; 7; 8]. Surprisingly, the entropy difference between the fcc and hcp structure is small ($\leq 10^{-3}$ k_B per sphere) [8], thus the fcc is favored during the self assembly of a colloidal solution of silica spheres.

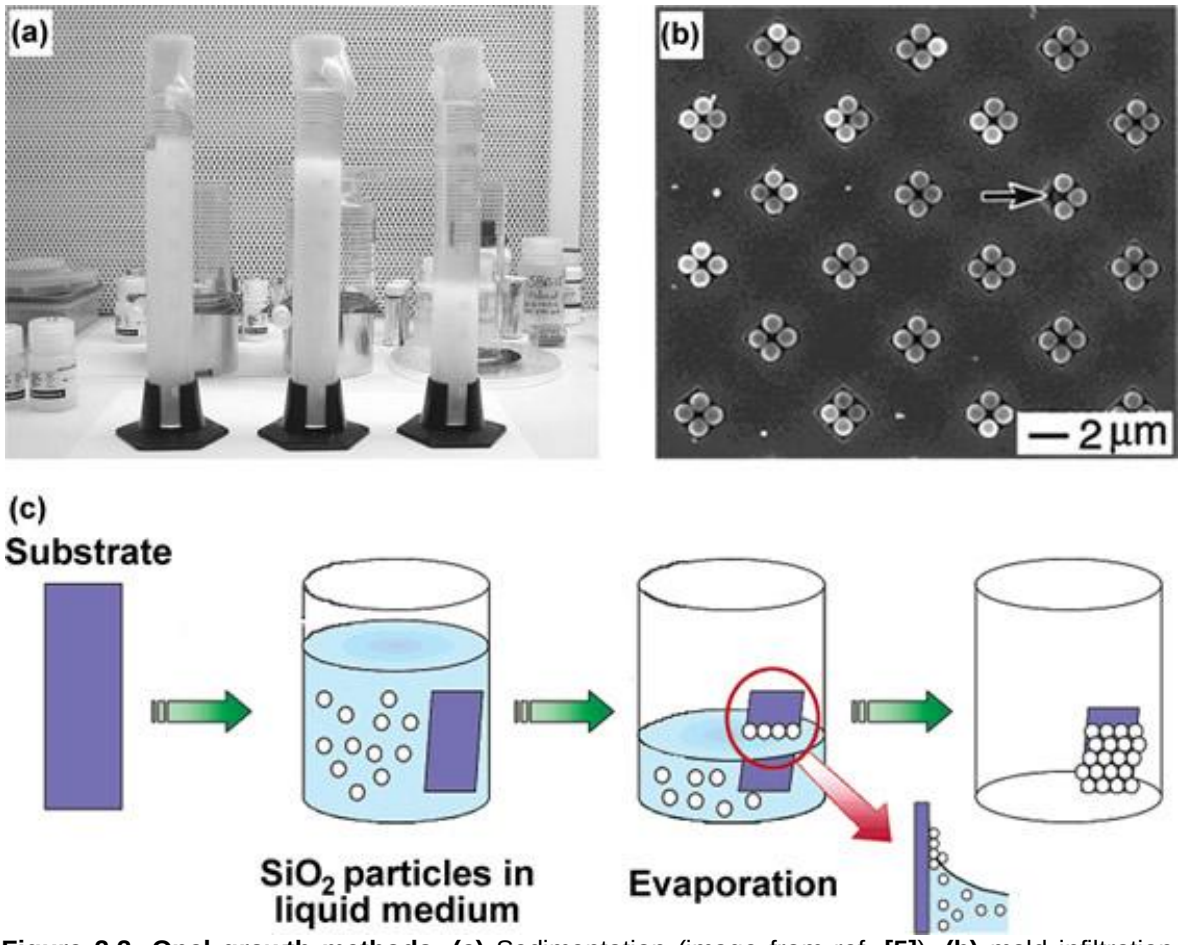

Figure 2.2: Opal growth methods. (a) Sedimentation (image from ref. **[5]**), **(b)** mold infiltration (image from ref. **[9]**), **(c)** dip coating (image from ref. **[10]**).

A way to aid the sedimentation process is via electrodeposition, which has been helpful to assemble semiconductor, polymer and metal particles [11]. Opals made in this way have a predominant fcc structure [12]. Some researchers consider the difference between the electric potential of the dispersing media and the layer of fluid adhered to the particle, this is commonly called ζ potential, which reflects the stability. This means that the electrical charge present in the colloidal suspension may also have an effect on the opal structure obtained. In order to have a control of the electrostatic interactions between the particles and particle-medium: several groups have used basic mediums to synthesize artificial opal [5; 13], this process also avoids the coagulation of particles produced by the electrical charges.

Soft-lithography has been used to produce arrays of particles, using an elastomeric stamp of polydimethylsiloxane (PDMS), here the surface of the stamp is in complete contact with a hydrophilic surface, this PDMS stamp presents a relief in the form of a channel, the channels are deep enough to allow the flow of the suspension at the ends by capillarity. After wetting the entire channel the system is left to dry and in the end of the process there is a colloidal array reflecting the inverse of the PDMS stamp [14; 15]. This process is considered as mold infiltration. A variation of this method would be tilting a fluid cell containing a colloidal suspension to promote a better accommodation of the particles within the channels (Figure 2.2 b) [9]. An alternative way to confine particles in one layer, is using hydrophobic and hydrophilic contrasts. For example the surface of a glass substrate is chemically altered by oxygen [16] or air [17] plasma, thus making the surface hydrophilic. Subsequently, a pattern of hydrophobic material (i. e. polymer or thiols) is imprinted on the surface of the substrate, making certain regions hydrophobic and the others remain hydrophilic. Further on, a suspension of particles is exposed to this surface with contrast (hydrophobic/hydrophilic) patterns and left to dry, here the particles would stay in the hydrophilic regions because they are immerse in a polar medium [17; 18].

Various groups use the dip coating method to make linear arrays of silica particles (Figure 2.2 c). This method consists of holding a substrate vertically in a liquid medium with suspended particles, left to rest and evaporate, thus avoiding external vibrations [10; 19; 20], this technique may be known as fluid-driven self-assembly [21]. During the evaporation of the fluid, the particles are moved along with the meniscus, allowing the spheres to deposit in “niches”, or depressions. Many factors may modify the arrays of the spheres, such as particle concentration and temperature of the fluid [22], sphere size [23], polydispersity and electrostatic interactions [13], centripetal force (i.e. spin coating) [24], dimensions of confinement [17], humidity [25], etc. In a similar way, the Langmuir-Blodgett technique is used, which consists of the retraction of a substrate from a solution containing the particles of interest. Here the velocity of retraction is slow enough in order to allow a proper ordering of the particles at the meniscus, thus making possible to have monolayers of silica particles [26]. This last technique is favorable for media that evaporates at a slow rate.

The use of sonication has been also helpful to produce opals within closed or semi-closed glass cells. The distance between the top and bottom substrates is enough to allow the flow of the suspension, and the ultrasonication contributes with another driving force to “push” the particles between the voids of the substrates and help the production of an ordered structure [14; 17; 27].

2.1.3 Properties and applications

2.1.3.1 Optical properties

In the words of Vukusic and Sambles [28] “millions of years before we began to manipulate the flow of light using synthetic structures, biological systems were using nanometer-scale architectures to produce striking optical effects. An astonishing variety of natural photonic structures exist: a species of Brittlestar uses photonic elements composed of calcite to collect light, butterflies use multiple layers of cuticle and air to produce their striking blue color “[Figure 2.3 a) and b)]” and some insects use arrays of elements, known as nipple arrays, to reduce reflectivity in their compound eyes.”

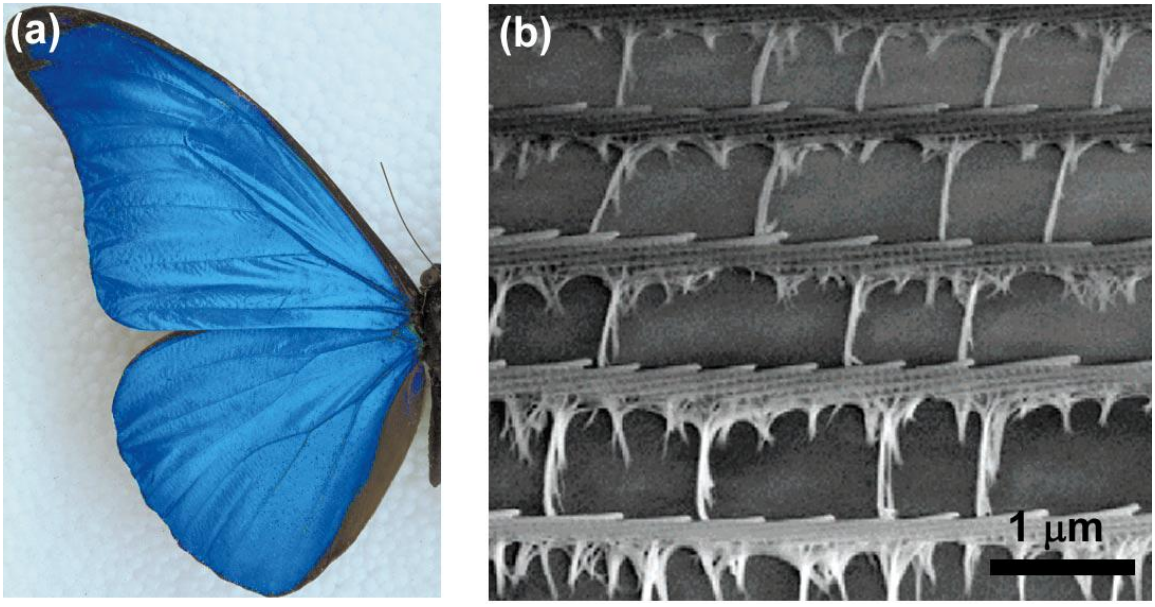

Figure 2.3: (a) Real color image of the blue iridescence from a M. rhetenor wing (image from Ref. **[28]**) and **(b)** scanning electron microscope image taken from the scale surface showing the structure of the lamellae (image from Ref. **[29]**).

Photonic crystals are arrays of periodic nanostructures which can be dielectric or metallo-dielectric. They affect the propagation of electromagnetic waves, similar to how semiconductors define the motion of the electrons, introducing allowed and forbidden electronic energy bands.

When increasing the number of layers of a photonic crystal, the depth of its photonic band gap increases, and the width of the main peak in transmission or reflection decreases [30; 31]. Synthetic opals exhibit an ordered FCC array of colloids (Figure 2.4 a), although they exhibit structural defects such as vacancies (Figure 2.4 b) and stacking faults (Figure 2.4 c). The most frequent defect is plane stacking fault in planes perpendicular to the growth direction. Despite of these

defects, it is possible to have single crystals up to 0.8-0.9 unit cells and up to several thousands of unit cells. Stacking faults cause the large broadening and doublet-like structure of the stop bands along directions other than the (111) growth direction of the fcc opal.

Opals with periods of 200–350 nm display photonic band gaps (PBG) in the visible region of the spectrum, 1.9–2.6 eV. With smaller particles (i. e. 150 nm), the PBG is in the ultraviolet (UV) region, and for larger particles (i. e. 350 nm) the PBG is located in the infrared region [32; 5] (Figure 2.4 d-g). The Bragg diffraction (equation 2.2) may tell us the wavelength of the reflection peak, where d is interplanar distance, n_{eff} is the effective refractive index, f is the filling factor (f=0.74 for a fcc structure) and θ is the angle measured from the beam to the planes. Knowing this, it is therefore possible to create a multibandgap photonic crystal, by stacking opal films with different particle size on top of one another. For example, layer A could be a film with 150 nm particle and layer B with 250 nm particles, and the entire material will show a PBG in the UV, and a PBG in the visible range for 150 and 250 nm particles, respectively [33].

Eq. 2.2 $$\lambda_{max} = 2dn_{eff}sin\theta$$

Eq. 2.3 $$n_{eff} = [(n_s^2)f + (n_p^2)(1-f)]^{1/2}$$

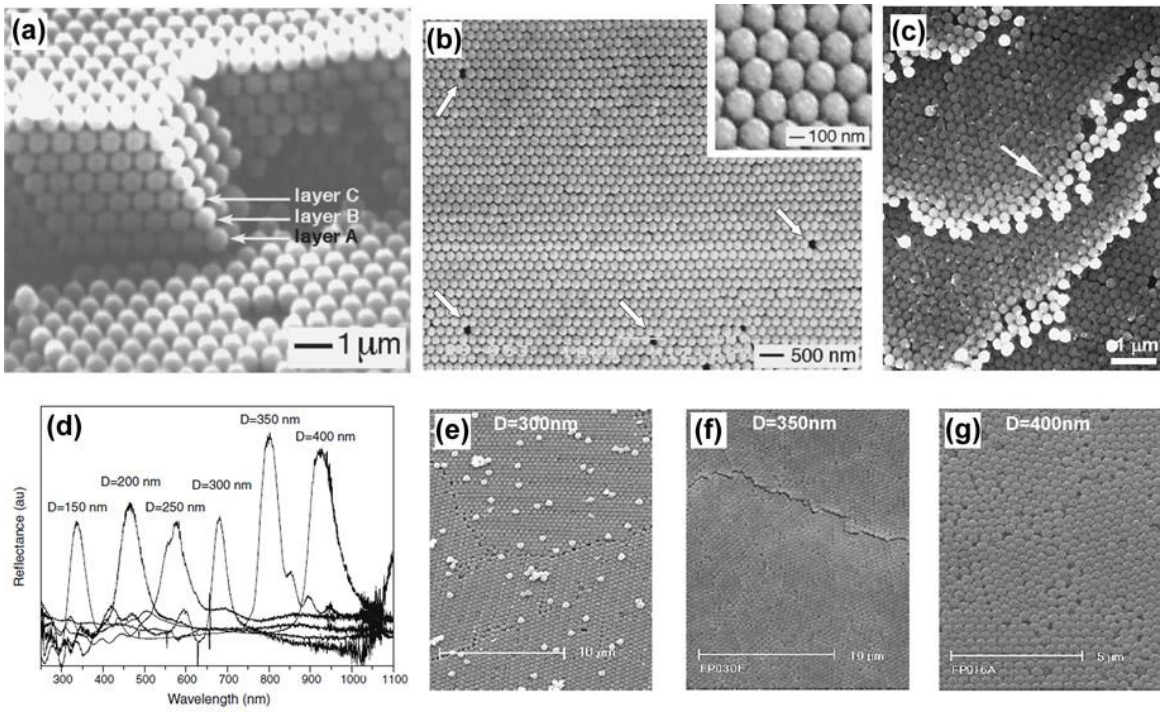

Figure 2.4: Scanning electron microscope (SEM) image of synthetic opal showing **(a)** FCC structure (image from Ref. **[32]**), **(b)** vacancy defect (image from Ref. **[32]**) and **(c)** stacking fault (image from Ref. **[34]**). **(d)** Reflection spectra showing characteristic diffraction peaks for opals made with particles between 150 and 400 nm. SEM images of opals with **(e)** 300, **(f)** 350 and **(g)** 400 nm particles (images from Ref. **[34]**).

2.1.3.2 Applications

Since opal and opal-like materials show interesting optical properties they could be used in the fabrication of devices such as sensors with a visible response. For example, a photonic crystal consisting of a polyacrylamide hydrogel with carboxylated polystyrene spheres has been used as a pH and ionic strength sensor (Figure 2.5 a). Depending upon the pH and the ionic strength, the hydrogel may change its volume thus shifting the diffraction wavelength [35]. The swelling of a photonic crystal by pH and the ionic strength have been used to fabricate a glucose sensor with a polymeric crystalline colloidal array (Figure 2.5 b-d). The glucose-induced hydrogel cross-links increase the elastic-restoring force and shrinks the hydrogel volume, which blue shifts the optical diffraction [36]. This property may be used to fabricate a small color sensitive glucose sensor.

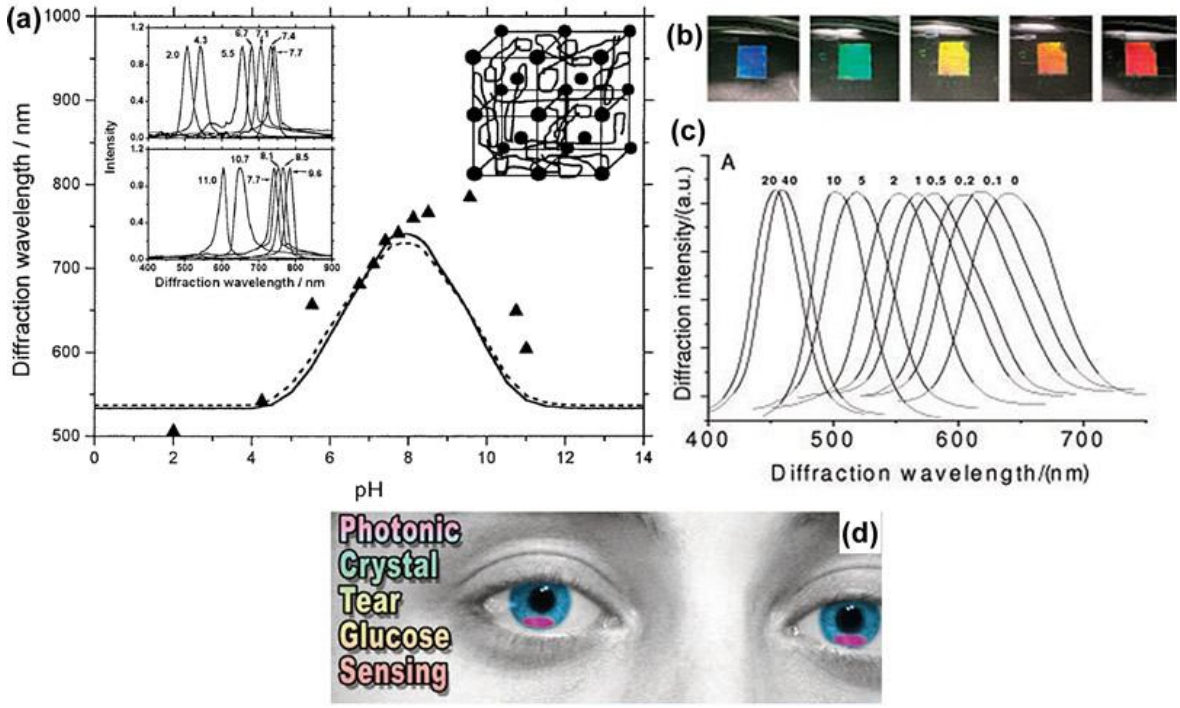

Figure 2.5: (a) pH dependence of the diffraction wavelength of a polymeric colloidal photonic crystal (image from ref. **[35]**). **(b)** Diffraction color changes from red to blue with increasing glucose concentration. **(c)** Dependence of diffraction peak maxima on glucose concentration **(d)** Representation of a contact lens with a photonic crystal to detect glucose concentration (images from ref. **[36]**).

2.2 Carbon Inverse Opal

2.2.1 Introduction

Porous materials are classified according to their size: in the range of 2 nm or less they are called micropores, between 2 and 50 nm they are known as mesopores and those with pores larger than 50 nm are macropores. The size distribution, geometry, volume and ordering of the voids are related to the capacity of the material to perform a specific function.

There are some porous structures with the capacity of interfering with light, because the interface wall-void deflects light according to Snell's Law. Now if these pores exhibit certain ordered crystal-like structure, then it behaves like a semiconductor, but in this case there is a forbidden photonic band gap [37; 38] (Figure 2.6 a). Since photons do not have correlation effects, band theory may be a good approximation to study porous materials. It has been observed that at a greater refraction index in the material, it is easier to obtain a photonic band gap; this was observed in a macrostructure with pores arranged in an fcc lattice (Figure 2.6 b) where this kind of lattice favors the appearance of the forbidden band gap [37]. Since a photonic crystal obeys Brag's equation, the optical characterization must take in to account the angle between the light source and the detector. It has been observed in carbon inverse opals that the diffraction peak suffers a shift depending on the incident angle of the light source [39; 40].

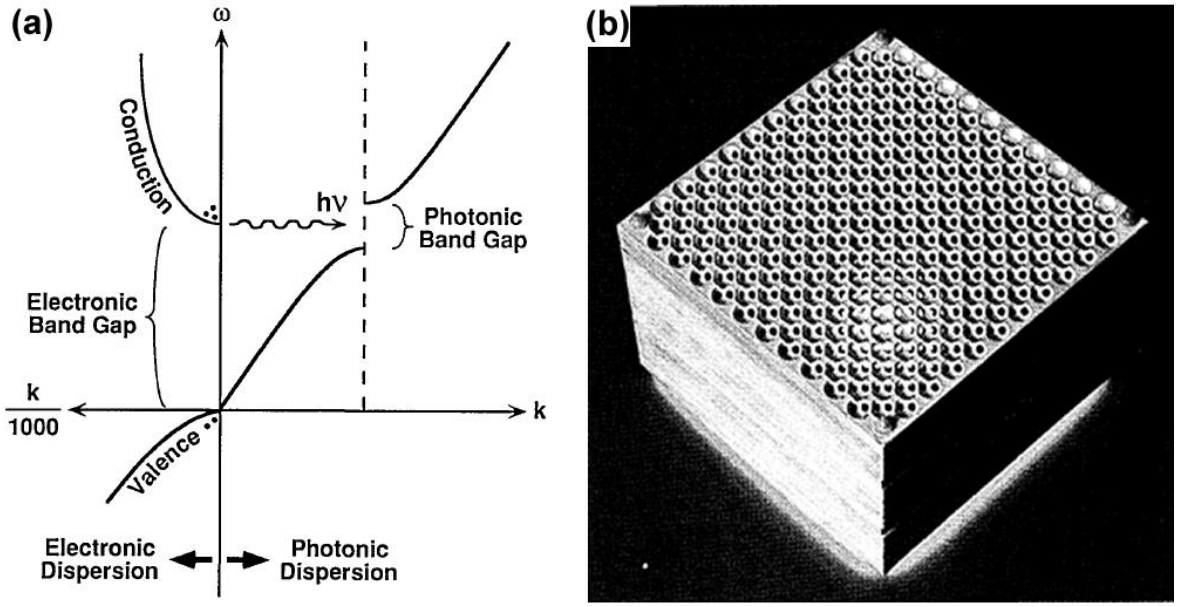

Figure 2.6: (a) Right side, electromagnetic dispersion with a forbidden band gap and left side, electron wave dispersion with a typical band gap for a semiconductor. **(b)** Photograph of an experimental macrostructure used to obtain a forbidden band gap for microwaves (images from ref. **[37]**).

Different materials have been infiltrated in opals in order to fabricate new inverse opals with unique properties. For example, semiconductors such as Si [41; 42] and ZnO [43; 44] and metal (Pb). When infiltrated with Pb, the inverse structure showed superconductivity at a higher temperate (7.325 K) compared to bulk Pb (7.196 K) [45].

2.2.2 Schwarzites

A periodic minimal surface [46] can divide space in two congruent regions (Figure 2.7 a). If these structures are constructed and decorated with carbon atoms in a graphitic-like manner, they are known as Schwarzites [47; 48; 49] (Figure 2.7 b). Schwarzites can be more energetically stable than C_{60} [50; 51; 52]. Heptagonal or octagonal rings exhibit little mechanical strain which is favorable to maintain a sp^2-like hybridization.

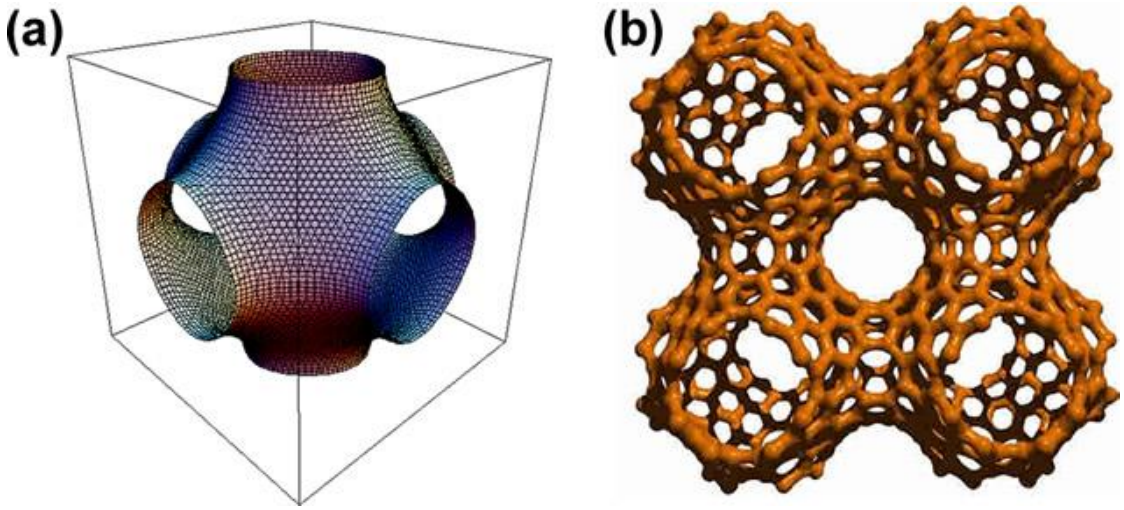

Figure 2.7: (b) P (primitive)triply periodic minimum surface (TPMS). **(c)** Four cubic cells of the P-TPMS decorated with graphite using hexagonal and octagonal rings of carbon (192 atoms per cubic cell) (image from ref. **[49]**).

In order to make a closed surface using sp^2-like hybridization one can use squares, pentagonal, heptagonal and octagonal rings (N_4,N_5,N_7,N_8 respectively) following a relationship that comes from the Gauss-Bonnet theorem to a closed orientable surface, and Euler's law to a graphitic sheet.

Eq. 2.4 $$2N_4 + N_5 - N_7 - 2N_8 = 12(1 - g)$$

The genus ‘g’ can be thought as the number of handles in the structure. For example a sphere has ‘g=0’, a torus has ‘g=1’. In order to produce negative curvature (saddle point) it is necessary to introduce heptagonal or octagonal rings in the lattice [48; 53; 54], and in order to introduce positive curvature pentagons must be introduced [49]. An example to illustrate the effect of the introduction of a

pentagon and a heptagon in a graphitic lattice is the observation by S. Ijima et al. [55; 56] of a nanotube cap showing positive and negative curvature due to the presence of pentagon–heptagon rings, respectively (Figure 2.8). One should keep in mind that a Schwarzite has only one layer of carbon and a carbon inverse opal may have several or hundreds of layers.

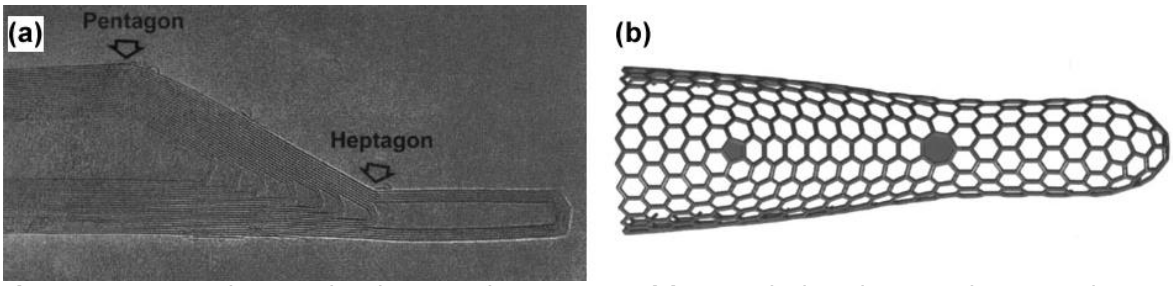

Figure 2.8: Nanotube cap showing negative curvature **(a)** transmission electron microscope image, **(b)** molecular model; on the left the presence of a pentagon induces positive curvature and on the right the heptagon induces negative curvature (images taken from ref. **[55; 56]**).

2.2.3 Carbon inverse opal structures

The first synthesis of porous carbon using silica particles as a template was achieved by Anvar A. Zakhidov et. al [57] in 1998, this was done by infiltrating an opal with carbon by a CVD or a phenolic route, followed by the subsequent removal of silica using an HF treatment.

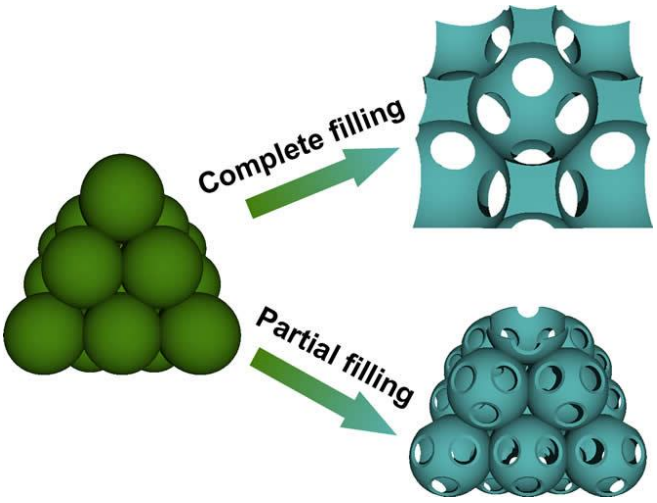

Figure 2.9: Schematic of possible structures obtained from an opal template. With a complete filling it is possible to obtain an inverse opal. However, with a partial filling shell-like structures can be produced. The connection between the spheres is reflected as “windows”, these windows connect all the pores between one another.

When the opal is completely filled with carbon it is possible to obtain carbon inverse opal. However, if the opal is partially filled a shell-like structure could be obtained, this structure would exhibit “windows” (Figure 2.9), which are the interconnections between the pores, random mesopores or ordered mesopores depending upon the structural units used as template. Three-dimensional interconnected porous carbons with mesoporous walls (Figure 2.10 a and b) have been fabricated by preparing a colloidal dispersion of particles with two different sizes: one for the larger pores and another for the walls to be mesoporous [58], this could

also be achieved using the infiltration of surfactants capable of producing several mesophases [59] (Figure 2.10 c). In addition, by controlling the amount of carbon precursor (i. e. sucrose, phenolic resin), it is possible to control the structure of the inverse material, from being a completely closed cage in to a cage with windows (Figure 2.10 d and e), where these windows are defined by the interconnection of the particles [60; 61].

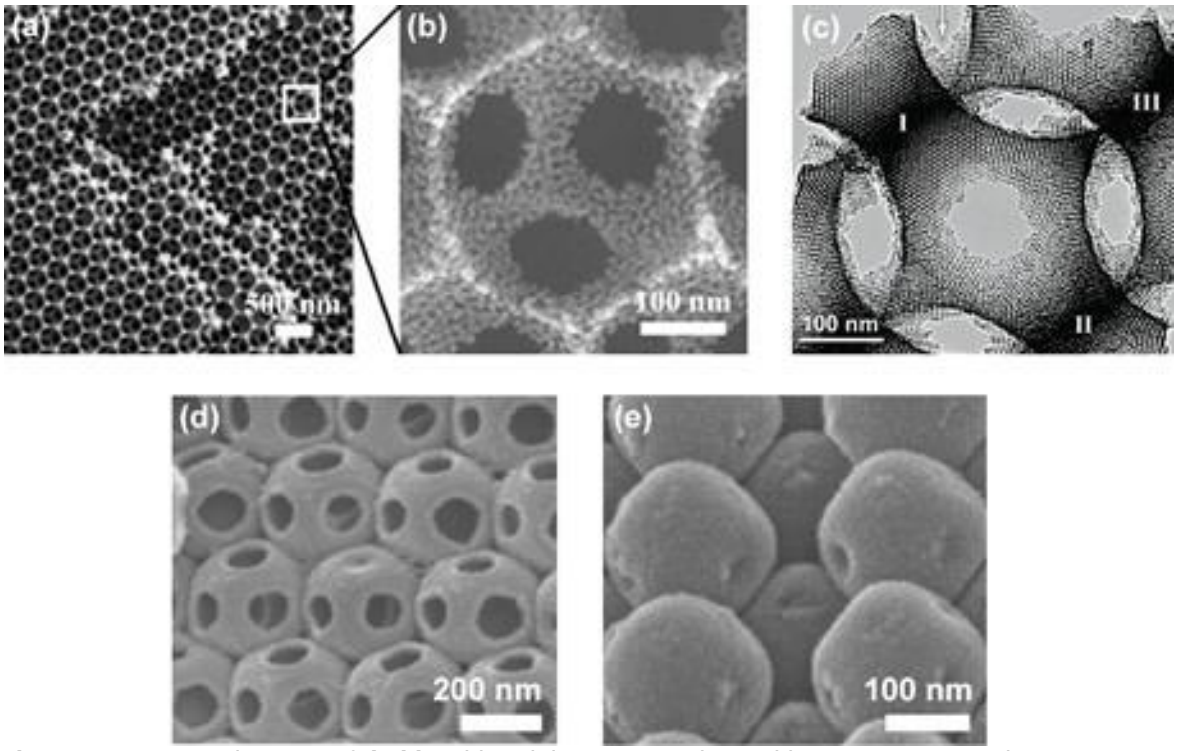

Figure 2.10: SEM images of **(a-b)** a bimodal porous carbon with macropores and mesoporous walls (image from ref. **[58]**), **(c)** transmission electron microscope image of a hierarchically macroporous carbon with mesoporous walls made with liquid crystals (image from ref. **[59]**), SEM images of **(d)** carbon cage with windows and **(e)** hollow carbon capsules (images from ref. **[19]**).

2.2.4 Synthesis methods

The silica templating method has been used with different kinds of carbon sources such as sucrose ($C_{12}H_{22}O_{11}$) [62; 63], polyacrylonitrile (C_3H_3N) [64], propylene (C_3H_6) [57], etc. Each kind of carbon source when pyrolized may be graphitizable, non-graphitizable or anthracitic [65].

Graphitizable carbons are generally produced by substances with a high content of hydrogen. It is a soft material with low porosity and it consists of hexagonal flat sheets (Figure 2.11 a).

Non-graphitizable carbons are hard and possess low density; they cannot be transformed in to crystalline graphite even at 3000 ^{o}C (Figure 2.11 b).

Generally, they are produced from substances that have a high content of oxygen and low content of hydrogen. S. J. Townsend et. al. [66] and P. J. F Harris [67] propose that non-graphitizable carbon structures are formed by discrete fragments of curved graphene-like planes, where pentagons and heptagons are dispersed randomly in the hexagonal lattices, thus resembling Schwarzite fragments (Figure 2.11 c).

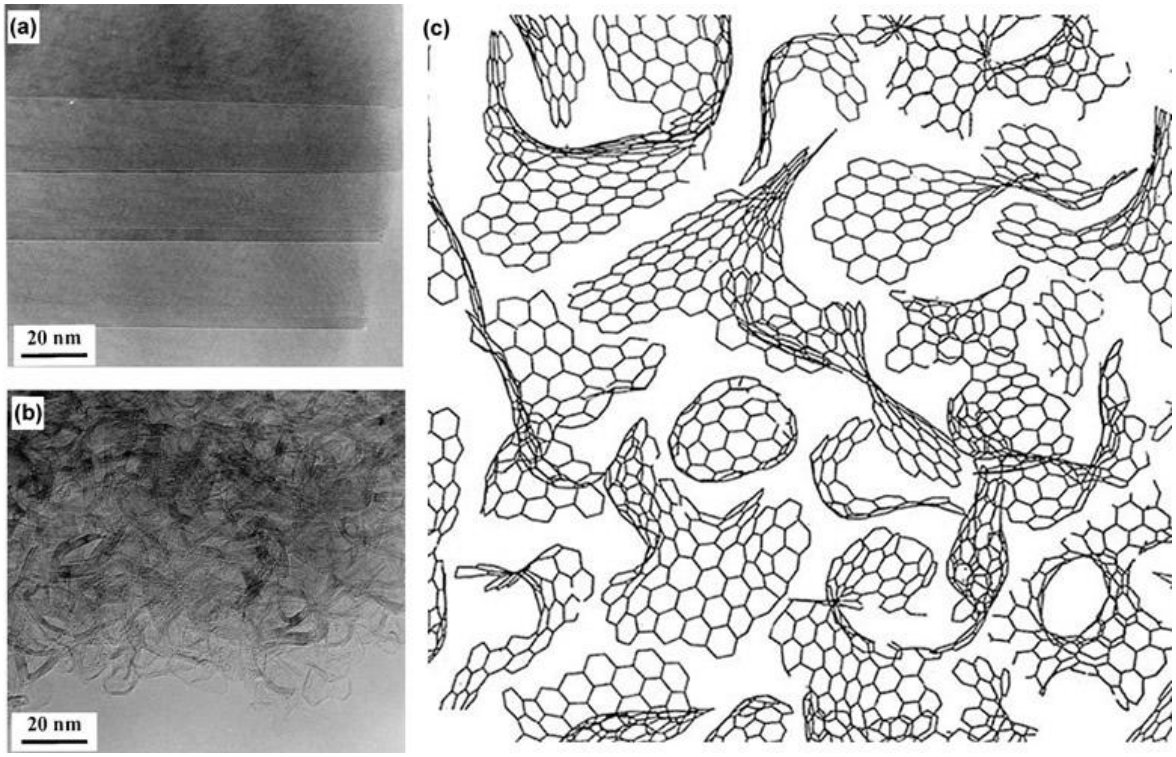

Figure 2.11. Graphitizable and non graphitizable carbons. (a) Graphitizable carbon (from anthracene) and **(b)** non-graphitizable carbon (from sucrose) pyrolized at 2300^{o}C. **(c)** Schematic illustration of a model for the structure of non-graphitizing carbons based on fullerene-like elements (images from ref. **[67]**).

Anthracite produced below 2000 ^{o}C is a strongly cross-linked, highly porous carbon which behaves like non-graphitizable carbon. The crystal in mass has a strong preferential orientation. At higher synthesis temperatures, there is a rapid crystal growth and thus highly graphitic carbons are formed.

2.2.5 Properties and applications

Ordered porous carbon materials are of great interest due to their photonic properties which can be harvested in order to create novel optical based devices and sensors. In addition, porous materials may be used as 3D scaffolds capable of cell regeneration [68; 69]. They can also be capable of storing molecules useful in filters, catalysis, hydrogen adsorption and oil sensors.

With a porous photonic crystal (PhC), it is possible to create a mode-selective type device. In this context B. Desiatov et al. fabricated a hybrid waveguide-PhC structure. Here the guiding mechanism is governed by the total internal reflection, but the PhC induces a dispersion relation to the propagating light [70].

Carbon inverse opal has shown a low thermal conductivity of 0.33W/mK, as reported by A. E, Aliev et. al. [71], where the electronic contribution is negligible. The authors proposed that the heat propagation occurs along the thin layer of graphene sheets, they also measured heat capacity being 30% higher than that of graphite.

2.2.5.1 Bio-scaffolds

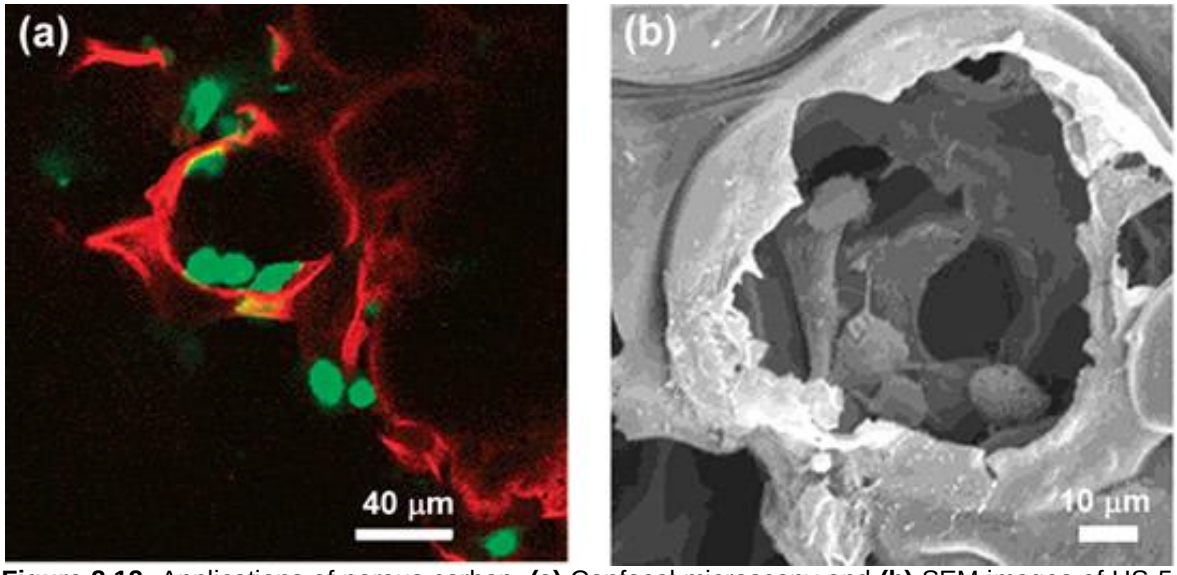

Figure 2.12: Applications of porous carbon. **(a)** Confocal microscopy and **(b)** SEM images of HS-5 human bone marrow cell grown in a macroporous carbon scaffold (images from ref. **[68]**).

Micrometric spheres have been used as templates to produce an inverted porous structure that have been tested as scaffolds for human tissue regeneration such as hepatocellular carcinoma and human bone marrow stromal cell (Figure 2.12 a). These inverse structures showed deep cell infiltration into the scaffold [68; 69].

2.2.5.2 Filters

Activated carbons are porous materials with a variety of pore sizes; they are potentially useful in water remediation. The presence of surface oxidation in these carbon materials provides them with cationic exchange properties, favorable for adsorption of foreign and heavy materials [72]. These have been able to remove mercury, copper, lead, chromium, cadmium, nickel, zinc, lithium, arsenic, etc. from

water [73; 72]. In addition, they have also been used to remove petroleum-hydrocarbon contaminated ground-water [74]. Mesoporous carbons have exhibited extremely high adsorption capacities for bulk dyes, thus their capability to act as a filter [75]. Also, they have been studied as humic acid adsorbent, exhibiting a higher adsorption when compared to conventional activated carbons. This material reaches an adsorption equilibrium within 15 minutes, up taking 60% of the initial humic acids [76]. Regarding carbon nanomaterials, multiwall carbon nanotubes have shown to be capable of presenting a higher adsorption capacity for polycyclic aromatic hydrocarbon when the surface area is large (Figure 2.13) [77].

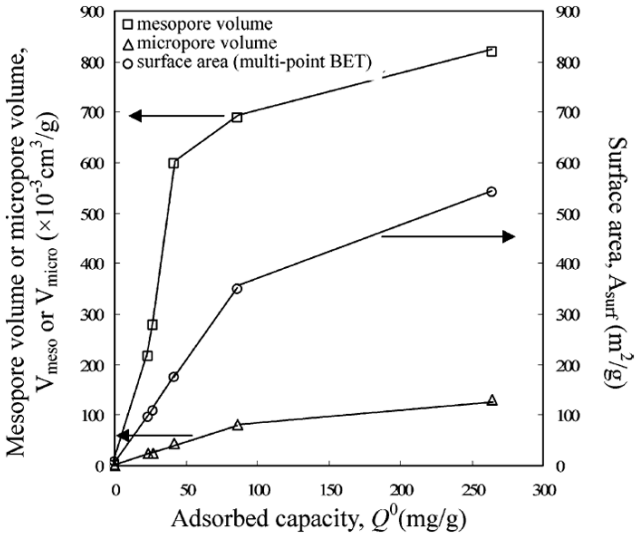

Figure 2.13: Plot of usrface area, micropore volumes and mesopore volumes of carbon nanomaterials against the estimated adsorbed capacity for phenanthrene (image from ref. **[77]**).

2.2.5.3 Hydrogen storage

Figure 2.14: Simulated absolute value of adsorption (hydrogen gravimetric weight percent) at 77 K from computer simulations. Q – quasi-periodic icosahedral nanoporous carbon material (inset figure), D – diamond nanoporous carbon material, P – primitive nanoporous carbon material, and G – gyroid nanoporous carbon material (images from ref. **[78]**).

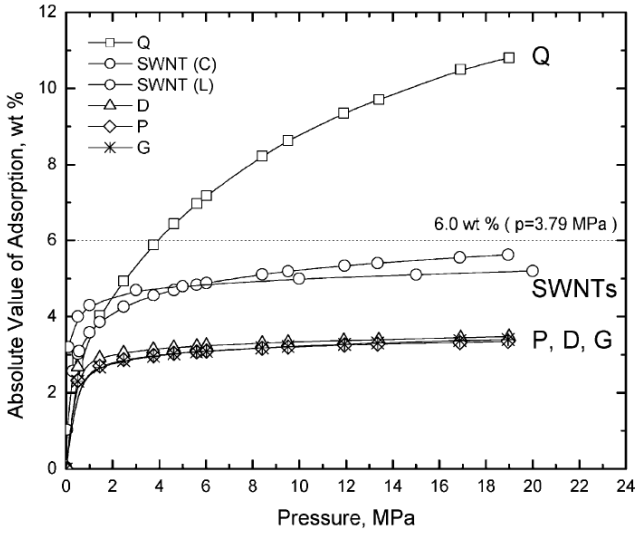

Mesoporous carbon structures have shown theoretically and experimentally to exhibit certain limitations for hydrogen storage. For example a quasi-periodic

icosahedral nanoporous carbon may have a hydrogen delivery capacity up to 6% by wt. at 3.8 MPa and 77 K [78], and other porous carbon materials with a pore size of 1.78 nm display similar capabilities [79]. However, it has been observed experimentally that at higher microporous volume there is an increase in the hydrogen adsorption capacity, i. e. up to 4.5 wt% at 77 K and 1 MPa for a porous (0.7 – 2 nm) carbon material [80; 81]

2.2.5.4 Sensors

A phenolic inverse opal has been tested as an oil sensor (Figure 2.15 a), in which the porous structure (600 nm pore) benefits the adsorption of oil, and the photonic crystal structure along with the variation in optical properties provide an optical signal once the oil is adsorbed. This material exhibits a specific reflectance peak for several oils (i.e., diesel oil, wax oil), and petroleum products (i.e., octane, tetradecane, hexadecane, isopropylbenzene) [82].

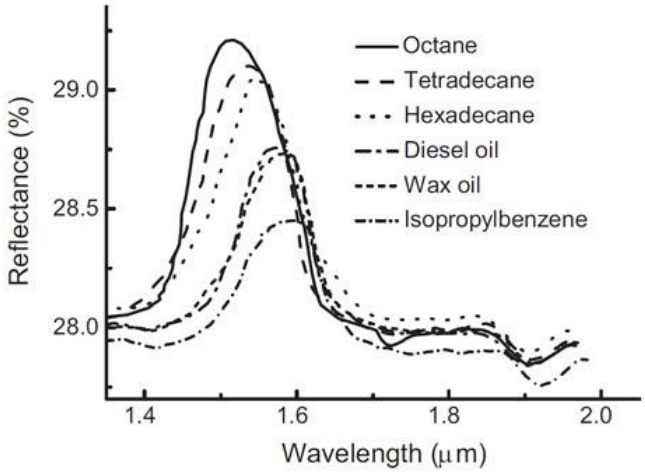

Figure 2.15: Applications of porous carbon. **(a)** An inverse opal was used as an oil sensor, where the diffraction wavelength depends on the type of oil to be sensed (image from ref. [82]).

2.2.5.5 Electrodes

Electrodes made of porous carbon materials have an increase in the coulombic efficiency when the pore size is decreased (Figure 2.16 a), behaving as a linear function of the surface area, although its porous structure results in a low volumetric capacitance [83]. However, the introduction of nanoparticles may enhance or give new properties to porous carbon materials. For example, when supporting SnO_2 nanoparticles, it increases its capacity, ionic conductivity, provides a good cycling stability as a carbon anode for lithium-ion batteries [84; 85], with Pt nanoparticles (Figure 2.16 b) the catalytic activity of oxygen reduction [86], and specifically the methanol electrochemical oxidation [87] is enhanced.

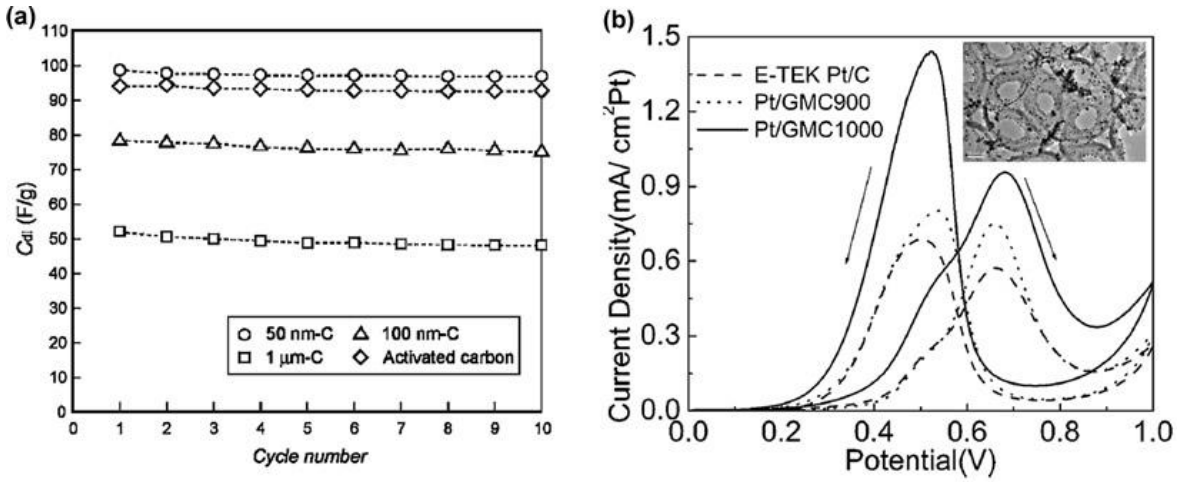

Figure 2.16. (a) Carbon inverse opal has been used as an electrode in a capacitor (image from ref. **[83]**). **(b)** Pt nanoparticles supported on porous carbon was used for electrochemistry (image from ref. **[87]**).

2.3 Experimental Methodology

In this work, the carbon inverse opals were synthesized by the infiltration of a carbon source using a carbon solution or by chemical vapor deposition (CVD). In the first case, a water solution with an organic precursor and a dehydrating acid were used to infiltrate a synthetic opal, an alternative route is to add silica nanoparticles to this solution. This solution was evaporated and then heat treated. For the CVD method, the synthetic opal was exposed to an inert atmosphere together with a flow of another organic precursor inside a furnace, in order to cover the silica nanoparticles. After the infiltration of carbon by either method, the composite silica-carbon was treated with HF to produce a porous carbon material. In the following paragraphs, the synthesis methods and the carbon inverse opals characterization are described.

The opal (300 nm silica nanoparticles, Figure 2.17 a) was held in a solution of sucrose, sulphuric acid (H_2SO_4) and water (according to Table 2.1) at 100 ^oC during 6.5 hours. Sucrose and sulphuric acid react leaving carbon and hydrated sulphuric acid in the medium (Eq. 2.4). After the evaporation of water, the samples were heated at 1000 ^oC for one hour in an Ar atmosphere (Figure 2.17 b). Finally, these were immersed in HF (30% in water) during approximately two days to remove the silica nanoparticles (Figure 2.17 (c)) (Eq. 2.5 and 2.6).

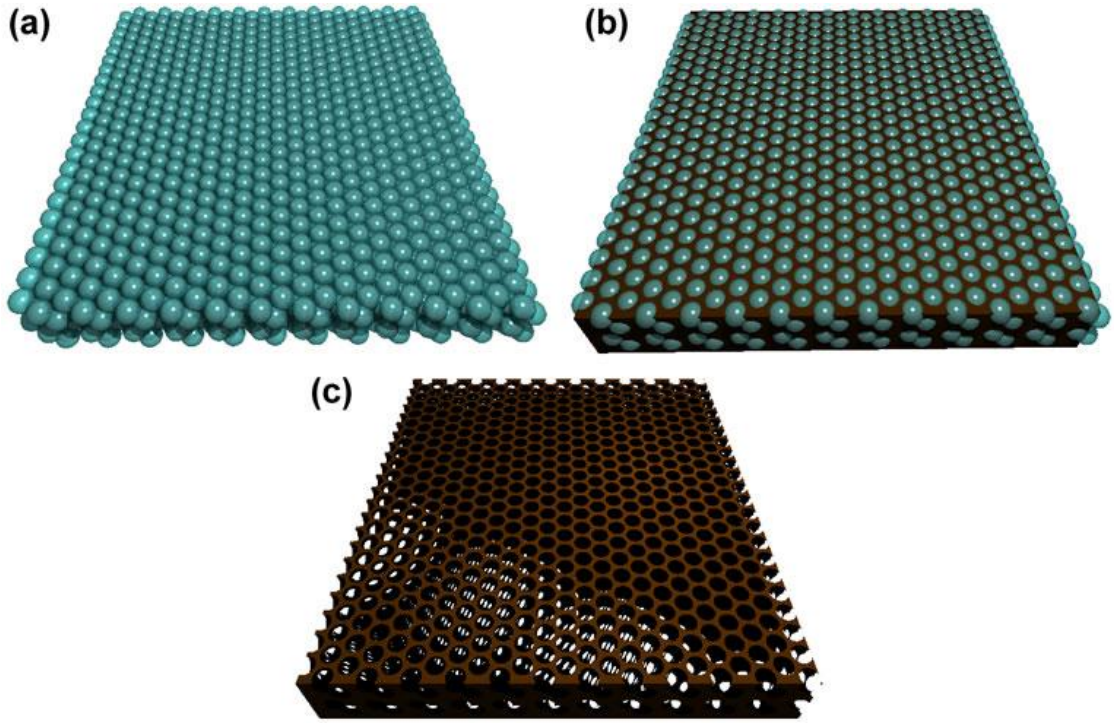

Figure 2.17: Carbon inverse opal synthesis. (a) Synthetic opal, **(b)** synthetic opal infiltrated with carbon and **(c)** carbon inverse opal.

Eq. 2.5 $$11H_2SO_4 + C_{12}H_{22}O_{11}(s) \rightarrow 12C(s) + 11H_2SO_4.H_2O$$

Eq. 2.6 $$SiO_2(s) + 4HF(l) \rightarrow SiF_4(aq.) + 2H_2O(l)$$

If the reaction is held with an excess of HF then it may react as follows:

Eq. 2.7 $$6HF + SiO_2 \rightarrow H_2SiF_6 + 2H_2O$$

Table 2.1: Carbon source solution concentrations. Quantities are in % by wt.

	1	2	3	4
Sucrose	10.00	15.00	25.00	30.00
Water	88.97	83.45	72.42	67.00
Sulphuric acid	1.03	1.55	2.58	3.00

Another infiltration method used is the chemical vapor deposition (CVD), using acetylene (C_2H_2) as a carbon source, and Argon as a carrier gas inside a quartz tube with the synthetic opal located in the center region of the furnace. Once the furnace is stabilized at 800 ^oC, the acetylene flow was introduced, after the desired reaction time the acetylene flow was ceased and the furnace was set to room temperature. The flows used are shown in Table 2.2, CVD11-CVD14 had a 2 hour synthesis, CVD21 and CVD22 for 5 hours, samples CVD23 and CVD24 were synthesized during 2 hours then the surface was polished to remove the

excess carbon and finally the synthesis was repeated for another 2 hours. Samples CVD11-CVD13 and CVD21-23 were synthesized at 800 ^{o}C and etched with HF (30% in water) during approximately two days. Another set of experiments was performed using conditions from CVD13 at 750 ^{o}C, 800 ^{o}C and 850 ^{o}C, the CVD13 conditions were chosen due to the uniformity of the carbon coverage on the silica spheres. These experiments were carried out in order to search for the highest infiltration of carbon in to the pores.

Table 2.2 CVD flow rates. Argon and Acetylene flow rates (l/min), synthesis time is given in hours and was realized at 800 ^{o}C.

	CVD11	CVD12	CVD13	CVD14
Argon	2	2	0.95	0.95
Acetylene	0.2	0.5	0.15	0.31
Synthesis time	2	2	2	2
	CVD21	CVD22	CVD23	CVD24
Argon	0.95	1.46	0.95	0.95
Acetylene	0.15	0.077	0.15	0.24
Synthesis time	5	5	2	2

The next experiments were performed in order to achieve the lowest amount of carbon, and being semi translucent in chloroform, the reason for latter condition will be explained in the next section (results and discussions). Flow rates and times were varied with the optimum conditions: 0.95 l/min Ar, once the furnace stabilized at 800^{o} C a flow of 0.00022 l/min of acetylene was introduced for 2 seconds.

These samples were analyzed by scanning electron microscopy (SEM) (XL 30 SFEG FEI operated between 10 - 20 kV) equipped with an energy dispersive X-Ray (EDX).

2.4 Results and discussions

The SEM images show the production of carbon inverse opals with 10% (Figure 2.18 a) of sucrose revealing that there is not a high filling factor. When using 25% of sucrose (Figure 2.18 c), the carbon coverage between silica nanoparticles reaches an optimum level, and at 30% of sucrose (Figure 2.18 d) thin layers are observed. An average of 100 pores were measured in order to obtain the average pore sizes. For all cases, the overall average pore size is around 292 ± 6 nm for 302 nm particle opal.

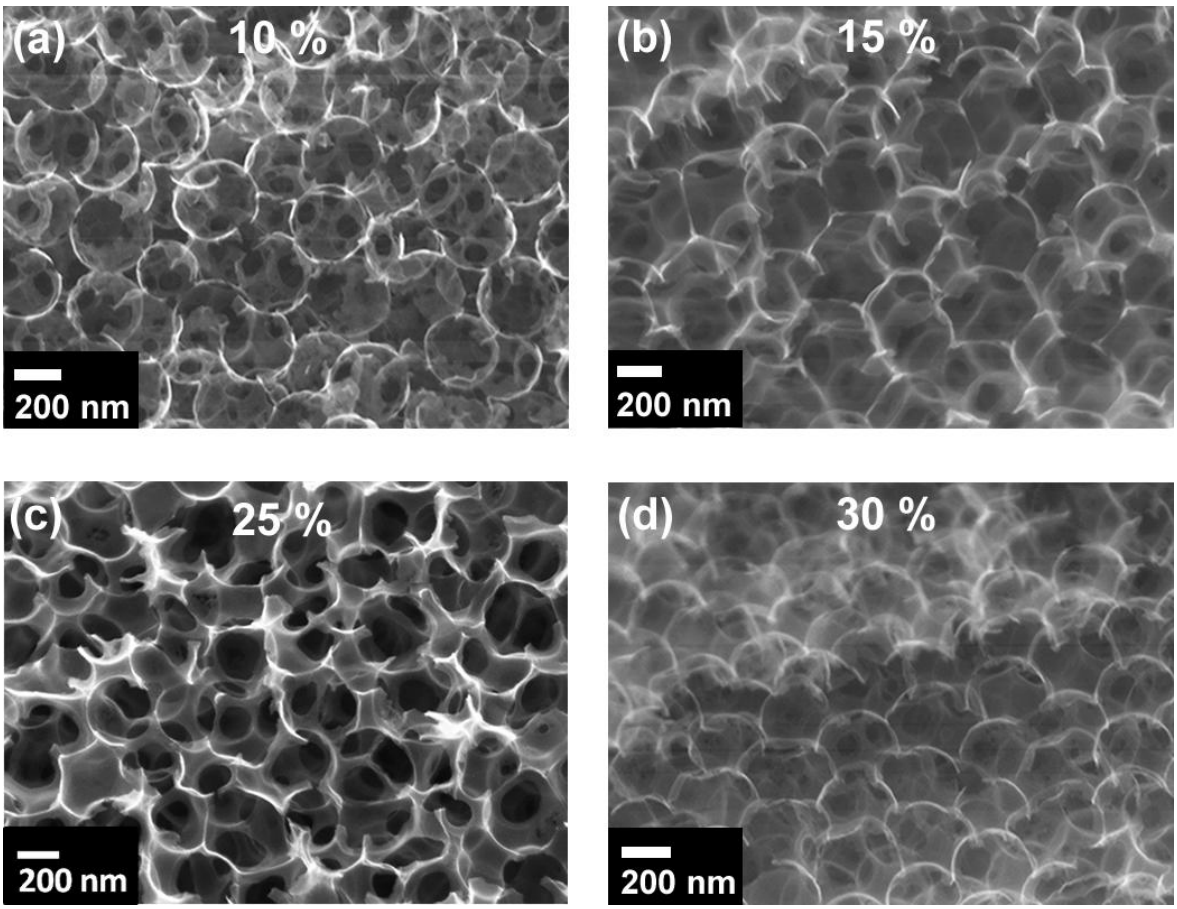

Figure 2.18: Sucrose based carbon inverse opal. SEM images of carbon inverse opal made with **(a)** 10%, **(b)** 15%, **(c)** 25%, **(d)** 30% by wt. of sucrose in the solution.

All of the SEM images for the CVD synthesis using the CVD11-CVD14 and CVD22 conditions (Figure 2.19) indicate an incomplete filling of the opal with carbon. For sample CVD12 (Figure 2.19 b), cage like carbon particles are shown, some of them are cracked revealing a hollow interior. CVD21 shows a slightly higher filling rate, shown by the presence of square-like structures between pores (Figure 2.19 e), this is also shown in Figure 2.9 for the complete filling of an opal.

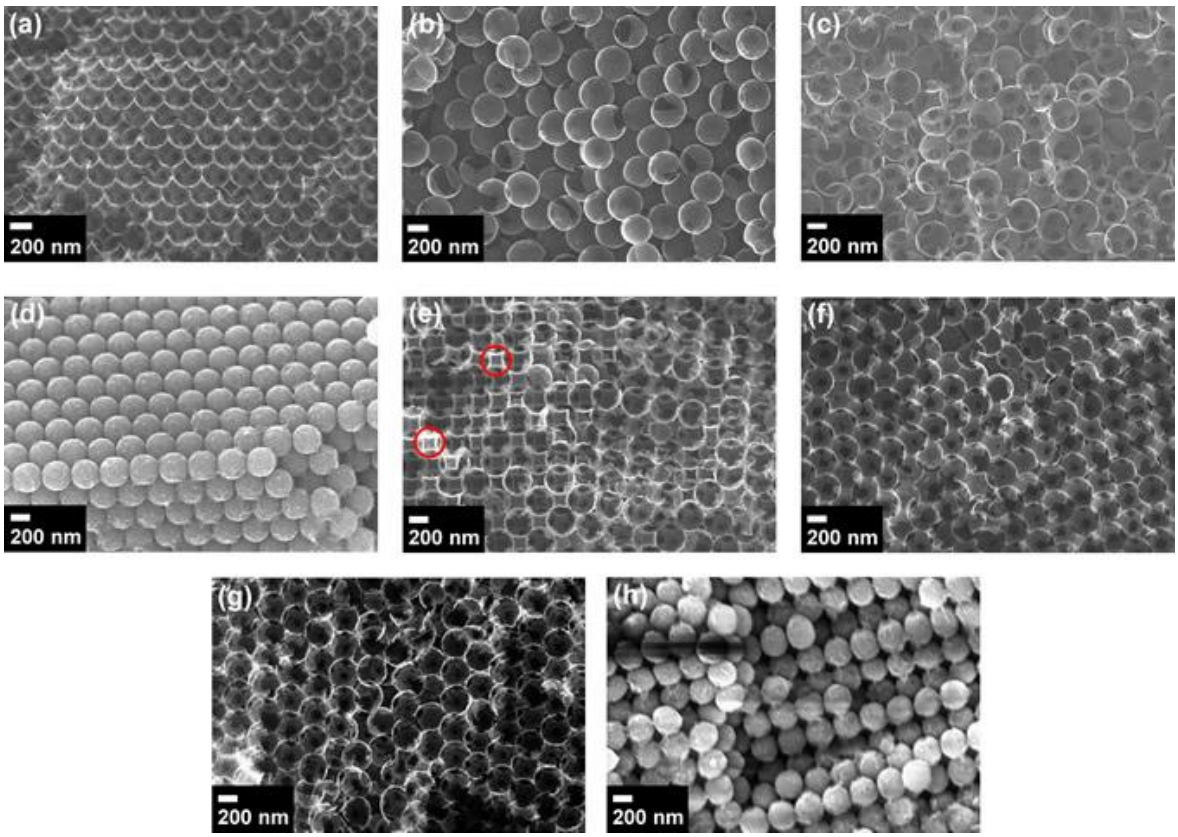

Figure 2.19: SEM of CVD made carbon inverse opals at different flow rates. **(a-d)** correspond to CVD11-CVD14 and **(e-h)** correspond to CVD21-24. Red circle highlights square-like structure, indicator of a complete filling.

Generally the degree of graphitization depends upon the synthesis temperature. For this reason we carried out CVD reactions at different temperatures (750-850 ^{o}C) in order to study its effect. At 750 ^{o}C, we can observe an amorphous-like carbon (Figure 2.20 a), at 800 ^{o}C there is a more uniform layered morphology (Figure 2.20 b), and at 850 ^{o}C there is a thin layer of carbon on the surface of the bulk opal (Figure 2.20 c) which may decrease the infiltration rate inside the sample.

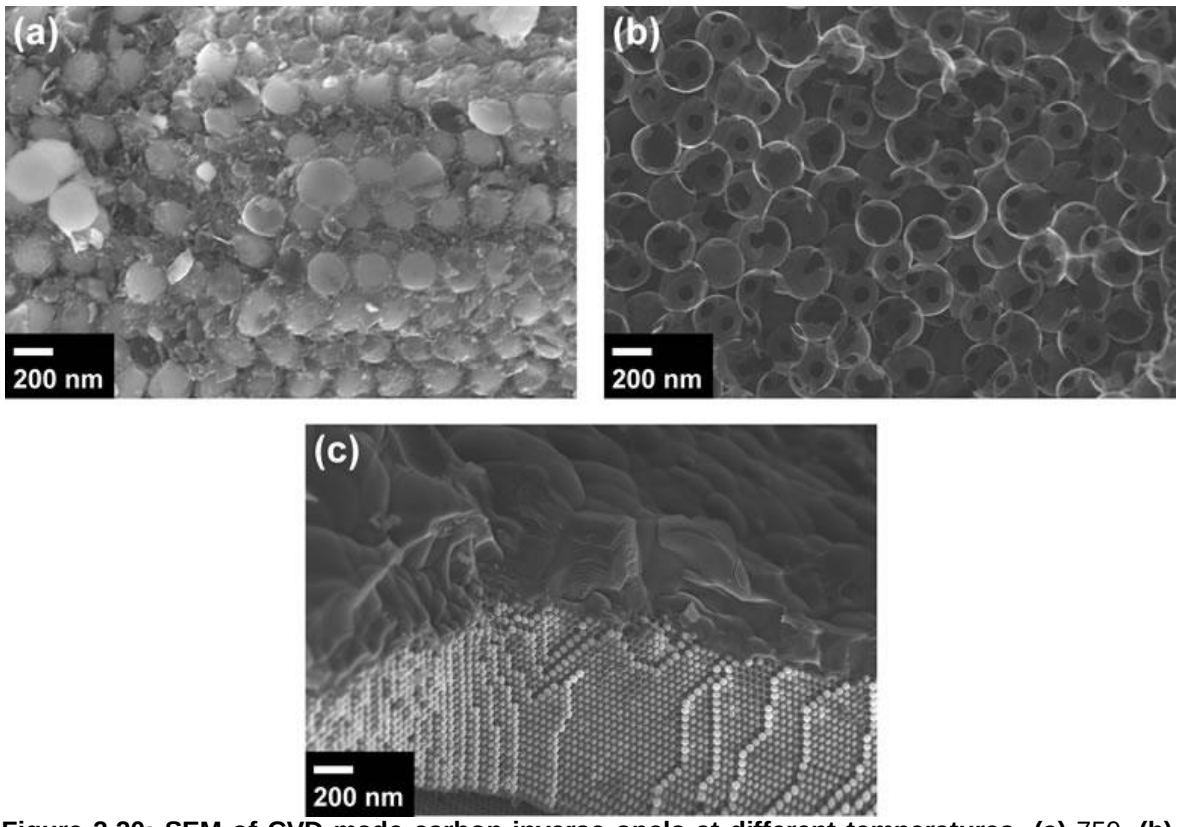

Figure 2.20: SEM of CVD made carbon inverse opals at different temperatures. (a) 750, **(b)** 800 and **(c)** 850^{o} using conditions from CVD21.

Due to the similarity between the refractive indexes of the opal (n=1.44) and chloroform (n=1.4), the sample shows certain degree of transmission in chloroform when the opal is cut along the (111) and the (101) plane (Figure 2.21 b and d), here the carbon layer covering the silica spheres is thin enough to allow certain degree of light transmission. For a two second CVD process, only the (101) plane cut exhibits some transmission (Figure 2.21 f) even though it has a higher content of carbon according to EDX spectroscopy data. The layers of carbon in both opal cuts only cover the surface of the silica nanoparticles (Figure 2.21 i and j). Y. A. Vlasov et al. [34] have demonstrated that a green opal transmits more light in glycerin for a (110) surface plane than a (111) surface plane. Results related to carbon coating using CVD clearly show this tendency, even though the carbon content is different (Table 2.3).

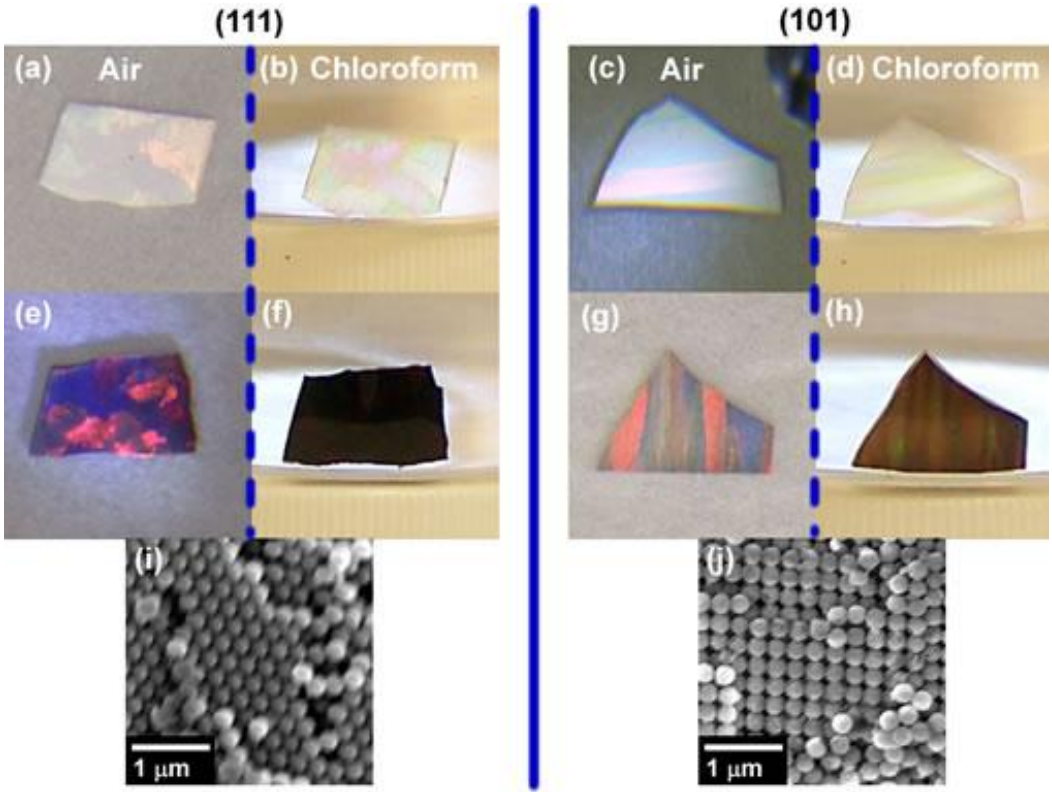

Figure 2.21: CVD-Opal different plane cuts. The left side images correspond to (111) planes surface and the right side correspond to (101) plane surface. First row is as set of photographs of the opal in air **(a, c)** and in chloroform **(b, d)**. The second row of images are 2 second CVD of opal in air **(e, g)** and in chloroform **(f, h)**. The last row corresponds to SEM images of **(i)** (111) and **(j)** (101) surface with 2 second CVD.

Table 2.3: EDX of opals in different plane cuts infiltrated with carbon in a 2 second CVD. (atomic % of each element)

Plane	(111)	(101)
C	3.32	4.53
O	59.31	62.71
Si	37.38	32.765

Different geometries and particle size opals were used. Clearly when using a thicker opal sample, the transmission of light decreases (Figure 2.22 b). This is due to the absorption of light in the material (this case carbon), which increases as its thickness increases. For the 300 and 200 nm opals (Figure 2.22 d) and h) respectively), we observed some transmission, but not for the 250 nm particle size (Figure 2.22 f).

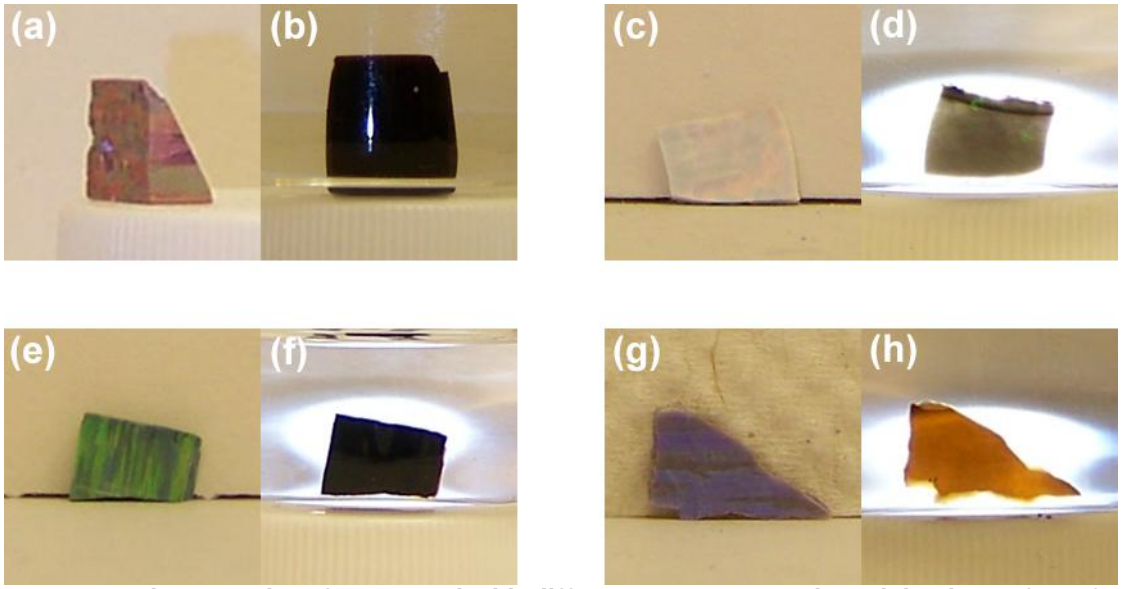

Figure 2.22: Photographs of CVD-Opal with different geometry and particle size. Prism of red opal (300 nm particle) in **(a)** air and **(b)** chloroform, red opal surface (111) plane in **(c)** air and **(d)** chloroform, green opal (250 nm particle) in **(e)** air and **(f)** chloroform, blue opal (200 nm particle) in **(g)** air and **(h)** chloroform.

2.5 Conclusions

When infiltrating the opal with a solution containing sucrose we were capable of obtaining thin walls and completely filled carbon inverse opal. The optimum sucrose concentration to fill the opal is 25 % by wt. This optimum condition may be a balance between viscosity which allows the penetration in the opal, and the amount of the precursor to fill the voids.

When infiltrating carbon by CVD we were capable of synthesizing thin walls resembling shell-like structures as well as semi-filled carbon inverse opal. In order to have a layer of carbon in the opal capable of allowing the transmittance of light, a short CVD reaction is needed, and the opals with particle sizes of 200 and 300 nm are capable of showing certain degree of transmittance in chloroform.

This chapter demonstrates that it is possible to synthesize different wall thicknesses using a solution containing carbon, or by CVD. These methods may be useful for controlling specific physico-chemical properties of the opals such as, stiffness or high surface area.

2.6 References

1. *Comparative analysis of sedimentary and volcanic precious opals from Australia.* **A.G. Smallwood, P.S. Thomas, A.S. Ray.** J. Aust. Cer. Soc., Vol. 44, pp. 17-22.
2. *Manual of mineralogy.* **J. D. Dana, C. Klein, C. S. Hurlbut.** [ed.] C. S. Hurlbut C. Klein. s.l. : Wiley, 1985.
3. *Controlled growth of monodisperse silica.* **W. Stober, A. Fink and E. Bohn.** 1968, J. Colloid Interface Sci., Vol. 26, p. 62.
4. *Sphere templating methods for periodic porous solids.* **Stein, A.** 2001, Micropor.Mesopor. Mater., Vols. 44-45, pp. 227-239.
5. *Chalcogenide inverted opal photonic crystal as infrared pigments.* **A. E. Aliev, A. A. Zakhidov, R. H. Baughman, E. Yablonovitch.** 2006, Int. J. Nanosc., Vol. 5, pp. 157-172.
6. *Crystallization of hard-sphere colloids in microgravity.* **Woodcock, L. V.** 1997, Nature, Vol. 387, p. 883.
7. *Entropy difference between crystal phases.* **P. G. Bolhuis, D. Frenkel, S.-C. Mau, D. A. Huse.** 1997, Nature, Vol. 388, p. 236.
8. *Stacking entropy of hard-sphere crystals.* **S.-C. Mau, D. A. Huse.** 1999, Phys. Rev. E, Vol. 59, p. 4396.
9. *Template-assisted self-assembly: A practical route to complex aggregates of monodispersed colloids with well-defined sizes, shapes, and structures.* **Y. Yin, Yu Lu, B. Gates, Y. Xia.** 2001, J. Am. Chem. Soc., Vol. 123, pp. 8718-8729.
10. *Self-assembly patterning of colloidal crystals constructed from opal structure or NaCl structure.* **Y. Masuda, T. Itoh, M. Itoh, K. Koumoto.** 2004, Langmuir, Vol. 20, pp. 5588-5592.
11. *Macroporous materials-electrochemically grown photonic crystals.* **P. V. Brauna, P. Wiltzius.** 2002, Current Opinion in Colloid and Interface Science, Vol. 7, pp. 116-123.
12. *Manifestation of intrinsic defects in optical properties of self-organized opal photonic crystals.* 2000, Phys. Rev. E, Vol. 61, p. 5784.
13. *Effect of electrostatic interactions on crystallization in binary colloidal films.* **A. Rugge, S. H. Tolbert.** 2002, Langmuir, Vol. 18, pp. 7057–7065.
14. *Two- and three-dimensional crystallization of polymeric microspheres by micromolding in capillaries.* **E. Kim, Y. Xia, G. M. Whitesides.** 1996, Adv. Mater., Vol. 8, pp. 245-247.
15. *Soft lithography.* **Y. Xia, G. M. Whitesides.** 1998, Angew. Chem. Int. Ed, Vol. 37, pp. 550-575.
16. *Polymer surface modification using microwave-oven generated plasma.* **B. T. Ginn, O. Steinbock.** 2003, Langmuir, Vol. 19, pp. 8117-8118.
17. *Regulación de regiones hidrofóbicas e hidrofílicas en materiales elastoméricos.* **Morelos-Gómez, A.** Universidad Autonoma de San Luis Potosi, San Luis Potosi : s.n., Septiembre 2005, Tesis profesional para optar por el título de Licenciatura en física.

18. *Micropatterns of colloidal assembly on chemically patterned surface.* **W. M. Choi, O. O. Park.** 2006, Colloids and surfaces. A, Vol. 277, pp. 131-135.
19. *Flow-controlled vertical deposition method for the fabrication of photonic crystals.* **Z. Zhou, X. S. Zhao.** 2004, Langmuir, Vol. 20, pp. 1524-1526.
20. *Suspended self-assembled opal membranes.* **A. K. Bohaty, I. Zharov.** 2006, Langmuir, Vol. 22, pp. 5533-5536.
21. *Opaline photonic crystals: how does self-assembly work.* **D. J. Norris, E. G. Arlinghaus, L. Meng, R. Heiny, L. E. Scriven.** 2004, Adv. Mater., Vol. 16, pp. 1393-1399.
22. *Convectively assembled nonspherical mushroom cap-based colloidal crystals.* **Liddell, Ian D. Hosein and Chekesha M.** 2007, Langmuir, Vol. 23, pp. 8810-8814.
23. *Single-crystal colloidal multilayers of controlled thickness.* **P. Jiang, J. F. Bertone, K. S. Hwang, and V. L. Colvin.** 1999, Chem. Mater., Vol. 11, pp. 2132-2140.
24. *Top-down approaches to the formation of silica nanoparticle patterns.* **D. Xia, D. Li, Z. Ku, Y. Luo, S. R. J. Brueck.** 2007, Langmuir, Vol. 23, pp. 5377-5385.
25. *Fabrication of high-quality colloidal crystals by a capillary-enhanced method.* **Y. W. Chung, I. C. Leu, J. H. Lee, M. H. Hon.** 2004, Appl. Phys. A, Vol. 79, pp. 2089–2092.
26. *Ordering and optical properties of monolayers and multilayers of silica spheres deposited by the Langmuir-Blodgett method.* **M. Szekeres, O. Kamalin, R. A. Schoonheydt, K. Wostyn, K. Clays, A. Persoons, I. Dékány.** 2002, J. Mater. Chem., Vol. 12, pp. 3268-3274.
27. *Assembly of mesoscale particles over large areas and its application in fabricating tunable optical filters.* **Xia, Sang Hyun Park and Younan.** 1999, Langmuir, Vol. 15, pp. 266-273.
28. *Photonic structures in biology.* **P. Vukusic, J. R. Sambles.** 2003, Nature, Vol. 424, p. 852.
29. *Controlled replication of butterfly wings for achieving tunable photonic properties.* **J. Huang, X. Wang, Z. L. Wang.** 2006, Nano Lett., Vol. 6, pp. 2325-2331.
30. *Ordering and optical properties of monolayers and multilayers of silica spheres deposited by the Langmuir–Blodgett method.* **M. Szekeres, O. Kamalin, R. A. Schoonheydt, K. Wostyn, Koen Clays, A. Persoonsc, I. Dékány.** 2002, J. Mater. Chem., Vol. 12, pp. 3268–3274.
31. *Single-crystal colloidal multilayers of controlled thickness.* **P. Jiang, J. F. Bertone, K. S. Hwang, V. L. Colvin.** 1999, Chem. Mater., Vol. 11, pp. 2132-2140.
32. *Fabrication of Three-Dimensional Photonic Crystals for Use in the Spectral Region from Ultraviolet to Near-Infrared.* **Y. Xia, B. Gates, S. H. Park.** 1999, J. Lightwave Tech. , Vol. 17, pp. 1956-1962.
33. *Silica colloidal crystals with uni- and multi-photonic bandgaps and controlled reflective properties.* **F. Piret, Y.-U. Kwon b, B.-L. Su.** 2009, Chem. Phys. Lett., Vol. 472, pp. 207–211.
34. *Manifestation of intrinsic defects in optical properties of self-organized opal photonic crystals.* **Y. A. Vlasov, V. N. Astratov, A. V. Baryshev, A. A. Kaplyanskii, O. Z. Karimov, M. F. Limonov.** Phys. Rev. E, Vol. 61, pp. 5784-5793.
35. *Photonic crystal chemical sensors: pH and ionic strength.* **K. Lee, S. A. Asher.** 2000, J. Am. Chem. Soc., Vol. 122, pp. 9534-9537.

36. *Photonic crystal glucose-sensing material for noninvasive monitoring of glucose in tear fluid.* **V. L. Alexeev, S. Das, D. N. Finegold, S. A. Asher.** 2004, Clin. Chemi., Vol. 50, pp. 2353-2360.
37. *Photonic band-gap structures.* **Yablonovitch, E.** 1993, J. Opt. Soc. Am. B, Vol. 10, pp. 283-295.
38. *Strong localization of photon in certain disordered dielectric superlattices.* **John, S.** 1987, Phys. Rev. Lett., Vol. 58, pp. 2486-2489.
39. *Electrical properties of a periodic porous carbon replica of opal.* **K. Yoshino., H. Kajii, Y. Kawagishi, M. Ozaki, A. A. Zakhidov, R. H. Baughman.** 1999, Jpn. J. Appl. Phys., Vol. 38, pp. 4926–4929.
40. *CVD Synthesis of carbon-based metallic photonic crystals.* **A. A. Zakhidov, I. I. Khayrullin, R. H. Baughman, Z. Iqbal.** 1999, NanoStruc. Mater., Vol. 12, pp. 1089-1095.
41. *Large-scale synthesis of a silicon photonic crystal with a complete three-dimensional bandgap near 1.5 micrometres.* **A. Blanco, E. Chomski, S. Grabtchak, M. Ibisate, S. John, S. W. Leonard, C. Lopez, F. Meseguer, H. Miguez, J. P. Mondia, G. A. Ozin, O. Toader, H. M. van Driel.** 2000, Nature, Vol. 405, pp. 437-440.
42. *Silicon inverse opal - a platform for photonic bandgap research.* **N. Tétreault, H. Míguez, G. A. Ozin.** 2004, Adv. Mater., Vol. 16, pp. 1471-1476.
43. *ZnO Inverse opals by chemical vapor deposition.* **B. H. Juárez, P. D. García, D. Golmayo, A. Blanco, C. López.** 2005, Adv. Mater., Vol. 17, pp. 2761–2765.
44. *Fabrication of 2D and 3D ordered porous ZnO films using 3D opal templates by electrodeposition.* **H. Yan, Y. Yang, Z. Fu, B. Yang, L. Xia, S. Fu, F. Li.** 2005, Electrochem. Comm., Vol. 2005, pp. 1117–1121.
45. *Superconductivity in Pb inverse opal.* **A. E. Aliev, S. B. Lee, A. A. Zakhidov, R. H. Baughman.** 2007, Physica C, Vol. 453, pp. 15-23.
46. *Periodic minimal surfaces.* **Mackay, A. L.** 1985, Physica B, Vol. 131, pp. 300-305.
47. *Diamond from graphite.* **A. L. Mackay, H. Terrones.** 1991, Nature, Vol. 355, p. 333.
48. *Hypothetical graphite structures with negative gaussian curvature.* **A. L. Mackay, H. Terrones.** 1993, Phil Trans. Soc. Lond. A, Vol. 343, pp. 113-127.
49. *Curved nanostructured materials.* **H. Terrones, M. Terrones.** 2003, New J. Phys., Vol. 5, pp. 126.1-126.37.
50. *Energetics of negatively curved graphitic carbon.* **T. Lenosky, X. Gonze, M. Teter, V. Elser.** 1992, Nature, Vol. 355, pp. 333-335.
51. *Negative-curvature analog of C60.* **D. Vanderbilt, J. Tersoff.** 1992, Phys. Rev. Lett., Vol. 68, pp. 511-513.
52. *Predicted new low energy forms of carbon.* **M. O'Keeffe, G. B. Adams, O. F. Sankey.** 1992, Phys. Rev. Lett., Vol. 68, pp. 2325-2328.
53. *the geometry of hypothetical curved graphite structures.* **H. Terrones, A. L. Mackay.** 1992, Carbon, Vol. 30, pp. 1251-1260.
54. *Triply periodic minimal surfaces decorated with curved graphite.* **H. Terrones, A. L. Mackay.** 1993, Chem. Phys. Lett., Vol. 207, pp. 45-50.
55. *Pentagons, heptagons and negative curvature in graphite microtubule grwoth.* **S. Ijima, T. Ichihashi, Y. Ando.** 1992, Nature, Vol. 356, pp. 776-778.

56. *Carbon nanotubes: synthesis and properties electronic devices and other emerging applications.* **Terrones, M.** 2004, Inter. Mater. Rev., Vol. 49, pp. 325-377.
57. *Carbon structures with three-dimensional periodicity at optical wavelengths.* **A. A. Zakhidov, R. H. Baughman, Z. Iqbal, C. Cui, I. Khayrullin, S. O. Dantas, J. Marti, V. G. Ralchenko.** 1998, Science, Vol. 282, pp. 897-901.
58. *Synthesis of ordered uniform, macroporous carbons with mesoporous walls templated by aggregates of polystyrene spheres and silica particles for use as a catalyst support in direct methanol fuel cells.* **G. S. Chai, I. S. Shin, J. -S. Yu.** 2004, Adv. Mater., Vol. 16, pp. 2057-2061.
59. *Controlling the shape and alignment of mesopores by confinement in colloidal crystals: designer pathways to silica monoliths with hierarchical porosity.* **F. Li, Z. Wang, N. S. Ergang, C. A. Fyfe, A. Stein.** 2007, Langmuir, Vol. 23, pp. 3996-4004.
60. *Replicating novel carbon nanostructures with 3D macroporous silica template.* **Z. Zhou, Q. Yan, F. Su, X. S. Zhao.** 2005, J. Mater. Chem., Vol. 15, pp. 2569–2574.
61. *Preparation of carbon microparticle assemblies from phenolic resin using an inverse opal templating method.* **G. Guan, K. Kusakabe, H. Ozono, M. Taneda, M. Uehara, H. Maeda.** 2007, J. Mater. Sci., Vol. 42, pp. 10196–10202.
62. *Synthesis of highly ordered carbon molecular sieves via template-mediated structural transformation.* **R. Ryoo, S. H. Joo, Shinae Jun.** 1999, J. Phys. Chem. B., Vol. 103, pp. 7743-7746.
63. *Ordered uniform porous carbon by carbonization of sugars.* **J. -S. Yu, S. B. Yoon, G. S. Chai.** 2001, Carbon, Vol. 39, pp. 1421 –1446.
64. *Template synthesis of polyacrylonitrile-based ordered macroporous materials and their derivatives.* **H. Bu, J. Rong, Z. Yang.** 2002, Macromol. Rapid Commun., Vol. 23, pp. 460-464.
65. *Crystallite growth in graphitizing and non-graphitizing carbons.* **Franklin, R. E.** 1951, Proc. Royal Soc. London. Series A, Math. and Phys. Science, Vol. 209, pp. 196-218.
66. *Negatively curved graphitici sheet model of amorphous carbon.* **S. J. Townsend, T. J. Lenosky, D. A. Muller. C. S. Nichols, V. Elser.** 1992, Phys. Rev. Lett., Vol. 69, pp. 921-924.
67. *New perspectives on the structure of graphitic carbons.* **Harris, P. J. F.** 2005, Critic. Rev. Solid State Mater. Sc., Vol. 30, pp. 235-253.
68. *Inverted colloidal crystals as three-dimensional cell scaffolds.* **N. A. Kotov, Y. Liu, S. Wang, C. Cumming, M. Eghtedari, G. Vargas, M. Motamedi, J. Nichols, J. Cortiella.** 2004, Langmuir, Vol. 20, pp. 7887-7892.
69. *Inverted-colloidal-crystal hydrogel matrices as three-dimensional cell scaffolds.* **Y. Zhang, S. Wang, M. Eghtedari, M. Motamedi, N. A. Kotov.** 2005, Adv. Mater., Vol. 15, pp. 725-731.
70. *Nanoscale mode selector in silicon waveguide for on chip nanofocusing applications.* **B. Desiatov, I. Goykhman, U. Levy.** 2009, Nano Lett., Vol. 10, pp. 3381-3386.
71. *Thermal properties of carbon inverse opal photonic crystals.* **A. E. Aliev, S. B. Lee, R. H. Baughman, A. A. Zakhidov.** 2007, J. Lum., Vol. 125, pp. 11-17.

72. *Removal of arsenic(III) from aqueous solution by activated carbons prepared from solvent extracted olive pulp and olive stones.* **T. Budinova, N. Petrov, M. Razvigorova, J. Parra, P. Galiatsatou.** 2006, Ind. Eng. Chem. Res., Vol. 45, pp. 1896-1901.
73. *Waste materials for activated carbon preparation and its use in aqueous-phase treatment: A review.* **J. M. Diasa, M. C.M. Alvim-Ferraza, M. F. Almeidaa, J. Rivera-Utrillab, M. Sánchez-Polo.** 2007, J. Env. Man., Vol. 85, pp. 833–846.
74. *Petroleum contaminated ground-water: remediation using activated carbon.* **M.J. Ayotamunoa, R. B. Kogbaraa, S.O.T. Ogajib, S.D. Probertb.** 2006, Appl. Energy , Vol. 83, pp. 1258-1264.
75. *Fabrication of new nanoporous carbons through silica templates and their application to the adsorption of bulky dyes.* **S. Han, K. Sohn, T. Hyeon.** 2000, Chem. Mater., Vol. 12, pp. 3337-3341.
76. *New nanoporous carbon materials with high adsorption capacity and rapid adsorption kinetics for removing humic acids.* **S. Han, S. Kim, H. Lim, W. Choi, H. Park, J. Yoon, T. Hyeon.** 2003, Micro. Meso. Mater., Vol. 58, pp. 131–135.
77. *Adsorption of polycyclic aromatic hydrocarbons by carbon nanomaterials.* **K.Yang, L. Zhu, B. Xing.** 2006, Environ. Sci. Technol., Vol. 40, pp. 1855-1861.
78. *Hydrogen storage in nanoporous carbon materials: myth and facts.* **P. Kowalczyk, R. Holyst, M. Terrones, H. Terrones.** 2007, Phys. Chem. Chem. Phys., Vol. 9, pp. 1786–1792.
79. *Molecular simulation of novel carbonaceous materials for hydrogen storage.* **D. Cao, P. Feng, J. Wu.** 2004, Nano Lett., Vol. 4, pp. 1489-1492.
80. *Hydrogen storage in activated carbon materials: Role of the nanoporous texture.* **N. Texier-Mandoki, J. Dentzer, T. Piquero, S. Saadallah, P. David, C. Vix-Guterl.** 2004, Carbon, Vol. 42, pp. 2735–2777.
81. *Hydrogen storage in spherical nanoporous carbons.* **E. Terrés, B. Panella, T. Hayashi, Y.A. Kim, M. Endo, J.M. Dominguez, M. Hirscher, H. Terrones, M. Terrones.** 2005, Chem. Phys. Lett., Vol. 403, pp. 363–366.
82. *Superoleophilic and superhydrophobic inverse opals for oil sensors.* **H. Li, J. Wang, L. Yang, Y. Song.** 2008, Adv. Funct. Mater., Vol. 18, pp. 1-7.
83. *Inverse opal carbons derived from a polymer precursor as electrode materials for electric double-layer capacitors.* **S. Tabata, Y. Isshiki, M. Watanabe, D. R. Wheeler, S. M. Brozik, R. Polsky.** 2008, J.l Elec. Soc., Vol. 155, pp. k42-k49.
84. *Synthesis and rate performance of monolithic maroporous carbon electrodes for lithium-ion secondary batteries.* **K. T. Lee, J. C. Lytle, N. S. Ergang, S. M. Oh, A. Stein.** 2005, Adv. Funct. Mater. , Vol. 15, pp. 547-556.
85. *Photonic crystal structures as a basis for a three-dimensionally interpenetrating electrochemical-cell system.* **N. S. Ergang, J. C. Lytle, K. T. Lee, S. M. Oh, W. H. Smyrl, A. Stein.** 2006, Adv. Mater., Vol. 18, pp. 1750–1753.
86. *Ordered nanoporous arrays of carbon supporting high dispersions of platinum nanoparticles.* **S. H. Joo, S. J. Choi, I. Oh, J. Kwak, Z. Liu, O. Terasaki, R. Ryoo.** 2001, Nature, Vol. 412, pp. 169-172.

87. *Synthesis of graphitic ordered macroporous carbon with a three-dimensional interconnected pore structure for electrochemical applications.* **F. Su, X. S. Zhao, Y. Wang, J. Zeng, Z. Zhou, J. Y. Lee.** 2005, J. Phys. Chem. B, Vol. 109, pp. 20200-20206.
88. *Tunable inverse opal hydrogel pH sensor.* **Y. -J. Lee, P. V. Braun.** 2003, Adv. Mater., Vol. 15, pp. 563-566.

3. Carbon Inverse Opal Doped with Nitrogen

3.1 Introduction

Nitrogen has five electrons in its outer shell and is therefore trivalent in most compounds. Common nitrogen functional groups include: amines, amides, nitro groups, imines, and enamines. It forms important industrial compounds such as ammonia, nitric acid, organic nitrates and cyanides. This element may be found in all living organisms, for example in amino acids, proteins and nucleic acids.

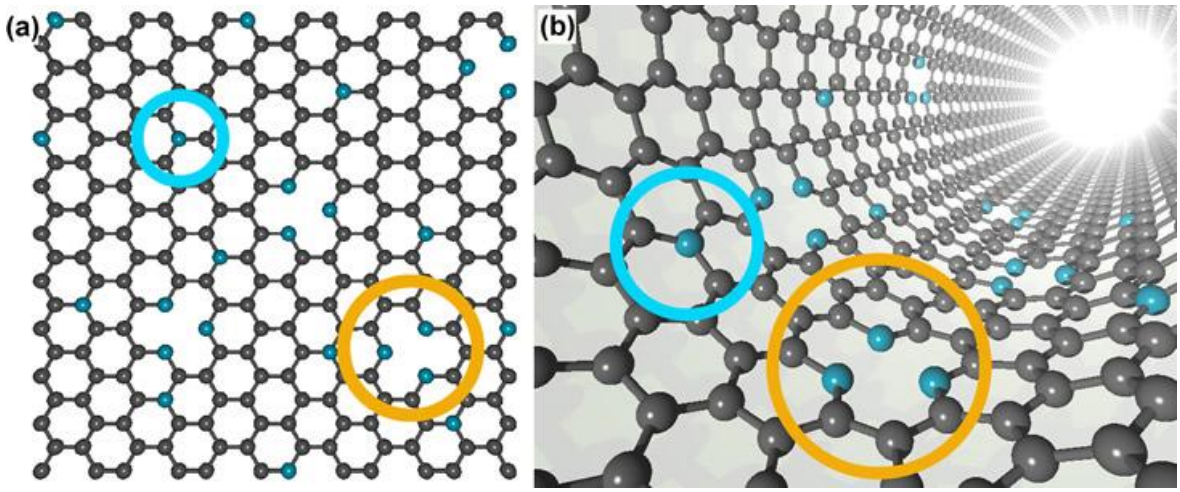

Figure 3.1: Nitrogen doped carbon materials. (a) Graphene sheet, and (**b)** carbon nanotube doped with pyridinc and substitutional nitrogen. Blue rings highlight substitutional nitrogen and orange rings highlights pyridinic nitrogen.

When nitrogen is bonded with carbon in an organic compound it can adopt sp (i. e. nitrile groups), sp^2 (i. e. pyrroles and amines) or sp^3 (quaternary bonding) hybridization. Since it has one electron more than carbon it can donate a free electron to the system. Nitrogen can be introduced into the hexagonal lattice of carbon in two manners:

Substitutional – nitrogen replaces the position of carbon, maintaining the hexagonal lattice, where nitrogen has an sp^2 hybridization (Figure 3.1 blue rings).

Pyridinic – a carbon atom is withdrawn from the lattice and its first neighbors are replaced by nitrogen, here nitrogen has an sp hybridization (Figure 3.1 orange rings).

3.1.1 Synthesis methods

Doping of porous carbon materials has been done by different methods:

- Reacting porous carbon with gas sources containing nitrogen [1].
- Cocarbonization of nitrogen-free and nitrogen-containing precursors [2].
- Carbonization of a precursor containing nitrogen [3].

As a nitrogen containing precursor, commonly polymers have been infiltrated in templates in order to produce a carbon-nitrogen porous material. Concerning carbon inverse opals, polyacrylonitrile has been used by H. Bu et al [4] but annealing at 1000 ^{o}C reduces the nitrogen content. Polyaniline has been infiltrated in mesoporous silica in order to produce an inverted structure which contains carbon and nitrogen [5].

Chemical vapor deposition with acetonitrile has been used to impregnate a zeolite producing a nitrogen doped carbon inverse structure [6]. Furthermore, an ammonium-form zeolite was used as a template to impregnate with furfuryl alcohol and used to synthesize a microporous carbon doped with nitrogen; here the nitrogen is provided by the ammonium cation from the zeolite [7].

3.1.2 Tunable photonic crystals

Ordered porous structures are very interesting due to their optical properties in the ultraviolet, visible and infrared region. Most of the photonic crystal materials depend upon the periodicity in order to determine the diffraction wavelength, regarding this parameter, several works have been done in order to change this periodicity upon external forces, and others have infiltrated foreign molecules such as oils or even liquid crystals to change the optical properties. Another way to vary the optical properties is by doping the material with other elements. All these routes will be discussed in this section.

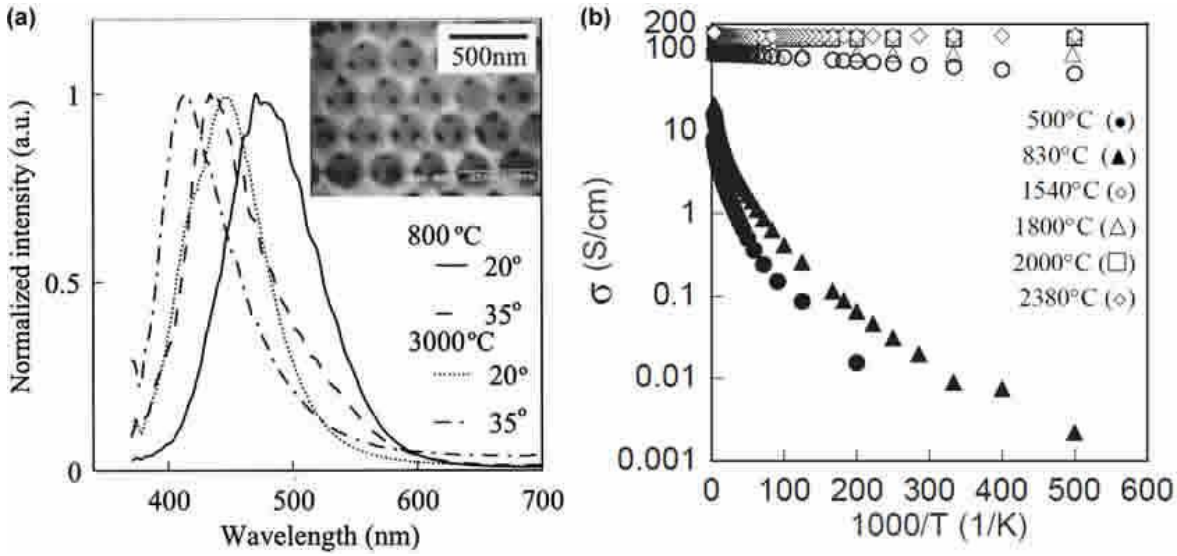

Figure 3.2: (a) Reflection spectra as a function of incident angle for the red opal carbon replicas with HTTs of 800 and 3000 °C. **(b)** Temperature dependence of the conductivity of various phenol replicas with HTT between 500 and 2380 ^{o}C (Images from ref. **[8]**).

The heat treatment of a carbon inverse opal can reduce the pore size, thus blue shifting its diffraction peaks (Figure 3.2 a). The gradual heat treatment of the sample showed an increase in its conductivity up to 450 S/cm at room temperature when heated at 3000 ^{o}C (Figure 3.2 b). They also show an increase in its negative magnetoconductance when heat treated at higher temperatures [8; 9].

A polymeric inverse opal hydrogel has been fabricated with the ability to swell at different ratios depending upon the pH and ionic strength, this shifts the diffraction wavelength (Figure 3.3 a). This swelling is reversible to a certain percent for a given number of cycles **[10]**.

The optical properties of opals and inverse opals have been tuned by the infiltration of nematic liquid crystals. The reflection spectrum varies as the nematic axes become parallel to the light propagation although the influence decreases in the experiments. However, the reflection peak can be tuned upon the electric field applied [11; 12] (Figure 3.3 b).

Theoretically P. Halevi et al. have proposed that a semiconductor photonic crystal may be tunable by external agents such as doping or temperature. For example, a Ge sample is delta doped by donor impurities; if the impurity density increases then the photonic band gap shall shift [13] (Figure 3.3 c). This concept has been observed by a K intercalation in a carbon inverse opal, observing a shift of the diffraction wavelength to a greater wavelength (Figure 3.3 d).

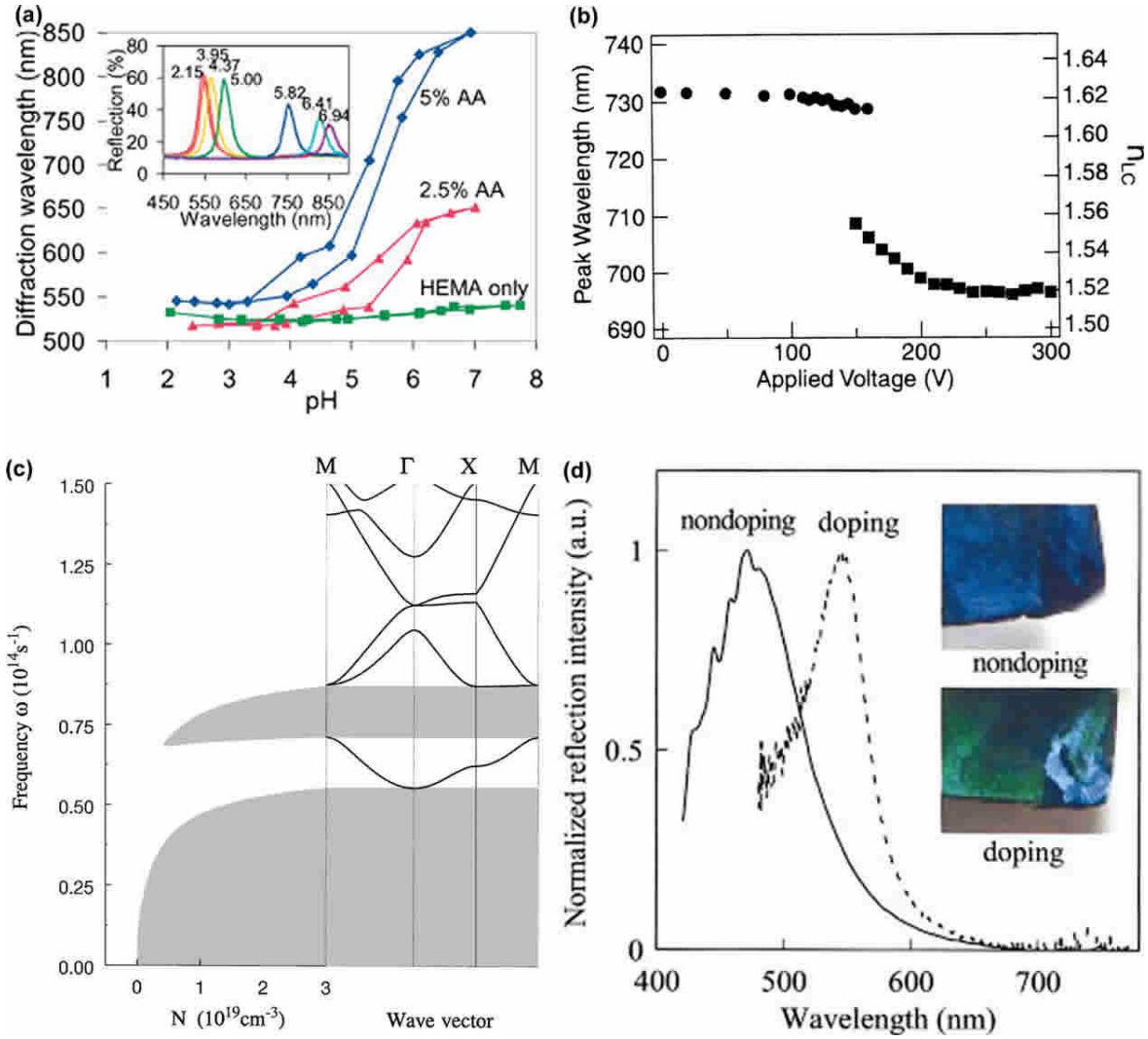

Figure 3.3: Tunable photonic crystals. (a) Diffraction wavelength vs. pH of a polymeric opal hydrogel (Image from ref. **[10]**). **(b)** Applied voltage dependence of the reflection peak wavelength of the inverse opal infiltrated with a liquid crystal (Image from ref. **[12]**). **(c)** Photonic band structure of circular cylinders generated by delta doping of an intrinsic Ge host. The right side of the figure corresponds to N = 3 X 10^{19} donor atoms per cm^3. The left side shows the variation of the two PBGs with N (Image from ref. **[13]**). **(d)** Diffraction wavelength shift caused by a K intercalation in a carbon inverse opal (Image from ref. **[8]**).

3.2 Possible properties and applications

Doped materials are commonly used in the semiconductor industry in order to alter its electrical properties; this may also be applied for carbon materials. When carbon structures are doped with nitrogen they may change its chemical, physical and even biocompatible properties; these amazing properties will be discussed in the following.

3.2.1 Optical properties

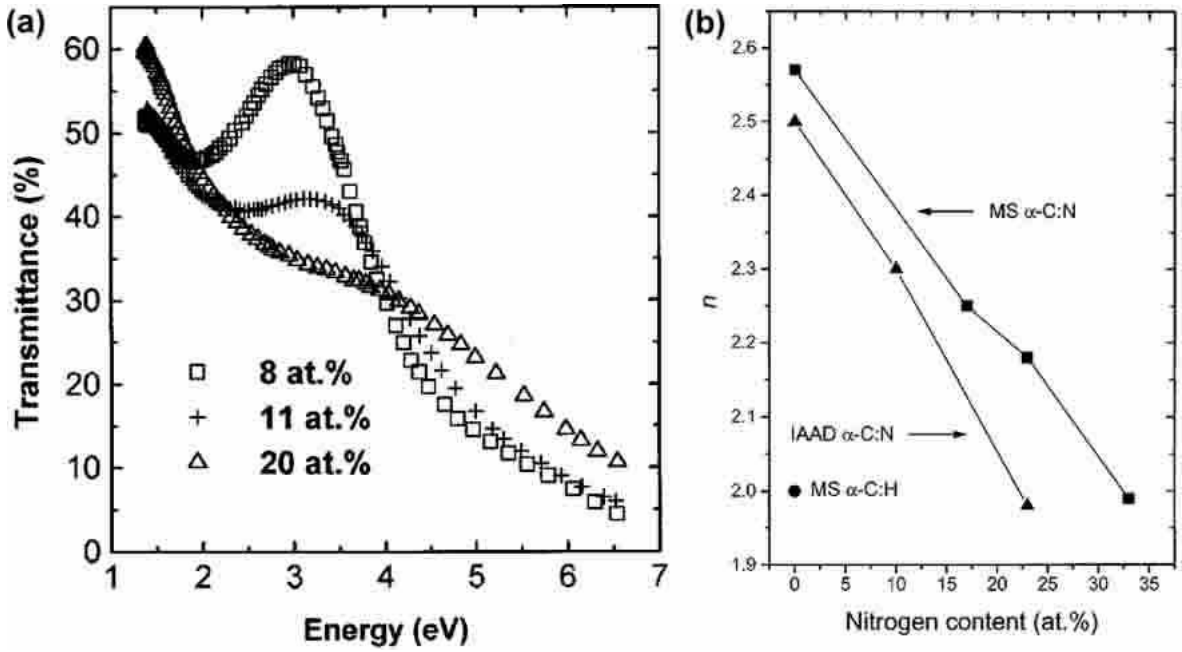

Figure 3.4: Optical properties of nitrogen doped carbon films. (a) Ultraviolet–visible transmittance spectra of a-C:N films with different nitrogen concentrations (Image from ref. **[14]**). **(b)** Refractive index *n* vs. nitrogen content in nitrogen doped carbon films (Image from ref. **[15]**).

When carbon materials are doped with nitrogen they also present variations in their optical properties. For example, the optical bandgap shifts when an amorphous carbon film is doped with nitrogen under different pressures during the arc deposition. The optical bandgap energy reaches a maximum at a certain nitrogen concentration and above this it may decrease to a lower energy than the pure carbon sample [16]. The real and imaginary part of the dielectric constant increase in value when raising the nitrogen content of an amorphous carbon film deposited by arc deposition, this variation agrees with the measured refractive index values [14], thus increasing the diffraction energy (Figure 3.4 a). Although other groups report otherwise, where at higher nitrogen content in amorphous carbon films the refractive index decreases [15] (Figure 3.4 b). All these works show that the optical properties of doped materials vary in different manners and further work needs to be performed in order to understand this phenomenon.

3.2.2 Conductivity

Since nitrogen has one electron more than carbon, it will add one electron per nitrogen in to the carbon system, thus it will increase its reactivity [17]. Also, these added electrons shall increase the conductivity, due to the isolated pair of electrons introduced by nitrogen (substitutional doping) which are conjugated with the π orbitals in a graphitic structure [18; 19; 20; 21]. In the case of doping carbon nanotubes with nitrogen there is a strong π peak, capable of converting a

semiconducting (zig-zag) carbon nanotube in to metallic (Figure 3.5 a) [22; 19]. Furthermore, the inverse behavior has been observed for graphene, were it originally has a linear current vs. voltage behavior but when it is doped with nitrogen this structure behaves as an n-type semiconductor (Figure 3.5 b) [23]. In amorphous carbon films, the resistivity changes in a non-linear manner with nitrogen content, reaching a minimum then increasing (Figure 3.5 c) [24]. These electronic properties make them candidates for electron field emission [25; 26; 27]. In a different study, films of pyrolized pyrazine have been studied and reported to have conductivity between 200 and 300 S cm^{-1} when pyrolized at 850 ^{o}C [28; 29].

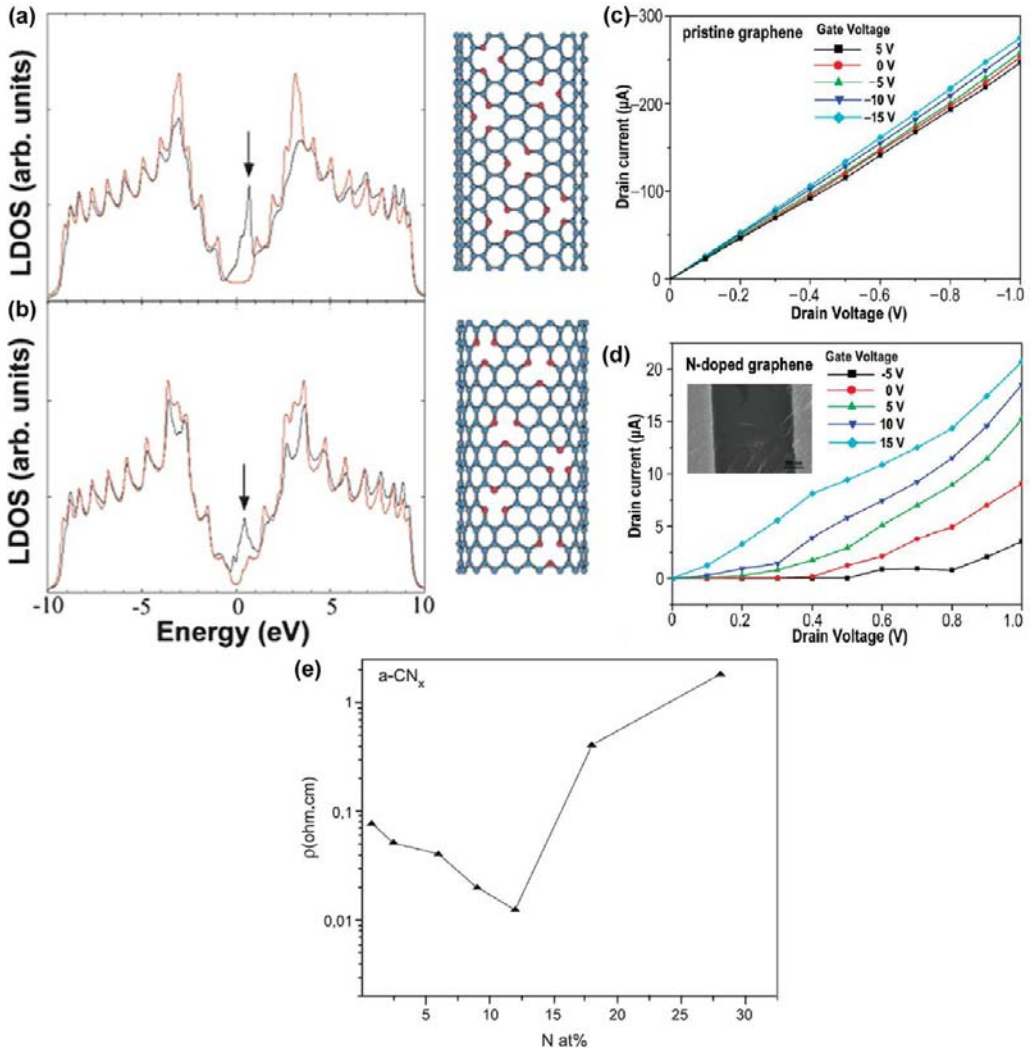

Figure 3.5: Electronic properties of carbon nanotubes doped with nitrogen. Density of states (DOS) of a doped (blue) and non (red) nitrogen doped **(a)** armchair and **(b)** zig-zag carbon nanotube (red line undoped, black line doped) (images from ref. **[22]**). I_{ds}/V_{ds} characteristics at various Vg for the **(c)** pristine graphene and the **(d)** N-doped graphene FET device (images from ref. **[23]**). **(e)** Resistivity as a function of nitrogen concentration in a amorphous carbon film (image from ref. **[24]**).

3.2.3 Biocompatibility

Nitrogen doped carbon materials have shown a higher chemical reactivity compared with their undoped counterparts. This has been studied theoretically and experimentally for O_2 reduction on nitrogen doped graphite, where substitutional nitrogen is more favorable than a non-doped structure [30]. Now for a porous carbon, it exhibits a higher catalytic activity for NO reduction when increasing its nitrogen content [31].

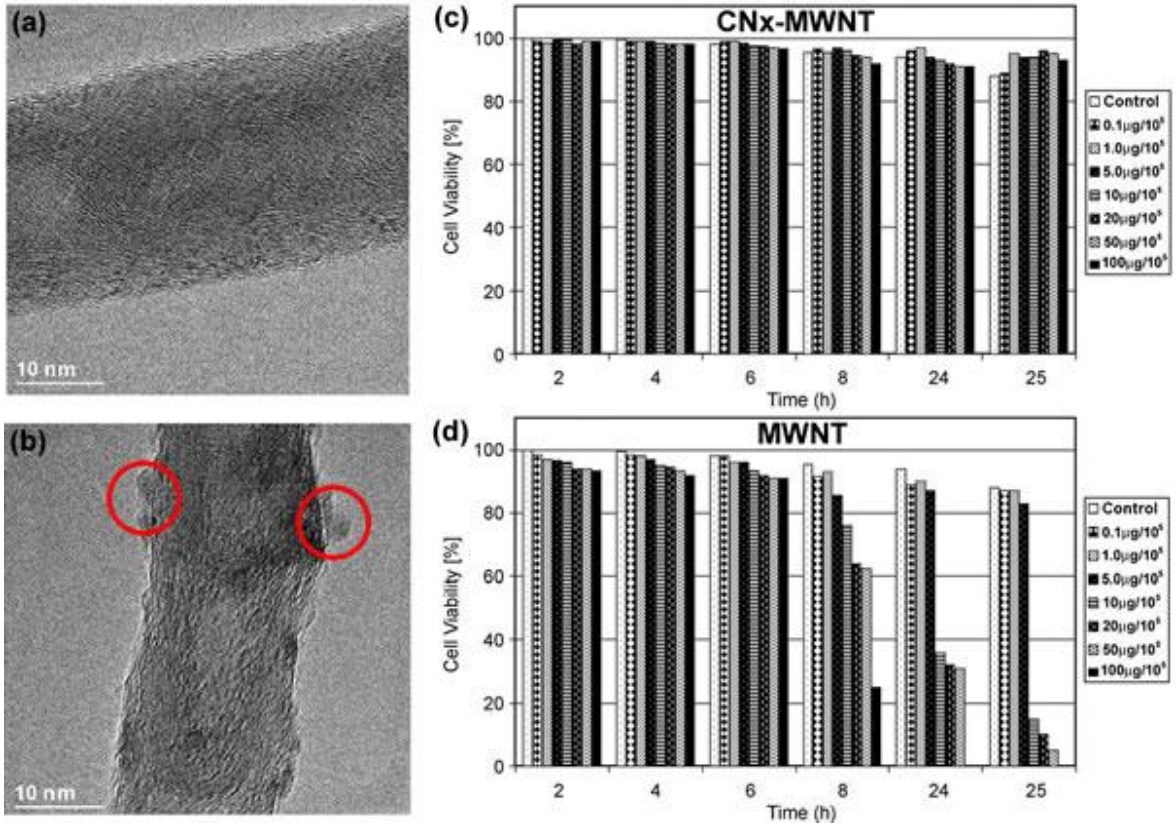

Figure 3.6: Transmission electron microscope images of **(a)** CN_x nanotubes and **(b)** glucose oxidase immobilized (red circle) on CN_x nanotubes (images from ref. **[32]**). Cell viability of entamoeba histolytica trophozoites incubated with different concentrations of **(c)** CN_x multiwall nanotubes (MWNT) and **(d)** undoped MWNT (images from ref. **[33]**).

If a carbon nanostructure is doped or functionalized with one of the mentioned elements (N or O) can increase its biocompatibility and biochemistry. For example, glucose oxidase has been immobilized on nitrogen doped carbon nanotubes (Figure 3.6 a) and b), this system exhibits good electrocatalytic bioactivity to glucose [32; 34]. Further on, metallo-proteins have been successfully immobilized on acid treated nitrogen doped carbon nanotubes, possibly due to hydrogen bonds between amino acid chains from the proteins and carboxyl moieties of the carbon nanotubes. Here, the nitrogen doped structures present a higher coverage when compared with the undoped materials [35]. Nitrogen doped carbon nanotubes have been proven to be non-toxic for cultures of *Entamoeba*

histolytica (Figure 3.6 c), which suggests higher biocompatibility, although it's undoped counterpart had the opposite effect [33].

On the other hand, the nitrogen sites can also act as an attractor for other molecules, once these foreign molecules interact with the carbon nanotube it may change the electronic properties (i. e. conductivity) and be used as a sensor [36; 37; 38], where the foreign entity may be chemisorbed or physisorbed.

3.3 Experimental methodology

Here two organic molecules were used as a precursor, one of them is a sugar and the other is an aromatic molecule containing nitrogen. These precursors are diluted in a water solution, with sulfuric acid as dehydrating agent and then infiltrated inside the opal or the solutions containing silica nanoparticles. Afterwards, the silica-carbon composite is annealed and the SiO_2 is etched. This section will describe the experimental and characterization methodology for nitrogen doped carbon inverse opal.

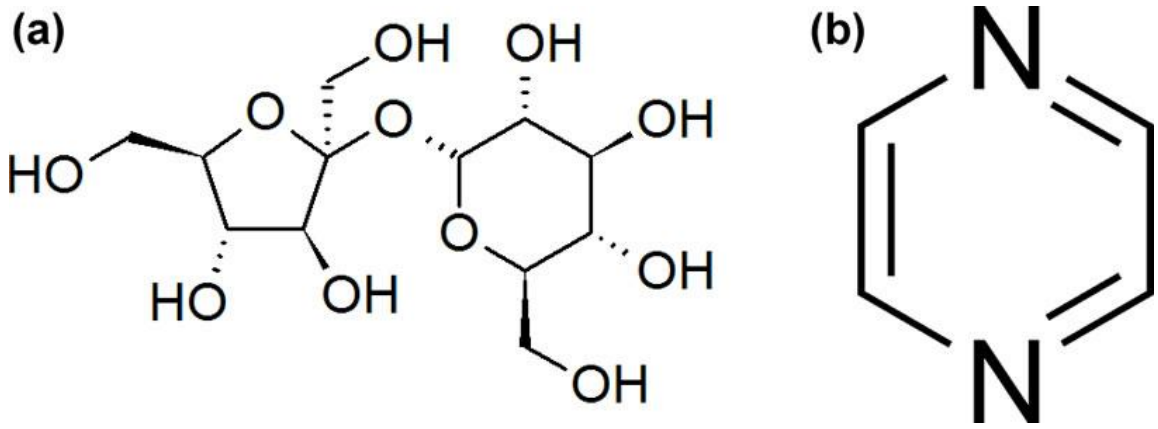

Figure 3.7: Carbon and nitogen source. (a) Sucrose as a carbon source and **(b)** pyrazine as a carbon and nitrogen source.

Opals with 300 nm particles ((101) surface plane), 100, and 10 nm (100 and 10 nm particles in a disordered array) were held in a solution of sucrose, pyrazine as nitrogen precursor (Figure 3.7), sulphuric acid (H_2SO_4) and water (according to Table 3.3.1 and Table 3.2) at 80^o C during 6.5 hours. Preliminary experiments were not successful when using only pyrazine, for this reason sucrose is added. Sucrose and sulphuric acid react leaving carbon and hydrated sulphuric acid in the medium, when increasing the amount of pyrazine we also added more sulphuric acid in order to avoid coagulation of the silica nanoparticles. After the evaporation of water, the samples were heat treated at 1000 ^{o}C during

one hour. Finally, these were immersed in HF (30% in water) during approximately one day to remove the silica nanoparticles.

Table 3.3.1: Carbon and nitrogen source solution concentrations for 300 and 100 nm particles. Quantities are in % by wt, the letter "y" stands for the particle size used (100 or 300 nm) as specified in the discussion below.

	ClOy	ClOy-N1	ClOy-N2	ClOy-N3
Sucrose	25.00	16.67	12.50	8.33
Pyrazine	0.00	8.33	12.50	16.67
Water	72.42	70.83	68.75	66.67
Sulphuric acid	2.58	4.17	6.25	8.33

Table 3.2: Carbon and nitrogen source solution concentrations for 12 nm particles. Quantities are in % by wt.

% by wt.	CIO10	CIO10-N1	CIO10-N2	CIO10-N3
Sucrose	8.502	8.167	5.455	2.312
Silica particles	17.004	16.611	16.555	16.611
Water	73.618	71.916	71.675	71.916
Sulphuric acid	0.876	0.856	0.853	0.856
Pyrazine	0.000	2.450	5.462	8.305

These samples were analyzed by scanning electron microscopy (SEM) (Zeiss-LEO Model 1530, Zeiss Supra 40 and XL 30 SFEG FEI operated between 10 – 20 kV),energy dispersive X-Ray (EDX), transmission electron microscopy (TEM) (HRTEM FEI TECNAI F30 STWIN G2), X-Ray diffraction (XRD) (Difractometer D8 Advanced Bruker), Raman spectroscopy (Renishaw inVia Raman microscope, Ar laser 514.5 nm and Jobin Yvon LabRam HR Micro-Raman), UV-VIS spectroscopy (Perkin Elmer Lambda 900 UV-Vis/NIR Spectrophotometer). Thermogravimetric analyses (TGA) of all samples were also performed (Cahn Versatherm HS; maximum sensitivity of 0.1 mg at a heating rate of 5 ^{o}C/min under air atmosphere). X-Ray photon spectroscopy was made with XPS110 electron analyzer employing monocromatic Al Ka X-ray ($h\omega$=1486.6 eV) at 100 W and electron take-off angle of 90°. The spectrometer is equipped with a seven-channel hemispherical detector. The lens mode using were small area XPS 600 µm with slit 0 and aperture 4. Pass energy of 100 eV for surveys and 50 eV for high resolution were used during the analysis of sample. All analyses were performed at a vacuum pressure of 3 x 10^{-10} Torr. The XPS spectra analysis was carried out using the AAnalyzer software [39].

3.4 Results and discussions

3.4.1 Pristine samples

When observing the SEM images of the carbon inverse opals doped with nitrogen using 10, 100, and 300 nm silica particles there are no morphological changes (Figure 3.8), meaning that the introduction of nitrogen did not inhibit the production of uniform carbon walls. It is clear that the synthesis procedure creates the inverse structure of the synthetic opal, maintaining the periodicity of the original opal. An average of 100 measurements were made to obtain average pore sizes, for all cases the overall average of pore size is around 292 ± 6 nm for a 302 nm particle opal, 112 ± 1 nm for a 117 nm particle, and 8 ± 0.5 nm for a 11 nm particle opal, the reduction of the pore size might be caused by the sintering of the silica particles during the heat treatment at 1000 ^{o}C. When an energy dispersive X-Ray analysis was done for CIO300 samples the content of nitrogen (Table 3.3) varied according to the concentration of pyrazine used in the solutions, this was made in order to corroborate the introduction of nitrogen in the carbon inverse opal.

TEM images of the carbon inverse opal show an ordered array of pores for the 300 nm pore size (Figure 3.9 a and d), however for smaller pore sizes these are disordered (Figure 3.9 g and j). The high magnification images show that all samples present a structure that is not lamellar like graphite (Figure 3.9 c,f,i and l). It is worthy to mention that the sample CIO300 presents small crystal like domains, which are not observed for the other analyzed samples. Now, when doped with the highest nitrogen content it is clear that it exhibits a disordered array of curved structures lacking the presence of crystal like structures (Figure 3.9 l). Similar curved structures have been observed by Harris et al. [40] proposing that these structures consist of Schwarzite-like fragments.

Table 3.3. EDX analysis of CIO300-Nx. Carbon inverse opal doped with nitrogen at different pyrazine concentrations using 300 nm silica particles.

At%	CIO300	CIO300-N1	CIO300-N2	CIO300-N3
C	96.07	94.42	93.52	92.32
N	0.00	3.10	3.24	4.17
O	3.35	2.12	2.44	2.80
Si	0.29	0.21	0.21	0.29
S	0.29	0.14	0.59	0.41

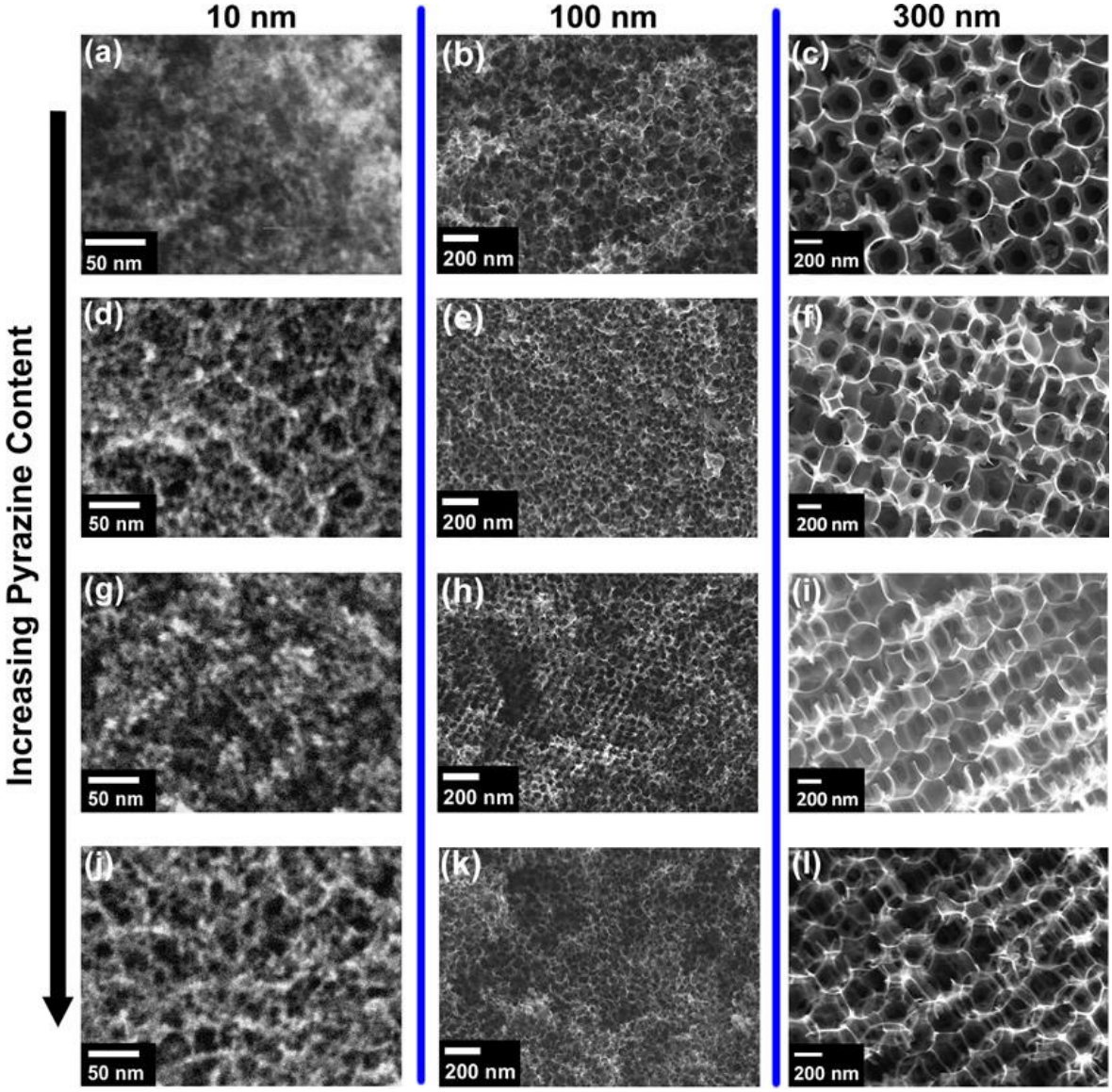

Figure 3.8: SEM images of carbon inverse opals. Particles of 10 nm (left column), 100 nm (middle column) and 300 nm (right column), with the solution concentrations **(a-c)** ClOy, **(d-f)** ClOy-N1, **(g-i)** ClOy-N2 and **(j-l)** ClOy-N3.

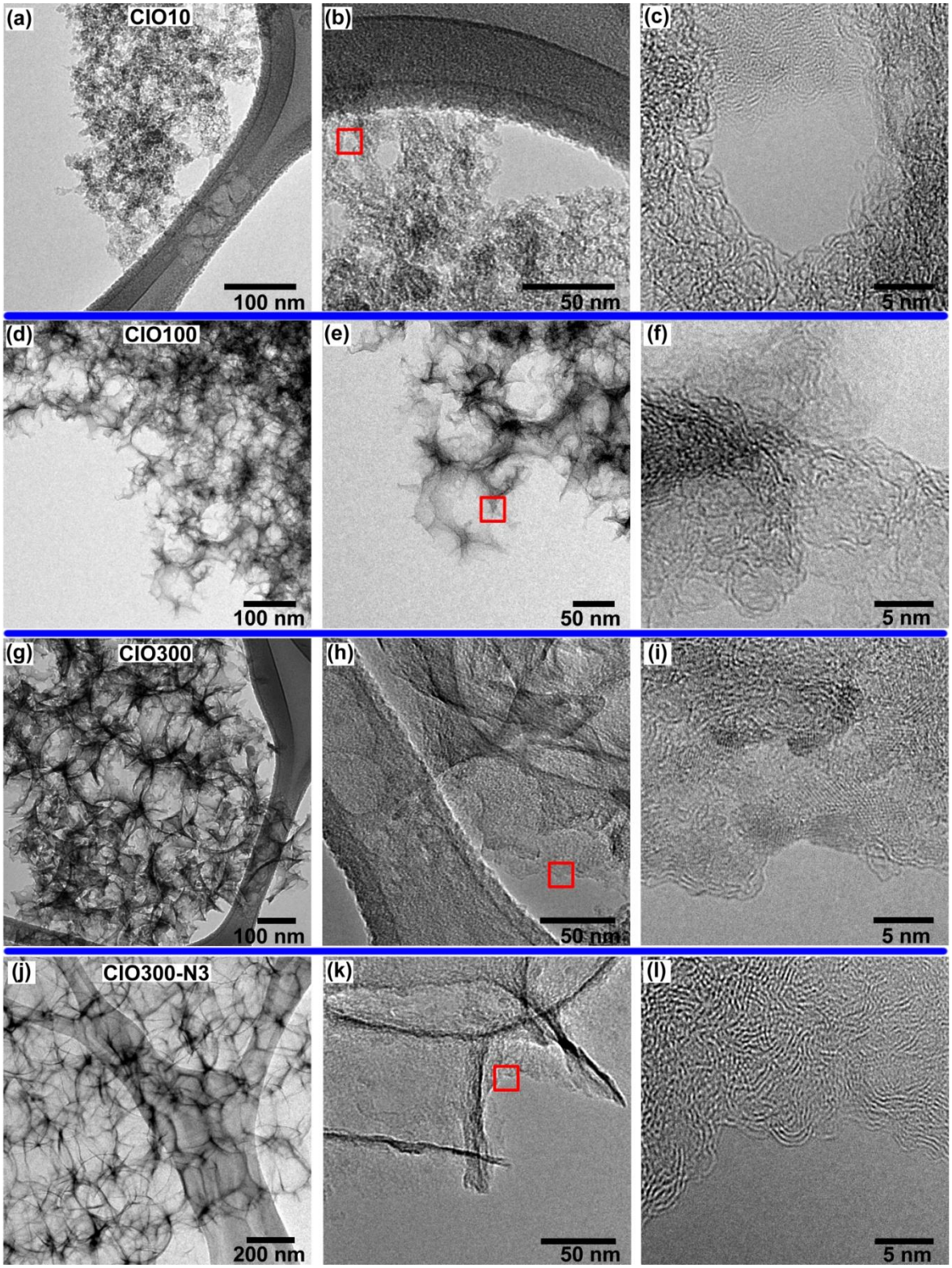

Figure 3.9: Transmission electron microscopy (TEM) images of carbon inverse opal **(a-c)** 10, **(d-f)** 100 and **(g-i)** 300 nm pore size. TEM images of **(i-k)** carbon inverse opal doped with the highest content of nitrogen (N3). **(Left)** Low magnification TEM images show porous structure and **(Right)** high magnification TEM images showing the structure of the carbon walls.

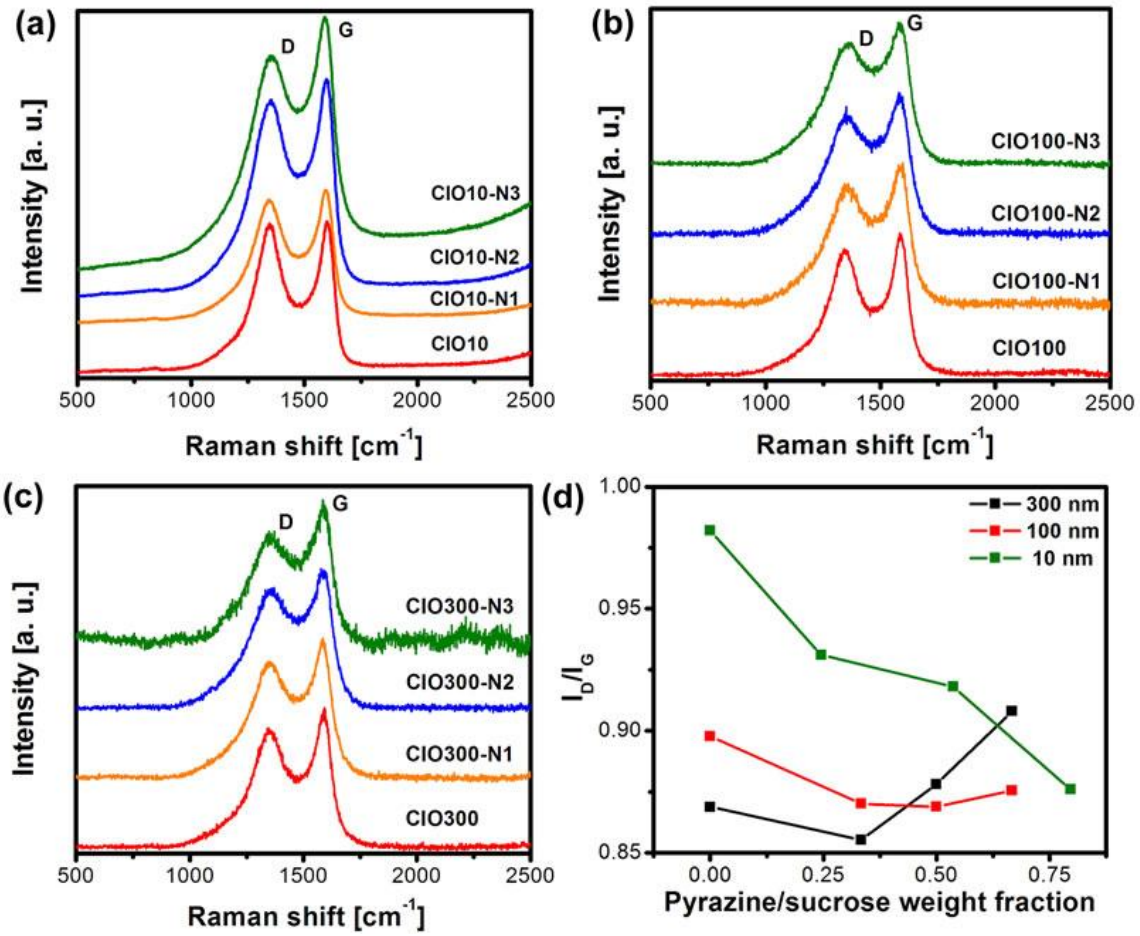

Figure 3.10: Raman spectroscopy ClOy-Nx. Carbon inverse opal doped with Nitrogen at different concentrations of pyrazine using **(a)** 10nm, **(b)** 100 and **(c)** 300 nm silica nanoparticles. **(d)** Tendency of I_D/I_G ratio of carbon inverse opals doped with different concentrations of nitrogen and silica nanoparticle sizes.

Figure 3.10 a-c shows the Raman spectra of the carbon inverse opals made with 10, 100 and 300 nm silica particles, respectively, all samples present D and G band at 1350 and 1590 cm^{-1}, respectively. The values for I_D/I_G are plotted in Figure 3.10 d for 10, 100 and 300 nm pore size. It is clear that using smaller silica nanoparticles and increasing the concentration of pyrazine in the solution this increases considerably the structural ordering of the samples, reflected by a lower value of I_D/I_G, the range of the measured ratio is between 0.98 and 0.85. Futhermore, when analyzing the position of the D and G peak there is a clear upshift for the D peak, for all the particle sizes, when increasing the amount of pyrazine used for synthesis, however the G peak does not present a clear tendency (Table 3.4). The shift in the D peak may indicate a higher degree of doping as observed by L. G. Bulusheva et al. [41]

Table 3.4: Position of peaks (cm^{-1}) in the Raman spectra measured for the samples synthesized with conditions ClOy, ClOy-N1, ClOy-N2 and ClOy-N3, the letter "y" corresponds to the particle size used (10, 100 and 300 nm). Notice that the D peak upshifts with increasing pyrazine content.

D	ClOy	ClOy-N1	ClOy-N2	ClOy-N3
10 nm	1346	1344	1350	1353
100 nm	1342	1352	1354	1365
300 nm	1344	1353	1356	1358
G				
10 nm	1600	1594	1598	1590
100 nm	1583	1589	1581	1580
300 nm	1592	1586	1588	1585

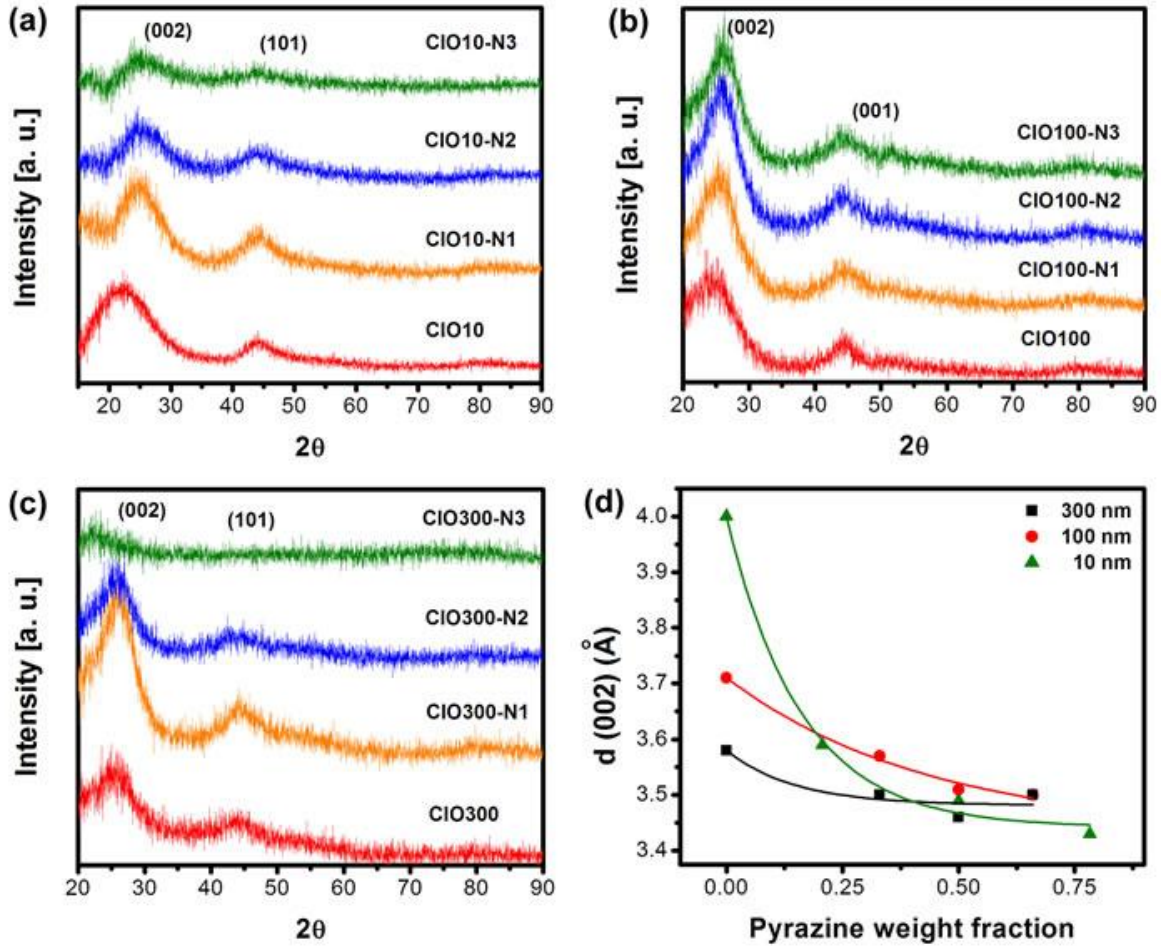

Figure 3.11: X-Ray diffraction patterns of ClOy-Nx. Carbon inverse opals made with **(a)** 12 nm, **(b)** 100 nm and **(c)** 300 nm size particles at different concentrations of pyrazine. **(d)** Interplanar distance of plane (002) of carbon inverse opals with different particle size and concentration of pyrazine.

X-ray diffraction analyses of all the samples were carried out, showing the presence of peaks corresponding to the (002) and (101) planes of graphite (Figure

3.11 a-c). When observing the undoped carbon inverse opals, it is clear that when using smaller particles the (002) interplanar distance increases. However, when the content of pyrazine increases the interplanar distance of the (002) plane tends to decrease for all cases.

Considering the classification of pyrolized carbon sources made by R. E. Franklin [42]; a non graphitizable carbon source contains a small amount of hydrogen and a higher amount of oxygen in its molecular composition, in contrast the graphitizable carbon source is vice versa, meaning that a high content of hydrogen and a small or null amount of oxygen is present in the molecular composition. In our case, sucrose is non graphitizable and pyrazine is graphitizable, it should also be noticed that pyrazine is an aromatic molecule.

From the structure characterization by TEM, Raman and XRD we observe that with a decrease in the particle size used there is an increase in the carbon structural disorder (I_D/I_G) and an increase in the (002) interplanar distance. On the other hand, with the introduction of pyrazine the structure tends to be more disordered for the 300 nm pore size, although more ordered for the 10 and 100 nm pore size; and the (002) interplanar distance decreases when introducing pyrazine in the synthesis.

X-Ray photoelectron spectroscopy was used to determine the chemical composition of the surface and provide information regarding the forms of species absorbed on the samples (see Figure 3.12). The high resolution for C 1s in all samples shows the presence of sp^2 and sp^3 binding (284.4 and 285.2 eV, respectively), for the undoped sample there is a peak corresponding to C-O and O-C-O (287.8 eV) and for the nitrogen doped samples there are peaks assigned to C=N (286 eV) , C-N, C-O and O-C-O (287.1 eV), and another peak for C=O (287.8 eV) [43; 44; 45; 46]. The nitrogen N 1s peak indicates the presence of substitutional (401.5 eV) and pyridinc (399.5 eV) sites [44; 46], here we qualitatively observe that there is a higher presence of substitutional than pyridinic nitrogen. The atomic concentrations obtained from the XPS analysis show that the sample CIO300-N1 has 2.35 at. % of nitrogen and a higher content of oxygen that the undoped sample (Table 3.5). The elemental quantification for both samples is shown in Table 3, where CIO300-N1 exhibits 2.35 at% of nitrogen, on the other hand the EDX analysis reveal a 3.10 at% of nitrogen however it reveals a lower content of oxygen in the samples (2.12 – 3.35 at% of oxygen).

Table 3.5: Elemental analysis obtained from XPS measurements for undoped and nitrogen doped (N1, N3) carbon inverse opals made with 300 nm particles.

at. %	CIO300	CIO300-N1
C	93.19	62.53
N	0.00	2.35
O	6.14	35.12

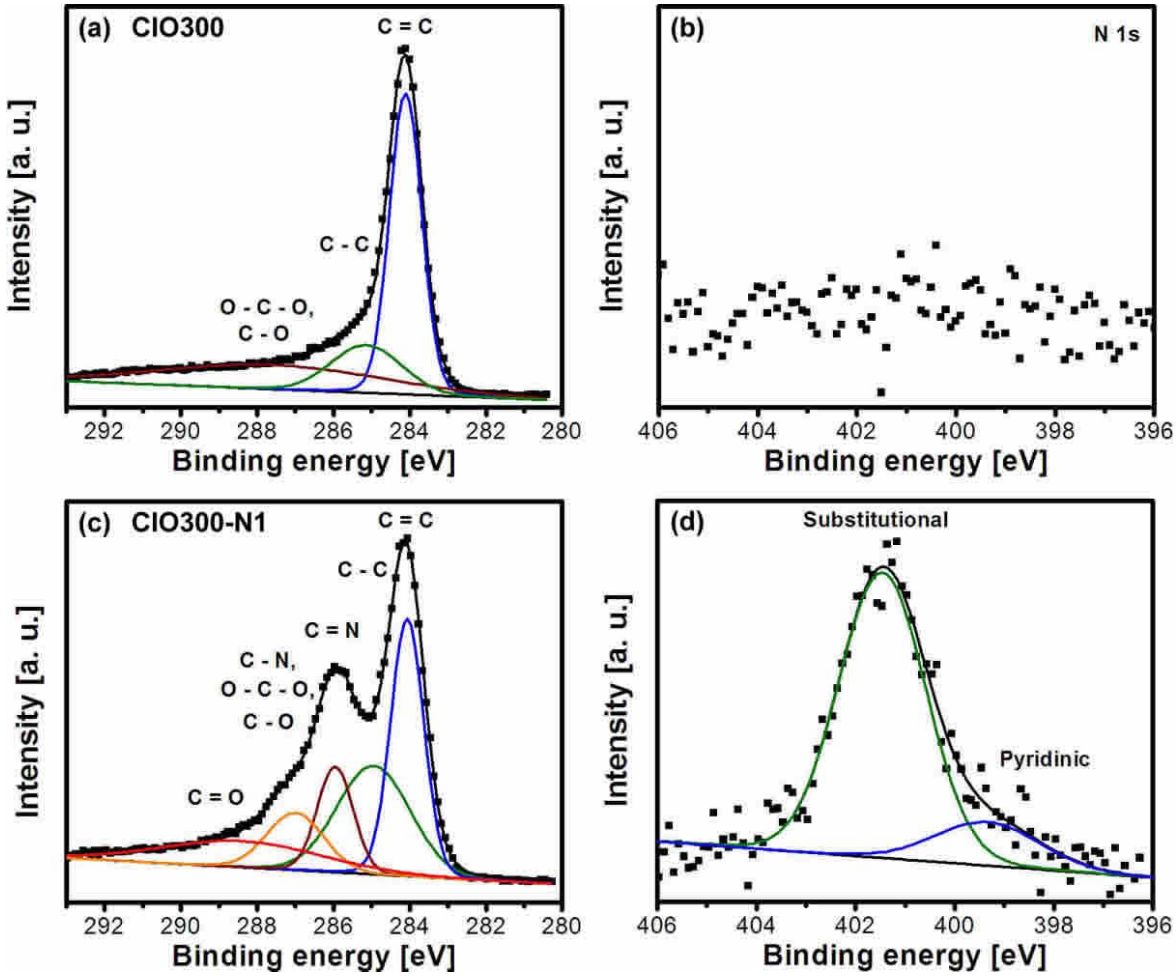

Figure 3.12. XPS of carbon inverse opal doped with nitrogen. High resolution x-ray photoelectron spectra of carbon inverse opal (CIO300, top) and nitrogen doped carbon inverse opal (CIO300-N1, bottom) of **(a,c)** C 1s, **(b,d)** N 1s. It is clear that the undoped carbon inverse opal does not contain nitrogen.

In the thermogravimetric analysis we observe the loss of the majority of the material, the residues may come from the undisolved SiO_2 during the etching process. The majority of the curves exhibit two weight losses, the first one between 20 and 300 ^{o}C which may be due to the loss of the stored humidity in the pores and the second loss (400 – 500 ^{o}C) corresponds to the decomposition of the carbon structure (Figure 3.13 a, b and c). It is clear that for samples with 10 and 300 nm pore size the decomposition temperature increases when increasing the

nitrogen content up to N2 (Figure 3.13 d), this might be caused by a higher degree of order in the structure as observed by Raman spectroscopy (Figure 3.10) and XRD (Figure 3.11). However, samples with 100 nm pore tend to decrease the decomposition temperature when increasing the nitrogen content. Regarding the pore size we observe that the carbon inverse opal with 10 nm pore exhibits the highest decomposition temperature, however the difference of decomposition temperature with the other pore sizes may not be significant.

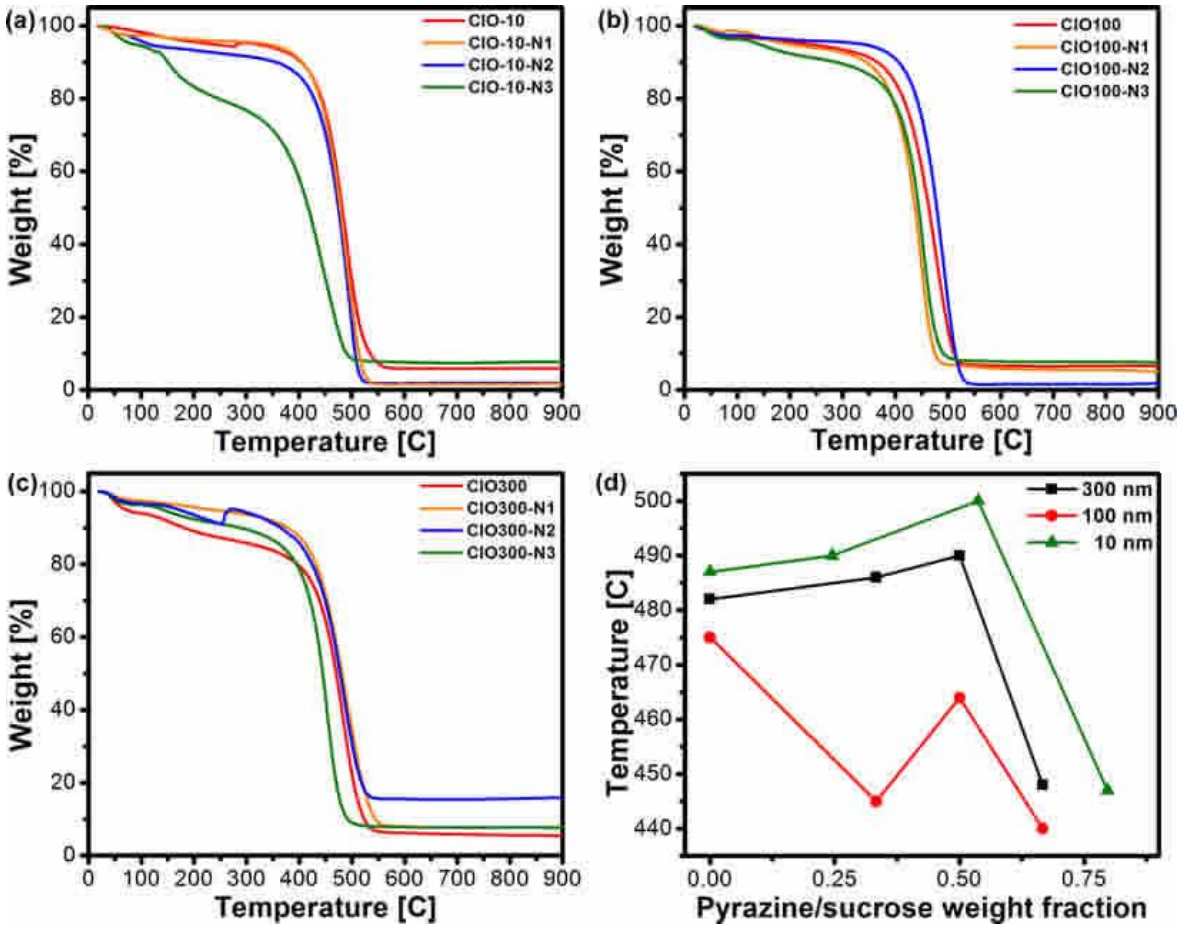

Figure 3.13: Thermogravimetric analysis (measured in air) of carbon inverse opal with **(a)** 10, **(b)** 100 and **(c)** 300 nm size pore at different contents of nitrogen (pyrazine content during synthesis). **(d)** Decomposition temperature of the studied samples.

We performed surface area analysis by nitrogen absorption of all the undoped and doped carbon inverse opals with different amounts of pyrazine and different particle size used for the synthesis (Figure 3.14). This characterization shows that the surface area depends upon the pore size as observed by others [47; 48], we obtain the highest surface area values (c. a. 1374.5 m^2/g) for pore size of 10 nm. Now, when observing the effect of nitrogen doping we observe that for 10 and 100 nm pore the surface area tends to decrease when the amount of

pyrazine is increased, however for 300 nm pore the surface area slightly increases. The effect of nitrogen content in porous carbon materials upon the surface area has been observed previously, showing a decrease when compared with the pure carbon material [49; 31; 50; 51].

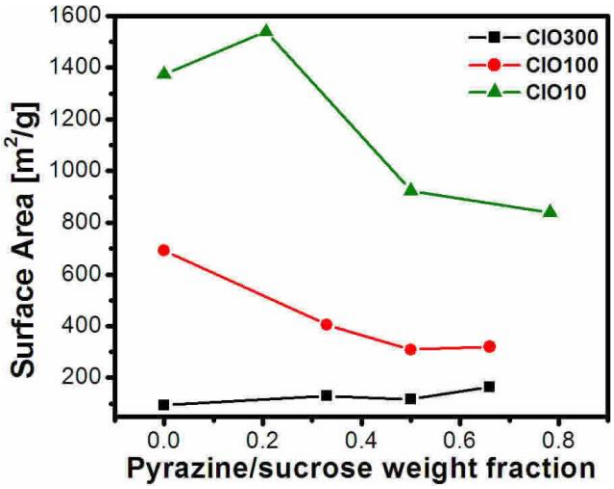

Figure 3.14: Surface area obtained by nitrogen absorption using BET for carbon inverse opal with 10, 100 and 300 nm pore at different amounts of pyrazine used for synthesis.

UV-VIS reflection spectra was taken for the opal, doped and undoped carbon inverse opal made with 300 nm silica particles (Figure 3.15 a). Under a bright light it is possible to observe the colors revealed by the UV-VIS reflection spectra (Figure 3.15 b-f). The opal shows a red diffraction color (609 nm) that is also observed for the undoped carbon inverse opal. When we introduce pyrazine up to CIO300-N2 as carbon source the reflection peak shifts down to a blue color (466 nm). For the undoped and doped carbon inverse opal CIO300-N1 of pyrazine as carbon source we can observe primary peaks at 609 and 568 nm, respectively, and secondary peaks at 493 and 483, respectively. Curiously, the CIO300-N3 sample's reflection peak shifts to a green color (528 nm).

It has been observed before that due to Brag diffraction the peak in the reflection spectrum may shift due to incident angle of the light source, for example to achieve a shift around 100 nm for a carbon inverse opal 40 θ (from 85 to 45 q) is enough [52]. Now, the experimental spectrum measured was at a 90 $\theta \pm 5$ incident angle. With these considerations we may think that the refractive index of the carbon inverse opal changes when the content of nitrogen is varied. It is worthy to mention that the doping of carbon inverse opal may change its optical and electrical properties, such is the case reported for K doping [8]. On the other hand, altering the photonic band gap by doping a semiconductor photonic crystal has been studied theoretically and experimentally, as shown in the section 2.2.1, these works support our the idea of tailoring optical properties of materials by doping.

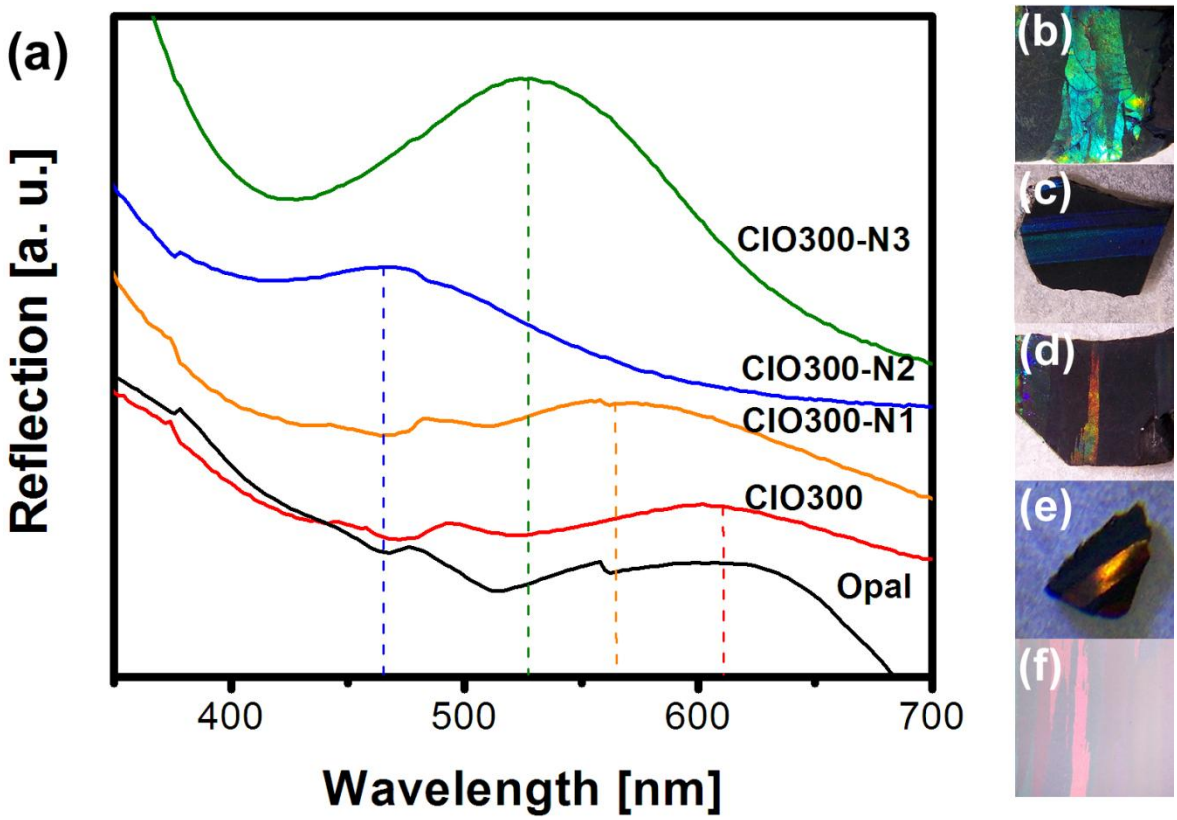

Figure 3.15: UV-VIS reflection spectra of CIO300-Nx. (a) UV-VIS reflection spectra of carbon inverse opal with 300 nm particle at different pyrazine concentrations. Photograph of carbon inverse opal from **(b-d)** N3-N1, **(e)** CIO and **(f)** opal.

3.4.2 Heat treated samples

Heat treatment of carbon materials above 1000 ^{o}C has been shown to increase the crystallinity, such is the case of amorphous carbon nanotubes that suffer a procces leading towards a graphitic like structure [53; 54; 55]. This may suggest that a similar effect might happen for carbon inverse opal, here we heat treated the carbon inverse opal after etching with HF.

SEM images show that the undoped samples heat treated at 1450 ^{o}C suffer wall decomposition (Figure 3.16 a) perhaps due to the presence of dangling bonds in the carbon lattice, on the other hand the nitrogen doped sample N3 does not show any changes when heat treated at 1450 ^{o}C (Figure 3.16 b), however, at 1750 ^{o}C (Figure 3.16 c) we observe carbon walls with rugosity which cleary suggests a structural transformation.

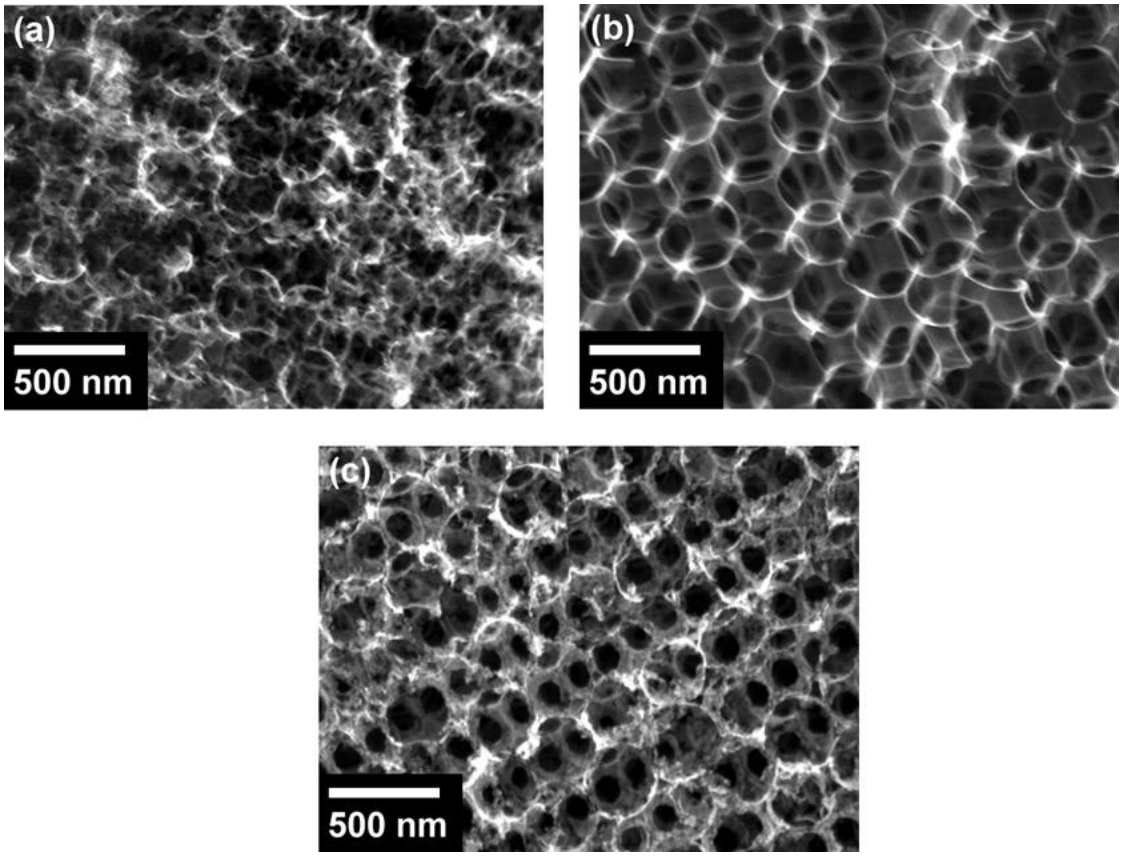

Figure 3.16: SEM images of heat treated CIO300 and CIO300-N3. Undoped carbon inverse opal heat treated at **(a)** 1450^{o} C and nitrogen doped N3 heat treated at **(b)** 1450 ^{o}C and **(c)** 1750 ^{o}C.

The heat treated sample CIO-N3 at 1450 ^{o}C has the presence of SiC, here the Si may come from remaining silica spheres or residues after etching with HF, by scanning electron microscopy this SiC was found to be in the form of amorphous particulates (Figure 3.17 a,b), with elemental mapping it is clear to observe a region with a low presence of C (Figure 3.17 c) and O (Figure 3.17 d) although rich in Si (Figure 3.17 e), in this region, EDX quantification analysis shows a relation of Si to C to be the unit (Table 3.6), corresponding with SiC. These SiC regions are abundant within the entire sample.

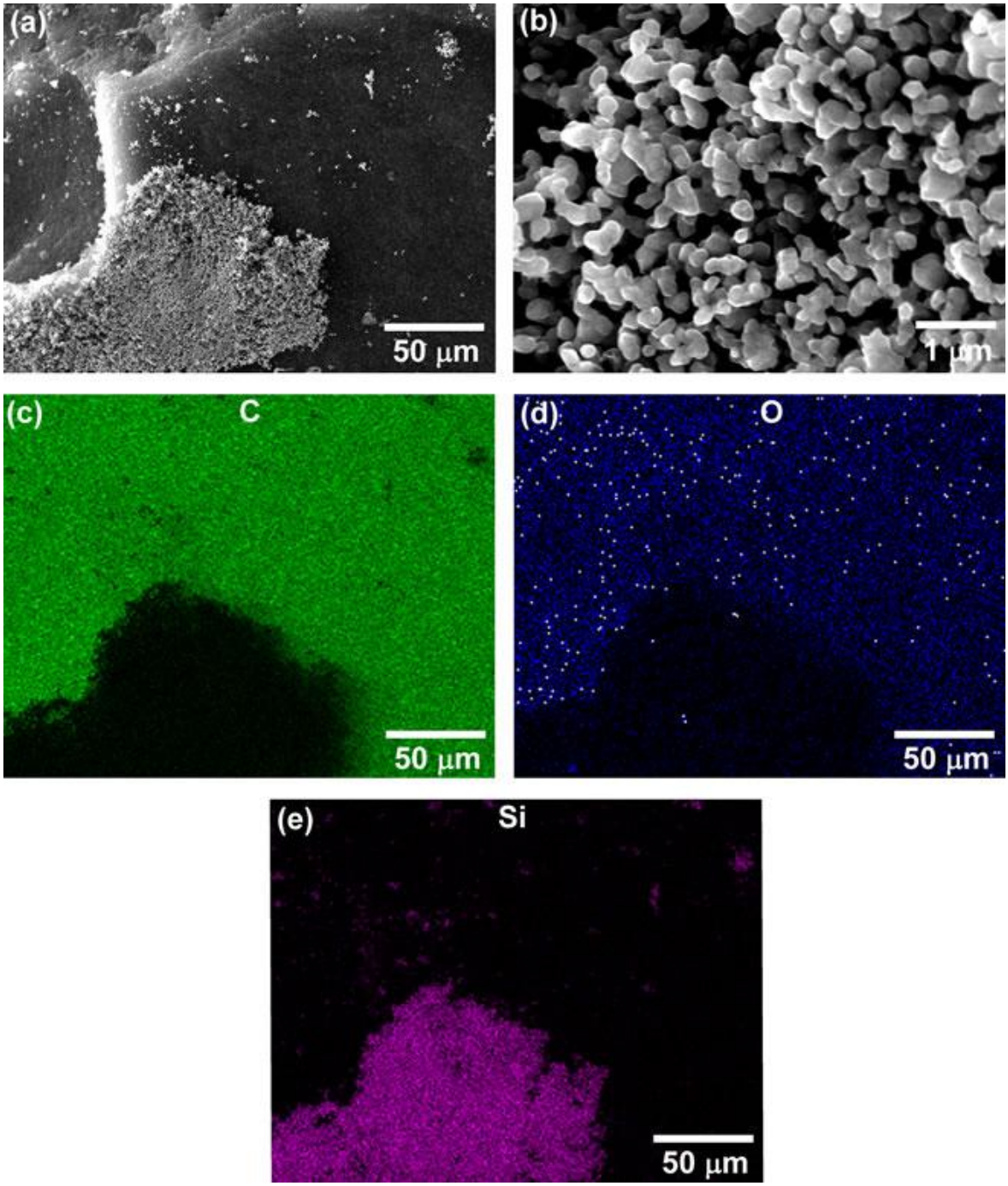

Figure 3.17: Elemental mapping of SiC formed at 1450 °C. (a) SEM image of CIO-N3 heat treated at 1450 °C and **(b)** high magnification of region with SiC particulates. Elemental maping of image (a) for **(c)** C, **(d)** O and **(e)** Si. It is clear that figure (b) is composed of Si and C. Observe that the presence of Si may decrease the C signal.

Table 3.6: EDX quantification of ClO-N3 heat treated at 1450 °C. Column A corresponds to a carbon region (Figure 3.17 c) and column B corresponds to the particulates composed of SiC (Figure 3.17 b and e)

	A	B
C	96.40	50.18
O	2.22	0.68
Si	0.08	48.60

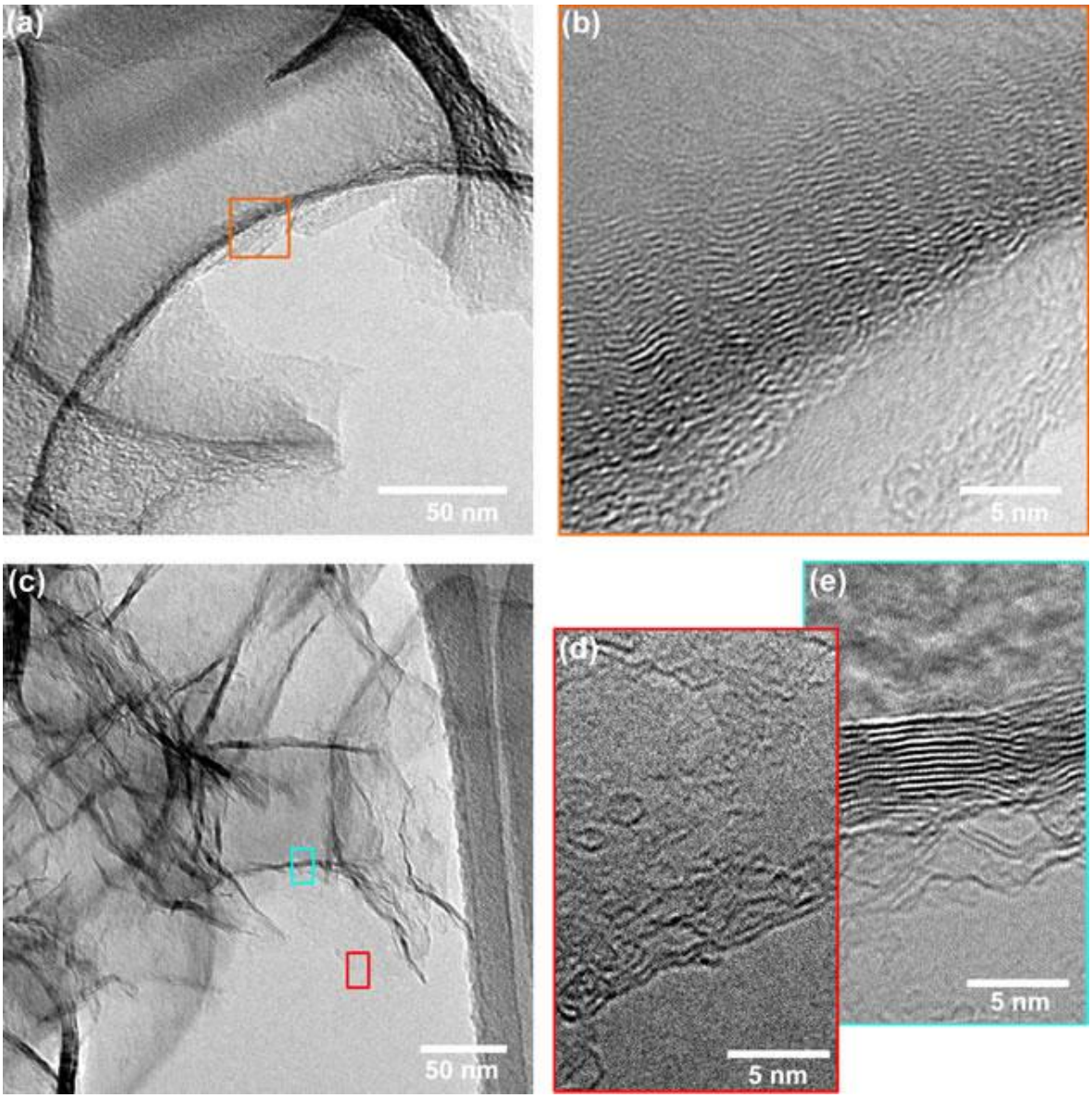

Figure 3.18: Transmission electron microscopy (TEM) images of carbon inverse opal doped with the highest content of nitrogen heat treated at 1450 (top) and 1750 °C (bottom). **(a and c)** Are images showing a characteristic void between pores. **(b)** Is a high magnification image of (a) where it is clear that carbon structure starts to become layered. **(d and e)** Are high magnification images of (c), showing a layered structure.

In the transmission electron microscopy images we observe that the sample doped with the highest content of nitrogen heat treated at 1450 ^{o}C starts to exhibit a layered-like structure (see Figure 3.18 a and b), further on, at 1750 ^{o}C the sample exhibits a layered structure (Figure 3.18 c-e), with an interlayer distance of 3.5 Å. The edge of the broken structure also reveals the presence of several ordered layers.

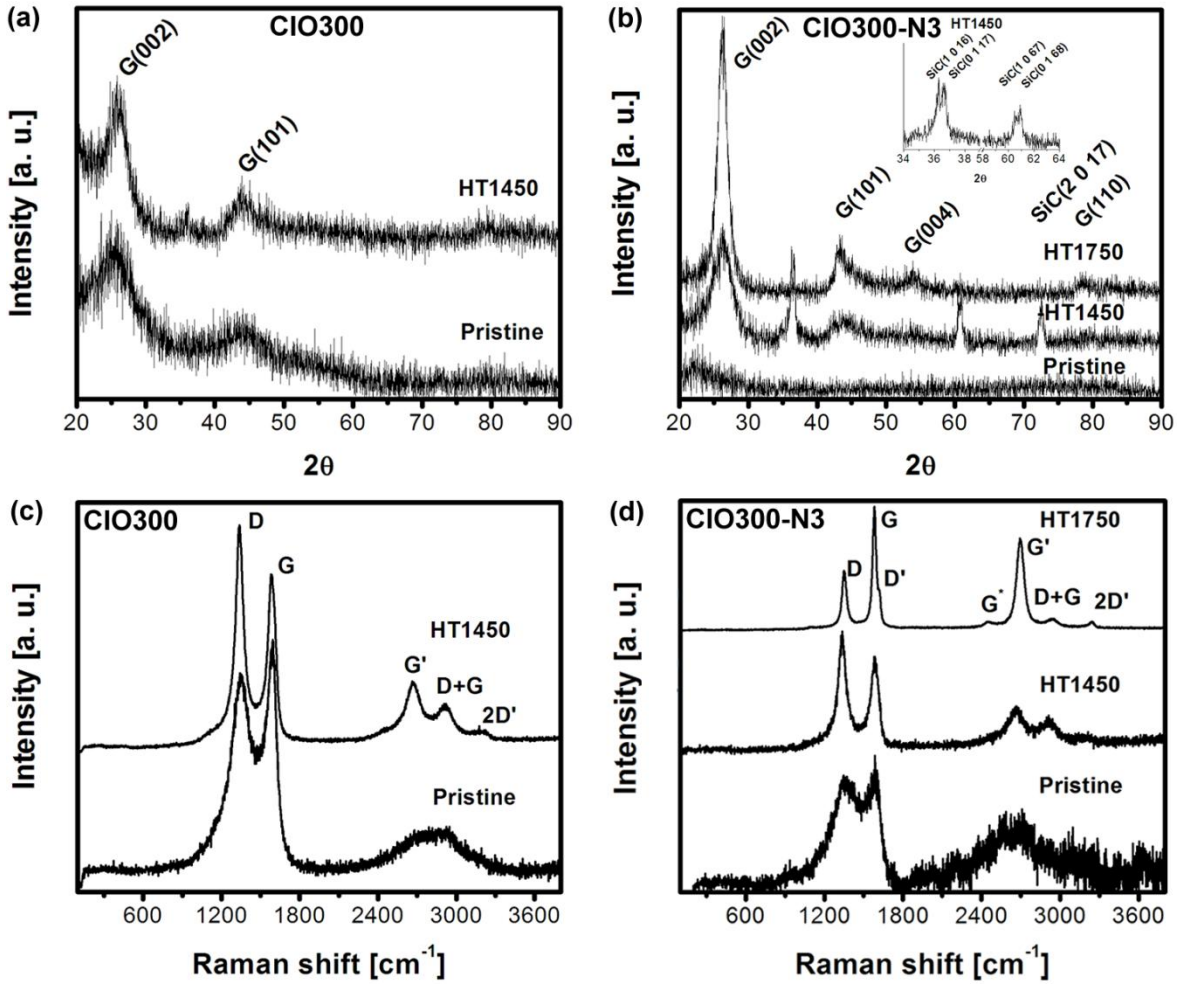

Figure 3.19: XRD and Raman of heat treated ClO300 and ClO300N3. XRD of **(a)** ClO300 and **(b)** ClO300-N3. Raman spectra of **(c)** ClO300 and **(d)** ClO300-N3.

Table 3.7: Interplanar distance of heat treat ClO300 and ClO300-N3.

	d(002)	ID/IG
ClO-HT1450	3.533	1.296
ClON3-HT1450	3.478	1.292
ClON3-HT1750	3.477	0.469

The heat treated samples show an increase of graphitization in the XRD spectra (Figure 3.19 a-b), where we cleary observe the (002) plane of graphite. The samples heat treated at 1450 ^{o}C indicate that the nitrogen doped carbon inverse opal has a lower (002) interplanar distance (Table 3.7). The sample CION3 presents the formation of SiC with a rhombohedral structure at 1450 ^{o}C, this is formed from the Si residues of the SiO_2 etching process, and due to the low content of Si at 1750^{o} the SiC structure is no longer present, which follows the phase diagram of SiC. Now it is worthy to notice that the formation of SiC could have been promoted by a catalytic action of the nitrogen present in the sample.

In the Raman spectra (Figure 3.19 c-d) we find that at 1450 ^{o}C the doped and undoped samples increase their degree of disorder possibly due to the formation of SiC, because the carbon from sample may have been used to form SiC therefore altering the carbon structure, and when CION3 is heated at 1750^{o} C the graphitization increases significantly.

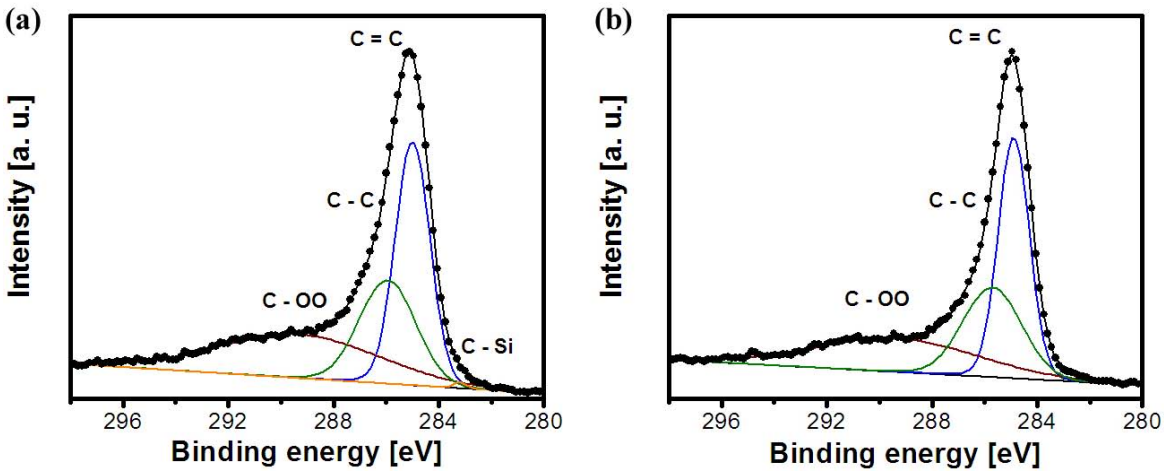

Figure 3.20: High resolution x-ray photoelectron spectra of C 1s for nitrogen doped (N3) carbon inverse opal heat treated at **(a)** 1450 and **(b)** 1750 ^{o}C.

In the X-Ray photoelectron spectroscopy for the samples heat treated at 1450 ^{o}C and 1750 ^{o}C synthesized with the highest content of nitrogen (CIO300-N3), we analyzed the regions of C 1s and O 1s. In all the samples there is the presence of sp^2 and sp^3 binding (Figure 3.20 a and b) (284.4 and 285.2 eV, respectively), there is also a peak corresponding to C-OO (289.3 eV). We notice that the heat treatment (1450 ^{o}C and above) is capable of eliminating the majority of the nitrogen in the samples. The doped sample heat treated at 1450 ^{o}C, has a small presence of Si (3 at. %) which is in the form of C-Si (284.2 eV), this is confirmed by the XRD spectra.

3.5 Conclusions

The doping of carbon inverse opal with nitrogen was studied systematically using different silica nanoparticle sizes and varying the concentration of nitrogen source (in this case pyrazine). First of all, smaller size particles produce a less graphitic carbon material, and the (002) interplanar distance increases. We also observed that with 10 nm pore size there is a higher thermal decomposition temperature and, on the other hand the surface area increases when decreasing the pore size.

Now, the use of non graphitizable (sucrose) and graphitizable (pyrazine) carbon sources with silica nanoparticles smaller than 300 nm may be a route to control the degree of crystallinity, in this case with a higher content of pyrazine we were able to reach a minimum value of I_D/I_G for the 10 and 100 nm pore size, however for 300 nm pore size this ratio increased. For all samples there was a decrease of the (002) interplanar distance when increasing the pyrazine/sucrose fraction. Regarding the TGA analysis, nitrogen doping with pyrazine increases the thermal decomposition temperature up to certain point for 10 and 300 nm pore sizes, however, for 100 nm pore size this decomposition point decreases. For the surface area, we observe a decrease when increasing the nitrogen content for the 10 and 100 nm pore. The chemical composition of all samples show certain oxidation of the carbon surface along with the presence of nitrogen, this nitrogen is present as substituional and pyridinic doping among the carbon lattice.

The optical properties of the materials were studied by UV-VIS spectroscopy, the introduction of nitrogen in the carbon structure clearly changes the optical band gap, by lowering the wavelength of the reflection peak to a minimum and afterwards shifting to higher values when varying the content pyrazine used in the carbon source solutions.

Now, when heat treating the doped and undoped samples there is a production of SiC at 1450 ^oC and the structure is more disordered, however when heat the samples at 1750 ^oC there is an increase in crystallinity reflected by a lower value of I_D/I_G and a lower (002) interplanar distance. The XPS chemical analysis does not show the presence of nitrogen for these heat treated samples, this only shows sp and sp^2 bonding of carbon along with a C-OO functional group.

This work shows capability to control the chemical composition of the carbon inverse opal, thus shifting its optical properties. This material may have

applications for sensors, field emitters, biomaterials, 3-dimensional scaffolds and photoconductive materials.

3.6 References

1. *Adsorption properties of nitrogen-alloyed activated carbon fiber.* **C.-M. Yang, K. Kaneko.** 2001, Carbon, Vol. 39, pp. 1075-1082.

2. *Structural and electrochemical characterisation of nitrogen enriched carbons produced by the co-pyrolysis of coal-tar pitch with polyacrylonitrile.* **J. Machnikowski, B. Grzyb, J.V. Weber, E. Frackowiak, J.N. Rouzaud d, F.Béguin.** 2004, Electrochim. Acta, Vol. 49, pp. 423-432.

3. *Porous structure and surface chemistry of nitrogen containing carbons from polymers.* **J. Lahaye, G. Nanséa, A. Bagreev, V. Strelko.** 1999, Carbon, Vol. 37, pp. 585-590.

4. *Template synthesis of polyacrylonitrile-based ordered macroporous materials and their derivatives.* **H. Bu, J. Rong, Z. Yang.** 2002, Macromol. Rapid Commun., Vol. 23, pp. 460-464.

5. *Fabrication of partially graphitic three-dimensional nitrogen-doped mesoporous carbon using polyaniline nanocomposite through nanotemplating method.* **A. Vinu, S. Anandan, C. Anand, P. Srinivasu , K. Ariga , T. Mori.** 2008, Microporous and Mesoporous Materials, Vol. 109, pp. 398–404.

6. *Synthesis of nitrogen-containing microporous carbon with a highly ordered structure and effect of nitrogen doping on H2O adsorption.* **P. -X. Hou, H. Orikasa, T. Yamazaki, K. Matsuoka, A. Tomita, N. Setoyama, Y. Fukushima, T. Kyotani.** 2005, Chem. Mater., Vol. 17, pp. 5187–5193.

7. *Synthesis and characterization of microporous carbons templated by ammonium-form zeolite Y.* **F. Su, X.S. Zhao, L. Lv, Z. Zhou.** 2004, Carbon, Vol. 42, pp. 2821–2831.

8. *Optical and electrical properties of opal carbon replica and effect of pyrolysis.* **H. Kajii, Y. Kawagishi, H. Take, K. Yoshino, A. A. Zakhidov, R. H. Baughman.** 2000, J. Appl. Phys. , Vol. 88, pp. 758-763.

9. *Electrical properties of a periodic porous carbon replica of opal.* **K. Yoshino, H. Kaji, Y. Kawagishi, M. Ozaki, A. A. Zakhidov, R. H. Baughman.** 1999, Jpn. J. Appl. Phys., Vol. 38, pp. 4926–4929.

10. *Tunable inverse opal hydrogel pH sensor.* **Y. -J. Lee, P. V. Braun.** 2003, Adv. Mater., Vol. 15, pp. 563-566.

11. *Tunable photonic band schemes of opals and inverse opals infiltrated with liquid crystals.* **H. Takeda, K. Yoshino.** 2002, J. Appl. Phys., Vol. 92, pp. 5658-5662.

12. *Properties of liquids and liquid crystals in nano-scale space.* **K. Yoshino, R. Ozaki, J. Matsumoto, M. Ojima, S. Hiwatashi, Y. Matsuhisa, M. Ozaki.** 2006, IEEE Trans. Dielec. Elec.l Ins., Vol. 13, pp. 678-686.

13. *Tunable photonic crystals with semiconducting constituents.* **P. Halevi, F. Ramos-Mendieta.** 2000, Phys. Rev. Lett., Vol. 85, pp. 1875-1878.

14. *Optical and electrical properties of nitrogen incorporated amorphous carbon films.* **Y. H. Yu, Z. Y. Chen, E. Z. Luo, W. Y. Cheung, J. P. Zhao, X. Wang, J. B.Xu, S. P. Wong, I. H. Wilson.** 2000, J. App. Phys., Vol. 87, pp. 2874-2879.

15. *Optical behavior of alpha-C:N films.* **X. Wang, P. J. Martin.** 1996, Appl. Phys. Lett., Vol. 68, pp. 1177-1179.

16. *Optical properties of CN, films prepared by filtered arc deposition.* **Z.Y. Chen, J.P. Zhao, Y.H. Yu, X. Wang, S.Q. Yang, T.S. Shi, X.H. Liu.** 1997, Mater. Lett., Vol. 33, pp. 85-89.

17. *O2 reduction on graphite and nitrogen-doped graphite: experiment and theory.* **R. A. Sidik, A. B. Anderson, N. P. Subramanian, S. P. Kumaraguru, B. N. Popov.** 2006, J. Phys. Chem. B, Vol. 110, pp. 1787-1793.

18. *New route to graphite flakes and films. Pyrolysis of aromatic and heteroaromatic compounds under dehydrogenation conditions.* **P. H. Chang, M. M. Labes.** 1989, Chem. Mater., Vol. 1, pp. 523-525.

19. *Identification of electron donor states in N-doped carbon nanotubes.* **R. Czerw, M. Terrones, J.-C. Charlier, X. Blase, B. Foley, R. Kamalakaran, N. Grobert, H. Terrones, D. Tekleab, P. M. Ajayan, W. Blau, M. Ru2hle, D. L. Carroll.** 2001, Nano Lett., Vol. 1, pp. 457-460.

20. *N-doping and coalescence of carbon nanotubes: synthesis and electronic properties.* **M. Terrones, P.M. Ajayan, F. Banhart, X. Blase, D.L.Carroll, J.C. Charlier, R. Czerw, B. Foley, N. Grobert,R. Kamalakaran, P. Kohler-Redlich, M. Ruhle, T. Seeger, H. Terrones.** 2002, Appl. Phys. A, Vol. 74, pp. 355-361.

21. *Electronic properties of nitrogen-doped graphite flakes.* **Dong-Pyo Kim, C. L. Lin, T, Mihalisin, P. Heiney, M. M. Labes.** 1989, Chem. Mater., Vol. 1, pp. 523-525.

22. *N-doping and coalescence of carbon nanotubes: synthesis and electronic properties.* **M. Terrones, P. M. Ajayan, F. Banhart, X. Blase, D. L. Carroll, J. C. Charlier, R. Czerw, B. Foley, N. Grobert, R. Kamalakran, P. Kohler-Redlich, M. Ruhle, T. Seeger, H. Terrones.** 2002, Appl. Phys. A, Vol. 74, pp. 355-361.

23. *Synthesis of N-doped graphene by chemical vapor deposition and its electrical properties.* **D. Wei, Y. Liu, Y. Wang, H. Zhang, L. Huang, G. Yu.** 2009, Nano Lett., Vol. 9, pp. 1752-1758.

24. *Nitrogen effect on the electrical properties of CNx thin films deposited by reactive magnetron sputtering.* **N.E. Derradjia, M.L. Mahdjoubia, H. Belkhira, N. Mumumbilab, B. Angleraudb, P.Y. Tessier.** 2005, Thin Sol. Films, Vol. 482, pp. 258– 263.

25. *Controllable growth, structure, and low field emission of well-aligned CNx nanotubes.* **X. Wang, Y. Liu, D. Zhu, L. Zhang, H. Ma, N. Yao, B. Zhang.** 2002, J. Phys. Chem. B, Vol. 106, pp. 2186-2190.

26. *Electron side-emission from corrugated CNx nanotubes.* **R. C. Che, L.-M. Peng, M. S. Wang.** 2004, Appl. Phys. Lett., Vol. 85, pp. 4753-4755.

27. *Bamboo-shaped aligned CNx nanotubes synthesized using single feedstock atdifferent temperatures and study of their field electron emission.* **P. Ghosh, M Zamri, M Subramanian, T Soga, T Jimbo, R Katoh, M Tanemura.** 2008, J. Phys. D: Appl. Phys., Vol. 41, p. 155405.

28. *New route to graphite flakes and films: pyrolysis of aromatic and heteroaromatic compounds under dehydrogenation conditions.* **P. -H. Chang, M. M. Labes.** 1989, Chem. of Mater., Vol. 1, pp. 523-525.

29. *Electronic properties of nitrogen-doped graphite flakes.* **D. -P. Kim, C. L. Lin, T, Mihalisin, P. Heiney, M. M. Labes.** 1991, Chem. Mater., Vol. 3, pp. 686-692.

30. *O2 Reduction on graphite and nitrogen-doped graphite: experiment and theory.* **R. A. Sidik, A. B. Anderson, N. P. Subramanian, S. P. Kumaraguru, B. N. Popov.** 2006, J. Phys. Chem. B, Vol. 110, pp. 1787-1793.

31. *Nitrogen-containing carbons from phenol–formaldehyde resins and their catalytic activity in NO reduction with NH3.* **M. -C. Huang, H. Teng.** 2003, Carbon, Vol. 41, pp. 951–957.

32. *Bioelectrochemistry and enzymatic activity of glucose oxidase immobilized onto the bamboo-shaped CNx nanotubes.* **N. Jia, L. Liu, Q. Zhoua, L. Wang, M. Yan, Z. Jiang.** 2005, Electrochimica Acta, Vol. 51, pp. 611–618.

33. *Viability studies of pure carbon- and nitrogen-doped nanotubes with entamoeba histolytica: from amoebicidal to biocompatible structures.* **A. L. Elias, J. C. Carrero-Sanchez, H. Terrones, M. Endo, J. P. Laclette, M. Terrones.** 2007, Small, Vol. 3, pp. 1723-1729.

34. *Bamboo-like CNx nanotubes for the immobilization of hemoglobin and its bioelectrochemistry.* **N. Jia, L. Wang, L. Liu, Q. Zhou, Z. Jiang.** 2005, Electrochem. Commun., Vol. 7, pp. 349-354.

35. *Doping of carbon nanotubes with nitrogen improves protein coverage whilst retaining correct conformation.* **H. J. Burch, S. A. Contera, M. R. R. de Planque, N. Grobert, J. F. Ryan.** 2008, Nanotech., Vol. 19, p. 384001.

36. *Ab Initio study of doped carbon nanotube sensors.* **S. Peng, K. Cho.** 2003, Nano Lett., Vol. 3, pp. 513-517.

37. *Fabrication of vapor and gas sensors using films of aligned CNx nanotubes.* **F. Villalpando-Pérez, A. H. Romero, E. Muñoz-Sandoval, L. M. Martínez, H. Terrones, M. Terrones.** 2004, Chem. Phys. Lett., Vol. 386, pp. 137-143.

38. *Humidity sensing properties of CNx film by RF magnetron sputtering system.* **J. G. Lee, S. P. Lee.** 2005, Sensors and Actuators B, Vol. 108, pp. 450-454.

39. *Analyzer: an analysis software for photoelectron and infrared spectra.* **Herrera-Gomez, A.** http://qro.cinvestav.mx/~AAnalyzer/.

40. *New perspectives on the structure of graphitic carbons.* **Harris, P. J. F.** 2005, Critic. Rev. Solid State Mater. Sc., Vol. 30, pp. 235-253.

41. *Effect of nitrogen doping on Raman spectra of multi-walled carbon nanotubes.* **28. L. G. Bulusheva, A. V. Okotrub, I. A. Kinloch, I. P. Asanov, A. G. Kurenya, A. G. Kudashov, X. Chen, H. Song.** 2008, Phys. Stat. Sol. B, Vol. 245, pp. 1971–1974 .

42. *Crystallite growth in graphitizing and non-graphitizing carbons.* **Franklin, R. E.** 1951, Proc. Royal Soc. London. Series A, Math. and Phys. Sci., Vol. 209, pp. 196-218.

43. *Irradiation-induced magnetism in carbon nanostructures.* **S. Talapatra, P. G. Ganesan, T. Kim, R. Vajtai, M. Huang, M. Shima, G. Ramanath, D. Srivastava, S. C. Deevi, P. M. Ajayan.** 2005, Phys. Rev. Lett., Vol. 95, p. 097201.

44. *Structure, composition, and chemical reactivity of carbon nanotubes by selective nitrogen doping.* **S. Maldonado, S. Morin, K. J. Stevenson.** 2006, Carbon, Vol. 44, p. 1429.

45. *X-ray photoelectron spectroscopy of carbon nitride films deposited by graphite laser ablation in a nitrogen postdischarge.* **M. Tabbal, P. Mérel, S. Moisa, M. Chaker, A. Ricard, M. Moisan.** 1996, Appl. Phys. Lett., Vol. 69, p. 1698.

46. *Elucidating the porous and chemical structures of ZnCl2-activated polyacrylonitrile on a fiberglass substrate.* **Z. Yue, K. R. Benak, J. Wang, C. L. Mangun, J. Economy.** 2005, J. Mater. Chem., Vol. 15, p. 3142.

47. *XPS and 15N NMR study of nitrogen forms in carbonaceous solids.* **S. R. Kelemen, M. Afeworki, M. L. Gorbaty, P. J. Kwiatek, M. S. Solum, J. Z. Hu, R. J. Pugmire.** 2002, Energy Fuels, Vol. 16, p. 1507.

48. *Synthesis and characterization of hexagonally ordered carbon nanopipes.* **M. Kruk, M. Jaroniec, T.-W. Kim, R. Ryoo.** 2003, Chem. Mater., Vol. 15, pp. 2815-2823.

49. *Molecular simulation of novel carbonaceous materials for hydrogen storage.* **D. Cao, P. Feng, J. Wu.** 2004, Nano Lett., Vol. 4, pp. 1489-1492.

50. *The role of different nitrogen functional groups on the removal of SO2 from flue gases by N-doped activated carbon powders and fibres.* **E. Raymundo-Piñero, D. Cazorla-Amorós, A. Linares-Solano.** 2003, Carbon, Vol. 41, pp. 1925–1932.

51. *Synthesis of nitrogen-containing microporous carbon with a highly ordered structure and effect of nitrogen doping on H2O adsorption.* **P.-X. Hou, H. Orikasa, T. Yamazaki, K. Matsuoka, A. Tomita, N. Setoyama, Y. Fukushima, T. Kyotani.** 2005, Chem. Mater., Vol. 17, pp. 5187-5193.

52. *CVD synthesis of carbon-based metallic photonic crystals.* **A. A. Zakhidov, I. I. Khayrullin, R. H. Baughman, Z. Iqbal, K. Yoshino, Y. Kawagishi, S. Tatsuhara.** 1999, NanoStructured Materials, Vol. 12, pp. 1089-1095.

53. *Crystallization behavior of the amorphous carbon nanotubes preparedby the CVD method.* **L. Ci, B. Wei, C. Xu, J. Liang, D. Wu, S. Xie, W. Zhou, Y. Li, Z. Liu, D. Tang.** 2001, J. Cryst. Growth, Vol. 233, pp. 823–828.

54. *Annealing amorphous carbon nanotubes for their application in hydrogen storage.* **L. Ci, H. Zhu, B. Wei, C. Xu, D. Wu.** 2003, Appl. Surf. Sci. , Vol. 205, pp. 39-43.

55. *Effect of thermal treatment on the structure of multi-walled carbon nanotubes.* **K. Behler, S. Osswald, H. Ye, S. Dimovski, Y. Gogotsi.** 2006, J. Nanopart. Res., Vol. 8, pp. 615-625.

56. *Optical behavior of alpha-C:N films.* **X. Wang, P. J. Martin.** 1996, Appl. Phys. Lett., Vol. 68, p. 1177.

57. *Tunable inverse opal hydrogel pH sensor.* **Y. -J. Lee, P. V. Braun.** 2003, Adv. Mater., Vol. 15, pp. 563-566.

58. *Fluorination of carbon nanotubes in CF4 plasma.* **N. O. V. Plank, Liudi Jiang, R. Cheung.** 2003, Appl. Phys. Lett. 83, 2426 (2003), Vol. 83, p. 2426.

59. *X-ray photoemission spectroscopy study of fluorinated single-walled carbon nanotubes.* **K. H. An, J. G. Heo, K. G. Jeon, D. J. Bae, C. Jo, C. W. Yang, C. -Y. Park, Y. H. Lee, Y. S. Lee, Y. S. Chung.** 2002, Appl. Phys. Lett., Vol. 80, p. 4235.

4. Physical Properties of Nitrogen Doped Carbon Inverse Opal

Once the nitrogen doped carbon inverse opal was synthesized and structurally characterized, we studied its electrical and magnetic properties, and more specific we measured the resistance, field emission, magnetoresistance and magnetization. For this purpose this chapter is divided in sections for each measured property.

4.1 Electrical properties

4.1.1 Introduction

Metallic materials present a resistivity at room temperature (i. e. 300 K) due to collisions of the electrons with the lattice phonons and at low temperatures (i. e. 4 K) it is dominated by collisions with impurity atoms and mechanical imperfections in the lattice. These phenomena contribute to the total resistivity as:

Eq. 4.1
$$\rho = \rho_L + \rho_i$$

Where ρ_L is the resistivity due to the thermal phonons and ρ_i is the resistivity caused by scattering of the electron waves by static defects that affect the periodicity of the lattice. The slope of resistance (R) vs. temperature (T) for a metal is $\delta R/\delta T > 0$ and for an insulator/semiconductor it is $\delta R/\delta T < 0$.

When these metals present a higher temperature, energy is transferred to the loose electrons, making them move in less organized patterns and thus decreasing its conductivity for higher temperatures.

On the other hand, the electron states in a semiconductor are filled up to the valence band, located below the gap. This means that under an electric field the electrons do not have enough kinetic energy to move around the lattice at low temperatures, making them insulators. When increasing the temperature the electrons gain more energy making them capable of crossing the gap to higher electronic bands. In some cases this is not enough to produce a transistor device, so additional carriers are introduced by doping.

When the temperature is low, the conduction of an insulator or a semiconductor is governed by variable range hopping (VRH), also known as Mott variable range hopping. This model describes conduction at low temperatures in strongly disordered systems with localized states. Consider two states with a

distance R between them and energies E_1 and E_2. An electron may go from one site to another if it adsorbs energy (ω) from a phonon. The number of states within a distance R per unit of energy corresponds to $(4\pi/3)R^3N(E_F)$, where $N(E_F)$ is the density of localized states. Therefore the energy difference for a state within a distance R is $\Delta E = 1/[(4\pi/3)R^3N(E_F)]$, this means that for the longer the carrier hops the activation energy is lower.

This carrier at a certain site posses a decay or localization length ξ. The probability of an electron to hop to a site at a distance R is governed by the factor $exp(-2R/\xi)$, meaning that at a larger tunneling distance, lower is the probability. Since there is a competition between long range hoping and tunneling, there will be an optimum distance (R) for the hopping to take place where the probability $exp(-2R/\xi)\ exp(\Delta E/k_BT)$ reaches a maximum. This point is reached when $1/R^4 = 8\pi N(E_F)k_BT/\xi$. Using this we find that the probability and therefore the conductivity is proportional to $exp(-(T_0/T)^{1/4})$, where $T_0 = (24/\pi)\xi^3/k_BN(E_F)$, k_B *is the Boltzmann constant*. For d-dimensional conduction (σ) dependent upon the temperature (T) the model is as follows (σ_o and T_o are parameters from the material that weakly depend on temperature, and *d* is an integer number giving the dimensionality of the VRH) [1; 2]:

Eq. 4.2
$$\sigma = \sigma_o e^{-(T_o/T)^{1/(d+1)}}$$

Now, if the temperature is high enough ($T>>\theta_D$, θ_D is the Debye temperature) the conductivity is governed by the electrons thermally excited across the gap, this probability obeys the Boltzmann distribution with exponential temperature dependence as follows:

Eq. 4.3
$$\sigma = \sigma_0 e^{-(E_g/2k_BT)}$$

E_g is the size of the energy gap, also called activation energy of the conductivity, and σ_o is the maximum conductivity determined by the scattering of electron by phonons at high temperatures.

Regarding the conductivity of carbon materials; a two dimensional net carbon (Figure 4.1 a) has shown a Mott like behavior (Figure 4.1 b), although at different ranges of temperature the potential scaling of the temperature-dependent resistivity varies. If the density of states enlarges far from the Fermi level, stronger dependences are visible [3].

The electrical properties of carbon inverse opal have been studied previously, showing a conductivity in the range of 12 – 80 S/cm [4; 5; 6], when the temperature of the measurements was increased their conductivity was increased which indicates that these materials are semiconductors. The effect of the pore size (Figure 4.1 c-f) has also been studied were the tendency was clear; for larger

pore sizes the conductivity was increased (Figure 4.1 g), which might be explained by that small pore sizes tend to constrain the crystal formation of carbon. The small pore size creates a greater interlayer spacing and a smaller crystalline size; this may cause the electronic system to behave in a two-dimensional manner [6].

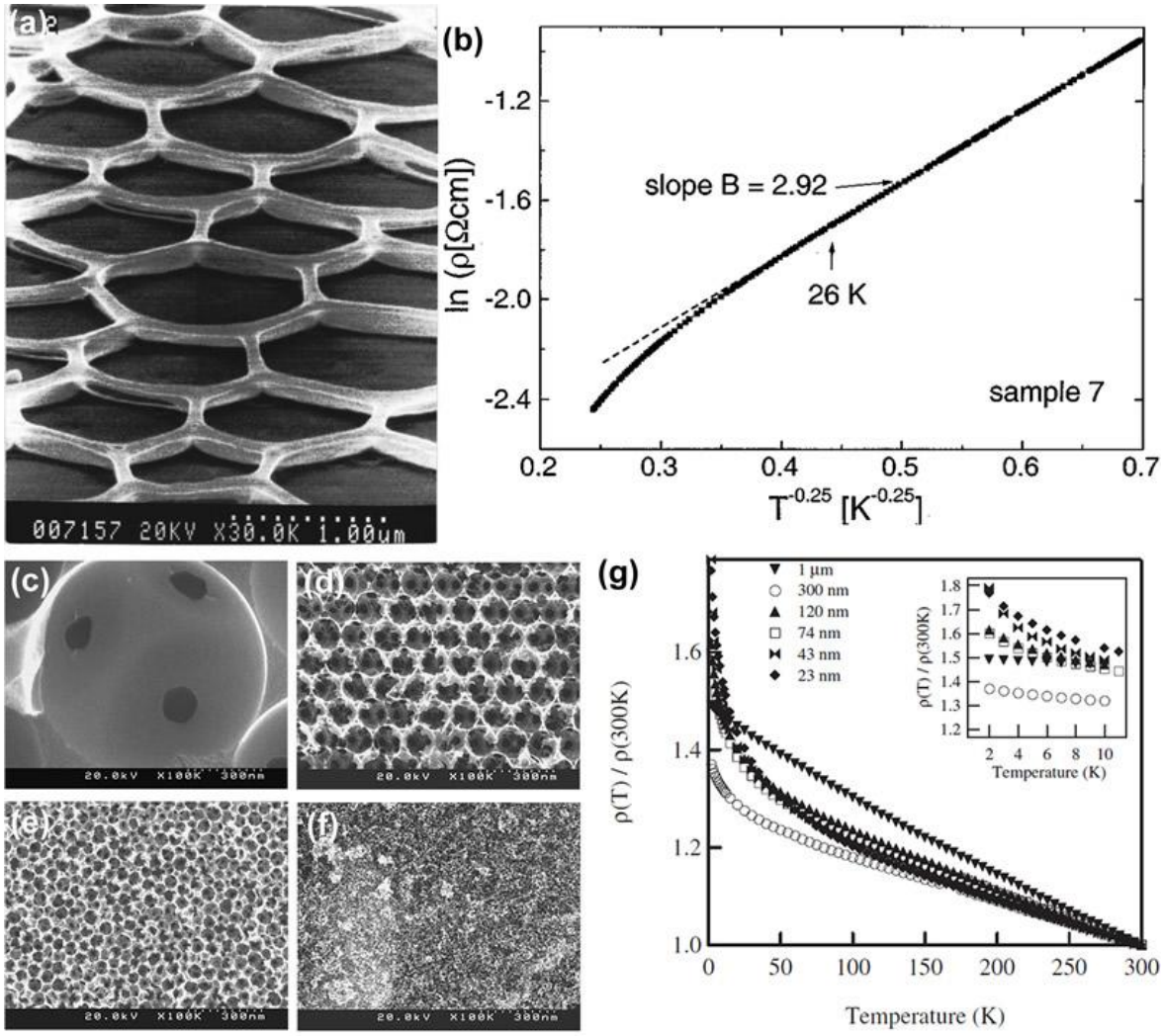

Figure 4.1: **(a)** Scanning electron microscope (SEM) image of a carbon net. **(b)** Specific resistivity vs temperature of a carbon net, on a semilogaritmic scale (images from ref. **[3]**). SEM images of a carbon inverse opal with **(c)** 1 mm, **(d)** 120 nm, **(e)** 43 nm, **(f)** 11 nm pore size. **(g)** Resistivty vs temperature of carbon inverse opal heat treated at 2800 ^{o}C with different pore sizes (images from ref. **[6]**).

When nitrogen is introduced in to a carbon system it may donate an electron that is harvested for a better conductivity [7], if it is introduced in a substitutional manner in the graphitic structure [8; 9; 10; 11]. For example, when carbon nanotubes are doped with nitrogen there is a strong π peak, which may convert them from a semiconducting (zig-zag) carbon nanotube in to metallic [9; 10]. Another example is that in a graphene structure the introduction of nitrogen

might change it from being metallic (non-doped graphene) to an n-type semiconductor (N-doped graphene) [12].

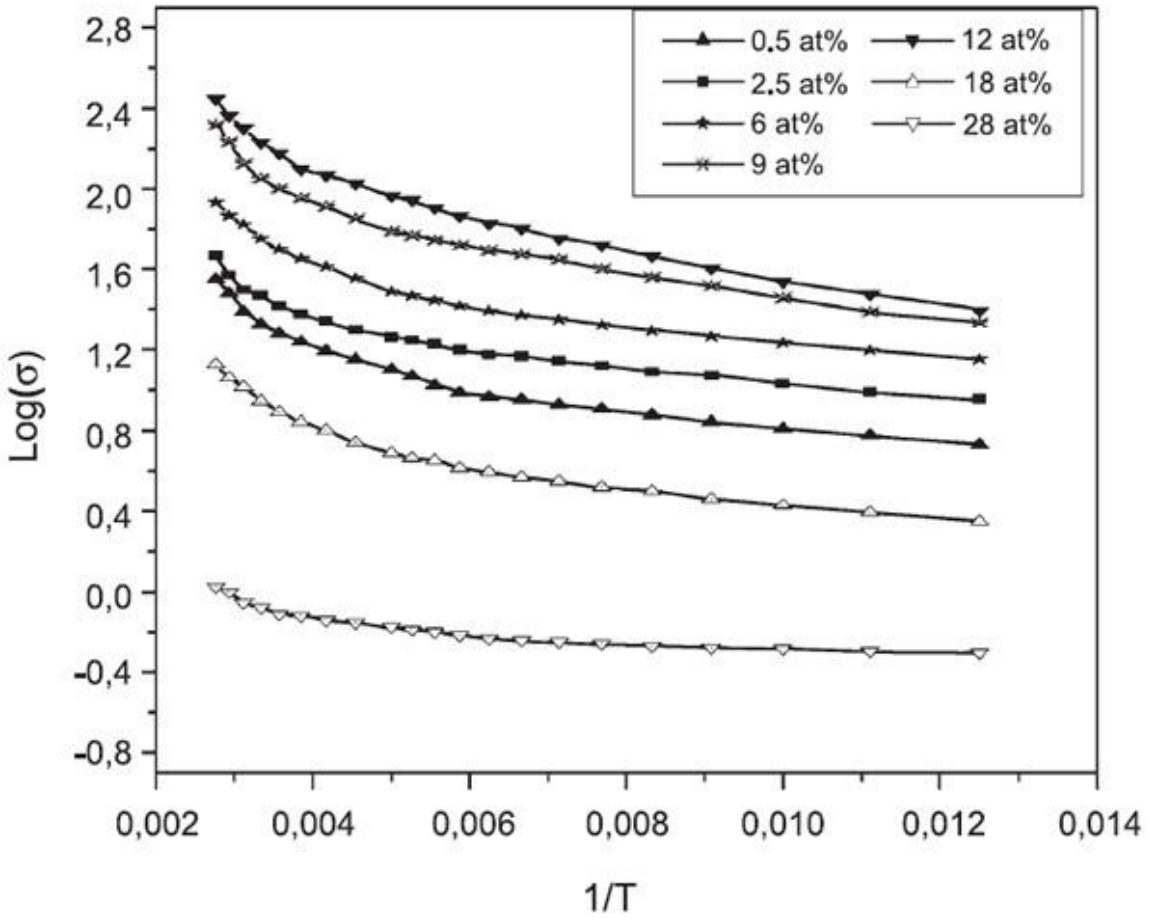

Figure 4.2: Temperature dependence of nitrogen doped carbon films (Log(s) vs 1/T) (image from ref. **[13]**).

It has been observed that for nitrogen doped amorphous carbon films the activation energy and resistivity increase with a higher content of nitrogen, this may be caused by a reduction in the density of states of the mobility gap, or by the amount of triple bonded carbon-nitrogen in the material [14]. However in other studies, the resistivity of similar films show a minimum resistivity at certain nitrogen content, later on, it has a dramatic increase in resistivity (Figure 4.2 a). The low resistivity was attributed to a high graphitic content among the entire structure [13].

The enhanced electronic properties by nitrogen doping make CN_x materials candidates for applications such as electron field emission [15; 16; 17], it has been tested as an electrode for Li batteries [18] and for electrochemical cells [19; 20].

4.1.2 Experimental methodology

The carbon inverse opals were made following the procedure explained in chapter 2 with different pyrazine content, using opals with 300 nm silica particles. The resistivity was measured with samples with a cross section of c.a. 1 mm^2 and length of c.a. 5 mm, using a PPMS Quantum Design Device. In the PPMS the resistivity was measured between 2 and 350 K for all samples, using a four probe setup. The labeling of the samples is the same used as in chapter 2, all the samples were synthesized using 300 nm silica nanoparticles; the lowest and highest pyrazine content are at *N1* and *N3*, respectively.

4.1.3 Results and discussions

The resistivity measurements against temperature for all samples, doped and undoped, (Figure 4.3 a) show that the value of resistivity decreases to a minimum when doping with nitrogen (until CIO300-N2), where at 300 K it reaches a value of 0.024 Ω cm, at higher nitrogen content the resistivity increases to a value higher than the undoped carbon inverse opal (Table 4.3), similar behavior of the decrease in resistivity has been observed previously for nitrogen doped carbon films by Derradjia et al [13]. The curves present a decrease in its resistivity in an exponential behavior when the temperature increases, this behavior is characteristic for semiconductors according to the following the Arrhenius equation:

Eq. 4.4
$$\sigma = \sigma_0 e^{(-\frac{E_a}{k_B T})}$$

In this equation σ is conductivity ($\sigma = 1/\rho$), σ_0 is a maximum conductivity determined by the scattering of electrons by phonons at high temperature, k_B is Boltzmann's constant, T is temperature and E_a is the activation energy. In a more detailed manner, at temperatures above 150 K the samples exhibit activation energies of 233, 357, 314 and 262 meV for CIO300, CIO300-N1, CIO300-N2 and CIO300-N3, respectively (Table 4.3), these values were obtained from the slope of the $\ln\rho$ vs. lnT plots (Figure 4.3 b). Other works have reported activation energies of 400-700 meV for amorphous carbon [21], 200-1000 meV for nitrogen doped amorphous carbon [22] and 13-290 meV for carbon nanotubes (single wall and multiwall) [23; 24].

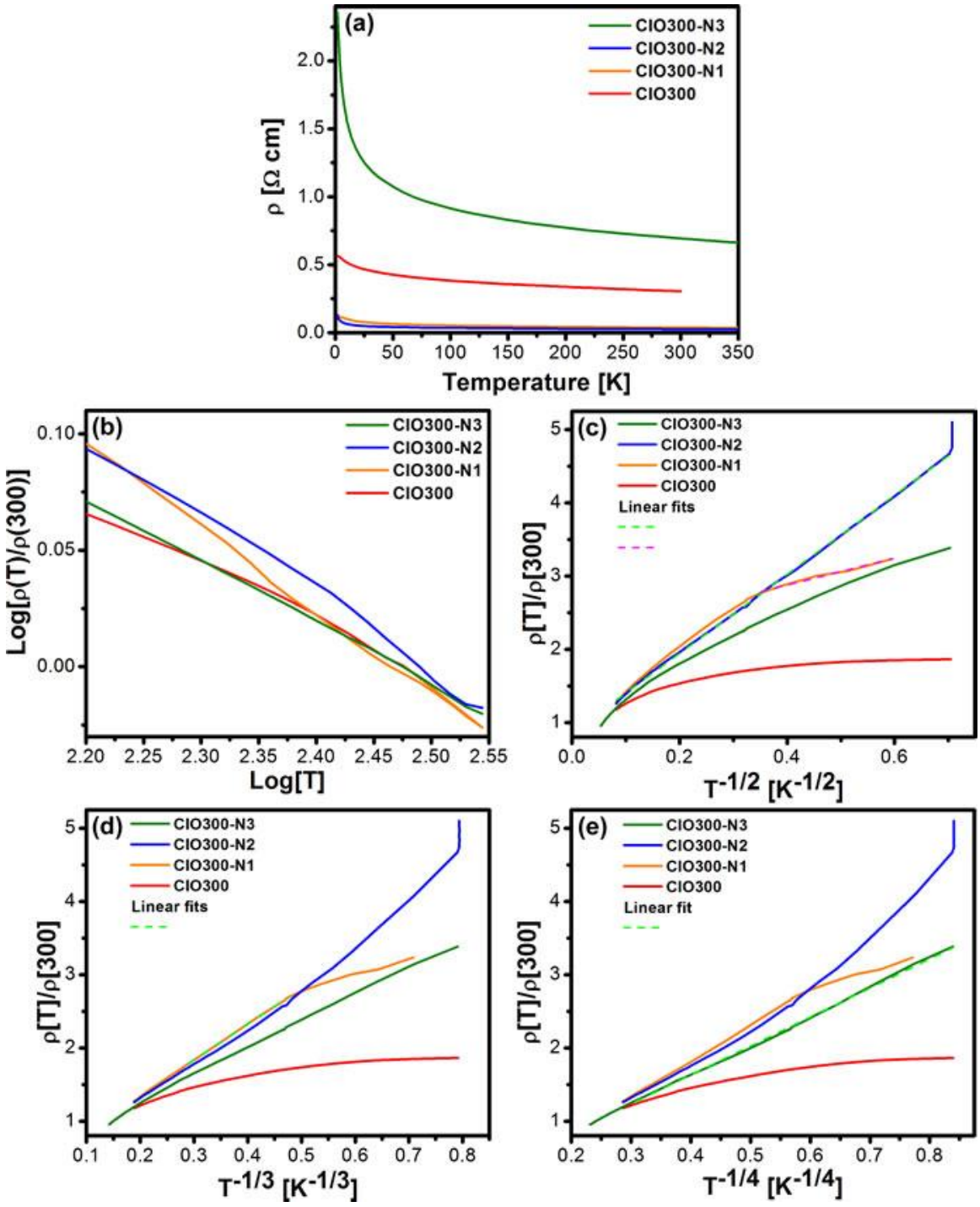

Figure 4.3: (a) Resistivity vs temperature of nitrogen doped carbon inverse opal at different contents, all samples present a semiconductor behaviour. **(b)** Log[ρ(T)/ρ(300)] vs Log[T] of all samples for T > 150 K. **(c)** Resistivity vs $T^{-1/2}$, **(d)** Resistivity vs $T^{-1/3}$, **(e)** Resistivity vs $T^{-1/4}$ for the studied samples. Notice that ClO300 does not have a linear behavior for any power of temperature.

Table 4.1: Room temperature activation energies (E_a) and resistivity of the undoped and doped carbon inverse opals at different nitrogen content.

	Ea (meV)	R (Ohm cm)
CIO300	233	0.537
CIO300-N1	357	0.038
CIO300-N2	314	0.024
CIO300-N3	262	0.696

When plotting the dependence of the normalized resistivity ($\rho(T)/\rho(300)$) vs. temperature (shown in Figure 4.3 b) in a double logarithmic scale we observe different behaviors for all the samples, it is noticeable that the doped samples suffer a greater change in resistivity when the temperature is increased, specially for CIO300-N2, this might be due to the introduction of a n-type doping element which may introduce more electrons in to the system thus increasing the probability for more electrons to conduct with the addition of thermal energy.

At low temperature (< 150 K), the samples exhibit different behaviors; the samples CIO300-N2 fit well for one dimensional variable range hopping (VRH) (Figure 4.3 c), sample CIO300-N1 also fits in this plot although for temperature below 8 K. For two dimensional VRH the sample CIO300-N1 fits well for temperatures between 9 – 11 K (Figure 4.3 d), and sample CIO300-N3 exhibits a three dimensional VRH (Figure 4.3 e). Surprisingly the undoped sample (CIO300) did not fit any plot for VRH, meaning that the system exhibits a different conduction mechanism possibly due to the degree of disorder in the atomic structure where the electrons may have a more complex path, however a more ordered structure along with determined nitrogen content, such as sample CIO300-N2, exhibits one dimensional conductivity.

4.1.4 Conclusions

All carbon inverse samples doped and undoped show a semiconductor behavior where the resistivity decreases when increasing the temperature of the environment. Along with this, they hay different activation energies at temperatures above 150 K depending upon the nitrogen content, clearly nitrogen doped samples present a lower resistivity (up to sample CIO300-N2) and all of them exhibit a higher activation energy when compared with the undoped samples. At low temperature, all the samples exhibit different conduction mechanisms, sample CIO300-N2 acts as a one dimensional VRH possibly due to an optimum crystallinity of the sample and proper nitrogen doping, however a more disordered sample like CIO300 does not exhibit any type of VRH. These

results show that the introduction of nitrogen in the carbon inverse opal is capable of altering the electrical properties such as the resistivity and the activation energy, this kind of control can be used for other applications such as sensors and electrochemical cells, due to the high surface area, conductivity and reactivity.

4.1.5 References

1. *Electronic processes in non-crystailline materials.* **N. F. Mott, E. A. Davis.** s.l. : Oxford University Press, 1979.

2. *Magnetism and electron transport in magnetoresistive lanthanum calcium manganite.* **Snyder, G. J.** Stanford University : Applied Physics, 1997, Dissertation for the degree of doctor of philosophy.

3. *Electrical properties of self-assembled carbon networks.* **L. V. Govor, M. Goldbach, I. A. Bashmakov, I. B. Butylina, J. Parisi.** 2000, Phys. Rev. B, Vol. 62, pp. 2201-2208.

4. *Electrical properties of a periodic porous carbon replica of opal.* **K. Yoshino, H. Kajii, Y. Kawagishi, M. Ozaki, A. A. Zakhidov, R. H. Baughman.** 1999, Jpn. J. Appl. Phys., Vol. 38, pp. 4926–4929.

5. *Optical and electrical properties of opal carbon replica and effect of pyrolysis.* **H. Kajii, Y. Kawagishi, H. Take, K. Yoshino, A. A. Zakhidov, R. H. Baughman.** 2000, J. Appl. Phys., Vol. 88, pp. 758-763.

6. *Preparation and electronic properties of nanoporous carbon inverse opal.* **H. Take, T. Matsumoto, S. Hiwatashi, T. Nakayama, K. Niihara, K. Yoshino.** 2004, Jpn. J. Appl. Phys., Vol. 43, No. 7A (2004), p. 4453, pp. 4453-4457.

7. *O_2 Reduction on graphite and nitrogen-doped graphite: experiment and theory.* **R. A. Sidik, A. B. Anderson, N. P. Subramanian, S. P. Kumaraguru, B. N. Popov.** J. Phys. Chem. B, Vol. 110, pp. 1787-1793.

8. *New route to graphite flakes and films. Pyrolysis of aromatic and heteroaromatic compounds under dehydrogenation conditions.* **P. H. Chang, M. M. Labes.** 1989, Chem. Mater., Vol. 1, pp. 523-525.

9. *Identification of electron donor states in N-doped carbon nanotubes.* **R. Czerw, M. Terrones, J.-C. Charlier, X. Blase, B. Foley, R. Kamalakaran, N. Grobert, H. Terrones, D. Tekleab, P. M. Ajayan, W. Blau, M. Ru2hle, D. L. Carroll.** 2001, Nano Lett., Vol. 1, pp. 457-460.

10. *N-doping and coalescence of carbon nanotubes: synthesis and electronic properties.* **M. Terrones, P.M. Ajayan, F. Banhart, X. Blase, D.L.Carroll, J.C. Charlier, R. Czerw, B. Foley, N. Grobert,R. Kamalakaran, P. Kohler-Redlich, M. Ruhle, T. Seeger, H. Terrones.** 2002, Appl. Phys. A, Vol. 74, pp. 355-361.

11. *Electronic properties of nitrogen-doped graphite flakes.* **D.-P. Kim, C. L. Lin, T, Mihalisin, P. Heiney, M. M. Labes.** 1989, Chem. Mater., Vol. 1, pp. 523-525.

12. *Synthesis of N-doped graphene by chemical vapor deposition and its electrical properties.* **D. Wei, Y. Liu, Y. Wang, H. Zhang, L. Huang, G. Yu.** 2009, Nano Lett., Vol. 9, pp. 1752-1758.

13. *Nitrogen effect on the electrical properties of CN_x thin films deposited by reactive magnetron sputtering.* **N.E. Derradjia, M.L. Mahdjoubia, H. Belkhira, N. Mumumbilab, B. Angleraudb, P.Y. Tessier.** 2005, Thin Sol. Films, Vol. 482, pp. 258– 263.

14. *Electrical properties of reactively sputtered CN_x films.* **M.A. Monclus, D.C. Cameron, A.K.M.S. Chowdhurry.** 1999, Thin Sol. Films, Vol. 341, pp. 94-100.

15. *Controllable growth, structure, and low field emission of well-aligned CN_x nanotubes.* **X. Wang, Y. Liu, D. Zhu, L. Zhang, H. Ma, N. Yao, B. Zhang.** 2002, J. Phys. Chem. B, Vol. 106, pp. 2186-2190.

16. *Electron side-emission from corrugated CN_x nanotubes.* **R. C. Che, L.-M. Peng, M. S. Wang.** 2004, Appl. Phys. Lett., Vol. 85, pp. 4753-4755.

17. *Bamboo-shaped aligned CNx nanotubes synthesized using single feedstock atdifferent temperatures and study of their field electron emission.* **P. Ghosh, M. Zamri, M. Subramanian, T. Soga, T. Jimbo, R. Katoh, M. Tanemura.** 2008, J. Phys. D: Appl. Phys., Vol. 41, p. 155405.

18. *Synthesis and rate performance of monolithic macroporous carbon electrodes for lithium-ion secondary batteries.* **K. T. Lee, J. C. Lytle, N. S. Ergang, S. M. Oh, A. Stein.** 2005, Adv. Funct. Mater., Vol. 15, p. 547.

19. *Synthesis of graphitic ordered macroporous carbon with a three-dimensional interconnected pore structure for electrochemical applications.* **F. Su, X. S. Zhao, Y. Wang, J. Zeng, Z. Zhou, J. Y. Lee.** 2005, J. Phys. Chem. B, Vol. 109, p. 20200.

20. *Photonic crystal structures as a basis for a three-dimensionally interpenetrating electrochemical-cell system.* **N. S. Ergang, J. C. Lytle, K. T. Lee, S. M. Oh, W. H. Smyrl, and A. Stein.** 2006, Adv. Mater. , Vol. 18, pp. 1750–1753 .

21. *Reduction in defect density by annealing in hydrogenated tetrahedral amorphous carbon.* **N. M. J. Conway, A. Ilie, J. Robertson, W. I. Milne, A. Tagliaferro.** 1998, Appl. Phys. Lett., Vol. 73, No. 17, 26 October 1998, Vol. 73, pp. 2456-2458.

22. *Nitrogen doping of highly tetrahedral amorphous carbon.* **V. S. Veerasamy, J. Yuan, G. A. J. Amaratunga, W. I. Milne, K. W. R. Gilkes, M. Weiler, L. M. Brown.** Phys. Rev. B, Vol. 48, p. 17958.

23. *Electrical transport in pure and boron-doped carbon nanotubes.* **B. Wei, R. Spolenak, P. Kohler-Redlich, M. Ruhle, E. Arzt.** 1999, Appl. Phys. Lett., Vol. 74, pp. 3149-3151.

24. *Water-vapor effect on the electrical conductivity of a single-walled carbon nanotube mat.* **A. Zahab, L. Spina, P. Poncharal, C. Marliere.** 2000, Phys. Rev. B, Vol. 62, pp. 10000-10003.

4.2 Field emission

4.2.1 Introduction

Field emission is the emission of electrons due to the presence of an external electromagnetic field. This emission can happen at the surface of a solid material, this being a metal or a semiconductor, here the electrons tunnel through a potential barrier. From a quantum mechanical point of view, this phenomenon is because the wave function of an electron decays exponentially in to the barrier, here the total energy of the electron is less than the potential energy. This means that there is a finite probability for the electron to be outside of the barrier. When thinking of this for a metal at low temperature, we may consider the metal as a potential box where the electrons are filled up to the Fermi level. Now defining the vacuum level as the energy level were the electron may escape from this potential box, so the energy needed to go from the Fermi level up to the vacuum level is known as the work function. Later, if we apply an external field the outside potential may be deformed in a triangular manner (Figure 4.5), making a tunneling effect for the electrons possible. From all the electrons in the system the ones at the fermi level will have a higher probability to tunnel trough the barrier than the ones below this level. This scheme is known as Fowler-Nordheim tunneling, this theory predicts that current (I) will obey the following equation:

Eq. 4.5
$$I = \frac{E^2}{\varphi} \exp\left(\frac{B\varphi^{3/2}}{E}\right)$$

Here E is the local electric field, φ is the work function and B is 6.83x109 $VeV^{-3/2}$ m^{-1}.

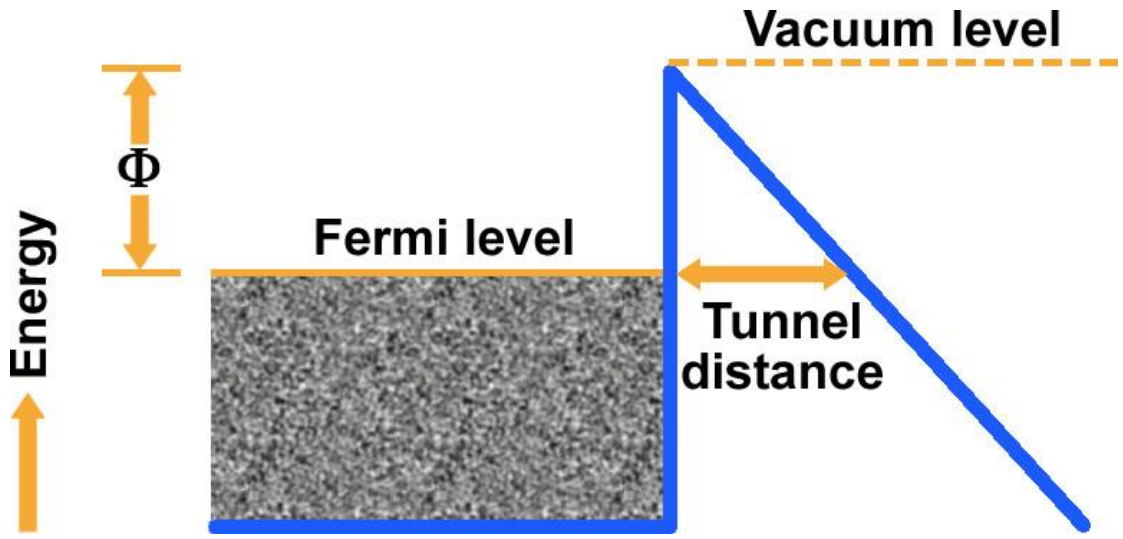

Figure 4.5: Energy level scheme for an electron of a metal at zero temperature. The external field creates a triangular potential barrier. The electrons tunnel better when having the highest energy equal to the work function Φ.

Regarding carbon inverse opal, as of now there are no reports for the field emission of nitrogen doped carbon inverse opals. However, it has been observed that Fowler-Nordheim (FN) theory may explain the field emission of carbon inverse opal according to Ojima et al. [1]. When decreasing the pore size, the field enhancement factor and the effective area are greater; further on, there is a higher current density at lower electric fields (Figure 4.6 a). It was found that the pore size and the effective emission area have an exponential relationship as $y=k/x^2$. Field emission is expected to be produced where the electric field is concentrated, this would correspond to the sharp edges between pores (Figure 4.6 b and c), and this means that there are six sites at the boundary of each pore. Taking this in consideration it can be thought that at smaller pore radius the number of field emission sites per area increases by a factor of r^{-2}. Furthermore, when the carbon inverse opal was heated at 2760 ^{o}C the threshold field was reduced [1].

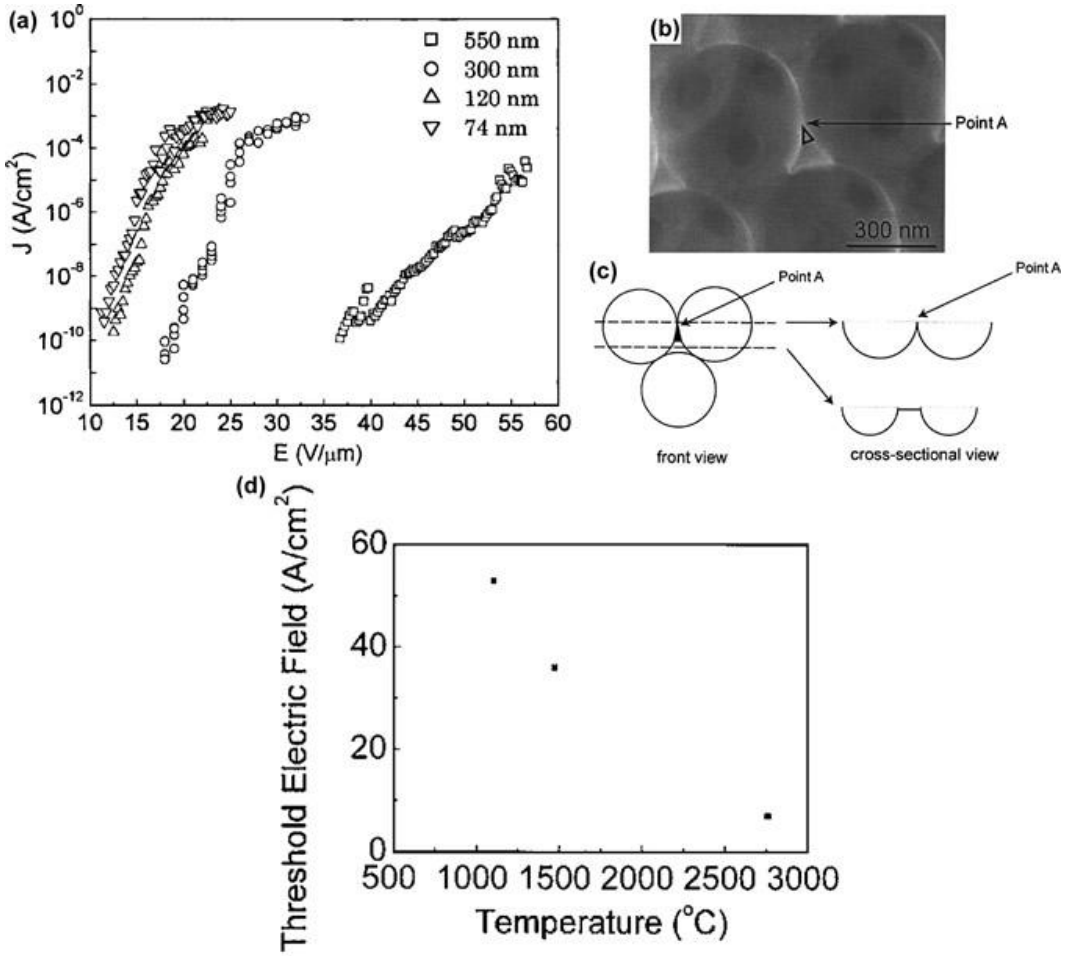

Figure 4.6: (a) Field emission curves measured at 40 mm of carbon inverse opals with different pore size. **(b)** SEM image and **(c)** scheme ilustrating emission site. **(d)** Threshold electric field vs heat treatment temperature (Images from ref. **[1]**)

Much work has been done with other carbon material, particularly with carbon nanotubes due to their interesting electrical properties. The electron emission from carbon nanotubes (CNTs) is originated at the tips [2], now if these CNTs are held in arrays on a substrate they may present current densities between 1 and 10 mA/cm^2, with electric fields from 2.7 to 6.1 V/μm [3]. Multiwall carbon nanotubes (MWNTs) have been used as electron emitters in different presentations. Random oriented MWNT films immersed in epoxy have shown a low turn on voltage between 1.5 and 4.5 V/μm [4]. It has been observed that CNTs present different electric field depending on the substrate material that is also used as a catalyst. When the CNT are grown on stainless substrates, the field emission presents a current density of 1 mA/cm^2 [5].

Now for nitrogen doped carbon materials, commonly carbon nanotubes have been studied regarding their field emission properties. When multiwall carbon nanotubes are doped with nitrogen (CN_x) they exhibit good electron emission,

experimentally its workfunction has been reported as 5.0 eV [6]. A route to improve its emission is by the introduction of a higher concentration of nitrogen at the tip, here a peak in the electronic structure near the Fermi-level is expected [7; 8]. This has been observed for CN_x synthesized at different temperatures (700, 800 and 900 ^oC) where the x-ray photoelectron spectroscopy showed a higher nitrogen content when synthesized at 800 ^oC, sample that showed a superior field emission performance with 10 mA/cm^2 at 3 V/μm [9]. Corrugated nitrogen doped carbon structures show considerable lower turn on fields for emission current density of 10 mA/cm^2 than the undoped carbon nanotubes (Figure 4.7 c). If the CN_x are corrugated they will present a more efficient emission from the side than from the tip since these corrugations present lower and narrower potential barriers for electron emission [10] (Figure 4.7 d and e).

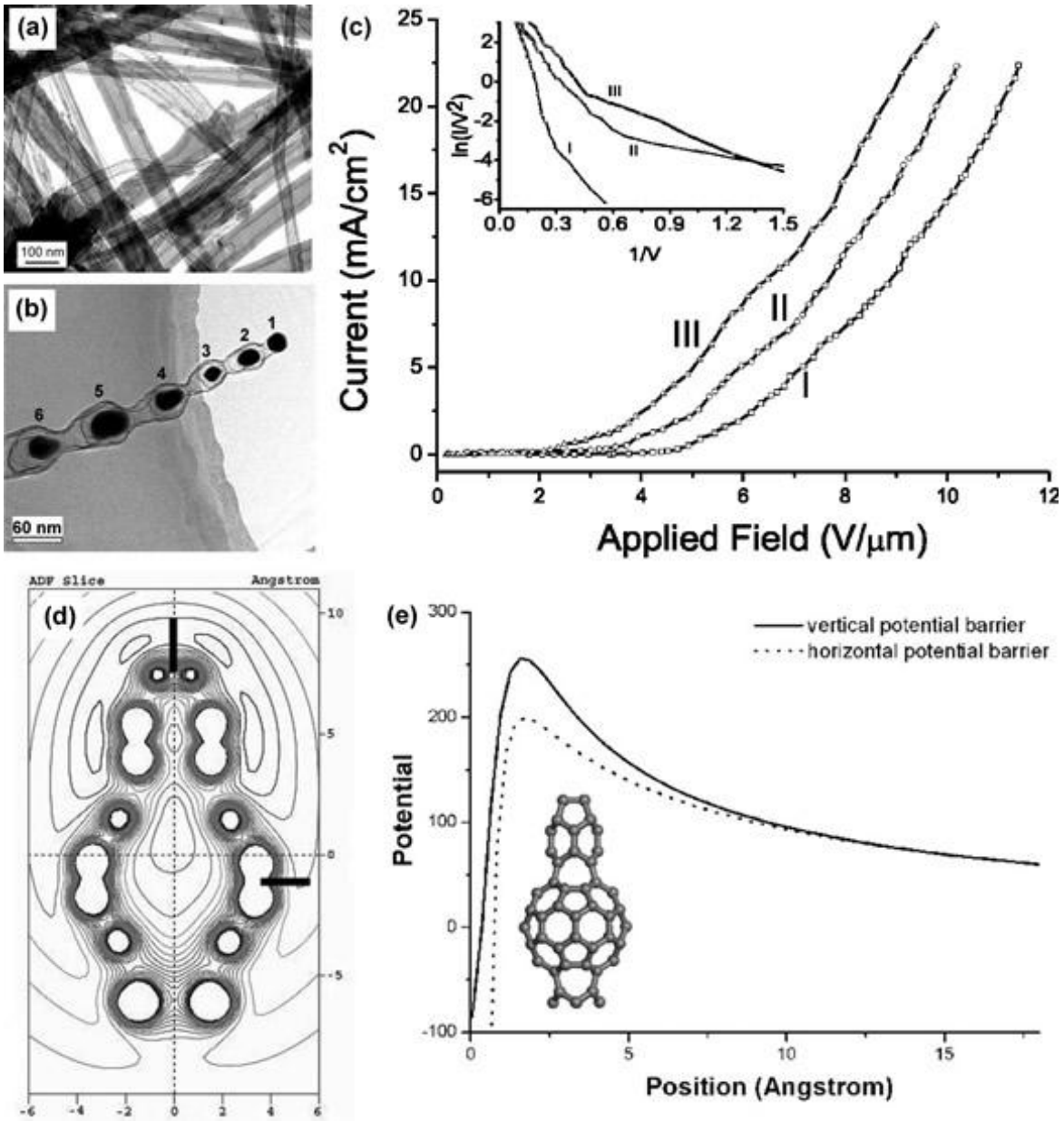

Figure 4.7: Transmission electron images of carbon nanotubes **(a)** undoped and **(b)** corrugated doped with nitrogen encapsulating Fe_2O_3. **(c)** Field emission current curves for carbon nanotubes I undoped and doped with nitrogen II film and III horizontally grown CNx-MWNTs. **(d)** Calculated electrosatic potential contour map for a peapod CNT. **(e)** Potential barrier "seen" by an electron tunneling in to the vacuum from the top and side of the inset CNT model. (Images from ref. **[10]**)

4.2.2 Experimental methodology

Following the synthesis of undoped and nitrogen doped carbon inverse opal from chapter 2; the samples were labeled according the Table 4.2. Further on sample CIO300 was heat treated in vacuum at 1450 ^{o}C and sample CIO300-N3 was also heat treated in vacuum at 1450 and 1750 ^{o}C.

Table 4.2: Carbon and nitrogen source solution concentrations for 300 nm silica nanoparticle opal.

	ClO300	ClO300-N1	ClO300-N2	ClO300-N3
Sucrose	25.00	16.67	12.50	8.33
Pyrazine	0.00	8.33	12.50	16.67
Water	72.42	70.83	68.75	66.67
Sulphuric acid	2.58	4.17	6.25	8.33

Preliminary electron field emission measurements were done in Nanotech Institute at the University of Texas at Dallas. These measurements were carried out in a vacuum chamber (Figure 4.8 c) at a base pressure of 10^{-6} Torr or lower. The chamber is first pumped with a scroll pump to 10^{-3} Torr, and then a turbo pump is turned on for further pumping. Working pressure of $5x10^{-7}$ Torr is usually achieved after 1-1.5 hours, whereas it would take 25-30 hours to obtain $5x10^{-8}$ Torr.

A diagram of the sample holder is shown in Figure 4.8 a. The aluminum anode and cathode holders are fixed on a metallic base. Insulating layer of a teflon tape on the base prevents shorting between the anode and cathode. It is also possible to adjust the anode-cathode spacing by moving the cathode during experiments. Using a linear motion feed through the spacing can be adjusted with an accuracy of 15 μm. The sample holder with the attached sample is placed into the chamber to a place shown in a red circle in Figure 4.8 b. Glass windows in front and on the top of the chamber allow visual observations of experiments. Electrical connections in the back of the chamber are needed for supplying voltage to a sample through the anode and cathode holders.

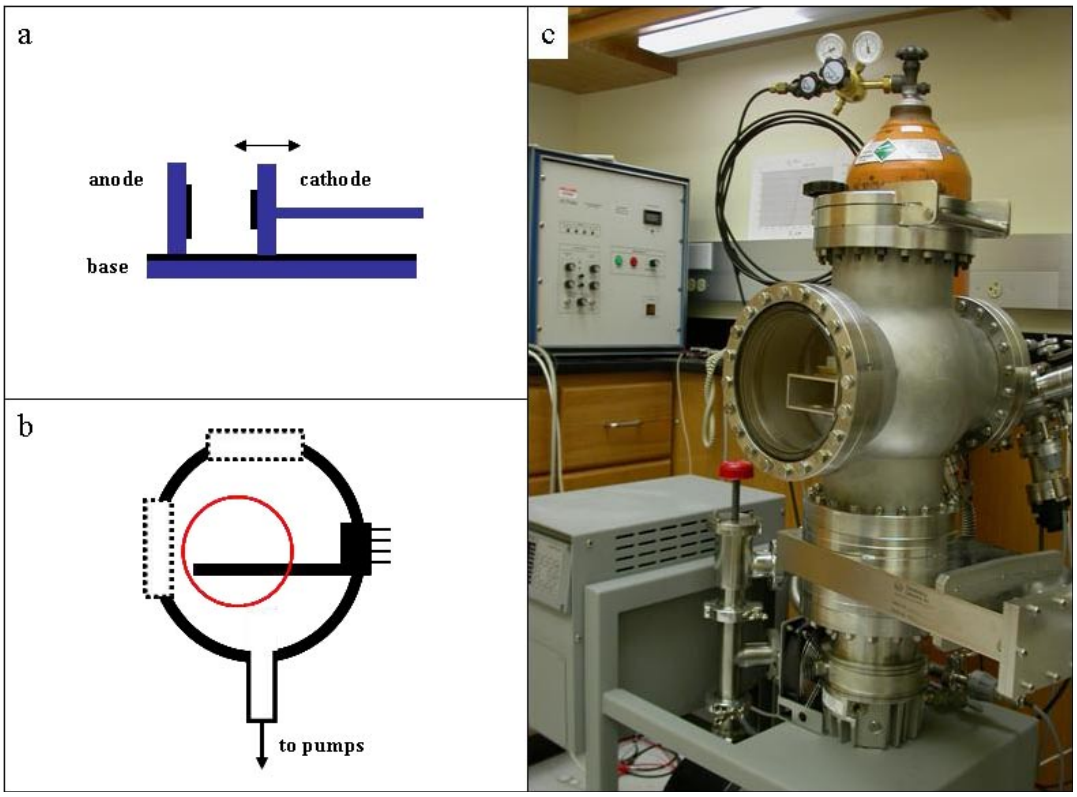

Figure 4.8: (a) Sample holder, **(b)** schematics of a vacuum chamber, and photograph of the electron field emission setup. Figure provided by Dr. Alexander Kuznetsov, Nanotech Institute, University of Texas at Dallas.

The undoped and nitrogen doped carbon inverse samples studied for field emission were usually attached to the cathode using double-sided carbon sticky tape. Silver paint is then applied to ensure electrical contact to the cathode holder.

In the experiments polished tungsten plate was used as anode. External control of anode-cathode spacing during the experiment is very useful since it allows adjusting the distance without opening the chamber. However, it has one significant drawback. It doesn't allow measuring the distance exactly, only relative change is measured. So the following indirect method was used to estimate the distance between the anode and the cathode, here in order to determine the distance is to measure threshold voltage of electron emission at different distances. This dependence is usually a straight line. In theory, this line should cross the origin because at the distance threshold voltage would be also zero. Having that, it is possible to find absolute distance between the anode and cathode. However, this method doesn't work for some samples in which threshold voltage is not linearly proportional to the distance.

A high-voltage source-measure unit (Keithley 237) was usually used for current-voltage measurements. Keithley 6517 was used when necessary. Both devices were connected to a computer and LabView program was created to control them. High voltage pulse generator model M25k-50N (HV Pulse Technology, Inc.) was used for taking images with the phosphorous anode.

The curves were plotted according to Fowler-Nordheim (FN) theory, and the slope of the curves were obtained and used in the following equation in order to obtain the field enhancement factor:

Eq. 4.6 $$\beta = -\frac{B\varphi^{3/2}d}{s}$$

Here B = 6.83×10^9 $VeV^{-3/2}$ m^{-1}, φ is the work function (5 eV), d is the inter-electrode distance and s is the slope of the FN plot.

4.2.3 Results and discussions

The field emission I-V curves clearly show an exponential behavior typical for field emitters. The nitrogen doped carbon inverse opal (CIO300-N1) has a low emission current (~10^{-1} mA, Figure 4.9 a) when compared with the heat treated samples (1 – 10 mA, Figure 4.9 b); the FN plots shows two linear behaviors, one for low 1/E and another for higher values, we obtained the slope for low 1/E values in order to obtain the enhancement factor (Figure 4.9 c); when analyzing the threshold voltage (V_{thr}) at 100 nA the non heat treated material exhibits higher V_{thr}, however it has a lower threshold field (E_{thr}) of 2.38 V/μm (Figure 4.9 d and e, Table 4.3). Now, regarding the heat treated samples we observe emission currents in the order of 1 – 10 mA, this increases with a higher annealing temperature, this has been previously observed for an amorphous carbon nitride film [11]. Now, the threshold field also decreases with a higher annealing temperature, for example sample CIO300-N3 changes from 6.8 to 4.5 V/μm for 1450 and 1750 ^oC, respectively (Figure 4.9 f, Table 4.), the decrease in the E_{thr} with higher heat treatment temperatures has been reported previously by Ojima et al. [1]. From the Fowler-Nordheim plots we obtain the slopes and calculate the field enhancement factors (β) of the studied samples, here we observe β of 528 for the non heat treated sample and higher values for the heat treated samples between 517 and 756. The enhancement of the field emission properties by heat treatment has been observed previously for carbon inverse opal [1], this can be due to an increase of the conductivity [12] that can be favored by a higher degree of graphitization [11; 13; 14; 15].

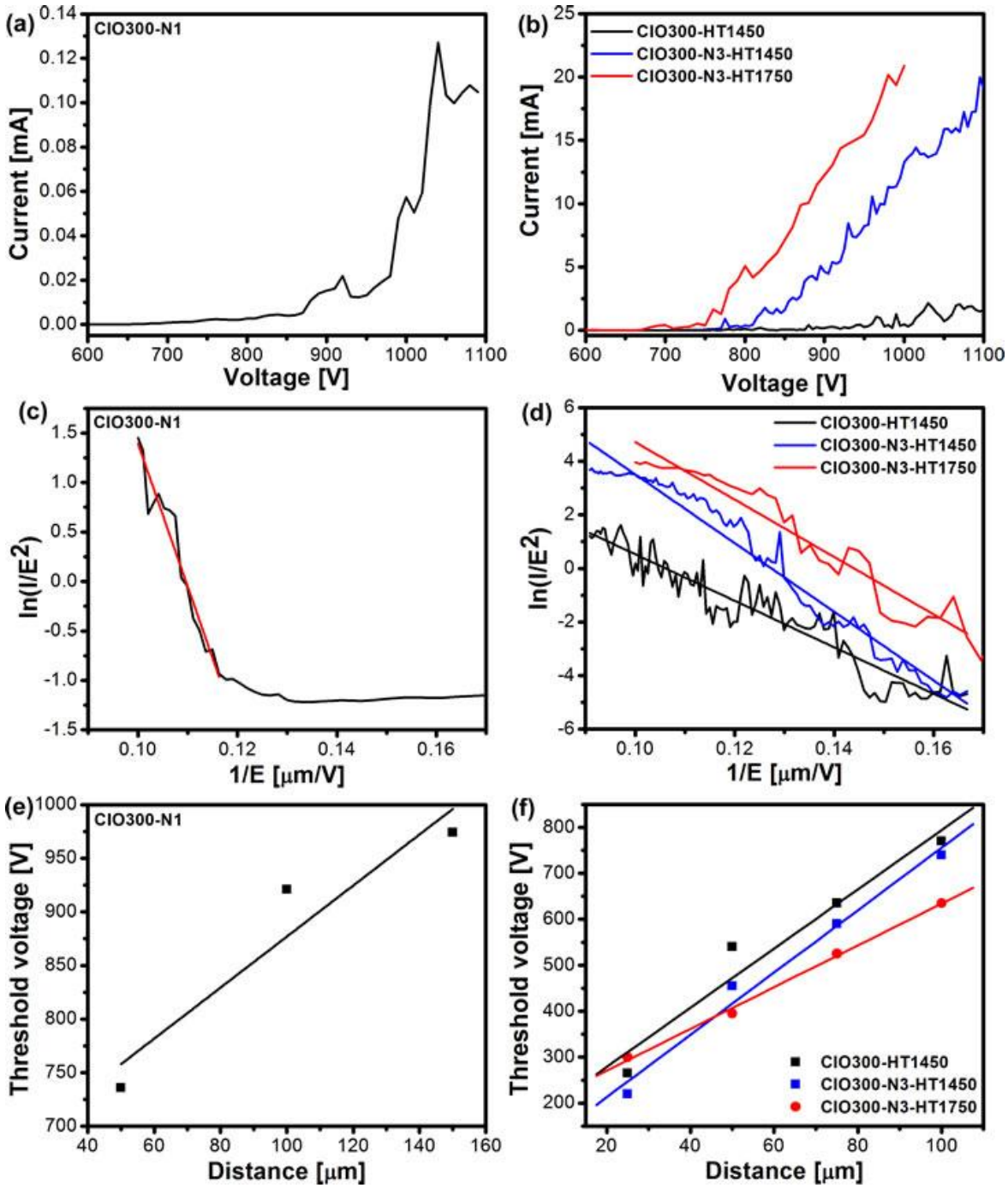

Figure 4.9: Field emission mesurements of nitrogen doped and heat treated carbon inverse opal. (a,b) I-V, **(b,c)** Fowler-Nordheim (FN) plots and **(c,d)** threshold voltage (left) CIO300-N1 and (left) heat treated samples. The I-V curves were measured at 100 μm, observe that the heat treated samples exhibit a higher slope in the FN and the E_{thr} vs distance plots.

Table 4.3: Treshold field (E_{thr}, eV) and field enhancement factor (β) for the nitrogen doped and heat treated samples of carbon inverse opal. Enhancement factor was calculated from Fowler-Nordheim plots.

CIO300-	E_{thr} (V/μm)	β
N1	2.38	528
HT1450	6.4	756
N3-HT1450	6.8	517
N3-HT1750	4.5	701

4.2.4 Conclusions

The nitrogen doped carbon inverse opal seems to exhibit a lower threshold field than the heat treated samples, meaning that the presence of nitrogen may also lower the turn on voltage in carbon inverse opals, however the field enhancement factor is not better than the heat treated samples. Further on, the heat treated samples clearly show a decrease of the threshold field upon a higher heat treatment temperature due to a higher degree of graphitization of the sample. In this study we found that the introduction of nitrogen or the increase in crystallinity of the carbon inverse opal may enhance the field emission, giving higher currents and lower threshold voltages.

4.2.5 References

1. *Pore size dependence of field emission from nanoscale porous carbon.* **M. Ojima, S. Hiwatashi, H. Araki, A. Fujii, M. Ozaki, K. Yoshino.** 2006, Appl. Phys. Lett., Vol. 88, p. 053103 .

2. *Large current density from carbon nanotube field emitters.* **W. Zhua, C. Bower, O. Zhou, G. Kochanski, S. Jin.** 1999, Appl. Phys. Lett., Vol. 75, pp. 873-875.

3. *Self-oriented regular arrays of carbon nanotubes and their field emission properties.* **S. Fan, M. G. Chapline, N. R. Franklin, T. W. Tombler, A. M. Cassell, H. Dai.** 1999, Science, Vol. 283, pp. 512-514.

4. *Carrier transport and electron field-emission properties of a nonaligned carbon nanotube thick film mixed with conductive epoxy.* **Y. -H. Lee, D. -H. Kim, Hoon-Kim, B. -K. Ju.** 2000, J. Appl. Phys., Vol. 88, pp. 4181-4185.

5. *Field emission from well-aligned, patterned, carbon nanotube emitters.* **H. Murakami, M. Hirakawa, C. Tanaka, H. Yamakawa.** 2000, Appl. Phys. Lett., Vol. 76, pp. 1776-1778.

6. *Electron emission from individual nitrogen-doped multi-walled carbon nanotubes.* **M. Doytcheva, M. Kaiser, M. A. Verheijen, M. Reyes-Reyes, M. Terrones, N. de Jonge.** 2004, Chem. Phys. Lett., Vol. 396, pp. 126–130.

7. *Identification of electron donor states in N-doped carbon nanotubes.* **R. Czerw, M. Terrones, J.-C. Charlier, X. Blase, B. Foley, R. Kamalakaran, N. Grobert, H. Terrones, D. Tekleab, P. M. Ajayan, W. Blau, M. Ru2hle, D. L. Carroll.** 2001, Nano Lett., Vol. 1, pp. 457-460.

8. *N-doping and coalescence of carbon nanotubes: synthesis and electronic properties.* **M. Terrones, P.M. Ajayan, F. Banhart, X. Blase, D.L.Carroll, J.C. Charlier, R. Czerw, B. Foley, N. Grobert,R. Kamalakaran, P. Kohler-Redlich, M. Ruhle, T. Seeger, H. Terrones.** 2002, Appl. Phys. A, Vol. 74, pp. 355-361.

9. *Bamboo-shaped aligned CN_x nanotubes synthesized using single feedstock at different temperatures and study of their field electron emission.* **P. Ghosh, M Zamri, M. Subramanian., T. Soga, T. Jimbo,R. Katoh, M. Tanemura.** 2008, J. Phys. D: Appl. Phys. , Vol. 41, p. 155405.

10. *Electron side-emission from corrugated CN_x nanotubes.* **R. C. Che, L.-M. Peng, M. S. Wang.** 2004, Appl. Phys. Lett., Vol. 85, pp. 4753-4755.

11. *Effects of heat treatment on the field emission property of amorphous carbon nitride.* **E. J. Chi, J. Y. Shim, D. J. Choi, H. K. Baik.** 1998, J. Vac. Sci. Technol. B, Vol. 16, pp. 1219-1221.

12. *Optical and electrical properties of opal carbon replica and effect of pyrolysis.* **H. Kajii, Y. Kawagishi, H. Take, K. Yoshino, A. A. Zakhidov, R. H. Baughman.** 200, J. Appl. Phys., Vol. 88, pp. 758-763.

13. *Crystallization behavior of the amorphous carbon nanotubes preparedby the CVD method.* **L. Ci, B. Wei, C. Xu, J. Liang, D. Wu, S. Xie, W. Zhou, Y. Li, Z. Liu, D. Tang.** 2001, J. Cryst. Growth, Vol. 233, pp. 823–828.

14. *Annealing amorphous carbon nanotubes for their application in hydrogen storage.* **L. Ci, H. Zhu, B. Wei, C. Xu, D. Wu.** 2003, Appl. Surf. Sc. , Vol. 205, pp. 39-43.

15. *Effect of thermal treatment on the structure of multi-walled carbon nanotubes.* **K. Behler, S. Osswald, H. Ye, S. Dimovski and Y. Gogotsi.** 2006, J. Nanopart. Res., Vol. 8, pp. 615-625.

4.3 Magnetoresistance

4.3.1 Introduction

Magnetoresistance (MR) is the change in electrical resistance when an external magnetic field is applied. Many materials are characterized by the MR percentage which is defined as follows:

Eq. 4.7 $$MR(\%) = \frac{\Delta R}{R}$$

Where ΔR is the change in resistance and R is the resistance in the absence of a magnetic field.

There are different kinds of magnetoresistance such as ordinary MR, anisotropic MR, giant MR, tunneling MR, colossal MR and ballistic MR [1]; the first three will be explained in the following paragraphs.

Ordinary MR exists in metals and semiconductors and has very small MR for moderate magnetic fields < 1%. In this case the resistance measured between point A and B of a sample increases when the magnetic field is applied. This is caused when the magnetic field is orthogonal to the current path, called transverse magnetoresistance effect, caused by the displacement of electrons from their trajectories due to the Lorentz force. [1]. When the magnetic field is applied along the current, ΔR is lower than the transverse MR, this is called longitudinal MR.

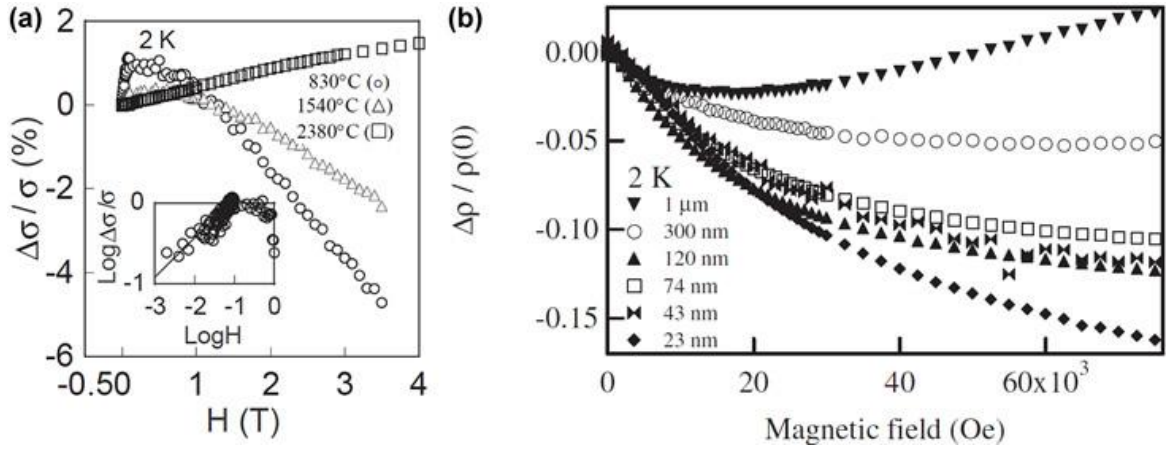

Figure 4.10: (a) Magnetoconductance of carbon inverse opal heat treated at 830, 1540 and 2380 ^{o}C (image from ref. **[2]**). **(b)** Magnetoresistance of carbon inverse opals with different pore size, measured at 2 K (image from ref. **[3]**).

Concerning magnetoconductance (MC) measurements by Yoshino et al. [2] have shown that it is dependent upon the heat treatment temperature, for 830 ^{o}C it is negative; 1540 ^{o}C presents a transition from negative to positive at 30 K and for 2380 ^{o}C it is always positive. For Take et al. [3] the magnetoresistance (MR) is negative at all temperatures and for smaller pore size its MR is more sensitive to the magnetic field (Figure 4.10 b). Remember that the conductance is inversely proportional to the resistance; therefore MC is proportional to the negative of MR.

Regarding other carbon materials, the positive MR has been attributed to electron-electron interactions for amorphous carbon films [4; 5], single wall carbon nanotubes [6] and carbon inverse opal [2]. V. Prasad studied amorphous carbon films [5], proposed that the positive MR is due to the wave function shrinkage of the electrons caused by the magnetic field, accompanied by a decrease of the probability of tunneling. On the other hand, negative MR may appear when sn electron is localized by the constructive interference of two paths of an electron wave function that are phase coherent in a closed loop. However, if a magnetic field is applied there will be a phase shift or incoherence in the loops, thus reducing the resistance [6], this phenomenon may be known as weak localization. Negative MR has been observed for single wall carbon nanotubes [6] and amorphous carbon films [4]. The effect of structural disorder in carbon fibers has been studied, varying the heat treatment temperature between 300 ^{o}C and 2500 ^{o}C. It was clear that at temperatures below 1200 ^{o}C the carbon fibers exhibited positive MR and at higher heat treatment temperatures this MR is negative and becomes more negative at higher temperatures, attributing the graphitization of the carbon fiber to this behavior [7].

4.3.2 Experimental methodology

The carbon inverse opals were made following the procedure explained in chapter 2 with different pyrazine content, using opals with 300 nm silica particles. The resistivity was measured with samples with a cross section of c.a. 1 mm^2 and length of c.a. 5 mm, using a PPMS Quantum Design Device. In the PPMS the resistivity was measured between 2 and 350 K for all samples under a magnetic field that varied between -5 and +5 T, using a four probe setup. The labeling of the samples is the same as used in chapter 2, all the samples were synthesized using 300 nm silica nanoparticles; the lowest and highest pyrazine content are at *N1* and *N3*, respectively.

4.3.3 Results and discussions

All the measurements show a non linear behavior that may be fitted by the equation AX^B for most of the cases. For the samples measured at 2 K we notice a non linear behavior of the magnetoresistance (MR) respect to the nitrogen content (Figure 4.11), when fitting this curves with the equation AX^B we that samples C300 and C300-N2 have B near 2, and the other samples have exponent B near 1.6. We may say that at low field the samples behave as H^2, and they somewhat deviate at fields approaching 5 T possibly tending towards $H^{1/2}$, as expected for electron-electron interactions. Further analysis at higher fields up to 10 T would be appropriate in order to confirm the $H^{1/2}$ behavior for high magnetic fields. Now when analyzing samples CIO300, CIO300-N2 and CIO300-N3, we observe that up to 10 K all samples present a positive MR and the MR response in nitrogen doped samples are higher (Figure 4.12). Several researchers attribute positive MR to electron-electron interactions for other carbon materials (amorphous carbon films, single wall carbon nanotubes and carbon inverse opal) [2; 4; 5; 6]. We propose the following possible scenarios causing the positive MR: 1) localization of electron at or around the nitrogen atoms that become more fixed at higher magnetic fields, 2) the electrons may also be trapped in ring currents around the periphery of the pores [8] thus increasing the resistivity at higher magnetic fields, 3) strongly disordered structure where spin effects prohibit certain charge transfer processes [7; 9].

Starting at 50 K the MR is less symmetric and changes to a negative response, similar transition (positive MR at low temperatures to negative MR at high temperatures) has been observed in polyaniline/multiwall carbon nanotube composite [10], boron doped amorphous carbon films [4] and carbon inverse opal [2]. At 100 K, we observe that the samples exhibit a similar negative MR response, although CIO300-N3 (parameter *A* between E-12 and E-10) gradually has a lower response than CIO300 and CIO300-N2. This negative MR has also been observed in single wall carbon nanotubes [6] and amorphous carbon films [4].

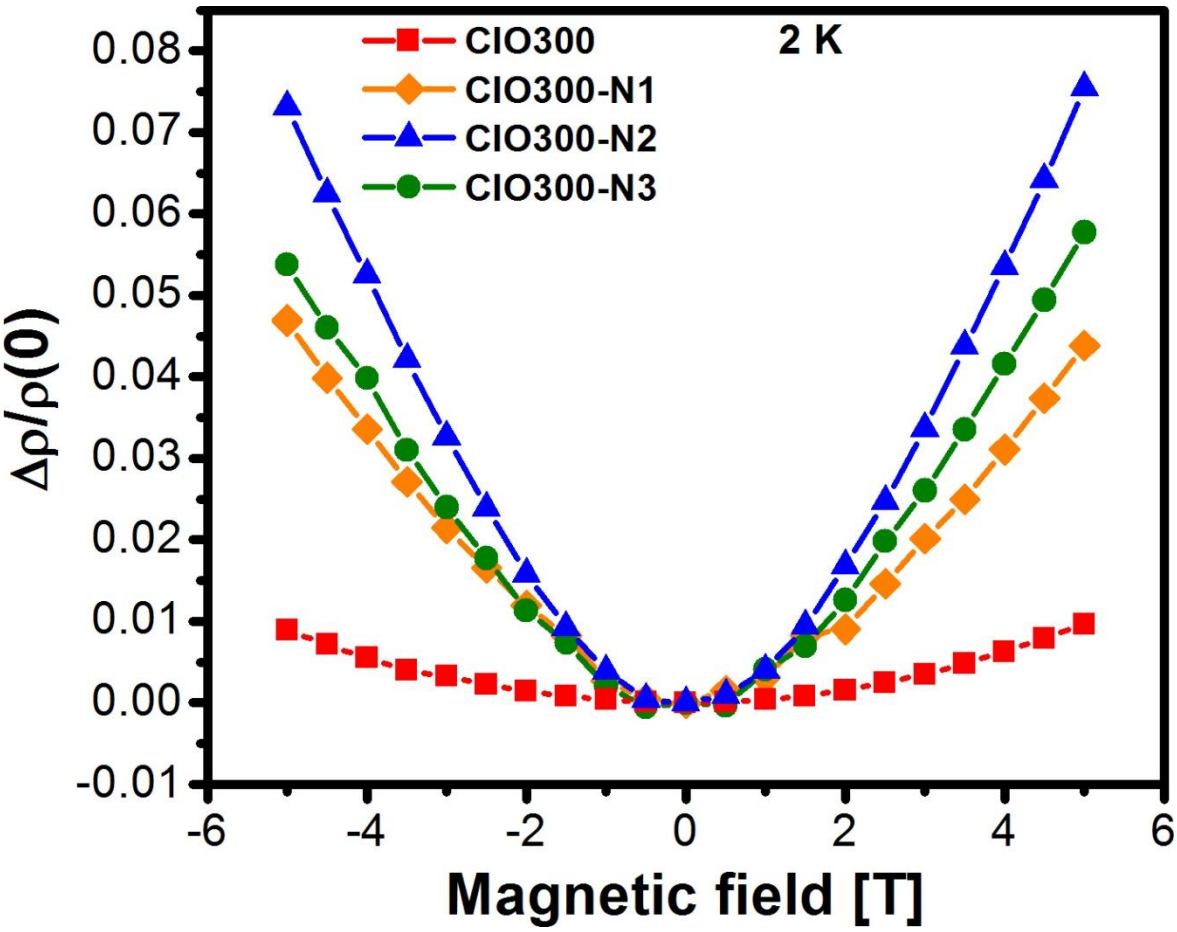

Figure 4.11: Normalized resistance vs. magnetic field for nitrogen doped carbon inverse opal at different contents, at 2 K.

Table 4.4: Fitting parameters for the magnetoresistance curves of the undoped and nitrogen doped carbon inverse opals measured between 2 and 300 K, using the equation $y=AX^B$

Parameter *A*						
	2 K	10 K	50 K	100 K	200 K	300 K
ClO300	4.51E-12	3.07E-12	7.48E-10	-1.12E-08	--	-2.31E-11
ClO300-N1	1.88E-09	--	--	--	--	--
ClO300-N2	8.74E-11	8.77E-12	4.23E-13	-2.23E-09	--	--
ClO300-N3	1.41E-09	2.14E-11	1.82E-08	-2.22E-12	-1.88E-11	-1.96E-10
Parameter *B*						
	2 K	10 K	50 K	100 K	200 K	300 K
ClO300	1.9862	1.9300	1.2615	0.9306	--	1.2220
ClO300-N1	1.5680	--	--	--	--	--
ClO300-N2	1.9131	1.8984	1.8918	0.9454	--	--
ClO300-N3	1.6211	1.8000	0.7181	1.7177	1.4090	1.5181

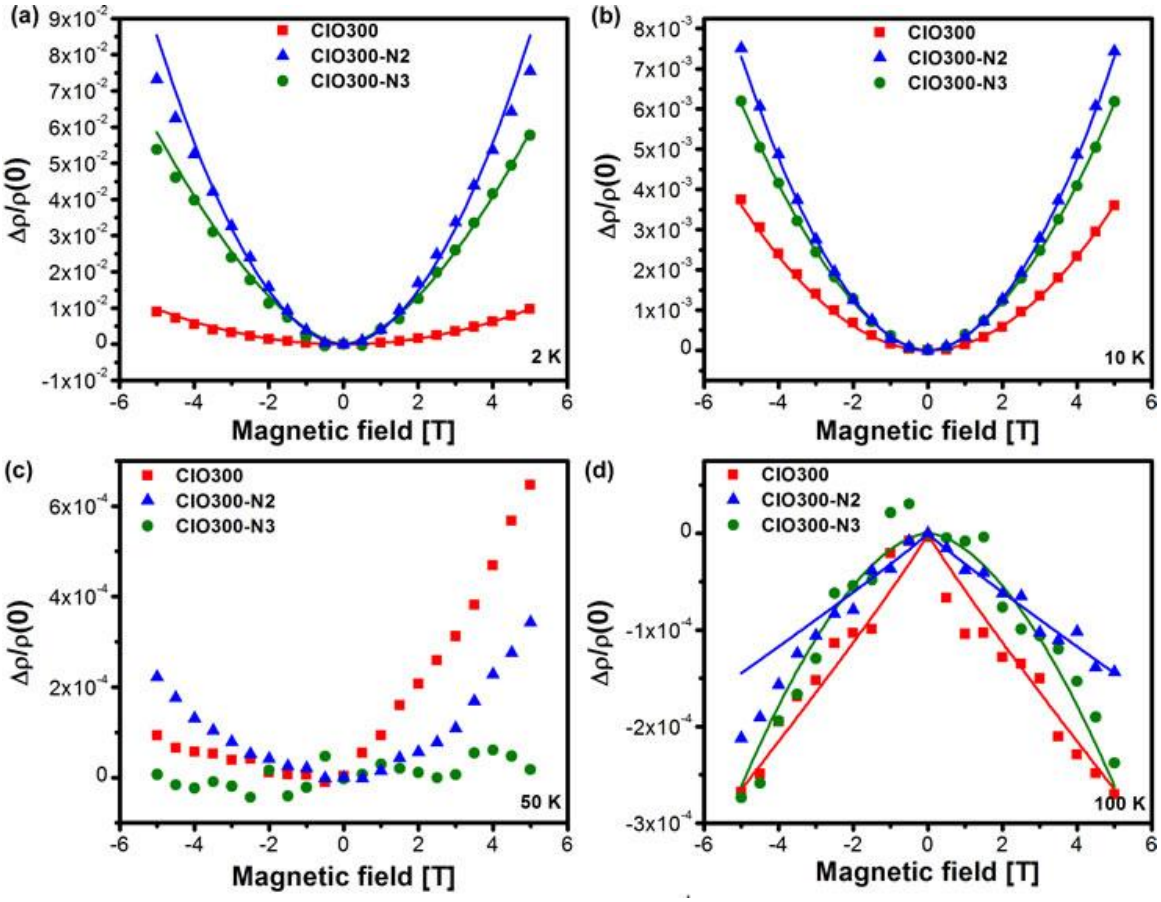

Figure 4.12: Normalized resistance vs. magnetic field for undoped and the highest nitrogen content in carbon inverse opal at **(a)** 2 K, **(b)** 10 K, **(c)** 50 and **(d)** 100 K. 2 and 10 K have positive MR, however, at higher temperatures it is negative and less symmetric.

4.3.4 Conclusions

Magnetoresistance measurements clearly show difference among samples, at temperatures below 50 K the nitrogen doped samples are more positive than the undoped sample, this possibly caused by a higher localization of electrons at or around the nitrogen atoms, or due to the degree of structural disorder. When the temperature increases, all samples show a transition towards negative MR were the undoped and doped samples exhibit similar values, along with a lower symmetric response. This transition from positive MR to negative MR may suggest the dominance of weak localization at high temperatures. This study is useful to understand better the electrical response of disordered carbon in the presence of a magnetic field, specifically the amount of defects doping or curvature may play a crucial role.

4.3.5 References

1. *In-situ magnetoresistance measurements during patterning of spin valve devices.* **Morecroft, D.** 2003, Dissertation submitted for the degree of doctor of philosophy at the university of cambridge.

2. *Electrical properties of a periodic porous carbon replica of opal.* **K. Yoshino, H. Kajii, Y. Kawagishi, M. Ozaki, A. A. Zakhidov, R. H. Baughman.** 1999, Jpn. J. Appl. Phys., Vol. 38, pp. 4926–4929.

3. *Preparation and electronic properties of nanoporous carbon inverse opal.* **H. Take, T. Matsumoto, S. Hiwatashi, T. Nakayama, K. Niihara, K. Yoshino.** 2004, Jpn. J. Appl. Phys., Vol. 43, No. 7A (2004), p. 4453, pp. 4453-4457.

4. *Metal–insulator transition in boron-doped amorphous carbon films.* **P. N. Vishwakarma, S. V. Subramanyam.** 2007, Philos. Mag. , Vol. 87, pp. 811–821.

5. *Magnetotransport in the amorphous carbon films near the metal-insulator transition.* **Prasad, V.** 2008, Sol. State Commun., Vol. 145, pp. 186-191.

6. *Magnetoconductance in single-wall carbon nanotubes: Electron-electron interaction and weak localization contributions.* **P. K. Choudhury, M. Jaiswal, R. Menon.** 2007, Phys. Rev. B, Vol. 76, p. 235432.

7. *Transport properties near the metal-insulator transition in heat-treated activated carbon fibers.* **A. W. P. fung, M. S. Dresselhaus, M. Endo.** 1993, Phys. Rev. B, Vol. 48, pp. 14953-14962.

8. *Magnetism in corrugated carbon nanotori: the importance of symmetry, defects, and negative curvature.* **J. A. Rodríguez-Manzo, F. López-Urías, M. Terrones, H. Terrones.** 2004, Nano Lett., Vol. 4, pp. 2179-2183.

9. *Magnetism in all-carbon nanostructures with negative curvature.* **N. Park, M. Yoon, S. Berber, J. Ihm, E. Osawa, D. Tománek.** 2003, Phys. Rev. Lett., Vol. 91, p. 237204.

10. *Low-temperature magnetoresistance studies on composite films of conducting polymer and multiwalled carbon nanotubes.* **Y. Z. Long, Z. H. Yin, Z. J. Chen.** 2008, J. Phys. Chem. C, Vol. 112, pp. 11507–11512.

11. *Anisotropic magnetoresistance in ferromagnetic 3d alloys.* **T. R. McGuire, R.I. Potter.** 1975, IEEE Trans. Mag., Vol. 11, pp. 1018-1038.

12. **Smit, J.** 1954, Physica (Utrecht), Vol. XVI, p. 612.

13. *Giant Magnetoresistance of (001)Fe/(001)Cr Magnetic Superlattices.* **M. N. Baibich, J. M. Broto, A. Fert, F. Nguyen Van Dau, F. Petroff, P. Etienne, G. Creuzet, A. Friederich, J. Chazelas.** 1988, Phys. Rev. Lett., Vol. 61, pp. 2472–2475 .

14. *Tunneling between ferromagnetic films.* **Julliere, M.** 1975, Phys. Lett. A , Vol. 54, pp. 225-226.

15. *Giant negative magnetoresistance in perovskitelike La2/3Ba1/3MnOx ferromagnetic films.* **R. von Helmolt, J. Wecker, B. Holzapfel, L. Schultz, K. Samwer.** 1993, Phys. Rev. Lett., Vol. 71, pp. 2331–2333 .

16. *Magnetotransport in iodine-doped single-walled carbon nanotubes.* **S. Ahn, Y. Kim, Y. Nam, H. Yoo, J. Park, Y. Park, Z. Wang, Z. Shi, Z. Jin.** 2009, Phys. Rev. B, Vol. 80, p. 165426 .

17. *Two-dimensional transport in disordered carbon and nanocrystalline diamond films.* **Bhattacharyya, S.** 2008, Phys. Rev. B, Vol. 77, p. 233407.

4.4 Magnetic properties

4.4.1 Introduction

Materials may be classified in different magnetic phases such as paramagnetism, diamagnetism, ferromagnetism or superparamagnetism.

Paramagnetic materials are attracted to magnetic fields, presenting a relative magnetic permeability ≥1; generally their magnetic susceptibility is in the order of 10^{-3} to 10^{-5}. When varying the magnetic field applied to this material its magnetization o magnetic moment is directly proportional to the field, this is because only a certain amount of the dipoles will be oriented along the field direction. Because of the thermal motion, the spins will be randomly oriented and the dipoles will not interact with each other, therefore they will not retain any magnetization in the absence of a magnetic field.

Materials with diamagnetism create a magnetic field in opposition of the external applied magnetic field; this is contributed from the paired electrons and the core electrons of an atom. Diamagnetic materials are water, wood, the majority of organic compounds and metals with a significant amount of core electrons such as mercury, gold and bismuth. These materials have a magnetic permeability less than 1 and a magnetic susceptibility < 0, which is weaker than materials with paramagnetism and ferromagnetism.

In a ferromagnetic material the magnetic moment of an atom tends to be the same as its neighbor, so all the moments in the system want to be parallel. Atoms with partially filled electronic shells may exhibit a net magnetic moment; this would be the case of metals. The exchange force tries to keep a parallel or antiparallel alignment of the moments of the atoms in a material. In the majority of ferromagnetic materials the exchange interaction is much stronger than the dipole-dipole interaction. A bulk ferromagnetic material can be divided in magnetic domains, in an unmagnetized state all these domains may exhibit a different magnetic orientation, in the presence of an external magnetic field they tend to be aligned, with a higher field the magnetic alignment improves. The boundary between two domains is called domain wall, which is seen as a gradual transition at an atomistic level. These domains may be caused by the poly crystallinity, crystal defects, impurities or even size and geometry. Pauli paramagnetism is the response of electrons near the Fermi level to an external field, here a small surplus of one spin type will dominate.

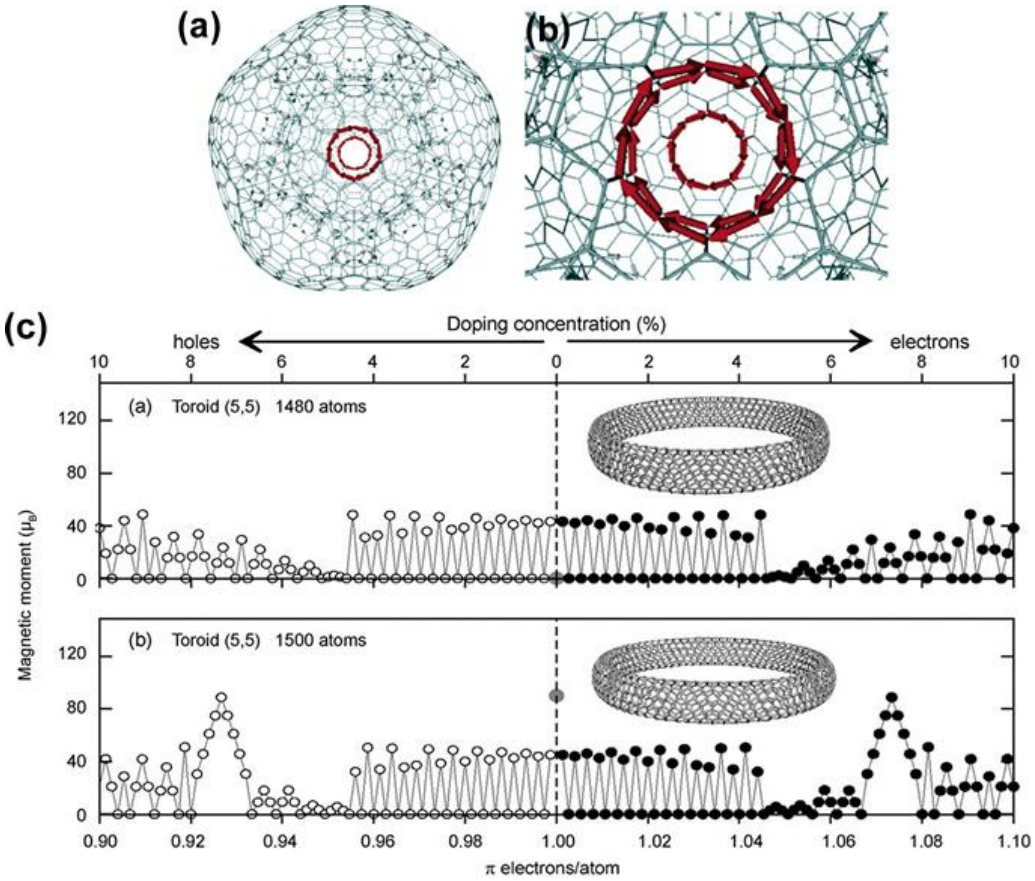

Figure 4.13: Molecular model of a "holey-ball" (interconnected concentric fullerenes joined by necks) containing 1320 atoms, which exhibits a maximum paramagnetic current in the heptagonal rings. **(a)** Close up of **(b)** revealing the heptagonal rings and the currents induced. (images from ref. **[1]**) **(c)** Magnetic moment (m) as a function of the number of π electrons per atom (or percentage of doping concentration). (image from ref. **[2]**)

In graphite it is thought that the π-electrons may travel free through the hexagonal lattice, even through the hexagonal rings, therefore inducing a magnetic field that opposes the external one. The magnetic susceptibility χ describes the response of the magnetization M to the applied magnetic field H, as $M = \chi H$. If the sign of χ is negative then it corresponds to diamagnetism and if it is positive it corresponds to paramagnetism. It is well known that graphite and diamond are diamagnetic. Linus Pauling observed that organic molecules such as benzene (C_6H_6), naphthalene ($C_{10}H8$), anthracene ($C_{14}H_{10}$), etc., which have planar hexagonal carbon rings allow the flow of ring currents along the bond paths when an external magnetic field is applied perpendicular to the molecule plane, however if this field is applied parallel to the plane no ring currents are produced [3]. This phenomenon may be explained by London theory [4; 5; 6], here the presence of ring currents induced by an external magnetic field give rise to

another field in the same direction as the external field although in the opposite direction. This has been used to explain colossal paramagnetism in metallic carbon nanotori with specific “magic radi” [7]. Further on J. A. Rodríguez-Manzo et al. [1], studied the magnetic properties of nanotori by coalesced C_{60} molecules and joining the ends of Haeckelite tubes [8] along the 2-fold axis exhibit an increase of the ring currents with size or diameter of the tori (Figure 4.13 c and d). When the C_{60} molecules are covalently connected along the 3-fold axis, in some cases the large ring currents are mainly localized on the heptagonal rings and are, surprisingly, parallel to the magnetic field and not perpendicular. Now, for concentric fullerenes termed “holey balls” [9], which could be a simplification of entangled graphene surfaces, therefore resembling porous carbon, the resemblance between them is the presence of negative curvature provided by heptagons or octagons. Here they observed a high paramagnetic response in holey balls, exhibiting maximum paramagnetic ring currents at the heptagonal rings (Figure 4.13 a and b). They suggest that the magnetism is sensitive to the presence of defects in the system, however for a toroid the paramagnetism may be reactivated if the magnetic field is applied with an inclination angle. Now, if these systems are doped with a small percentage (0.02–4%) of electrons or holes they could exhibit unusually large paramagnetism. These systems will have a diamagnetic response if when the HOMO occupation is a closed shell, however if the HOMO is partially filled there will be large and positive magnetic moments. Interestingly, when the electronic gap of these systems approaches zero, the local ring currents are enhanced [2].

Theoretical studies of carbon nanoribbons show that when the edges are armchair they are diamagnetic but when the edges are zig-zag these are paramagnetic and temperature dependent. The total paramagnetism of the system is a competition between the Pauli paramagnetism susceptibility and the orbital diamagnetic susceptibility, due to the localized states near the edges the paramagnetism is dominant at narrow width nanoribbons, when increasing this width the temperature dependence increases and it becomes diamagnetic at lower temperatures [10] (Figure 4.14 a and b).

The bombardment of protons and helium on graphite creates defects. Samples bombarded with protons had a much greater magnetic signal than those bombarded with helium [11]. When a single vacancy is created two free bonds from the neighbors join and form a pentagon, leaving one atom with a sp^2 dangling bond. When hydrogen atoms are close to a vacancy they will bond with two of the free carbon atoms, this configuration creates a magnetic moment on the sp^2 dangling bond (Figure 4.14 c and d), but if another hydrogen atom is introduced this will bond with the remaining free bond and the magnetism of the vacancy is

lost, although steric hindrance may be an obstacle for this configuration [11]. Theoretical studies show that nanopatterned graphite films may present magnetism. When these present triangular holes or zig-zag edge channels, ferromagnetism starts to manifest. In these systems magnetism is originated at the localized edge were the sp^2 bonding is broken, the magnetic moments decay away from the nanoholes or nanochannels [12] (Figure 4.14 e).

For schwarzite-like structures it has been observed theoretically that the presence of higher polygons, which introduce negative Gaussian curvature, are necessary for the presence of a magnetic ground state. Magnetism in these structures requires the presence of radicals that introduce unpaired spins. The negative curvature in a carbon lattice may introduce trivalent carbons which are the source of spin polarization [13] (Figure 4.15).

Ferromagnetism has been reported in highly oriented pyrolitic graphite (HOPG) when the magnetic field is applied parallel to the graphene layers (Figure 4.16 a). This phenomenon may be caused by topological defects or by strong Coulomb interaction between electrons in graphite [14]. On the other hand, carbon activated fibers heated at temperatures below 1100 ^oC show a paramagnetic behavior at low temperatures, these materials turn diamagnetic at certain low temperatures for samples heat treated up to 1100 ^oC, this magnetic transition temperature is higher for samples heated at lower temperatures [15] (Figure 4.16 b).

A carbon nanofoam with a $sp^3/(sp^2+sp^3)$ ratio between 35% and 60%, consisting of clusters with diameter between 4 to 9 nm, these clusters have hyperbolic schwarzites structures. This material is paramagnetic (Figure 4.17 a) presenting a coercive force at low temperatures, and it presents a strong paramagnetic relaxation in time [16].

Carbon nanofoams produced from laser ablation at different Ar pressures show a magnetic response that may be caused by three case scenarios.

(1) Higher order carbon rings may alter the alternation of double and single bonds in the graphite structure. These may localize the π-electron clouds and localize unpaired spins.
(2) sp^3 hybridization may be a barrier for π-electron delocalization and provide a trap for spins.
(3) Vacancies in lattice may also cause a localization of the π-electrons.

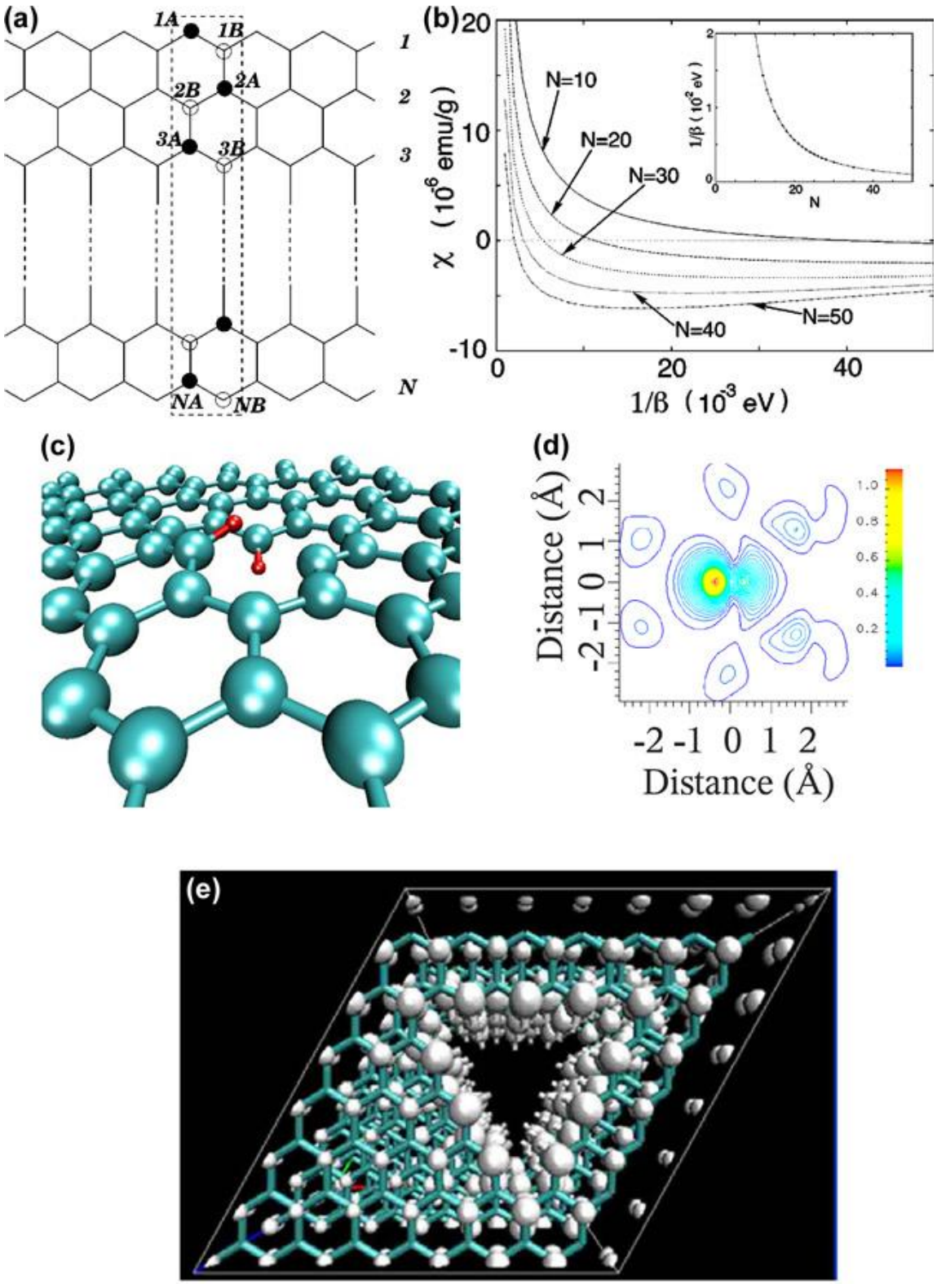

Figure 4.14: (a) Schematic structure of a carbon ribbon with zig-zag edges and **(b)** variation of the susceptibility against tempereature of carbon ribbons at different widths (images from ref. **[10]**). **(c)** Charge density and **(d)** spin density of a vacancy in graphite with thwo hydrogen atoms (images from ref. **[11]**). **(e)** Spin density in a nanochannel in graphite (image from ref. **[12]**).

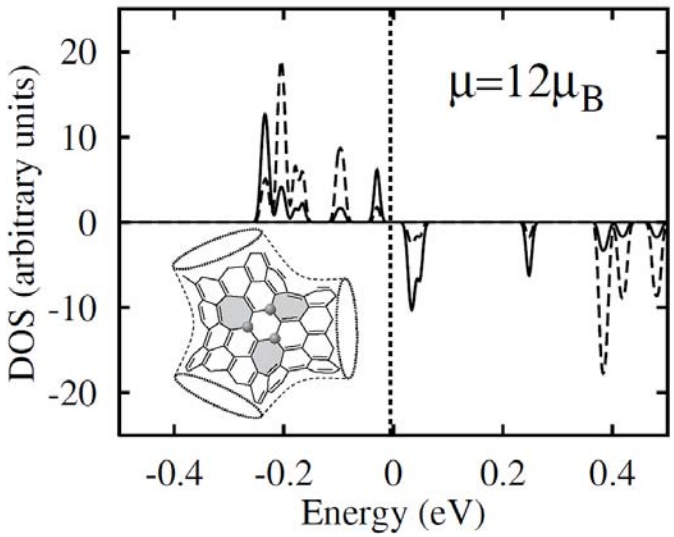

Figure 4.15: Density of states (DOS) of a C_{264} tetrapod, solid lines are the projection of the DOS of the core carbon atoms and the dashed lines is the DOS of the zig-zag edge carbon atoms. Inset figure is the structure of the carbon tetrapod, the gray sphere are sites with trivalent carbon atoms. (image from ref. **[13]**)

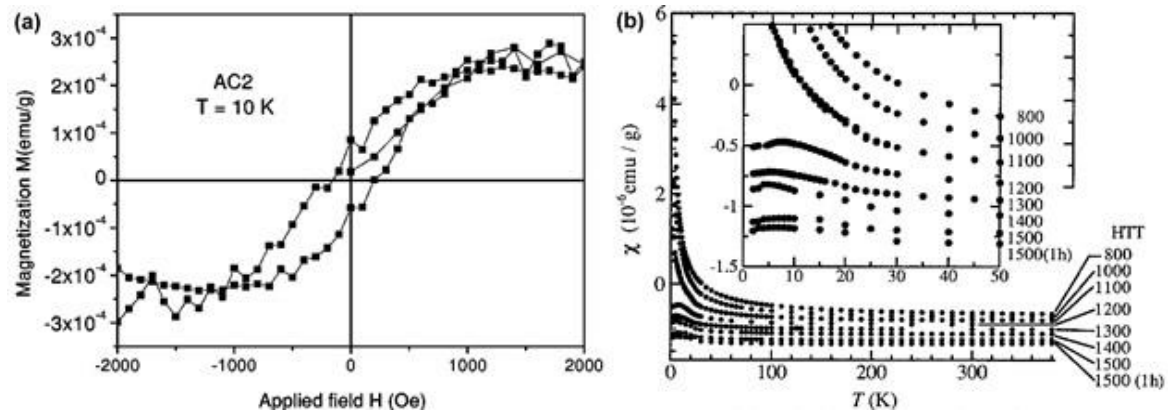

Figure 4.16: (a) M vs H of highly oriented pyrolitic graphite with background subtraction (image from ref. **[14]**). **(b)** Susceptibility vs temperature of activiated carbon fibers heat treated between 800 and 1500 ^{o}C (image from ref. **[15]**).

Susceptibility vs. temperature measurements of these materials show a maximum which may correspond to the freezing temperature T_f of the spin glass (Figure 4.17 b). This phenomenon may be caused by the topology or local variations of the exchange couplings between magnetic moments. At low temperatures there is a rapid increase in susceptibility that might suggest that some spins are unfrozen at T_f and may not couple strongly, this might indicate a near zero T_c. The complex susceptibility suggests the presence of frustrated coupling and negligible coupling. These moments may be originated from carbon dangling bonds that are exchange coupled with other moments [17].

Ferromagnetism has been observed in nanodiamond irradiated with ^{15}N, this irradiation creates defects in the structure and at higher doses of irradiation nitrogen atoms are incorporated in the lattice, these can introduce lone pair

electron spins that can favor ferromagnetism and higher magnetization saturation [18] (Figure 4.17 c).

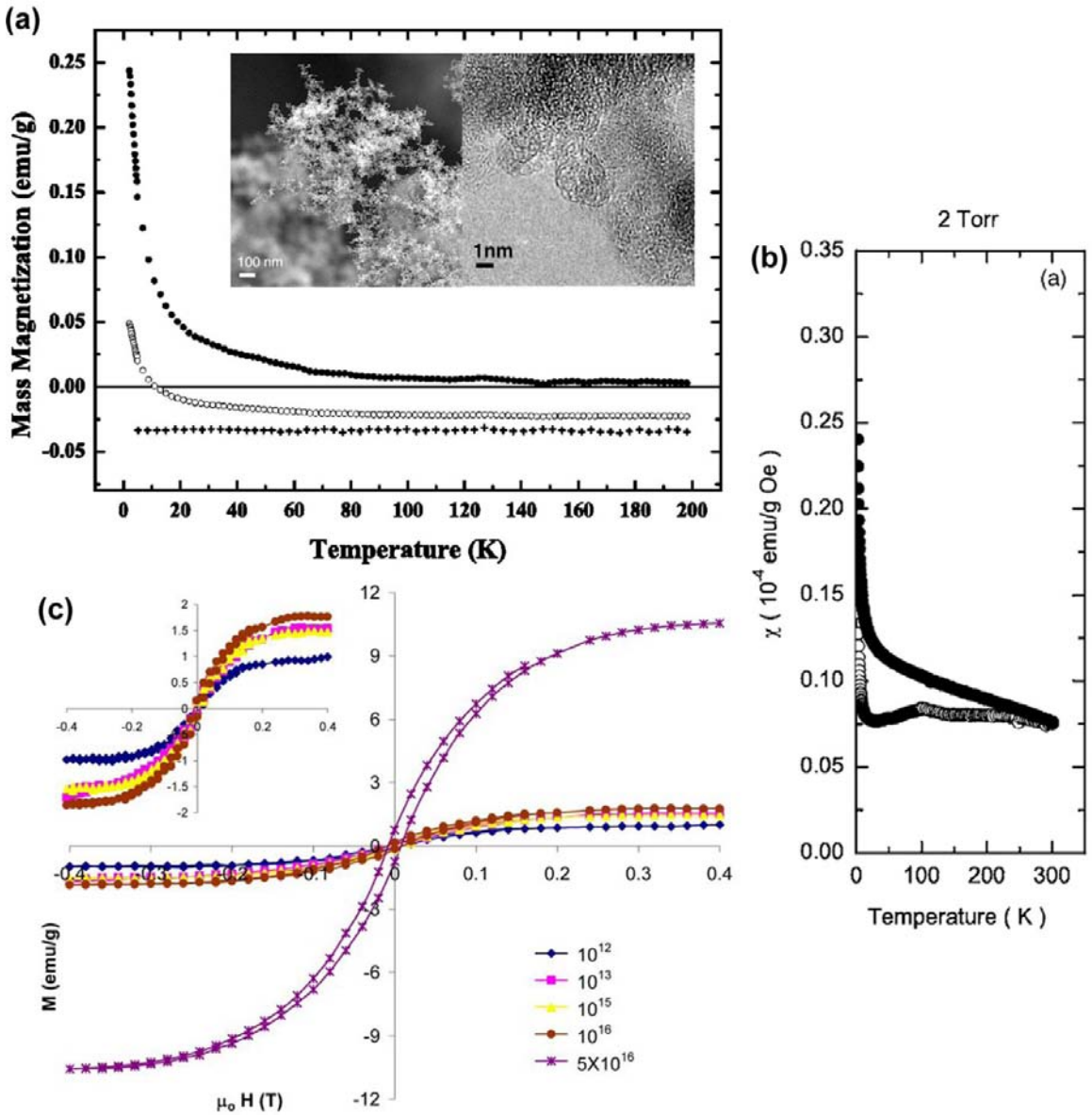

Figure 4.17: (a) Magnetizatin vs temperature of carbon nanofoam (filled circles), sample holder (open circles) and gelatine sample holder (crosses), inset images are SEM (left) and transmission electron microscope (right) images of the carbon nanofoam (images from ref. **[16]**). **(b)** Temperature dependence of the suscpetibility of carbon nanofoam (image from ref. **[17]**). **(c)** M vs H of nitrogen doped nanodiamond fabricated at different dose sizes (image from ref. **[18]**).

4.4.2 Experimental methodology

The carbon inverse opals were made following the procedure explained in the chapter 2 with different pyrazine content, using opals with 300 nm silica

particles. The magnetic moment was measured for powder samples held in a plastic capsule with the aid of a Quantum Design PPMS. The labeling of the samples is the same used as in chapter 2, all the samples were synthesized using 300 nm silica nanoparticles; the lowest and highest pyrazine content are at *N1* and *N3*, respectively.

4.4.3 Results and discussions

The hysteresis curves for all the non doped and doped carbon inverse opals show a paramagnetic behavior for temperatures below 50 K, although they do not behave in a completely linear manner, this may suggest the formation of some frustrated magnetic states that gradually change. Similar curves have been reported before for other porous carbon materials [16; 17]. It is clear that there is a gradual change from a paramagnetic to a diamagnetic magnetic state when increasing the measurement temperature. In our magnetic analysis we discard the possible influence of metallic impurities due to the absence of them during the synthesis of the samples.

The moment vs. temperature curves clearly show a transition from a paramagnetic to diamagnetic state for all the studied samples (Figure 4.18), similar behavior has been observed for other porous carbon materials [16; 17]. When increasing the pore size the value of the magnetic moment decreases. Furthermore, when observing the temperature range were the carbon inverse opal changes from paramagnetic to diamagnetic, this range varies according to the pore size (Table 4.5), this transition temperature is located at higher values for a smaller pore size (Figure 4.18), this perhaps may be caused by a favored formation of ring currents for smaller pore sizes, these ring currents have been reported to form at the peripheria of the pores by Rodríguez-Manzo et al. [1] (Figure 4.13 a, b), and a higher content of pores per volume. It is clear that below this magnetic transition temperature there is a splitting from the measurements the lower curves correspond to zero-field cooling and the others correspond to field cooling, this splitting and the MvsH curves (Figure 4.18) suggest us that the material is superparamagnetic at low temperatures. Another observation is the the presence of a peak between 50 and 100 K, this has been attributed to a spin glass state by D. Arčon et al. [17] in a mesoporous carbon material.

It is clear that the magnetic transition temperature is more sensitive to the pore size than nitrogen doping, thus suggesting that the ring currents are more sensitive to thermal fluctuations, this can also be observed at temperatures above 150 K were there are fluctuations in the magnetization, those samples with higher

magnetization fluctuations are those who have a lower magnetic transition temperature (i.e. CIO300-N2, Figure 4.19 f), this may suggest that the relaxation times are higher for samples with greater pore size, exhibiting a higher thermal agitation which may cause the magnetization to suffer a stochastic process [19]. Further study of thermal conductivity may help understand, for now we may think that the the sample with lower pore size is a better thermal conductor, since heat is transferred perpendicular to the graphitic layers, therefore thinner carbon wall thickness may cause it to be a better thermal conductor [20]. In the case of larger carbon wall sizes the heat transfer may exhibit a greater heat gradient, thus also causing a greater mangetization gradient throughout the carbon wall thus originating a stochastic process.

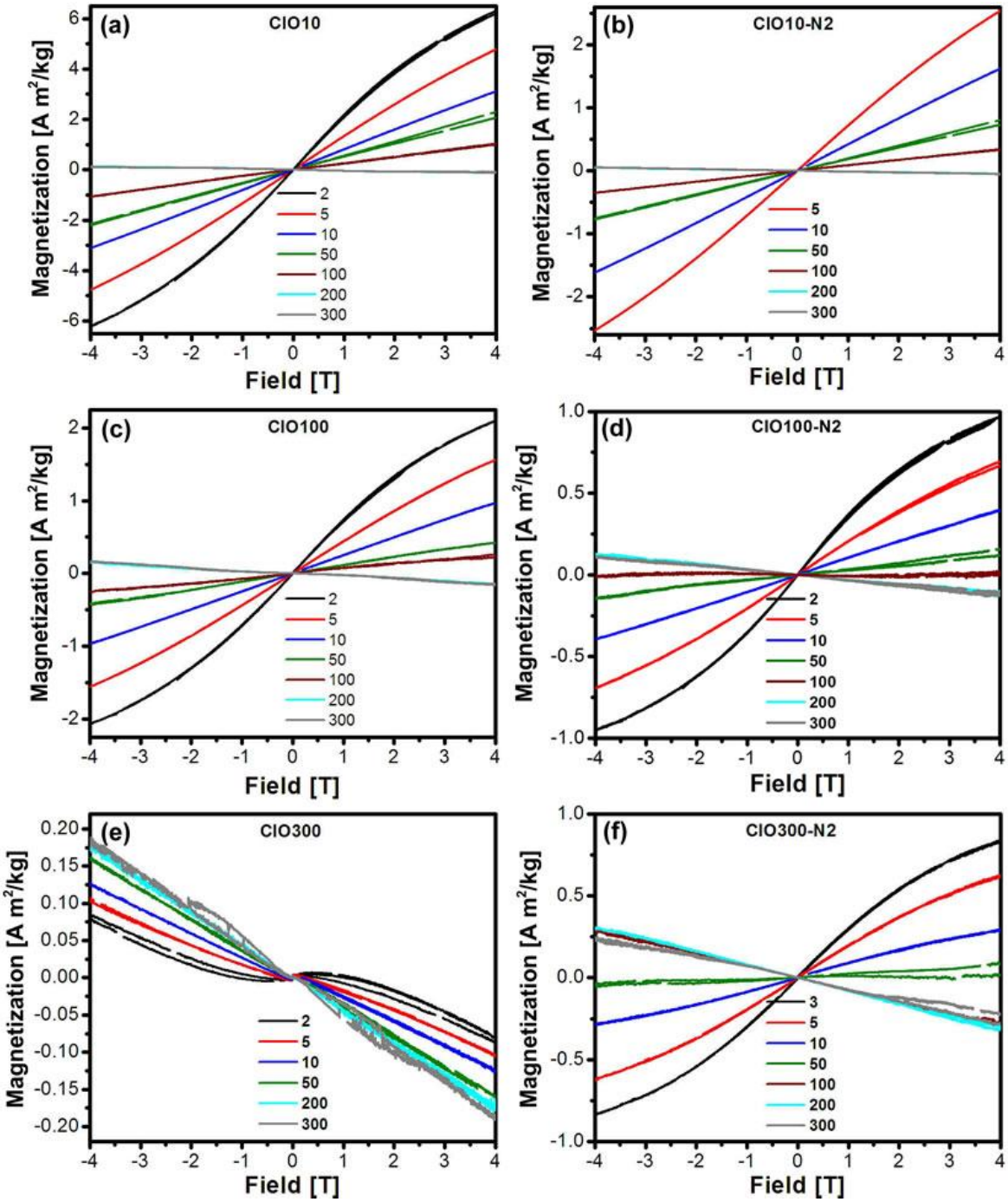

Figure 4.18: Hysteresis curves for non doped carbon inverse opals (left) and nitrogen doped (N2) carbon inverse opals (right) with pore size of **(a,b)** 10, **(c,d)** 100 and **(e,f)** 300 nm, all curves were measured at 3 K.

Table 4.5: Magnetic transition temperature (K) where the sample changes from paramagnetic to diamagnetic, measuremente for undoped and N2 doped carbon inverse opals with 10, 100 and 300 nm pore size.

	10 nm	100 nm	300 nm
CIO300	127	87	NA
CIO300-N2	129	78	36

The magnetic properties of this porous carbon may arise due to following mechanisms:

(1) Ring currents may arise at the necks of the pores [1], therefore those samples with a higher content of pores will exhibit a higher content of ring currents, exhibiting higher magnetizations and higher magnetic transition temperatures. This tendency is observed for the samples with 10 nm pores (Figure 4.18 and Figure 4.19). However, when doping the system with more electrons it is not easy to predict the magnetic properties [2].

(2) Higher order carbon rings may localize the π-electron clouds and localize unpaired spins [17; 13]. It has been studied before that the presence of an odd number of pentagons or heptagons in a carbon structure may induce trivalent carbon, therefore originating a net magnetism that can be exhibited in positive or negative curved carbon nanostructures. A higher amount of these rings may be present due to a greater content of pores per volume, this would happen for smaller pore sizes [21]. The introduction of nitrogen in the hexagonal lattice may localize electrons; however the proximity between these dopants and curvature sites may be crucial for the magnetic properties.

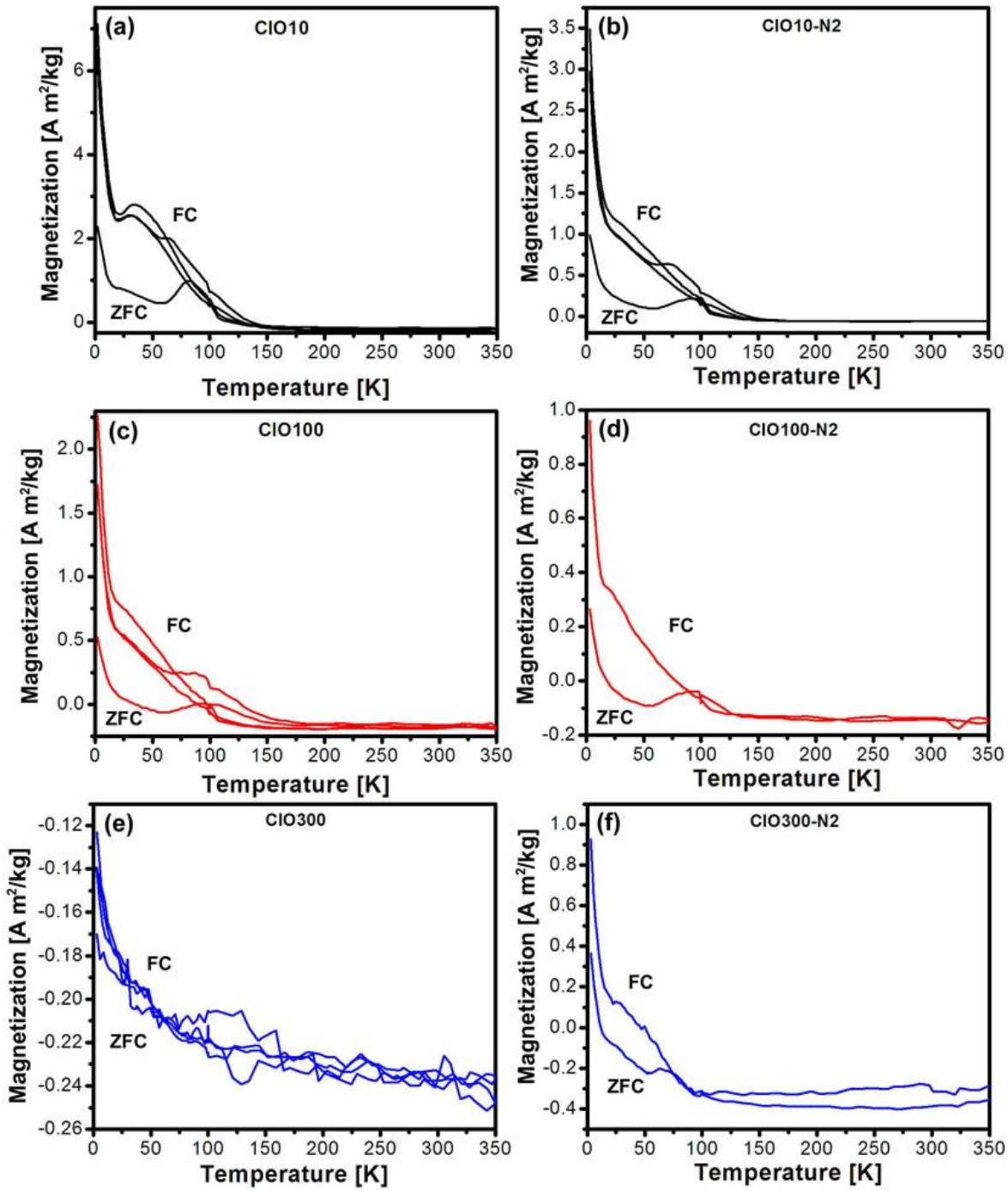

Figure 4.19: Magnetic moment vs temperarure for non doped carbon inverse opals (left) and nitrogen doped (N2) carbon inverse opals (right) with pore size of **(a,b)** 10, **(c,d)** 100 and **(e,f)** 300 nm. All the curves were measured with an external magnetic field of 5 T applied. Zero field cooling (ZFC) are the lower curves and field cooling (FC) are the higher curves in each plot.

4.4.4 Conclusions

Porous carbon materials such as carbon inverse opals present a paramagnetic behavior when its temperature is below 100 K, although above this temperature they suffer a transition to diamagnetic, the magnetic transition temperature varies upon the pore size, i. e. smaller pore size gives a higher magnetic transition temperature due to the favoring of and higher content of ring currents. Now when they are doped with nitrogen their magnetic moment decreases as well as the magnetic transition temperature decreases. The paramagnetic properties may be due to localization of electrons around nitrogen atoms and curvature sites, along with the formation of ring currents at the periphery of the pores. These magnetic measurements aid the understanding of magnetism in disordered carbon, especially for porous carbon. In order to increase the magnetization of carbon, smaller pore sizes would be needed, a structure similar to a Shwarzite, the introduction of rings with a higher order than 6 may even favor the presence of ferromagnetism; therefore bringing a new class of ferromagnetic material, where several ferromagnetic metals have a disadvantage.

4.4.5 References

1. *Magnetism in corrugated carbon nanotori: the importance of symmetry, defects, and negative curvature.* **J. A. Rodríguez-Manzo, F. López-Urías, M. Terrones, H. Terrones.** 2004, Nano Lett., Vol. 4, pp. 2179-2183.

2. *Anomalous paramagnetism in doped carbon nanostructures.* **J. A. Rodríguez-Manzo, F. López-Urías, M. Terrones, H. Terrones.** 2007, Small, Vol. 3, pp. 120–125.

3. *The diamagnetic anisotropy of aromatic molecules.* **Pauling, L.** 1936, J. Chem. Phys., Vol. 4, pp. 673-677.

4. *Theorie quantique des courants interatomiques dans les combinaisons aromatiques.* **London, F.** 1937, J. Phys. Rad., Vol. 8, pp. 397-409.

5. *Ring currents in topologically complex molecules: application to C60, C70, and their hexa-anions.* **A. Pasquarello, M. Schlüter, R. C. Haddon.** 1993, Phys. Rev. A, Vol. 47, pp. 1783-1789.

6. *Ring currents in icosahedral C60.* **A. Pasquarello, M. Schlüter, R. C. Haddon.** 1992, Science, Vol. 257, pp. 1660-1661.

7. *Colossal paramagnetic moments in metallic carbon nanotori.* **Lei Liu, G.Y. Guo, C. S. Jayanthi, S.Y. Wu.** 2002, Phys. Rev. Lett., Vol. 88, p. 217206.

8. *New metallic allotropes of planar and tubular carbon.* **H. Terrones, M. Terrones, E. Hernández, N. Grobert, J-C. Charlier, P. M. Ajayan.** 2000, Phys. ReV. Lett., Vol. 84, p. 1716.

9. *Quasiperiodic icosahedral graphite sheets and high-genus fullereneswith nonpositive Gaussian curvature.* **H. Terrones, M. Terrones.** 1997, Phys. ReV. B, Vol. 55, pp. 9969-9974.

10. *Electronic and magnetic properties of nanographite ribbons.* **K. Wakabayashi, M. Fujita, H. Ajiki, M. Sigrist.** 1999, Phys. Rev. B, Vol. 59, pp. 8271-8282.

11. *Irradiation-induced magnetism in graphite: a density functional study.* **P.O. Lehtinen, A. S. Foster, Yuchen Ma, A.V. Krasheninnikov, R.M. Nieminen.** 2004, Phys. Rev. Lett., Vol. 93, p. 187202.

12. *Magnetism in nanopatterned graphite film.* **L. Chen, D. Yu, F. Liu.** 2008, Appl. Phys. Lett., Vol. 93, p. 223106.

13. *Magnetism in all-carbon nanostructures with negative gaussian curvature.* **N. Park, M. Yoon, S. Berber, J. Ihm, E. Osawa, D. Tománek.** 2003, Phys. Rev. Lett. , Vol. 91, p. 237204.

14. *Ferromagnetism in oriented graphite samples.* **P. Esquinazi, A. Setzer, R. Hohne, C. Semmelhack, Y. Kopelevich, D. Spemann, T. Butz, B. Kohlstrunk, M. Losche.** 2002, Phys. Rev. B, Vol. 66, p. 024429.

15. *Disordered magnetism at the metal-insulator threshold in nano-graphite-based carbon materials.* **Y. Shibayama, H. Sato, T. Enoki, M. Endo.** 2000, Phys. Rev. Lett. , Vol. 84, pp. 1744-1747.

16. *Unconventional magnetism in all-carbon nanofoam.* **A. V. Rode, E. G. Gamaly, A. G. Christy, J. G. Fitz Gerald, S. T. Hyde, R. G. Elliman, B. Luther-Davies, A. I. Veinger, J. Androulakis, J. Giapintzakis.** 2004, Phys. Rev. B HYSICAL REVIEW B, Vol. 70, p. 054407.

17. *Origin of magnetic moments in carbon nanofoam.* **D. Arčon, Z. Jagličič, A. Zorko, A. V. Rode, A. G. Christy, N. R. Madsen, E. G. Gamaly, B. Luther-Davies.** 2006, Phys. Rev. B, Vol. 74, p. 014438.

18. *Irradiation-induced magnetism in carbon nanostructures.* **S. Talapatra, P. G. Ganesan, T. Kim, R. Vajtai, M. Huang, M. Shima, G. Ramanath, D. Srivastava, S. C. Deevi, P. M. Ajayan.** 2005, Vol. 95, p. 097201.

19. *Hysteresis in magnetism for physicists, materials scientists, and engineers.* **Bertotti, G.** Torino, Italy : Academic Press, 1998.

20. *Thermal properties of carbon inverse opal photonic crystals.* **A. E. Aliev, S. B. Lee, R. H. Baughman, A. A. Zakhidov.** 2007, J. Lumin., Vol. 125, pp. 11-17.

21. *Spin polarization in carbon nanostructures with disclinations.* **S. Azevedo, R. de Paivaa, J. R. Kaschny.** 2008, Phys. Lett. A, Vol. 372, pp. 2315–2318.

22. *Irradiation-induced magnetism in graphite: a density functional study.* **P.O. Lehtinen, A. S. Foster, Yuchen Ma, A.V. Krasheninnikov, R.M. Nieminen.** 2004, Phys. Rev. Lett., Vol. 93, p. 187202.

4.5 Conclusions regarding electrical and magnetic properties

From the studies of the physical properties of the carbon inverse opal undoped and doped with nitrogen we clearly observed that both behave as semiconductors, where the resistivity decreases to certain point when increasing the pyrazine content used for synthesis. The obtained thermal activation energies increased with introduction of nitrogen in the structure. Perhaps due to the degree of crystallinity and nitrogen content, the sample CIO300-N2 exhibits one dimensional variable range hopping, however a more disordered and undoped sample (CIO300) does not exhibit variable range hopping.

Regarding the magnetoresistance, at temperatures below 50 K it was clear that the nitrogen doped carbon inverse opal exhibits a higher positive magnetoresistance, possibly due to a higher localization of electrons at or around the nitrogen atoms. When increasing the temperature the MR becomes negative due to weak localization.

The size of the pores significantly determines the magnetic properties of the studied mesoporous carbon materials, at smaller pore size there is a higher magnetization and the magnetic transition (paramagnetic/diamagnetic) temperature slightly increases possible due to a higher number of ring currents. On the other hand, the nitrogen doped sample has a lower magnetization although possibly due to proximity between defects (nitrogen atoms and curvature) that localize electrons; the magnetic transition temperature does not change. It is evident that the ring currents are more sensitive to thermal fluctuations than the localization of electrons around nitrogen or curvature sites, regarding the magnetic properties.

When analyzing the resistivity, magnetoresistance and magnetic measurements it is clear that the carbon inverse opal changes its electrical and magnetic properties around 50 K. At low temperatures (below 50 K), the variable range hopping, positive MR and paramagnetic behavior suggest that the material tends to localize electrons near the curvature sites thus increasing resistivity and magnetization. The resistivity increases with the introduction of nitrogen, however the magnetization of the material decreases. We conclude that the degree of order of the structure significantly determines the electrical and magnetic properties of mesoporous carbon materials.

Now, when heat treating the carbon inverse opal the higher degree of graphitization clearly improves the field emission properties. However, further

experiments need to be done in order to elucidate the influence of nitrogen doping upon the field emission of the carbon inverse opal.

4.6 Sensing applications

4.6.1 Introduction

4.6.1.1 Carbon nanostructure sensors

Since the discovery of carbon nanostructures such as fullerenes [1], carbon nanotubes [2; 3], and the isolation of graphene [4], there has been many research to explore their interesting properties such as mechanical, electrical, biocompatible, sensing, among many others. Regarding sensing capabilities, commonly carbon nanotubes have been studied as sensors for O_2, NO_2, CO_2, Acetone, Ethanol, Chloroform, Toluene, etc. [5; 6; 7; 8; 9; 10; 11], these sensing properties take advantage of the adsorption of an analyte by a physical o chemical interaction, this interaction creates a different electronic state in the system CNT-analyte, in the macro-world this may be visualized as a change in the current or resistivity of the device, therefore indicating the presence of a foreign molecule in the medium.

Single wall carbon nanotubes (SWNT) have been used as CO_2 sensors, where the desorption is slow for high concentrations of the analyte [8]. The oxygen sensitivity of SWNT has been studied, revealing that a modest band gap semiconductor is less sensitive than a small band gap SWNT [5]. On the other hand, when comparing SWNT with multiwall carbon nanotubes (MWNT) for its sensitivity with NO_2, SWNT may be up to six times more sensitive than MWNT [7] (Figure 4.20 d).

Polymeric composites with carbon nanotubes have proven to be capable of sensing NO_2, acetone, chloroform, dichloromethane [6; 9]. For PMMA, the sensor response is attributed to the swelling of the polymer and the polar nature of the solvent, for the last possibility, it may be caused by hydrogen bonding with the carbon nanotube. Also, when comparing the sensitivity of polypyrolle (PPy), SWNT and the composite PPy/SWNT the composite showed a higher response for sensing NO_2 (Figure 4.20 e).

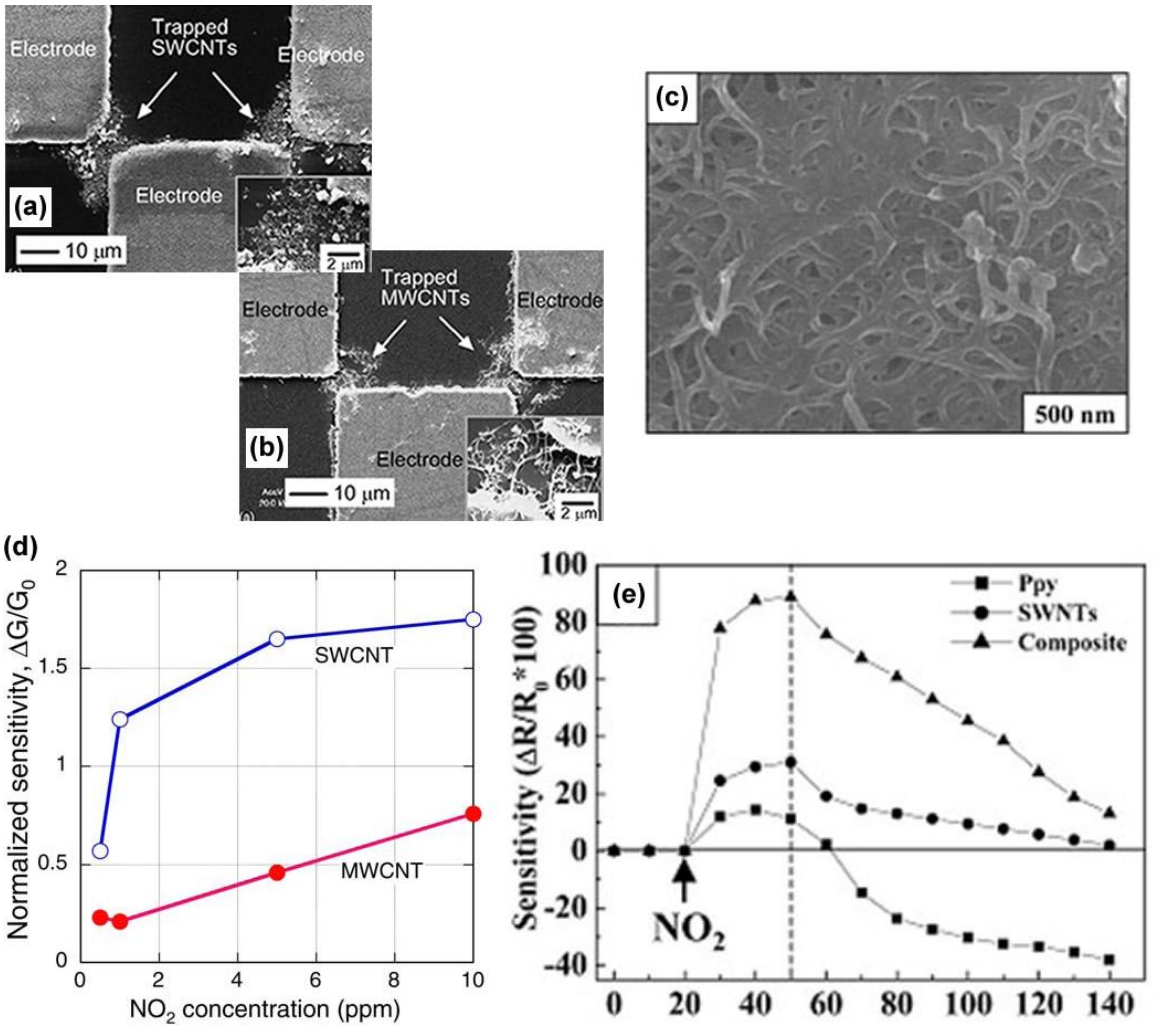

Figure 4.20: Carbon nanotube based sensors..Scanning electron image (SEM) of **(a)** single wall (SWNT) and **(b)** multiwall carbon (MWNT) nanotube device (images from ref. **[7]**). SEM image of **(c)** SWNT polypyrrole composite. **(d)** Normalized sensitivity for NO_2 at various concentrations for SWNT and MWNT. **(e)** Sensitivity comparison for NO_2 for polypyrrole, SWNT and the composite SWNT/polypyrrole (images from ref. **[6]**).

Even the new wave of graphene research has started to study its sensing properties for H_2O, NH_3, CO, NO_2, NO [12; 13; 14]. Most of the carbon sensing materials research has been done with individual nanostructures and carbon nanotubes prepared as aligned forests or two-dimensional foils, but there has not been many research regarding porous carbon materials.

Polyelectrolyte stabilized enzymes glucose oxidase has been immobilized on porous carbon structures. This material was used as an electrode inside a flow cell in order to sense glucose, hydrogen peroxide transported by the solvent [15] [16]. In a different study, a phenolic resin inverse opal has been studied as an oil sensor. Here its optical properties were embraced in order to have a visual

response. To the best of our knowledge porous carbon materials have not been explored as gas sensors.

4.6.1.2 Theoretical simulations

Theoretical simulations of the sensing process are important in order to have an idea of the mechanism and affinity of analytes to the desired system. The introduction of defects such as oxidation form low-energy sorption sites on a carbon nanotube promoting the nucleation for the condensation of the analyte vapor. By controlling the oxidation it is possible to increase the sensitivity and the chemical selectivity. On the other hand, calculations have shown that acetone presents a hydrogen bond with a –COOH group [10] (Figure 4.21 a), this shows a possible mechanism for sensing polar molecules with a functional oxygen group.

Theoretical calculations of graphene as sensors show that the orientation of the molecule adsorbates (i. e. H_2O, NH_3, CO, NO_2, NO) is important according to the charge transfer [14]. Another study shows that when comparing paramagnetic and diamagnetic adsorbates such as NO_2 and N_2O_4, respectively, the paramagnetic molecules induce a strong p-type doping. Thus T. O. Wehling et. al. suggest that an open-shell is capable of doping graphene as long as the chemical potential mismatch $\Delta\mu$ between the adsorbate and graphene is higher than half the Hund exchange splitting [13].

Y. -H. Zhang et al. made first principle studies for CO, NO, NO_2 and NH_3 with pristine, N-doped, B-doped and vacancy within a graphene structure [17]. With a vacancy in a graphene sheet it becomes a greater attractor for CO, NO, NO_2 than pristine, N- or B- doped graphene, this vacancy causes a strong orbital overlap between the analyte and graphene (Figure 4.21 b and c). Now, B-doped structures show a N-B bonding for those molecules containing nitrogen, with the strongest interaction with NH_3. All the molecules studied in this work show physisorption to pristine graphene.

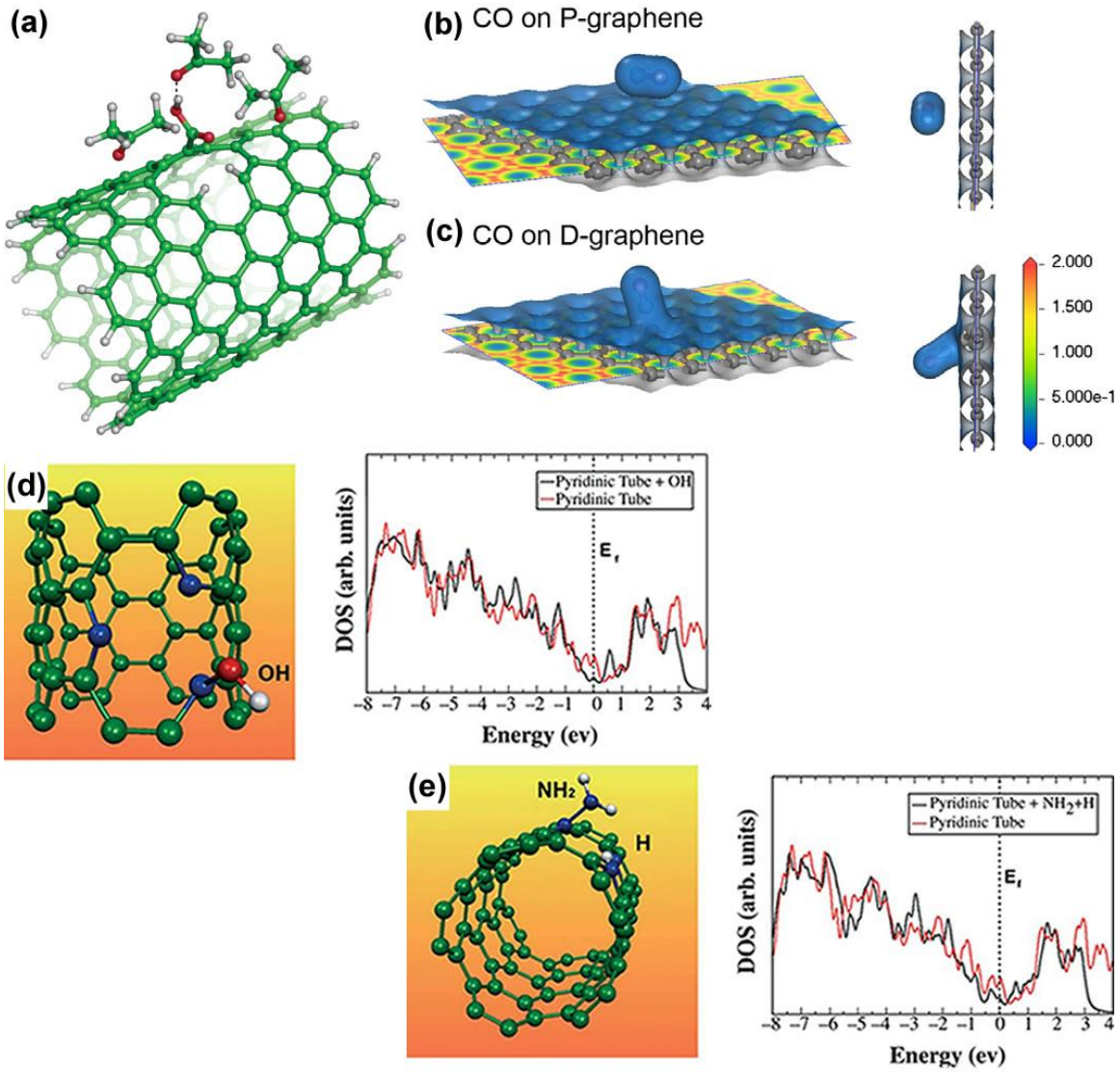

Figure 4.21: (a) Hydrogen binding of acetone to a carboxylic acid defect on a SWNT sidewall (images from ref. **[10]**). Electronic total charge densities for CO on **(b)** pristine (P-) graphene and **(c)** a vacancy defect (D-) on graphene (images from ref. **[17]**). A (5,5) SWNT doped with pyridinic nitrogen sites with an **(d)** OH group and **(e)** NH_3, left sides are models and right side images are the corresponding total density of states (images from ref. **[18]**).

Boron doped carbon nanotubes exhibit a chemical adsorption for CO and H_2O, but with nitrogen doping they exhibit physical adsorption. The binding between these molecules and the CNT is ionic type [19]. Another study shows that pyridine-type sites promote chemisorption of molecules with OH groups [18].

4.6.1.3 Doped carbon nanostructure sensors

Nitrogen doped carbon (CN_x) materials such as films [20], graphene [17] and carbon nanotubes [19; 18] add interesting properties to such materials, making them more biocompatible [21], increasing its conductivity and chemical reactivity. These CN_x materials have been studied for sensor applications of humidity, ethanol, acetone, chloroform, gasoline, pyridine, etc [18; 22]. When exposing gas vapors to CN_x materials it has been observed that their resistance increases and decreases gradually after exposure, the original resistance may not be reached possibly due to chemisorption.

Pellets of CN_x nanotubes are sensitive to acetone, ethanol, gasoline, chloroform, and ammonia (Figure 4.22 a). These devices present a short response, in the order of tens of a second [18]. On the other hand, amorphous carbon nitride films have been integrated in MEMS as a sensor device, this device proved to be a good humidity (Figure 4.22 b) and ammonia sensor with short response and recovery time [23; 20].

Clean graphene devices show a low response to NH_3, but when it is contaminated this response is enhanced (Figure 4.22 c), thus proving that functionalized graphene is more convenient for sensor devices [24].

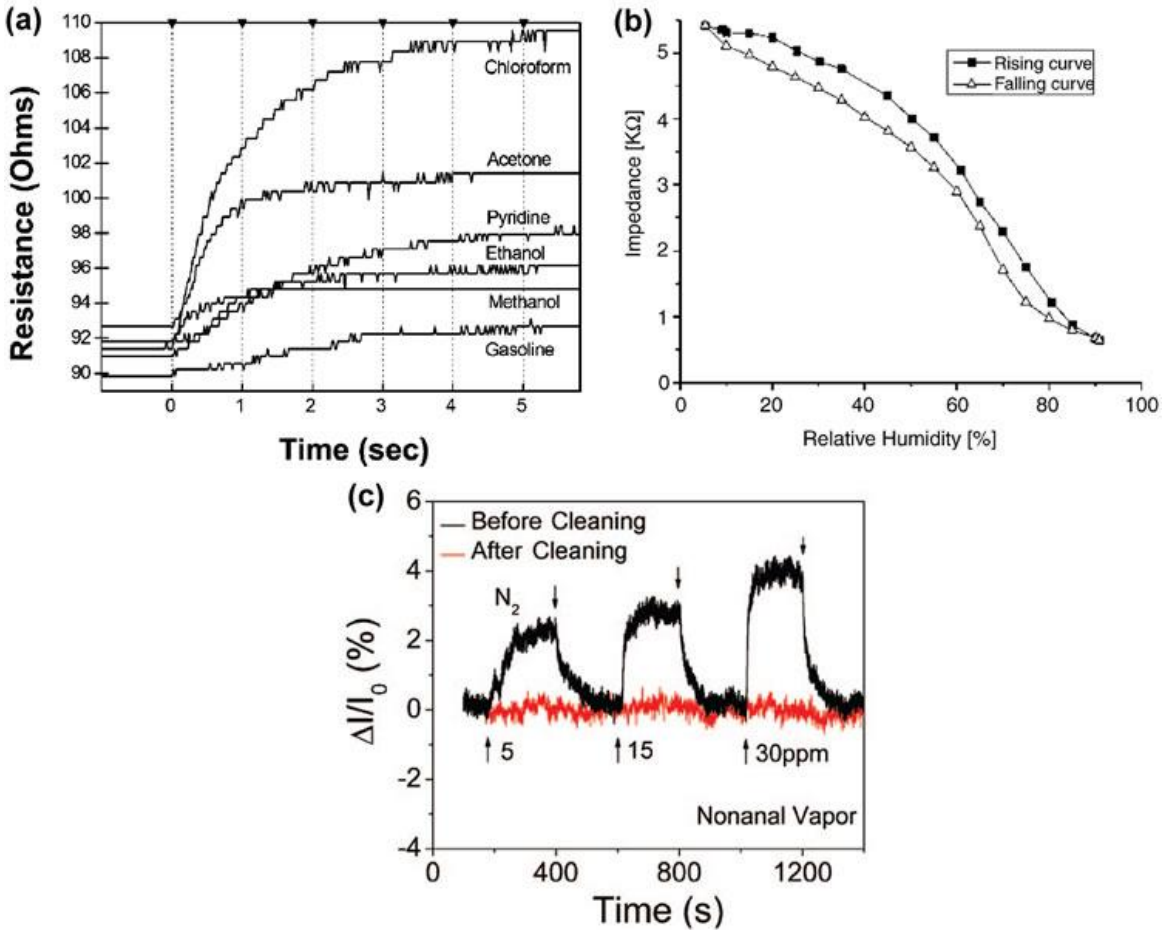

Figure 4.22: (a) Sensitivity (resistance vs time) of CN_x nanotube film for chloroform, acetone, pyridine, ethanol, menthanol and gasoline vapors (image from ref. **[18]**). **(b)** Humidity sensor (impedance vs humidity) of nitrogen doped carbon films (image from ref. **[20]**). **(c)** Sensor response for a clean and non clean graphene (image from ref. **[24]**).

4.6.1.4 Photosensitive carbon nanostructures

Carbon nanostructures such as single wall nanotubes (SWNT) have the ability to respond under illumination. A bundle of SWNT may present an elastic deformation when illuminated with visible light; it can stretch, bend or be repelled [25]. The photoconduction excitation energies of SWNT film samples agree with the optical adsorption spectra of semiconducting SWNTs (Figure 4.23 a). This photo response increases at lower temperatures and with higher light intensities (Figure 4.23 b) [26; 27]. Infrared light may be used to induce resonant excitation in a single semiconductor SWNT, where it can create a pair electron-hole [28]. The photocurrent is proportional with the light intensity, in a film of SWNT the photo induced relaxation time may take 4 seconds or more depending on the quality of the semiconducting nanotubes [29; 27]. A particular study shows that NH_3 may

adsorb on SWNT but under UV illumination it may be desorbed, and recover the nanotube's original electrical properties [30]. Another study shows that graphene films have shown even a higher photoconductivity when compared with a SWNT film (Figure 4.23 c), with a higher response when increasing light intensity and external electric field [31].

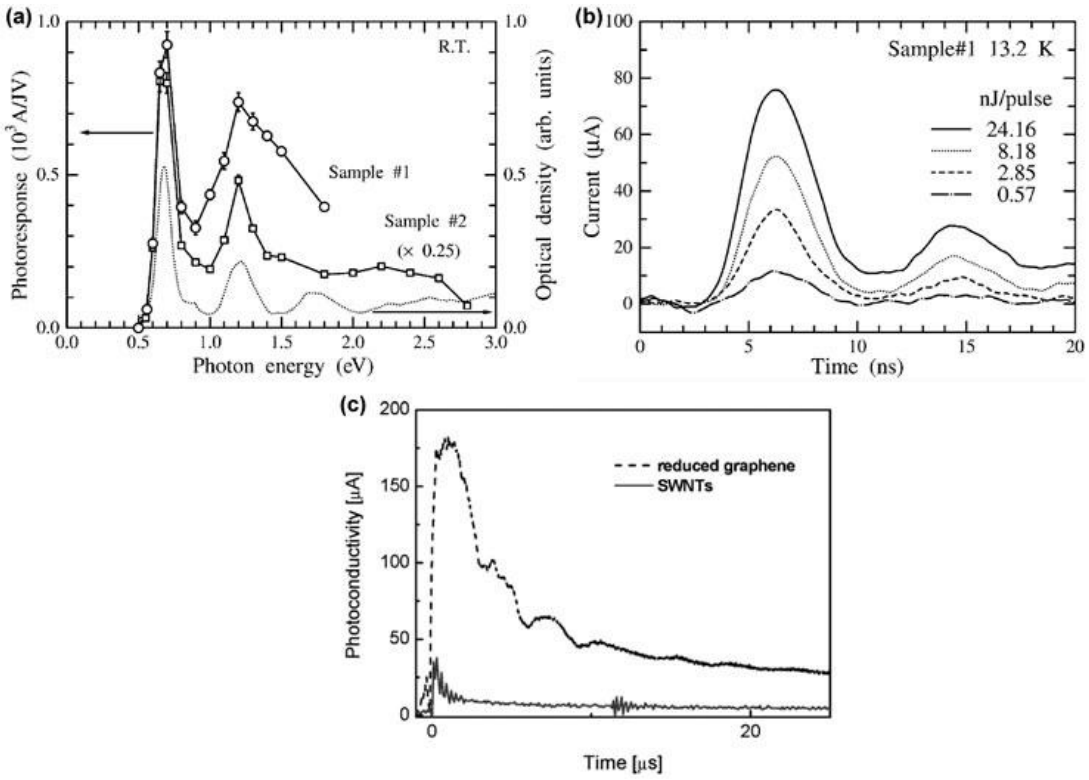

Figure 4.23: (a) Photoconduction spectra for SWNT film samples and optical adsorption spectra (dotted line). **(b)** Photocurrent vs time at different incident light intensities of SWNT films (images a and b from ref. **[26]**). **(c)** Photocurrent vs time of SWNT and graphene films (image from ref. **[31]**).

In this work, we study the gas and photo sensitivity of carbon inverse opal undoped and doped with different contents of nitrogen, as well as two different pore sizes of 100 and 300 nm. These materials were used to sense different vapors (acetone, ethanol, chloroform).

4.6.2 Experimental methodology

Synthetic opal from SOLARNO was used as a template to infiltrate a water solution of sucrose, pyrazine and sulphuric acid, following the procedure reported in chapter 2. The concentrations of the reactants are according to Table 4.6.

Table 4.6. Carbon and nitrogen source solution concentrations. Quantities are in % by wt, the letter "y" corresponds to the particle size used.

	ClOy	ClOy-N1	ClOy-N2	ClOy-N3
Sucrose	25.00	16.67	12.50	8.33
Pyrazine	0.00	8.33	12.50	16.67
Sulphuric acid	2.58	4.17	6.25	8.33
Water	72.42	70.83	68.75	66.67

All samples were characterized by scanning electron microscopy (SEM) using a FEI XL30-FEG microscope, operated between 10 and 20 kV, equipped with energy dispersive X-ray spectroscopy (EDX).

The carbon inverse opal plates were cut into different pieces exhibiting millimeter-size dimensions. Two copper contacts were placed on opposite extremes of the carbon inverse opals in order to measure the electrical resistance of the samples (Figure 4.24). The contacts were attached with silver paint (Chemtronics conductive paint). This device was then placed inside a sealed Pyrex chamber at room temperature and atmospheric pressure. The electrical resistance measurements were performed using a *SourceMeter* (*Keithley 2400*) system, providing a current of 3 mA. We used two gas flow controllers (*MKS Instruments*). One channel carried Ar with a constant flow of 3 l/min, whereas the other controller was used to carry 0.2 l/min Ar which is flowed through a bubbler containing the solvent desired. The resistance acquisition data were recorded with a PC card (*National Instruments, SCB-68*), which was connected to the gas flow controllers and operated with a *LabView®* software.

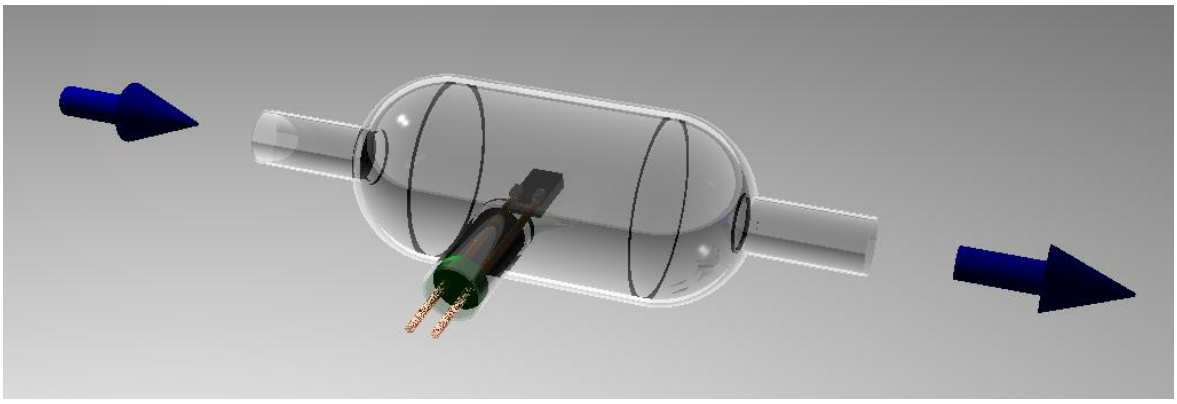

Figure 4.24: Experimental set up for gas sensing. The entire system is closed allowing a flow Ar and the entrance of electrodes to the sample (located in the center of the system).

4.6.3 Results and discussions

4.6.3.1 Gas sensors

We measured the normalized electrical resistance in the presence of different gas vapors (chloroform, ethanol, acetone). We then plotted the normalized resistance which is defined by $R_N = (R-R_0)/R_0$, where R is the electrical resistance registered in the measurement; R_0 is the mean value of the resistance. For our analysis, five cycles have been chosen, 80 s have been allowed for the solvent vapor to enter in the reaction chamber, and 100 s for the purging of the system with pure Ar.

The sensing properties measured are plotted in Figure 4.25, it is clear that all samples present resistance changes when exposed with the gas vapor. The overall tendency is that the introduction of nitrogen in the carbon inverse opal increases its sensitivity, reflected by more pronounced peaks of resistance when exposed to the vapors (Figure 4.25). For chloroform vapor (Figure 4.25 a and b), the sensors show that the resistance after all cycles almost reaches its initial value, this could suggest that there is no chemical reaction with the samples. Unfortunately, the response intensity to the gas decreases after each exposure, this could mean that there is a physisorption saturating the exposure sites. When exposed to ethanol (Figure 4.25 c and d) the intensity of the responses does not vary significantly, but the background resistance increases which could mean a chemisorption, clearly the samples with 300 nm pores present a better response when being exposed. Now in the case of acetone, the signals do not show significant variations after several cycles, with 100 nm pores all the samples show an increase of the background resistance, contrary for some cases of 300 nm pores. Curiously the sample with the highest content of nitrogen shows a negative signal when exposed to acetone in both pore sizes, this case also happens with the undoped material with 100 nm pore. Regarding pore size, 300 nm pore shows a slightly higher response for all the tested solvents than the 100 nm pore samples, this may be due to a higher degree of graphitization which may contribute to a better resistance sensitivity to the exposure of these vapors.

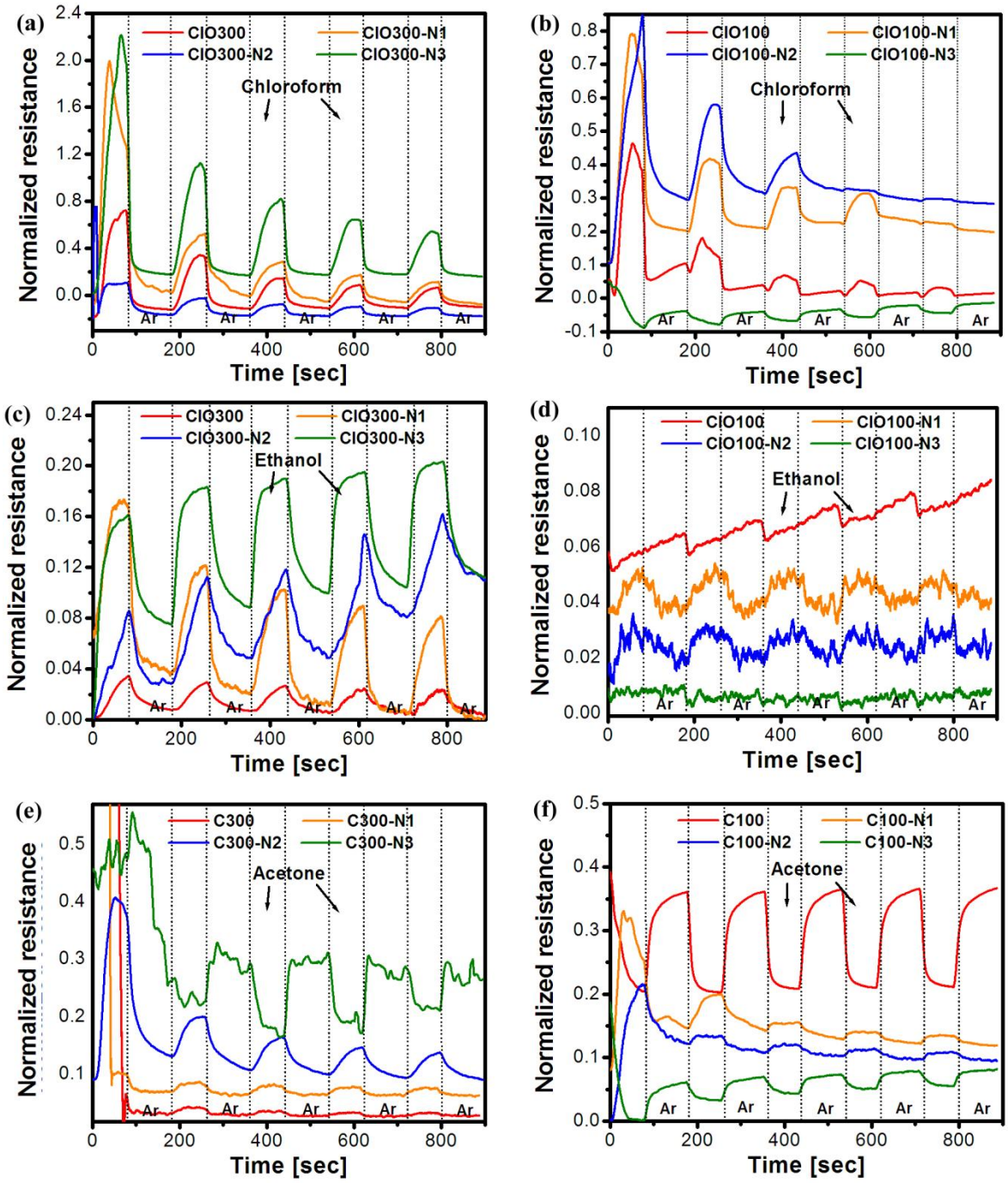

Figure 4.25: ClO300-Nx sensor measurements. Normalized electrical resistance for carbon inverse opals at different nitrogen content with 300 (left) and 100 nm (right) pores exposed to **(a,b)** chloroform, **(c,d)** ethanol and **(e,f)** acetone.

4.6.3.2 Photosensors

The photoresponse of carbon inverse opal with different nitrogen content and pore size (300 and 100 nm) was measured by exposing the sample at some mm (1-10 mm) of distance from a camera flashlight (ZENIT, BY-28A). The exposure to the flash decreases the resistivity of all samples reaching a maximum after several milliseconds (Figure 4.26), the samples with a pore size of 100 nm present a greater change in its resistivity compared with 300 nm pore. It seems that the introduction on nitrogen does not increase significantly its photosensitivity, in the case of 100 nm pore it decreases the response. Furthermore, the relaxation times after exposure are in the order of hundreds of milliseconds (i.e. 500 milliseconds), however graphene and SWNT films have shown faster response times in the order of few microseconds or even nanoseconds with higher response percentage variations [26; 31], nevertheless to the best of our knowledge to this date there are no publications regarding the photoresponse of carbon inverse opals.

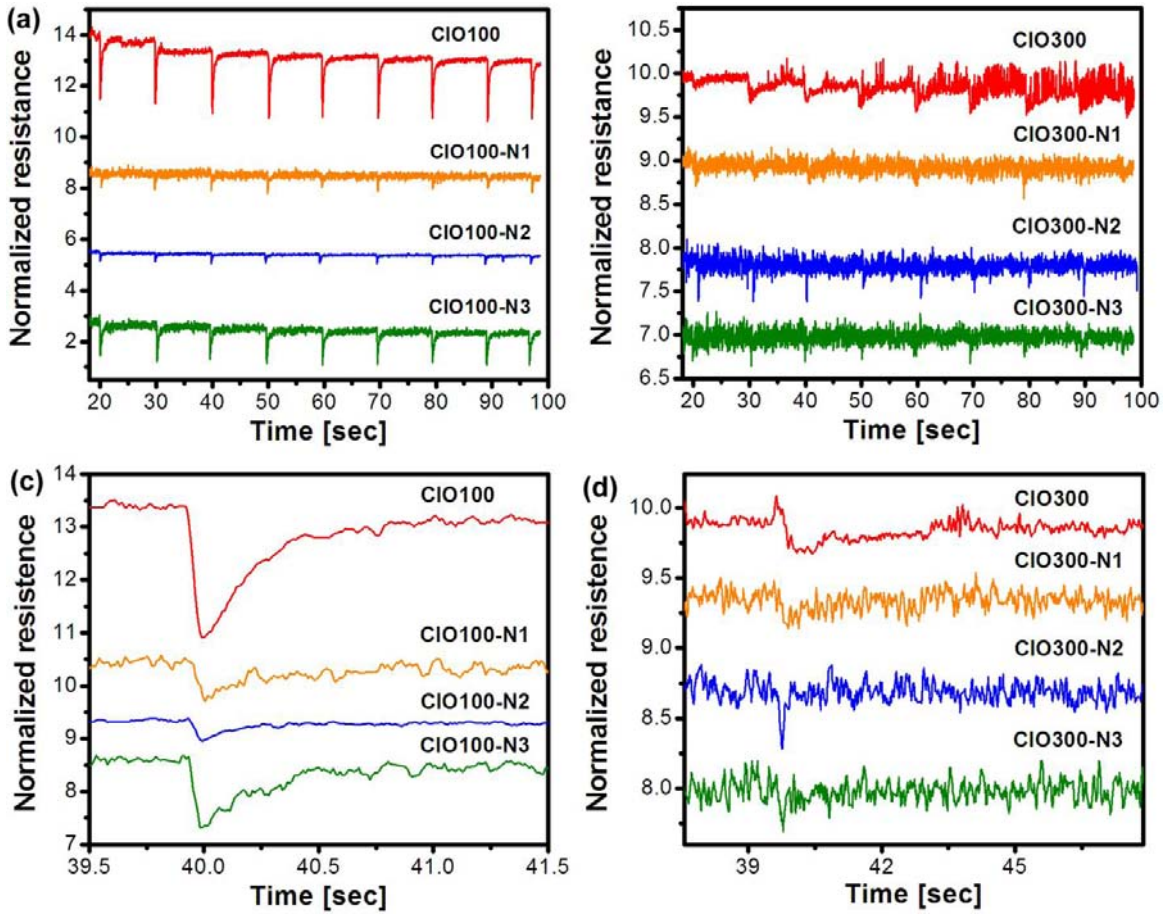

Figure 4.26: Photosensor measurements. Data was obatined with a light flash exposed to nitrogen doped carbon inverse opal at different contents. The samples with 100 nm pores present a higher change in its resistance.

4.6.4 Conclusions

It is clear that the carbon inverse opals with 300 nm pores have a greater change in resistance when exposed to the solvent vapors, although with 100 nm pores still have a clear response. The introduction of a certain amount of nitrogen in the samples increases its sensitivity to these vapors, especially for chloroform. In some cases the highest content of nitrogen shows an inverted response to the vapors, meaning that its resistance decreases when the other sample increase their resistance. This work shows that doped or chemically reactive porous carbon may be further studied in order to be used as gas sensors,

Concerning photoconductivity measurements, it is clear that samples with 100 nm pore size present a greater response than 300 nm pores. When doping with nitrogen the photoconductivity was not enhanced significantly. The relaxation

times after flash exposure have a maximum of 500 milliseconds, these results show that the response time to the flash exposure is relatively fast.

The combination of the semiconductor and photoconductive properties make this material candidate for photosensors or perhaps in photovoltaic devices as electrodes and photoconductive materials.

4.6.5 References

1. *C_{60}: Buckminsterfullerene.* **H.W. Kroto, J.R. Heath, S.C. O'Brien, R.F. Curl, R.E. Smalley.** 1985, Nature, Vol. 318, pp. 162-163.

2. *Filamentous growth of carbon through benzene decomposition.* **A. Oberlin, M. Endo, T. Koyama.** 1976, J. Cryst. Growth, Vol. 32, pp. 335-349.

3. *Single-shell carbon nanotubes of 1-nm diameter.* **S. Iijima, T. Ichihashi.** 1993, Nature, Vol. 363, pp. 603-605.

4. *Electric field effect in atomically thin carbon films.* **K. S. Novoselov, A. K. Geim, S. V. Morozov, D. Jiang, Y. Zhang, S. V. Dubonos, I. V. Grigorieva, A. A. Firsov.** 2004, Science, Vol. 306, pp. 666-669.

5. *Extreme oxygen sensitivity of electronic properties of carbon nanotubes.* **P. G. Collins, K. Bradley, M. Ishigami, A. Zettl.** 2000, Science, Vol. 287, p. 1801.

6. *Enhanced sensitivyt of a gas sensor incoporating single-walled carbon nanotube-polypyrrole nanocomposite.* **K. H. An, S. Y. Jeong, H. R. Hwang, Y. H. Lee.** 2004, Adv. Mater., Vol. 16, p. 1005.

7. *Controlled fabrication of carbon nanotube NO_2 gas sensor using dielectrophoretic impedance measurement.* **J. Suehiro, G. Zhou, H. Imakiire, W. Ding, M. Hara.** 2005, Sensors and Actuators B, Vol. 108, pp. 398-403.

8. *CO detection using carbon nanotube networks and micromachined resonant transducers.* **A. Zribi, A. Knobloch, R. Rao.** 2005, Appl. Phys. Lett., Vol. 86, p. 203112.

9. *A compact wireless gas sensor using a carbon nanotube/PMMA thin film chemiresistor.* **J. K. Abraham, B. Philip, Ashwin Witchurch, V. K. Varadan, C. C. Reddy.** 2004, Smart Mater. Struct. , Vol. 13, p. 1045.

10. *Role of defects in single-walled carbon nanotube chemical sensors.* **J. A. Robinson, E. S. Snow, S. C. Bădescu, T. L. Reinecke, F. K. Perkins.** 2006, Nano Lett., 1747 (2006).

11. *Carbon nanotube gas and vapor sensors.* **D. R. Kauffman, A. Star.** 2008, Angew. Chem. Int. Ed., Vol. 47, pp. 6550–6570.

12. *Detection of individual gas molecules adsorbed on graphene .* **F. Schedin, A. K. Geim, S. V. Morozov, E. W. Hill, P. Blake, M. I. Katsnelson, K. S. Novoselov.** 2007, Nature Materials, Vol. 6, p. 652.

13. *Molecular doping of graphene.* **T. O. Wehling, K. S. Novoselov, S. V. Morozov, E. E. Vdovin, M. I. Katsnelson, A. K. Geim, A. I. Lichtenstein.** 2008, Nano Lett., Vol. 8, p. 173.

14. *Adsorption of H2O, NH3, CO, NO2, and NO on graphene: A first-principles study.* **O. Leenaerts, B. Partoens, F. M. Peeters.** 2008, Phys. Rev. B, Vol. 77, p. 125416.

15. *Improved operational stability of biosensors based on enzyme-polyelectrolyte complex adsorbed into a porous carbon electrode.* **V. G. Gavalas, N. A. Chaniotakis, T. D. Gibson.** 1998, Biosensors & Bioelectronics, Vol. 13, pp. 1205-1211.

16. *Novel carbon materials in biosensor systems .* **S. Sotiropoulou, V. Gavalas , V. Vamvakaki, N.A. Chaniotakis.** 2003, Biosensors and Bioelectronics, Vol. 18, pp. 211-215.

17. *Improving gas sensing properties of graphene by introducing dopants and defects: a first-principles study.* **Y. -H. Zhang, Y. -B. Chen, K. -G. Zhou, C. -H. Liu, J. Zeng, H. -L. Zhang, Y. Peng.** 2009, Nanotechnology 20, 185504 (2009), Vol. 20, p. 185504.

18. *Fabrication of vapor and gas sensors using films of aligned CNx nanotubes.* **F. Villalpando-Páez, A.H. Romero, E. Muñoz-Sandoval , L.M. Martínez , H. Terrones , M. Terrones.** 2004, Chem. Phys. Lett., Vol. 386, p. 137.

19. *Ab initio study of doped carbon nanotube sensors.* **S. Peng, K. Cho.** 2003, Nano Lett., Vol. 3, pp. 513-517.

20. *Humidity sensing properties of CN_x film by RF magnetron sputtering system.* **J. G. Lee, S. P. Lee.** 2004, Sensors and Actuators B , Vol. 108, pp. 450-454.

21. *Viability studies of pure carbon- and nitrogen-doped nanotubes with entamoeba histolytica: from amoebicidal to biocompatible structures.* **A. L. Elías, J. C. Carrero-Sánchez, H. Terrones, M. Endo, J. P. Laclette, M. Terrones.** 2007, Small, Vol. 3, pp. 1723-1729.

22. *Efficient vapor sensors using foils of dispersed nitrogen-doped and pure carbon multiwalled nanotubes.* **B. Rebollo-Plata, E. Muñoz-Sandoval, F. López-Urías, E. L. Hernández-Cortina, H. Terrones, M. Terrones.** 2010, J. Nanosci. Nanotechnol., Vol. 10, pp. 3965-3972.

23. *Gas-sensitive properties of nitrogen-rich carbon nitride films.* **L. M. Zambov, C. Popov, N. Abedinov, M. F. Plass, W. Kulisch, T. Gotszalk, P. Grabiec, I. W. Rangelow, R. Kassing.** 2000, Adv. Mater., Vol. 12, pp. 656-660.

24. *Intrinsic response of graphene vapor sensors.* **Y. Dan, Y. Lu, N. J. Kybert, Z. Luo, A. T. C. Johnson.** 2009, Nano Lett., Vol. 9, pp. 1472-1475.

25. *Elastic response of carbon nanotube bundles to visible light.* **Y. Zhang1, S. Iijima.** 1999, Phys. Rev. Lett., Vol. 82, pp. 3472-3475.

26. *Photoconductivity in semiconducting single-walled carbon nanotubes.* **A. Fujiwara, Y. Matsuoka, H. Suematsu, N. Ogawa, K. Miyano, H. Kataura, Y. Maniwa, S. Suzuki, Y. A.** 2001, Jpn. J. Appl. Phys., Vol. 40, pp. 1229–1231.

27. *Photoconductivity of single-wall carbon nanotube films.* **A. Fujiwara, Y. Matsuoka, Y. Matsuoka, H. Suematsu, N. Ogawa, K. Miyano, H. Kataura, Y. Maniwa, S. Suzuki, Y. Achiba.** 2004, Carbon, Vol. 42, pp. 919–922.

28. *Photoconductivity of single carbon nanotubes.* **M. Freitag, Y. Martin, J. A. Misewich, R. Martel, Ph. Avouris.** 2003, Nano Lett., Vol. 3, pp. 1067-1071.

29. *Photoconductivity of single-wall carbon nanotubes under continuous-wave near-infrared illumination.* **I. A. Levitsky, W. B. Euler.** 2003, Appl. Phys. Lett., Vol. 83, pp. 1857-1859.

30. *Molecular photodesorption from single-walled carbon nanotubes.* **R. J. Chen, N. R. Franklin, J. Kong, J. Cao, T. W. Tombler, Y. Zhang, H. Dai.** 2001, Appl. Phys. Lett., Vol. 79, pp. 2258-2260.

31. *Photoconductivity of bulk-film-based graphene sheets.* **X. Lv, Y. Huang, Z. Liu, J. Tian, Y. Wang, Y. Ma, J. Liang, S. Fu, X. Wan, Y. Chen.** 2009, Small, Vol. 5, pp. 1682–1687.

5. Magnetism of Fe and FeCo Encapsulated in Aligned Carbon Nanotube Arrays

5.1 Introduction

5.1.1 Metals encapsulated in carbon nanotubes

Different metals have been encapsulated in multiwall carbon nanotubes (MWNTs) such as Re, Pd, Ag, Au, Pb, Ni, Cr, Ge, Fe, Co, Cu, FeCo, FePt and FeNi [1; 2; 3; 4; 5; 6; 7; 8; 9; 10] [11] (Figure 5.1).

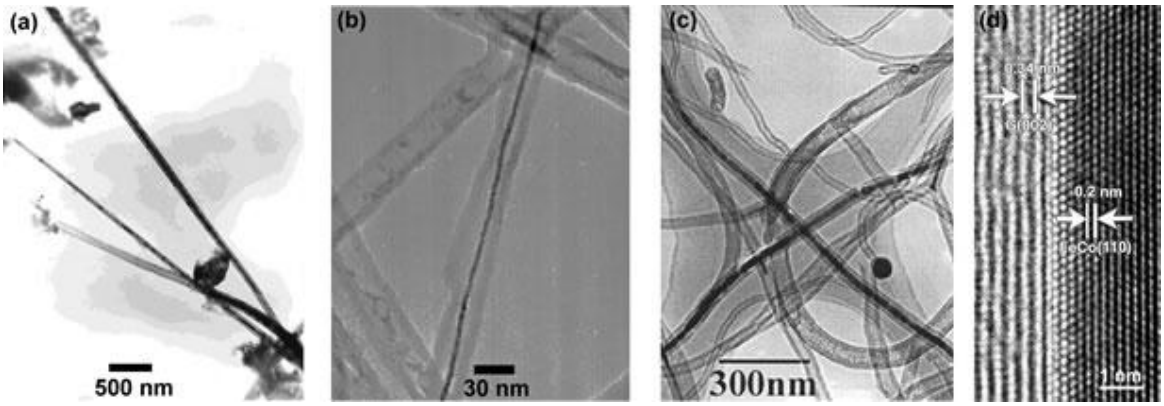

Figure 5.1: Metal filled carbon nanotubes. Carbon nanotubes with elongated nanoparticles of **(a)** Co (image from ref **[6]**), **(b)** Ni (image from ref **[3]**), **(c)** Cu (image from ref **[7]**) and an alloy of **(d)** FeCo (image from ref **[8]**).

There are two methods to encapsulate particles inside carbon nanotubes. One them occurs during the synthesis where the catalyst promotes the carbon nanotube (CNT) growth and at the same time it is encapsulated [4]. The other method consists in opening the CNT tips followed by filling of the void with an external material [1; 2; 11].

Chemical vapor deposition method is one of the most used experimental methods to encapsulate foreign materials. Regarding magnetic nanoparticles and nanowires inside carbon nanotubes these materials exhibit large coercive fields and a coherent reversal magnetization process [4; 5].

5.1.2 Iron nanowires

Fe nanowires have been synthesized using different methods. One of them is the templating method; generally the template is porous anodic aluminum oxide

(Figure 5.2). The nanoparticles obtained by this method are polycrystalline with large aspect ratio (length of the order of microns) [12; 13]. These materials present high coercivities (0.22-0.42 T) [12; 13; 14; 15; 16]. Another method is related with the pyrolysis of organometallic precursors, with this method it is possible to encapsulate ferromagnetic nanowires inside carbon nanotubes. Also high coercivities have been obtained by this method (H_c=0.13-0.23 T) [17; 18; 19]. Using the laser pyrolysis method, Fe_3C spherical nanoparticles with diameter c.a. 20 nm have been produced [20; 21] showing a coercivity of 0.056 T and a saturation magnetization around 120 A m^2/kg (emu/g). It is important to remark that the magnetic properties of the nanosized systems are very different to the corresponding bulk properties. For Example: Fe-Bulk exhibits very low coercive field ($6.0x10^{-3}$ T) with a saturation magnetization around 200 A m^2/kg (emu/g) and a Curie temperature of 1043 K. In the case of cementite structures (Fe_3C) they exhibit a magnetic saturation of 169.3 A m^2/kg (emu/g) and a Curie temperature of 480 K.

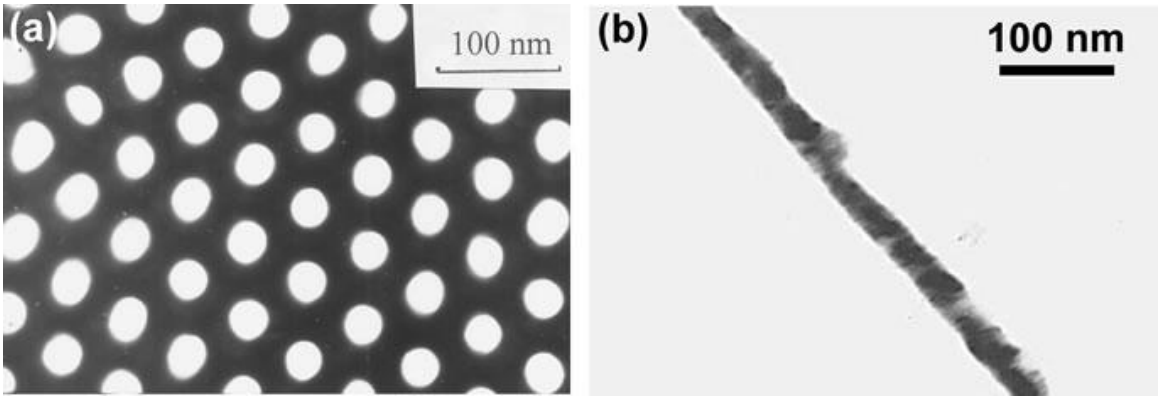

Figure 5.2: Fe nanowires made by porous anodic aluminum oxide template. (a) Anodic aluminum oxide template with an ordered 2-D array of pores. **(b)** Fe nanowire with irregular shape and polycrystallinity obtained by templating method. (images from ref **[14]**)

The magnetic properties of metallic nanowires (Fe, Co, Ni) have been studied, by other research groups, regarding the effect of the dimensions. It has been observed that the coercivity and the remanence (M_r) are inversely proportional to the diameter of the nanowire [22; 19; 15; 23], furthermore, the coercivity may also increase when increasing the length of the nanowire [24]. Also, the magnetic saturation (M_s) may increase if the diameter of the nanowires is smaller [23]. Regarding the ordering of these nanowire, if the distance between nanowires decreases the dipole interactions shall increase therefore the hysteresis curves will be less square-like (a lower value of M_r/M_s) [19; 25].

5.1.3 Applications

Encapsulated materials are an interesting current topic from the point of view of fundamental physical-chemical properties and applications. Research concerning magnetic nanomaterials have attracted attention due to the potential applications in magnetic recording industry [26; 27] (Figure 5.3 a), biological entities separation (Figure 5.3 b), targeted transportation of medicine, agents to improve contrast in magnetic resonance imaging [28; 29] (Figure 5.3 c). Magnetic recording industry requires smaller bits each generation. In order to satisfy this demand, recently the fabrication of patterned magnetic nanostructures and perpendicular magnetic recording has taken importance [26; 27]. In this context, one alternative is to use small magnetic nanowires encapsulated in carbon nanotubes.

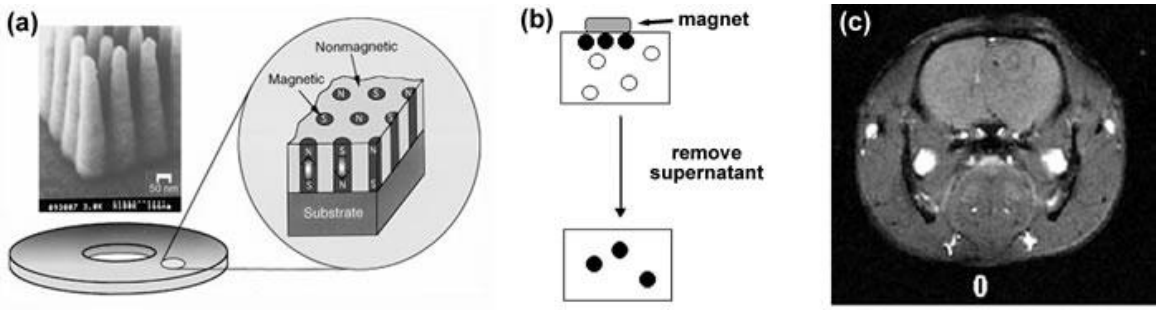

Figure 5.3: Applications of magnetic nanowires. (a) Nano pillars may be used for magnetic recording devices (images from ref **[26]**). Magnetic nanoparticles linked with biological entities may be **(b)** targeted or act as a filtering agent (image from ref **[28]**). **(c)** Iron oxide particles are studied as magnetic resonance imaging contrast agents (image from ref **[29]**).

In this work, we investigated the magnetic properties of ferromagnetic nanowires (Fe and FeCo) inside multiwall carbon nanotubes (MWNT), nitrogen doped multiwall carbon nanotubes (CN_x) and multiwall carbon nanotubes with carbonyl groups (CO_x). Ferrocene and/or cobaltocene in toluene or benzylamine precursors are used in our chemical vapor deposition method. By controlling the synthesis temperature, we could understand the size dependence of the magnetic properties. In addition, by controlling the toluene concentration in the synthesis, it is possible to change the chemical composition of the ferromagnetic nanowires.

5.2 Experimental Methodology

The iron encapsulated multiwall carbon nanotubes (Fe-MWNT) were synthesized by pyrolyzing toluene/ferrocene solution (2.5% of ferrocene by weight

in toluene) at 750, 800 and 850 ^{o}C by an aerosol pyrolysis system (Table 5.1) [30; 31] and by powder pyrolysis of ferrocene at 850 and 1050 ^{o}C in Ar atmosphere. Iron encapsulated nitrogen doped carbon nanotubes (Fe-CN_x) were synthesized by CVD [32] with a solution of ferrocene in benzylamine at temperatures between 750 and 850 ^{o}C in Ar atmosphere according to Table 5.1. MWNT with carbonyl groups on their surface (Fe-CO_x) where synthesized to produce short and tall forest morphologies [33] (see Appendix B), short CO_x (FxxEyySh) had a synthesis time of 15 minutes and the long CO_x (FxxEyyL) had a synthesis time of 3 hours; the solution concentrations are shown in Table 5.1. Now, regarding the production of FeCo nanowires the solutions used are a mixture of two with a 1:1 ratio, the solutions for FeCo-MWNT are ferrocene 2.5% by wt in toluene and cobaltocene 2.5% by wt. in toluene this based on the work of Elías et al. [8], and for FeCo-CN_x the same concentrations are used, although with benzylamine instead of toluene. TEM grids were prepared by sonicating the MWNTs in isopropanol using an ultrasonic bath during 30 minutes. All CNTs samples were analyzed by scanning electron microscopy (SEM) and scanning transmission microscopy (STEM) using a Philips FEG-XL30 microscope also by transmission electron microscopy (TEM) with a HRTEM 300KV FEI TECNAI F30 STWIN G2 and a TEM 200 KV JEOL JEM 200CX. Iron content was analyzed with a thermogravimetric analyzer (TGA) (Thermo Cahn, model VersaTherm) at a heating rate of 10 °C/min in air atmosphere. The magnetic properties of the samples were measured using PPMS (Quantum Design) equipment at different temperatures. The corrected hysteresis loops were obtained by subtracting the offset background signals (sample holder) as a function of the external field. The growth mechanism of encapsulated nanowires in CNT is discussed in Appendix A.

Table 5.1: Solution concentrations, argon flow and synthesis temperature for Fe encapsulated in MWNT, CN_x and CO_x.

Fe Nanowires	Toluene (% by wt.)	Ferrocene (% by wt.)	Ethanol (% by wt.)	Temperature (^{o} C)
MWNT-800	97.5	2.5	0.0	750
MWNT-800	97.5	2.5	0.0	800
MWNT-850	97.5	2.5	0.0	850
F25E10Sh	96.5	2.5	1.0	750
F25E25Sh	95.0	2.5	2.5	750
F25E10L	96.5	2.5	1.0	820
F50E25L	92.5	5.0	2.5	820
	Benzylamine			
CN_x750	97.5	2.5	0.0	750
CN_x800	97.5	2.5	0.0	800

5.3 Results and discussions

5.3.1 Simulation

In order to compare our experimental results, we calculated the magnetic behavior of iron nanowires. We used the micromagnetic theory based on the total magnetic Gibbs free energy (**E**). In our simulations, we introduced the exchange energy, magneto-crystalline anisotropy energy, magnetostatic energy and the Zeeman energy. The effective magnetic field H_{eff} at a position inside the ferromagnetic materials is given by $H_{eff}=-(\partial \mathbf{E}/\partial \mathbf{M})$, where **M** is the magnetization. The magnetization orientation follows the Landau-Lifshitz-Gilbert equation,

Eq. 5.1

$$\frac{dM}{dt} = \frac{-\omega}{1+\lambda^2} M \times H_{eff} - \frac{\lambda\varpi}{(1+\lambda^2)M_s} M \times (M \times H_{eff})$$

where ω is the gyromagnetic ratio, λ is the damping coefficient. In order to solve the Landau-Lifshitz-Gilbert equation the finite difference method is used. Our calculations have been computed by Oriented Object Micro Magnetic Frame (OOMMF) [34]. In the input parameters of the software we used a magnetic saturation of 1.7 x 10^3 A/m, exchange stiffness of 21 x 10^{-12} J/m, anisotropy constant of 48 x 103 J/m^3 and a damp coefficient of 0.5. More information about the OOMMF software can be found in Appendix D.

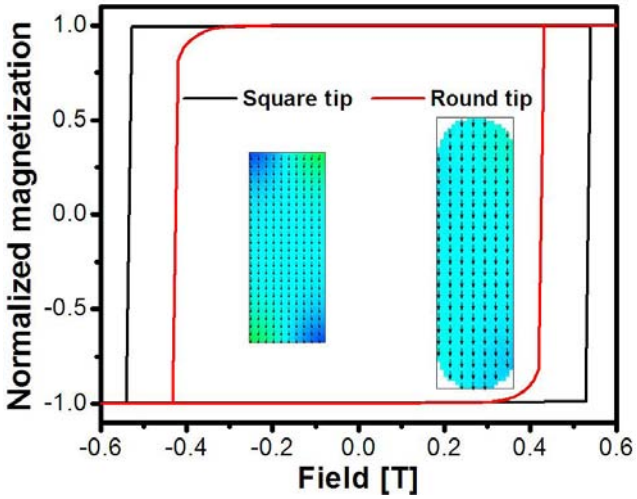

Figure 5.4: Microgmanetic simulation of rectangular particle with square tip and round tip. The particle thickness and width are 20 nm, with a height of 50 and 70 nm for square and round tip, respectively

In order to understand the role of the applied external magnetic field, we have carried out magnetic simulations of Fe nanowires with semicircular tips using the OOMMF code [34]. We started with the simulation of two separate nanowires; one with a square tip and the other with a semicircular tip (see Figure 5.4). For the square tip we observed that the reversal process is not gradual, it is step like, and however, with semicircular tips this process is gradual between 0.3-0.4 T thus showing the importance of the tip geometry for the demagnetization process.

Further on, we studied a single nanowire with semicircular tip maintaining its diameter constant of 20 nm (see Figure 5.5 a) varying the height from 40 to 70 nm. All calculated hysteresis loops are squared indicating single domain magnetization with curling nucleation sites at the round tips and the rest of the body remains with a homogeneous magnetization during the entire reversal process. This curling process has been reported previously for Fe_xPt_y and Ni nanowires [35; 36]. The coercive field values recorded in this study have large values, ranging from 0.426 to 0.342 T. (see Figure 5.5 a). However, when the length of the nanowires is kept constant (80 nm) and the diameter varied (20-50 nm), the hysteresis curves exhibited significant modifications. The values obtained for coercive fields ranged from 0.069 to 0.450 T (see Figure 5.5 b), similar diameter dependency of nanowires has been reported by Jian-Hua Gao et al. in which a change from approximately 20 to 50 nm in diameter may reduce the coercivity almost by 400 Oe [36]. Both results depicted in Figure 5.5 a and b, demonstrate that the magnetic behavior is tightly dependent of the aspect ratio of elongated nanowires; significantly more dependent upon diameter. Furthermore, the demagnetization factor is more sensitive to variations upon the diameter for a finite cylinder with similar dimensions [37; 38].

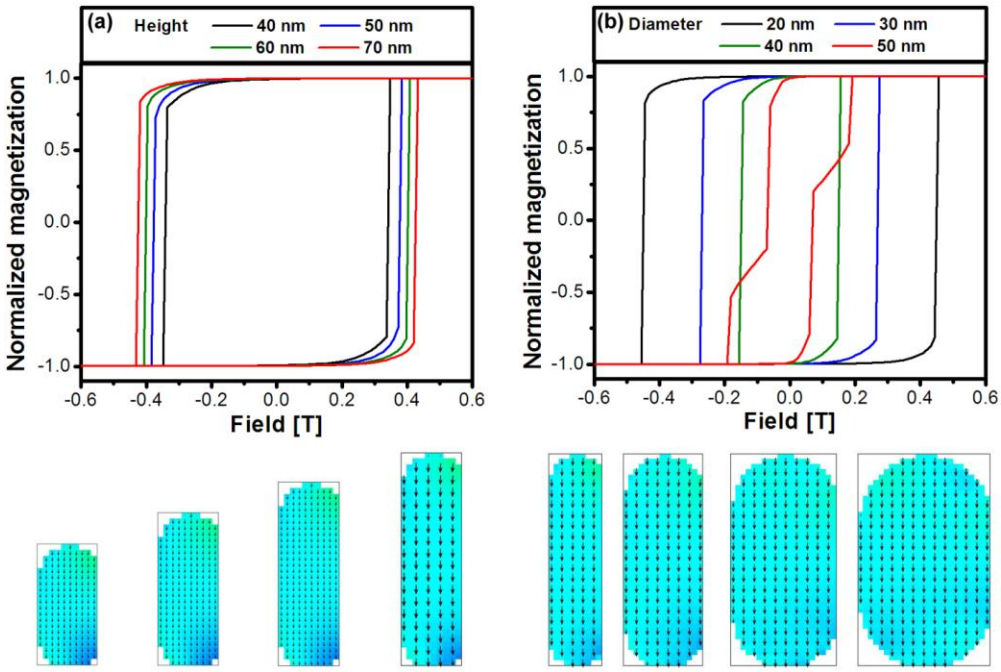

Figure 5.5: Microgmanetic simulation made with OOMMF of a single Fe particle at different **(a)** heights with constant 20 nm diameter and **(b)** diameter variation with constant 80 nm height. Top row corresponds to hysteresis curves of the external magnetic field applied along the wire axis and lower row corresponds to representations of the studied systems.

The next system studied consists of Fe nanowires with semicircular tips were the diameter is constant (20 nm) whereas the height is chosen randomly between 20-40 nm. The spacing between particles was varied between 50 and 10 nm (see Figure 5.6 a). The demagnetization process varies depending upon the spacing between particles, for a lower spacing the first step of demagnetization is at lower magnetic fields, this is caused by higher interactions between particles where they start to behave as a single entity or particle, when increasing this spacing the interactions decreases and the entire system behaves as the contribution of each isolated particle where each step in the hysteresis curve corresponds to the magnetization flip of a single nanowire. In order to assess the effect of particle distribution we introduce between 1 and 3 disk-like particles (20 nm diameter) (see Figure 5.6 b), with one disk the hysteresis curves show the introduction of a new step at lower magnetic field, now with three disks these curves show a higher change in magnetization for the first step. This shows that a non uniform particle distribution decreases the area of the curve but does not affect the magnetic remanence nor the coercive field.

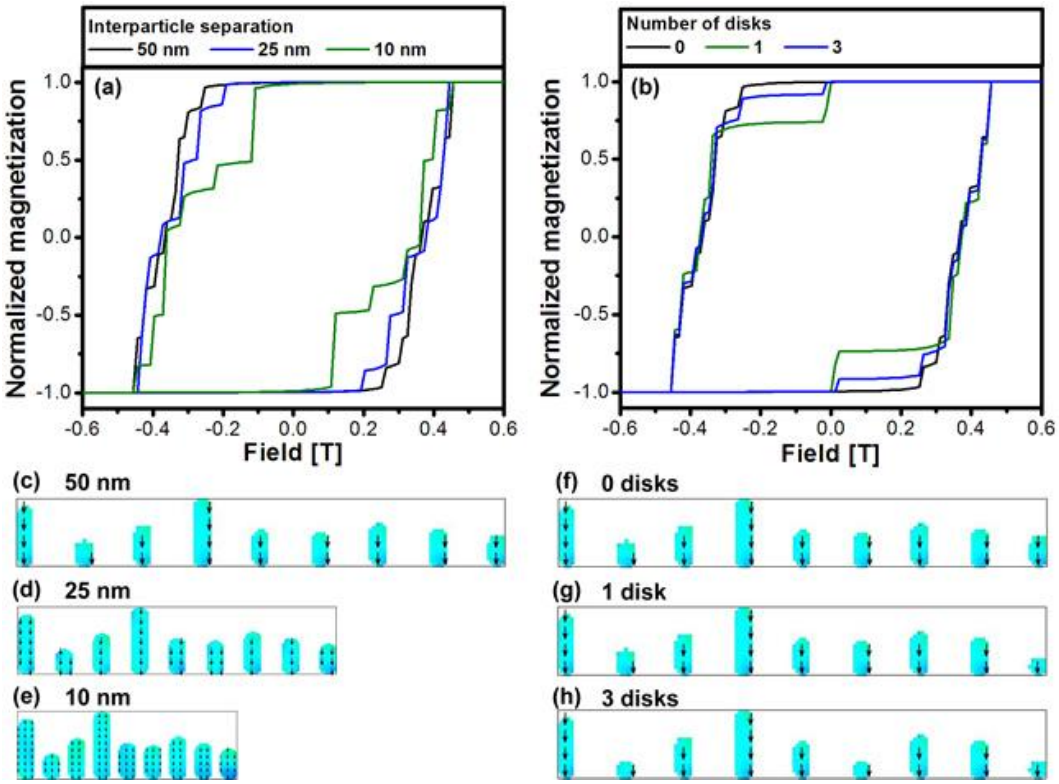

Figure 5.6: Micrognanetic simulation of an array of aligned Fe particles with several heights. (a) Hysteresis loops of a particle array varying interparticle separation from 50 to 10 nm. **(b)** Hysteresis loops of a particle array varying the number of disks from 0 to 3, for statistical analysis. Vector field of the magnetization in the array of particles with interparticle separation of **(c)** 50, **(d)** 25 and **(e)** 10 nm, and increasing the number of disks **(f)** 0, **(g)** 1 and **(h)** 3 disks.

In another case, we studied linear arrays of Fe nanowires with different average inclinations (73^o and 66^o). It is clear that the coercive field (from 0.245 to 0.209 T) and the magnetic remanence (from 0.94 to 0.89) decrease when the nanowires are less aligned (see Figure 5.7 a). We have also performed micromagnetic simulations for a linear array formed by Fe nanowires with 20 nm diameter distributed uniformly with spacing between wires of 50 nm. The height was chosen randomly between 20-40 nm. The external magnetic field was applied in three different directions (0^o, 45^o, and 90^o). We observed that the demagnetization process is gradual; each step in the hysteresis curve corresponds with the magnetization flip of nanowires with specific length. The first steps that appear when the external field is decreased, correspond to the shortest wires. The small aspect ratio of these wires makes the transition of the single-domain at low magnetic field as shown in Figure 5.8. In any case, the process of demagnetization of the system is more difficult when the external magnetic field is applied parallel to the wire's axis (0^o). The hysteresis curves become smoother (few steps), easier to demagnetize and the remanence reaches a minimum when the field is applied perpendicular (90^o) (see Figure 5.8). The changes in coercivity

and magnetic remanence experimentally measured are in agreement (qualitatively) with our micromagnetic simulations.

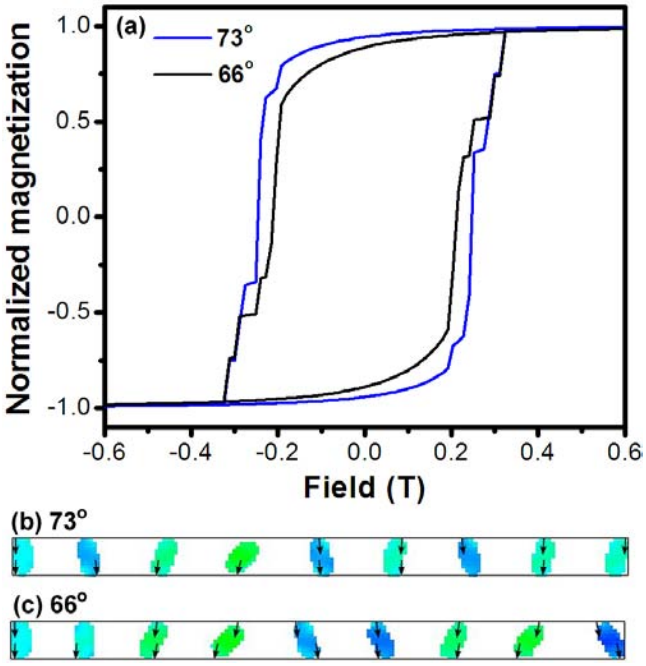

Figure 5.7: Micromagnetic simulations of a linear array of Fe nanowires with same dimensions although with different average inclinations. **(a)** Hysteresis loops for linear arrays with an average inclination of 73 and 66°. Vector field of the magnetization of a linear array with an average inclination of **(b)** 73 and **(c)** 66°.

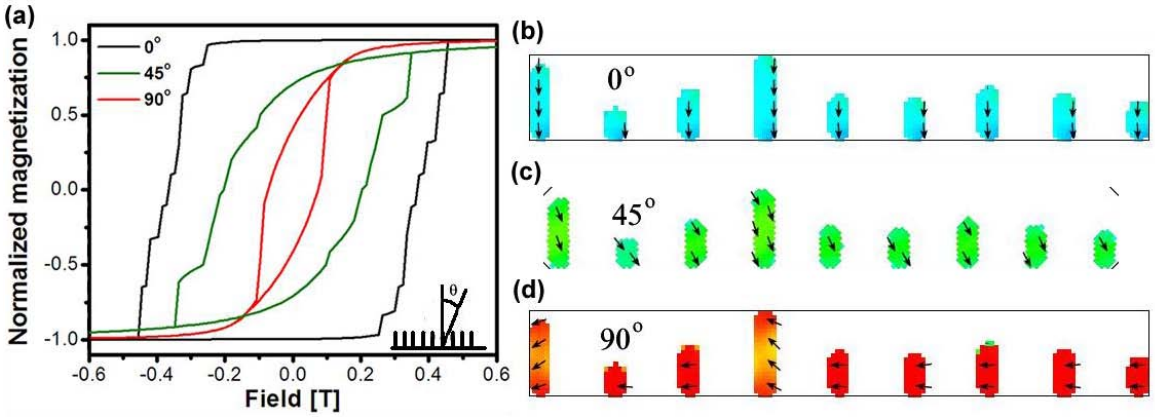

Figure 5.8: Microgmanetic simulation made with OOMMF of an array of aligned Fe particles with several heights. **(a)** Hysteresis curves of the external magnetic field applied at 0, 45 and 90 ° respect the nantube axis. Vector field of the magnetization in the Fe particle array with the external magnetic field applied at **(b)** 0, **(c)** 45 and **(d)** 90 θ respect the particle axis.

5.3.2 Experimental

5.3.2.1 Fe@MWNT

Figure 5.9 depicts the scanning electron microscopy images of pure multiwall carbon nanotubes forests encapsulating ferromagnetic nanowires synthesized with toluene/ferrocene mixtures (MWNT-TF) at 800 ^{o}C and 850 ^{o}C and ferrocene powder (MWNT-F) at 850 ^{o}C and 1050 ^{o}C. The SEM images show that all samples exhibit forest like morphologies with multiple packed carbon nanotubes (see Figure 5.9 a, c, e and g). High magnification images are shown in Figure 5.9 b, d, f and h. From these images, it is able to observe that the sample synthesized with toluene/ferrocene at 800 and 850 ^{o}C contain amorphous carbon particles on the walls of the nanotubes. When ferrocene powder is pyrolyzed at 850 ^{o}C we observed from SEM and TEM the presence of some Fe nanoparticles on the walls of the MWNTs (see Figure 5.9 f). However, if the temperature is increased up to 1050 ^{o}C, the sample contains several byproducts of non-cylindrical morphologies (see Figure 5.9 h). In all cases, the diameter of MWNTs remains almost constant (50-65 nm). We have also observed that the length of MWNTs strongly depends on the used precursor and the synthesis temperature. For ferrocene-toluene mixtures, the carbon nanotubes exhibit lengths of 150 μm, 290 μm and 340 μm for 750, 800 and 850 ^{o}C respectively. When the material is synthesized only by the ferrocene pyrolysis, the nanotube lengths are 11 and 6 μm for 850 and 1050 ^{o}C, respectively.

Table 5.2 shows the length, diameter, and the coercive field of the different encapsulated nanowires produced in this work. We measured the dimensions of the Fe nanowires by STEM and found that the pyrolysis of toluene/ferrocene at 750 ^{o}C, 800 ^{o}C, 850 ^{o}C yield average diameters of 9.2, 16 and 8.8 nm, respectively (Figure 5.10 a, b, c). The average length of the Fe nanowires is 97.3, 49.2 and 49.4 nm for 750 ^{o}C, 800 ^{o}C and 850 ^{o}C, respectively. When ferrocene powder is used in the nanotube synthesis at 850 ^{o}C, the length of the Fe-nanowires ranges from 100-317 nm, with an average diameter of 19.5 nm. The MWNT-TF have an average distance between MWNT of 145, 69 and 77 nm for 750 ^{o}C, 800 ^{o}C and 850 ^{o}C, and the MWNT-F 850 ^{o}C has an average distance between MWNT of 78 nm however the samples at 1050 ^{o}C do not have data because they exhibit particle by-products on the walls.

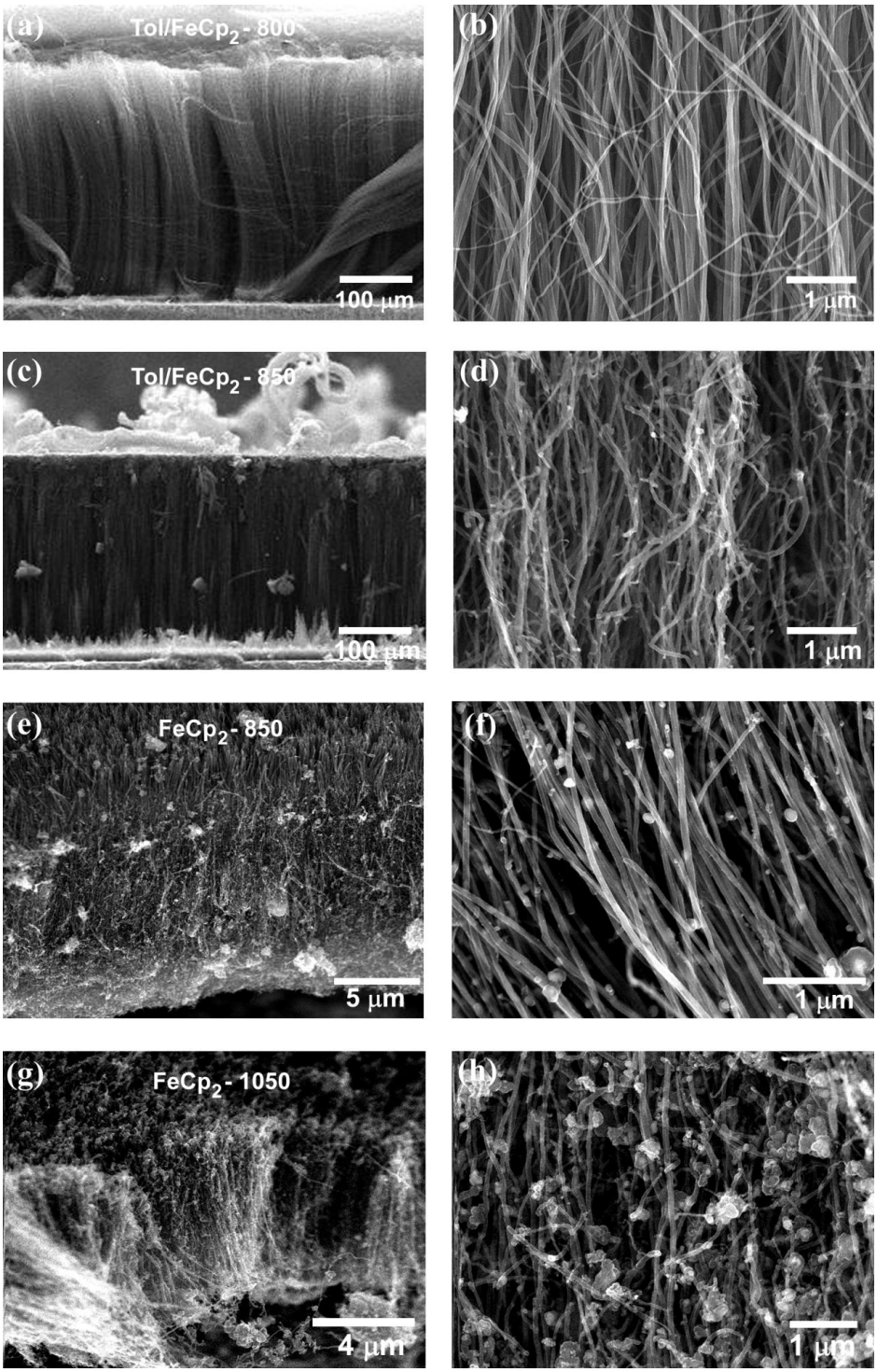

Figure 5.9: Scanning electron microscopy (SEM) images for ferromagnetic nanowires inside multiwall carbon nanotubes synthesized with ferrocene and toluene/ferrocene mixture at temperatures between 800 and 1050 ^{o}C. Samples synthesized with toluene/ferrocene synthesized at **(a)** and **(b)** 800 ^{o}C, whereas in **(c)** and **(d)** at 850 ^{o}C. Notice that the sample corresponding to 800 ^{o}C exhibits nanotubes with larger lengths and a dense forest. In **(e)** and **(f)** the sample was synthesized only by pyrolysis of ferrocene at 850 ^{o}C and **(g)** and **(h)** at 1050 ^{o}C this last temperature gives a higher yield of byproducts (not MWNT).

TEM analysis of the Fe nanowires indicates that there is a clear difference among the particle dimensions within the samples. The pyrolysis of toluene/ferrocene yielded products having diameters below 16nm, and samples produced by the ferrocene thermolysis exhibit larger diameters and lengths fairly longer than those obtained using toluene/ferrocene mixtures (see Figure 5.11 a, c and e). High resolution TEM images show the crystalline structure of these particles, the interplanar distances for the particles in all samples is 2 Å (Figure 5.11 3b, 3d and 3f), and the interlayer distance for MWNTs was ca. 3.4 Å. After observing several nanowires for all the different samples produced in this study, it was difficult to determine the general crystal growth direction, because of the different crystal orientations observed. Several electron diffraction patterns were obtained for MWNT-TF and MWNT-F at 850 ^{o}C (see Figure 5.12 b and d), for MWNT-TF the planes (220) and (221) of the Fe_3C phase are present and for MWNT-F a twinning effect in the electron diffraction pattern was observed, thus suggesting the coexistence of two phases, namely alpha-Fe and Fe_3C. The crystalline planes are coupled as follows: Fe (110) - Fe_3C (112), Fe (111) - Fe_3C (031) and Fe (200) - Fe_3C (240).

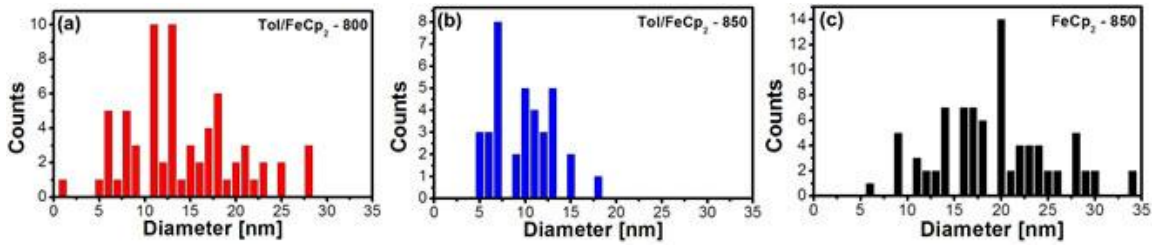

Figure 5.10: Diameter distribution of the samples formed by ferromagnetic nanowires inside carbon nanotubes. Under different synthesis conditions: toluene/ferrocene at **(a)** 800 and **(b)** 850 ^{o}C and **(c)** only ferrocene at 850 ^{o}C.

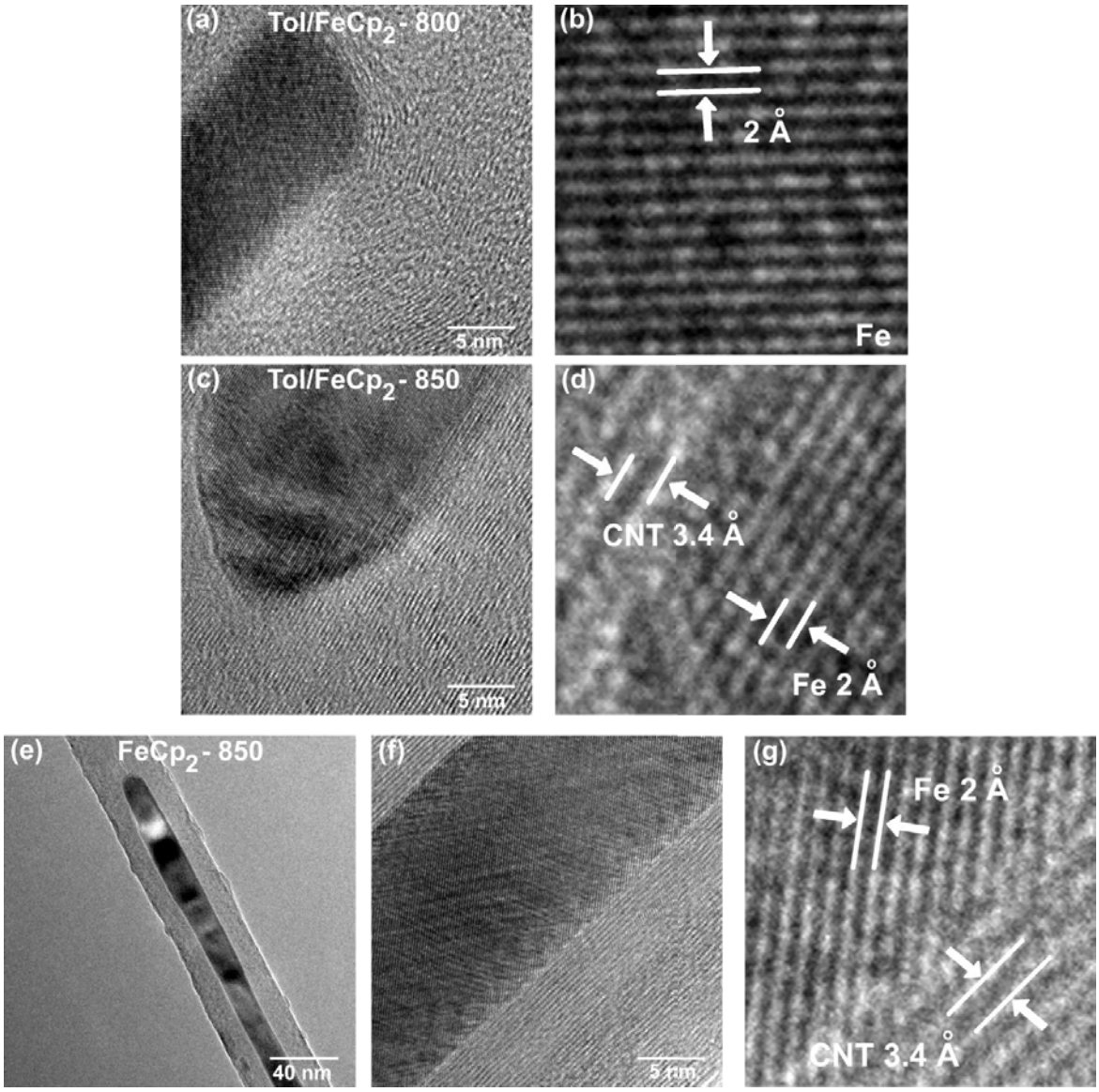

Figure 5.11: Transmission electron microscopy (TEM) images of Fe nanowires encapsulated in multiwall carbon nanotubes (MWNT) synthesized with toluene/ferrocene at **(a)** and **(b)** 800 and **(c)** and **(d)** 850 ^{o}C whereas in **(e-g)** only ferrocene was used as precursors in the chemical vapor deposition (CVD). **(a,c,f)** Are high magnification images showing crystal order. **(e)** Is a TEM image showing a long nanoparticle synthesized only with ferrocene at 850 ^{o}C. The right column shows **(b,d,g)** a close up of the crystal lattice indicating interplanar distances.

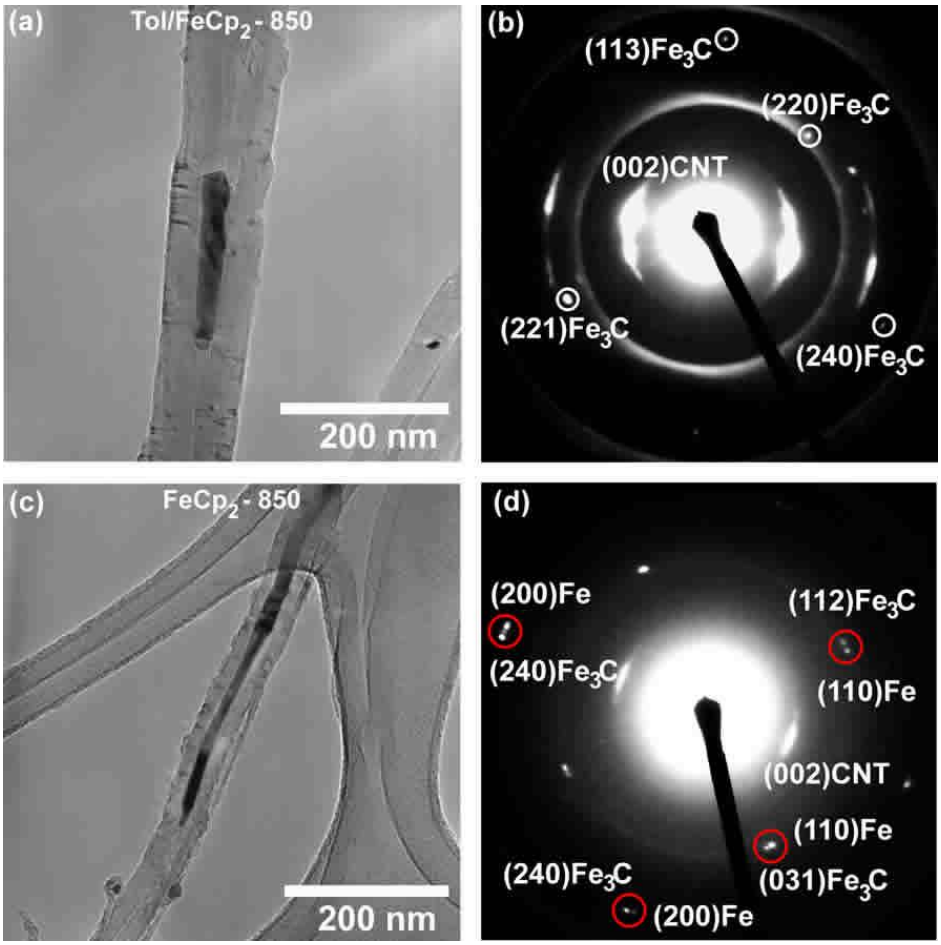

Figure 5.12: Left side are TEM images of magnetic nanowires encapsulated in multiwall carbon nanotubes and right side are electron diffraction patterns of these nanowires. Top **(a,b)** correspond to toluene/ferrocene and bottom **(c,d)** to ferrocene both synthesized at 850 ^{o}C. It is clear that both samples present encapsulated Fe_3C nanowires.

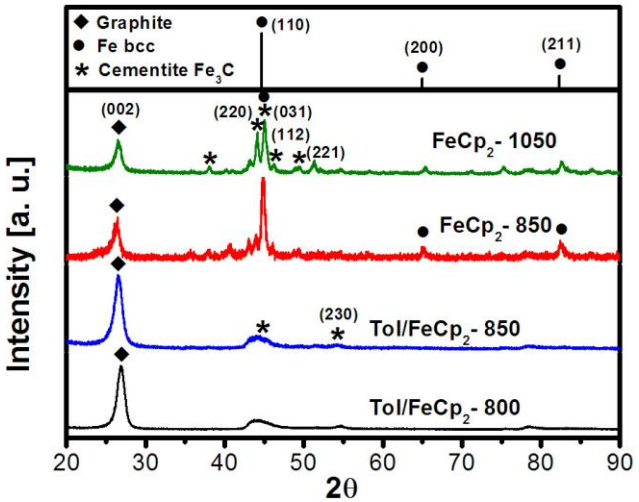

Figure 5.13: X-ray powder diffraction patterns of ferromagnetic nanowires inside multiwall carbon nanotubes synthesized with ferrocene at 850 and 1050 ^{o}C and toluene/ferrocene at 800 and 850 ^{o}C. Notice that with only ferrocene the peaks correspond to the planes of the α-Fe phase and Fe_3C phase, with toluene/ferrocene there are no clear α-Fe planes.

X-ray powder diffraction analysis demonstrated that the ferromagnetic nanowires encapsulated in MWNT-TF contain mainly Fe_3C (Figure 5.13). Our XRD analysis also reveals the presence of the typical graphitic reflections (002), which is associated to the nested carbon nanotubes. For MWNT-TF, we observed intensities attributed to the planes (021), (004), and (313) of cementite (Fe_3C). Even though, we identify a peak of α-Fe (attributed to the plane (110)) (see Figure 5.13), the other intensities relating to the planes (200) and (211) are almost negligible. In order to understand the role of toluene solution in the synthesis, we have performed the pyrolysis using only ferrocene at 850 and 1050 ^{o}C. In contrast with the case of toluene/ferrocene, here we found two different phases of the ferromagnetic nanowires: α-Fe and Fe_3C as shown in the XRD pattern (see Figure 5.13). Note that the α-Fe and Fe_3C phases coexist; the intensities of the different planes are well associated to these two phases. Note that for the pyrolysis temperature of 1050 ^{o}C, the peaks corresponding to cementite are more intense. The presence of α-Fe and Fe_3C nanowires inside MWNTs has already been observed previously by other groups by pryolyzing ferrocene in an inert atmosphere [17; 37; 38]. Our XRD, SEM and TEM analysis show that the MWNTs encapsulate Fe_3C nanowires in MWNT-TF. On the other hand, there is a coexistence of α-Fe and Fe_3C for MWNT-F. We are proposing that for this last case, the Fe nanowires have a Fe_3C shell as described in Figure 5.14 in a similar manner as observed by A.P. Shpak et al [39]. The Fe_3C nanowires may be grown by the excess of carbon (toluene and ferrocene) during the synthesis; on the other hand with lower carbon content by pyrolizing only ferrocene there is a production of Fe nanowires with a Fe_3C shell.

The TGA analysis revealed that the MWNTs-TF samples synthesized at 750 ^{o}C, 800 ^{o}C and 850 ^{o}C contain byproducts that could not be oxidized, considering that at the termination of the TGA they are in the form of Fe_2O_3 we estimate an Fe content of 5.74, 1.71 and 3.81 % (Figure 5.15) in the samples. Therefore, we propose that the sample corresponding to 750 ^{o}C, which results in the formation of more Fe_3C nanowires, causes the inhibition of nanotube growth (Figure 5.14 a). The different contents of Fe_3C could therefore result in significant variations of the magnetic saturation; for samples with higher iron content, the magnetic saturation tends to display a larger value.

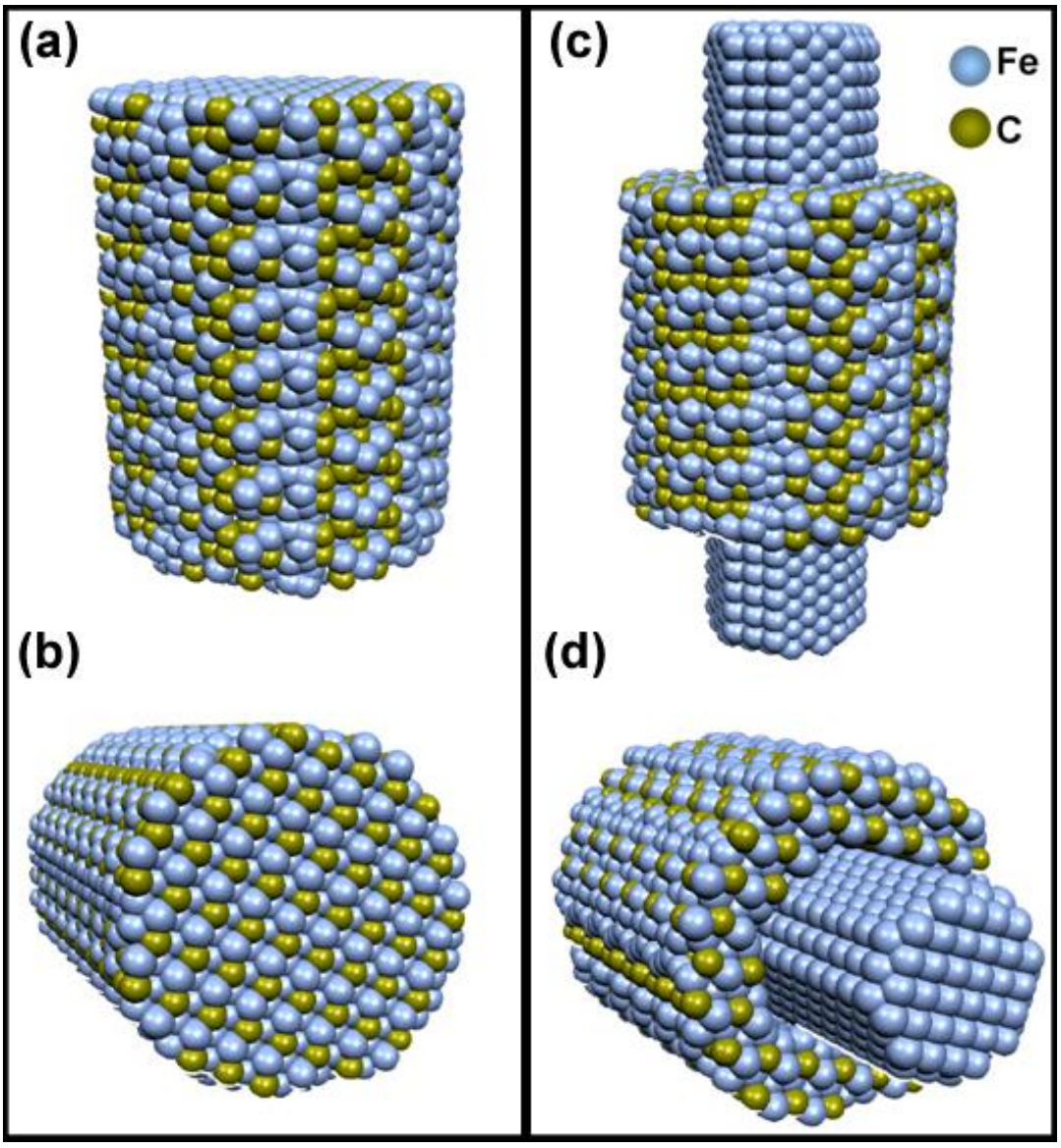

Figure 5.14: Structure modeling of ferromagnetic nanowires. The images in **(a)** and **(b)** represent a single crystal iron carbide (Fe_3C) nanowires whereas in **(c)** and **(d)** the images represent an α-Fe nanowires coated by Fe_3C. It is important to remark that we have used ferrocene and toluene in our pyrolysis process. The structure depicts in (a) and (b) is favored for high for a mixture of toluene/ferrocene (see Figure 5.13). The structure shown in (c) and (d) is favored for a synthesis of only ferrocene (see Figure 5.13).

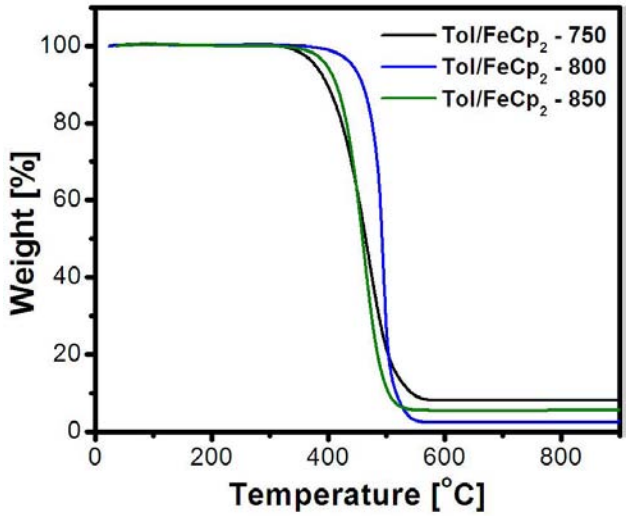

Figure 5.15: Thermogravimetric analysis of MWNT synthesized with a mixture of toluene/ferrocene with temperatures bewteen 750 and 850 ^{o}C.

Interesting results on the magnetic properties were obtained when these samples were exposed to an external magnetic field (see Table 5.2). The hysteresis loops were obtained for the samples exhibiting the forest-like morphology, see Figure 5.16. Here, the external magnetic field was applied at different angles with respect to the nanotube's axis 0, 45 and 90 degrees. The hysteresis loops at 2 K indicate that when the field is applied parallel to the nanotube's axis (0 degrees), MWNT-TF 750 ^{o}C sample presents a value of 0.22 T for H_c and MWNT-TF 800 ^{o}C exhibit H_c 0.19 T, whereas at MWNTs-TF 850 ^{o}C H_c = 0.21 T. For MWNT-F, the H_c values obtained were 0.18 and 0.11 T for 850 ^{o}C and 1050 ^{o}C, respectively. These values of coercivity are in the same range as other reports of Fe encapsulated in multiwall carbon nanotubes (H_c =0.13-0.23 T) [17; 18; 40]. These magnetic measurements suggest that the diameter and length of ferromagnetic nanowires, produced using toluene are important to determine the mechanisms of magnetization reversal mode in these nanowires. We observed that for MWNTs-TF, the highest coercivity corresponds to the particles with a thinner diameter (c.a. 9 nm); notice that MWNTs synthesized at 750 ^{o}C and 850 ^{o}C have similar diameters and coercivities despite having a considerable difference in length (see Table 5.2). Now, for MWNTs-F, the length of the nanowires was above 100 nm, and diameters ranged between 16 and 20 nm, however this greater aspect ratio does not provide a higher coercivity when compared to the previous case. These results suggest that the diameter of magnetic particles has a greater impact on the coercivity than the length of these. Other Fe nanowires have shown a tendency to exhibit higher coercivities for narrower diameters, although these samples were prepared using porous alumina having nanowire lengths of a few micrometers [15; 23; 41]. We also observed that when the sample presents impurities (MWNT-F 1050 ^{o}C), such as magnetic particles located outside the MWNTs, these impurities heavily reduce the magnetic properties of the entire sample. Furthermore, the normalized remanence (M_r/M_s at 2 K) exhibits values of 0.46 for MWNTs-TF, and 0.48 and 0.29 for MWNTs-F at 850 ^{o}C and 1050 ^{o}C

respectively (see Figure 5.17 b), these values that approach 0.5 are in accordance with the expected value for an isotropic orientation of an array of particles [42].

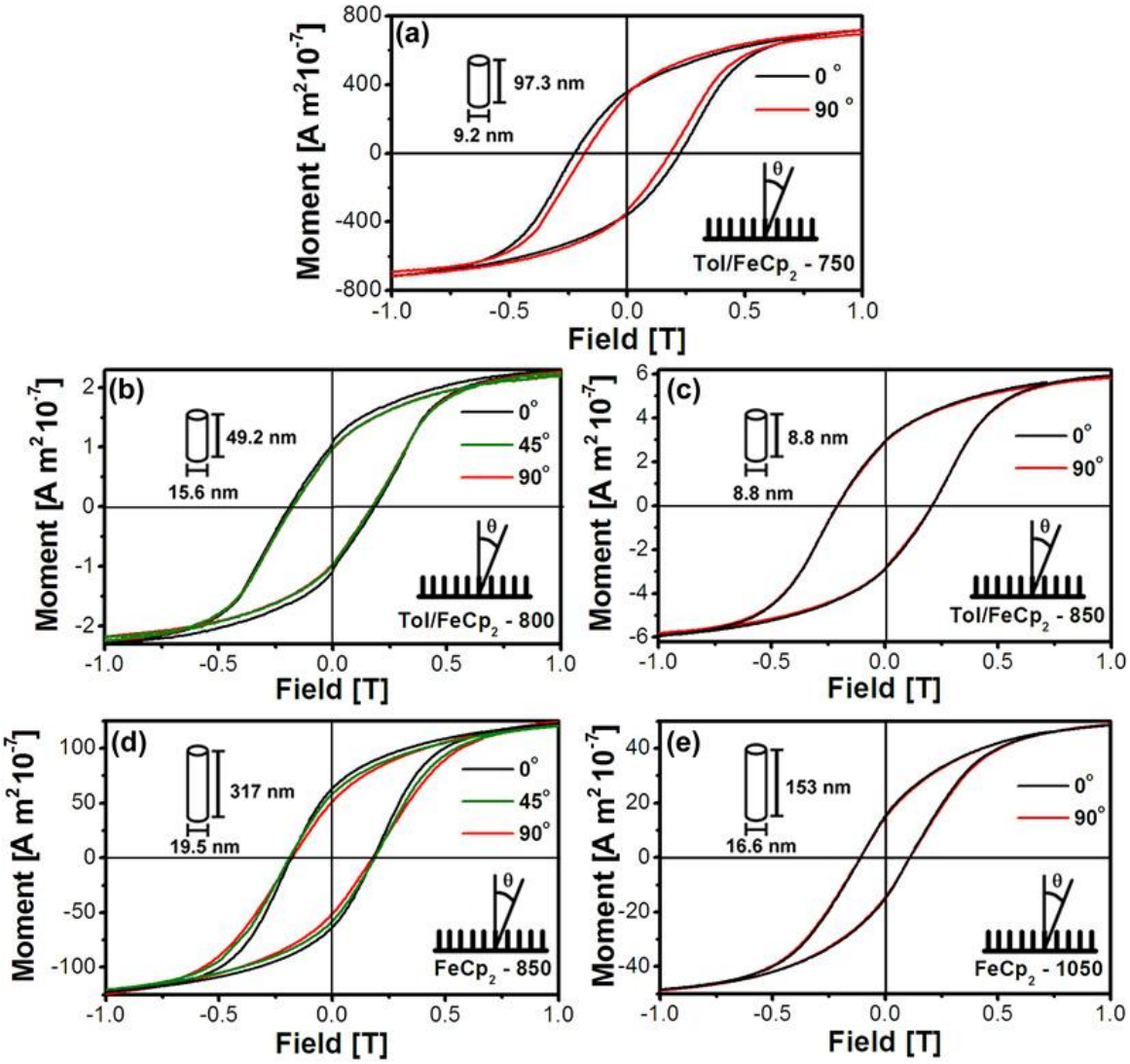

Figure 5.16: Hysteresis curves for Fe encapsulated in MWNT synthesized with toluene/ferrocene at **(a)** 800 and **(b)** 850 ^{o}C and only ferrocene at **(c)** 850 and **(d)** 1050 ^{o}C. Measurements with applied field at 0, 45 at 90 θ to the MWNT's axis at 2 K. Notice that in (b) the values of the coercive field (0.21 T) are larger than in the other samples studied.

Table 5.2. Fe nanoparticle average dimensions and magnetic properties for samples synthesized with and without toluene at different temperatures. All values shown here were measured at 2 K.

	Synthesis temperature (^oC)	MWNT separation (nm)	Diameter (nm)	Length (nm)	H_c (T)	M_r/M_s
Tol/$FeCp_2$	750	145	9.2	97.3	0.22	0.46
	800	69	15.6	49.2	0.19	0.46
	850	77	8.8	49.4	0.21	0.46
$FeCp_2$	850	78	19.5	317	0.18	0.47
	1050	--	16.6	154	0.11	0.29

In addition, we have performed several measurements varying the direction of the external magnetic field from 0 degree (parallel to the nanotube´s axis) to 90 degree (perpendicular to the nanotube´s axis). The coercive field and remanence exhibit a minimum value at 90 degree since it is difficult to magnetize perpendicularly large aspect ratio nanowires (observed for sample MWNT-F 850, see Figure 5.16 d). The low variations among the coercivity and remanence when changing the external magnetic field angle could be caused by the spacing between nanotubes (c.a. 70 nm). However this phenomenon has been observed for larger magnetic wires with micrometer length and more than a 100 nm in diameter, with a greater spacing among them (c.a. 800 nm). In figure 8 we show the variation of the coercivity and the squareness upon temperature (3 – 300 K), sample MWNT-TF 750 ^oC exhibits a linear variation from 0.22 T – 0.07 T, similar linear behavior has been observed for other Fe-CNT reports [4; 5; 40], according to these authors this variation may be due to the temperature dependent intrinsic domain-wall pinning [37], however in our case we are studying monodomains due to the size of the nanowires approaches the critical radius of 15 nm for Fe when a magnetic particle behaves as a single domain [43].

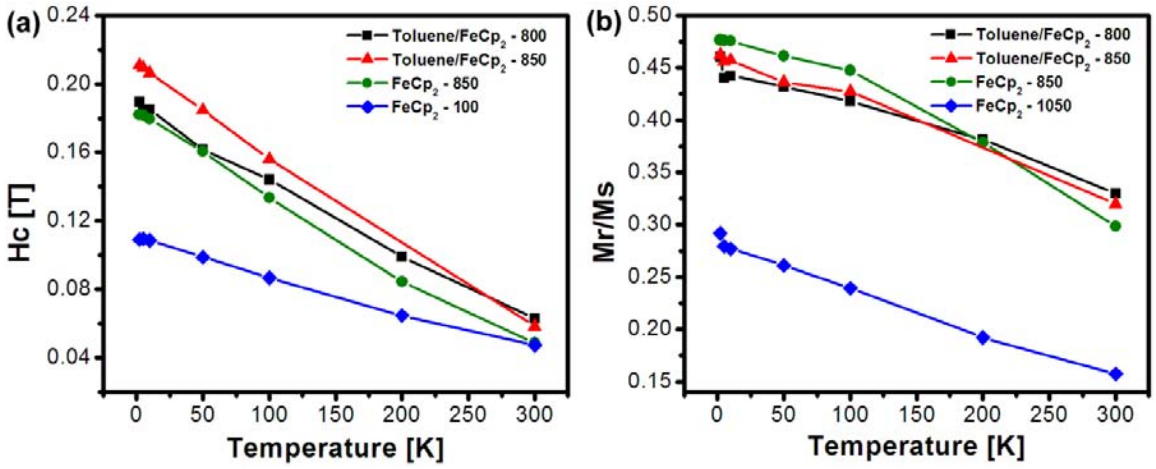

Figure 5.17: Coercive fields (H_c) in **(a)** and normalized remanence magnetization (M_r/M_s) in **(b)** as a function of the temperature for all samples toluene/ferrocene synthesized at 800, 850 ^{o}C and ferrocene pyrolysis at 850, 1050 ^{o}C.

From the experimental characterization presented above, we could conclude the following: 1) the samples produced using a solution of toluene/ferrocene (TF) are cleaner (less formation of non-nanotube byproducts) than the samples produced via pyrolysis of pure ferrocene (F); 2) the MWNT-TF nanowires tend to be an order of magnitude shorter and have a lower average diameter when compared to the MWTN-F samples; 3) MWNT-TF encapsulated nanowires are mostly in the form of Fe_3C, whereas MWNT-F containing mainly Fe nanowires appear to be covered with a thin layer of Fe_3C (core shell type); 4) We have also observed that in both cases, the nanowires are generally randomly oriented, thus excluding the effect of crystal orientation upon the magnetic properties, this random orientation is responsible for M_r/M_s to approach 0.5; 5) the slight change in coercive values agrees with the diameter variation between samples, despite the huge length difference of the nanoparticle; 6) The purity of the sample is another crucial factor, for MWNT-F nanowires produced at 1050 ^{o}C there are more side products, which are responsible of decreasing the coercive field and the magnetic remanence.

5.3.2.2 Fe@CN$_x$

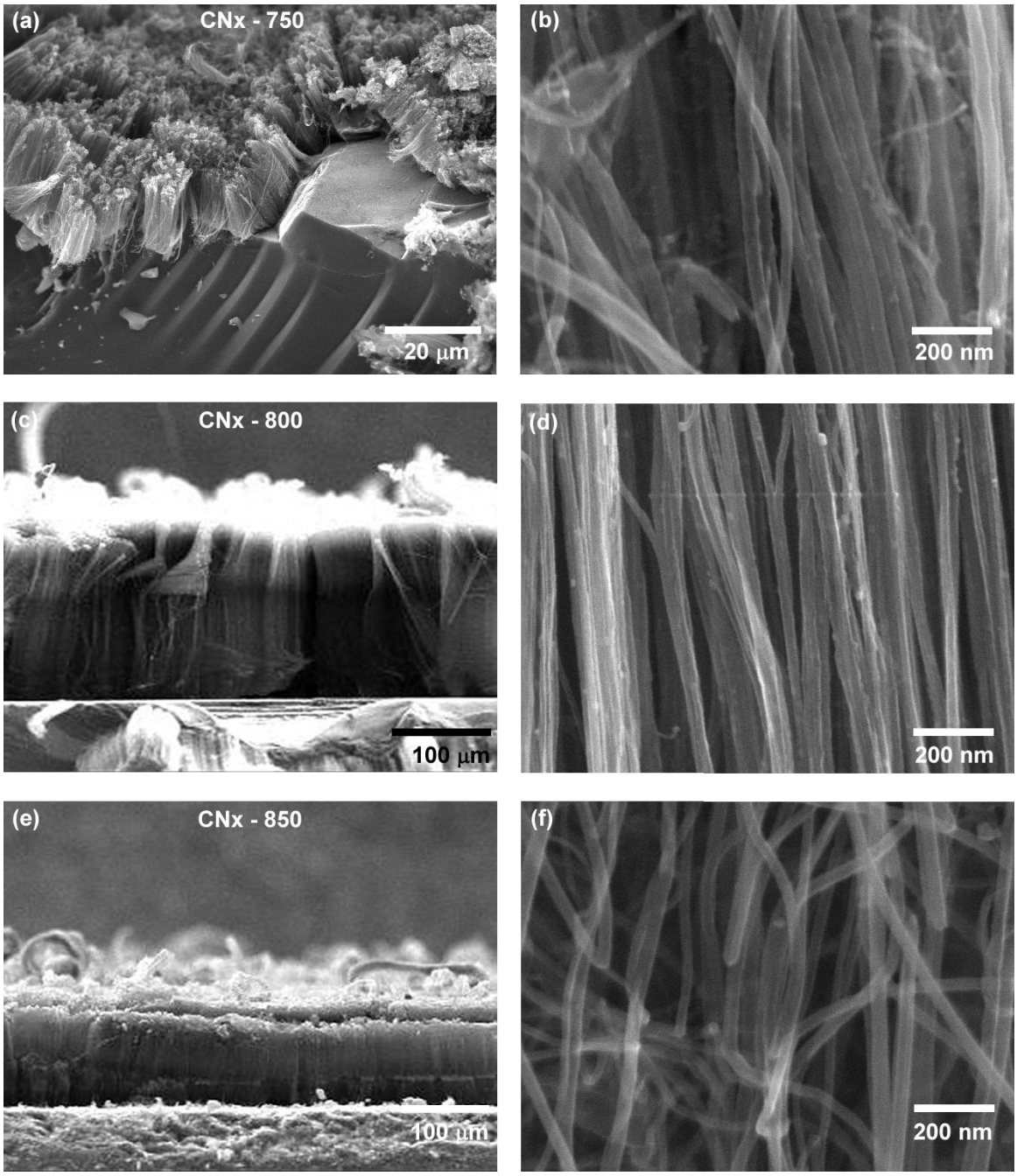

Figure 5.18 Scanning electron microscopy (SEM) images for ferromagnetic nanowires (Fe) inside multiwall carbon nanotubes doped with nitrogen (CN_x) synthesized at temperatures between 750 and 850 ^{o}C. Samples synthesized at **(a)** and **(b)** 750 ^{o}C, in **(c)** and **(d)** at 800 ^{o}C, in **(e)** and **(f)** at 850 ^{o}C. Notice that the sample corresponding to 800 ^{o}C exhibits nanotubes with larger lengths and a dense forest.

The SEM images show that the CN_x forest-morphology present a shorter length when synthesized at 750 ^oC (11 μm) (Figure 5.18 a, b) however the diameter and separation between nanotubes are similar for 750 and 800 ^oC (c. a. 24 nm) (Figure 5.18 b, d). When synthesized at 750 ^oC the Fe nanowires are more sphere-like and are closer between each other (Figure 5.19 a and b). We also notice that the nanowires are conical at the tips and they are sphere like along the carbon nanotubes (Figure 5.19 e). We measured the nanoparticle diameter in the samples observing that by increasing the synthesis temperature the nanoparticle diameter distribution widens and slightly shifts to larger diameters, 8.7, 7.6 and 12.3 nm for 750 ^oC, 800 ^oC and 850 ^oC respectively (Figure 5.20).

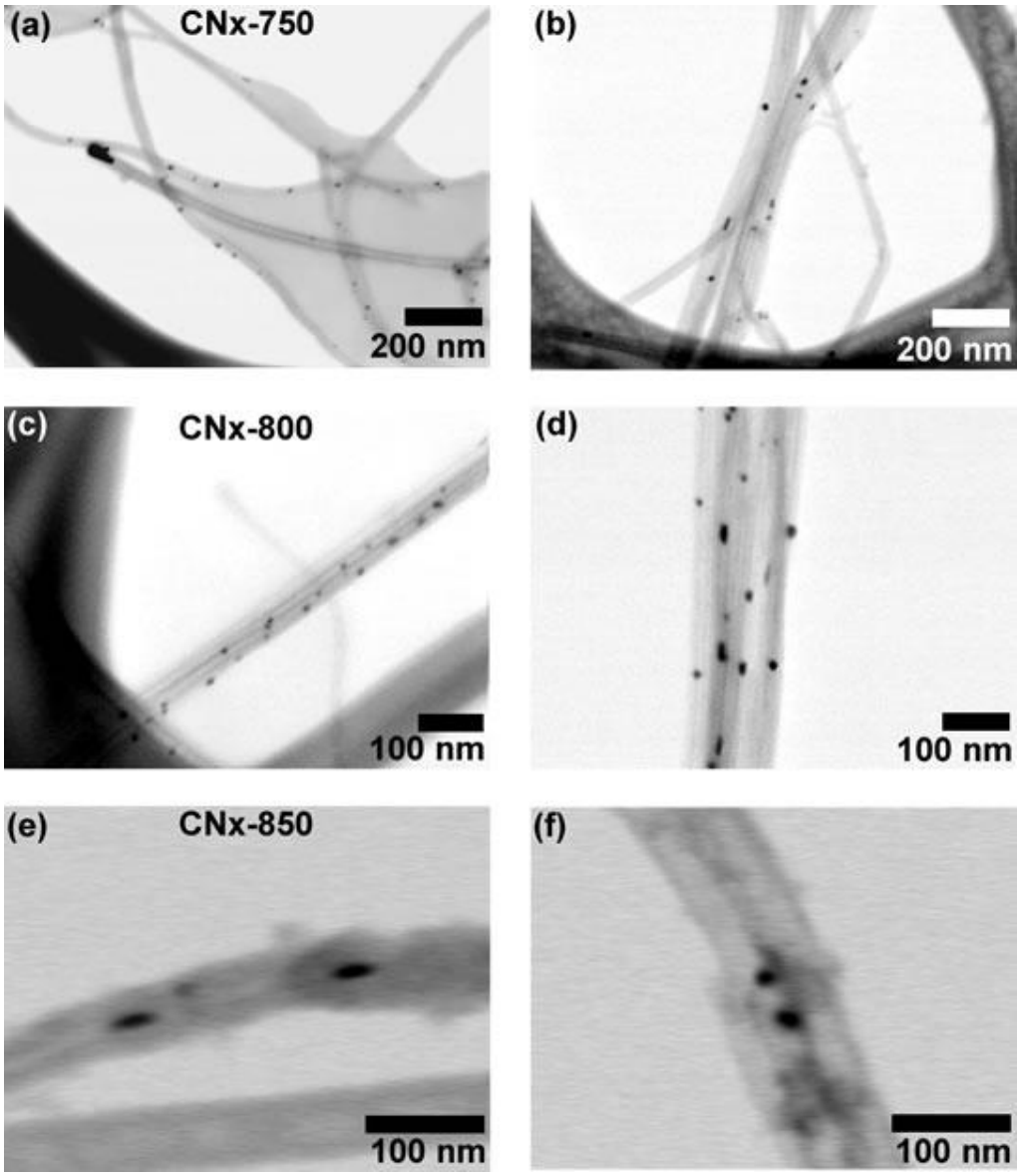

Figure 5.19: Scanning transmission electron microscopy images of the Fe nanopartices encapsulated in **(a,b)** CN_x-700, **(c,d)** CN_x-800, **(e,f)** CN_x-850.

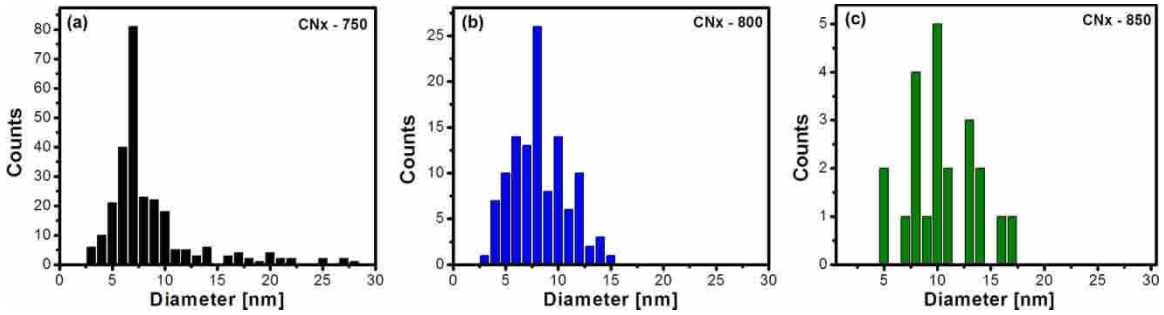

Figure 5.20: Diameter distribution of Fe nanowires encapsulated in carbon nanotubes doped with nitrogen synthesized at **(a)** 750, **(b)** 800, **(c)** 850 ^{o}C.

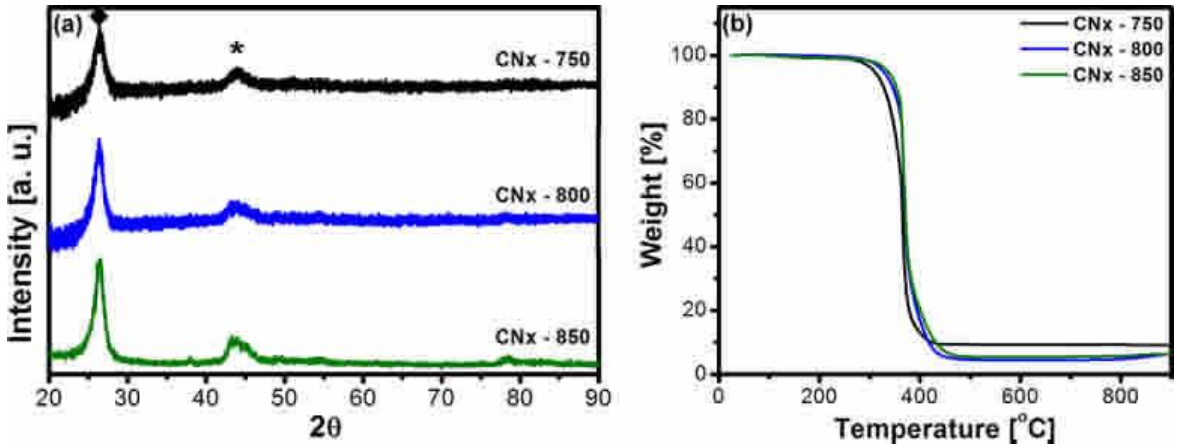

Figure 5.21: (a) XRD pattern where (♦) is the (002) plane of graphite and (*) is the (220) plane of Fe_3C. **(b)** Thermogravimetric analysis of CN_x synthesized with between 750 and 850 ^oC.

When analyzing the XRD pattern the crystallinity of Fe_3C is not clear, we only observe the (220) plane and along with this the (002) plane of graphite is evident (Figure 5.21 a). From the TGA analysis we estimate that the nitrogen doped CNTs have an Fe content of 6.37, 3.11 and 3.85 % by wt. for CN_x-750, CN_x-800 and CN_x-850, respectively, and the decomposition temperature for all the samples is between 350 and 400 ^oC (Figure 5.21 b). Surprisingly CN_x-750 has the shortest forest morphology (11 μm) regarding its high content of iron, and vice versa the lowest iron content CN_x-800 has the tallest forest morphology (188 μm).

The forest synthesized at 750 ^oC presents a higher coercivity (0.22 T at 2K) and squareness (M_r/M_s) (0.43 at 2K) at all the temperatures measured (Figure 5.22), however this sample does not have the lowest nanowire diameter which does not agree with the finding for Fe-MWNT, previously described. The table 5.3 has the nanowire dimensions and magnetic properties for comparison. We also notice that the squareness of all samples do not present a linear behavior for M_r/M_s vs. T, here there is a maximum at 50 K (Figure 5.22 c). Perhaps a) the shape and short length of these nanowires give rise to a different magnetization process; b) a mixture of conical and sphere like nanowires need to be taken in account in order to explain the findings.

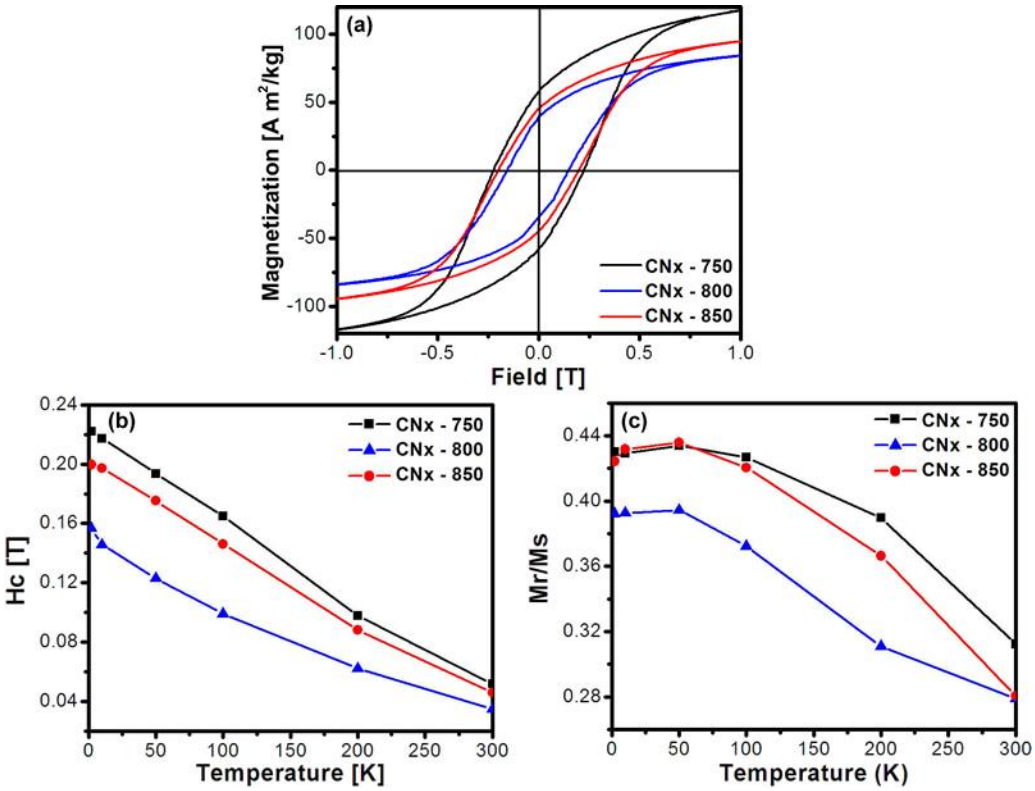

Figure 5.22: (a) Hysteresis curves for Fe_3C encapsulated in CN_x synthesized at 750, 800 and 850 ^oC, measured at 2 K. Coercive fields (H_c) in **(b)** and normalized remanence magnetization (M_r/M_s) in **(c)** as a function of the temperature for all samples synthesized at 750, 800 and 850 ^oC. Measurements were made with powder sample.

Table 5.3: Fe nanowires encapsulated in CN_x; average dimensions and magnetic properties. All values shown here were measured at 2 K.

Temp (^oC)	Diameter (nm)	Length (nm)	H_c (T)	M_r/M_s
750	8.7	11.9	0.22	0.43
800	7.6	24.2	0.16	0.39
850	12.3	47.5	0.20	0.42

5.3.2.3 Fe@CO_x

By observing the SEM images we found that for the short CO_x forests the CNTs are taller at 1.0% by wt. of ethanol (43 μm) (Figure 5.23 a-b). Now, for the long CO_x the forest morphology is taller for 2.5% by wt. of $FeCp_2$ with 1.0% by wt. of ethanol (2500 μm). We performed a statistical analysis for the encapsulated magnetic nanowires and we observe that they tend to be longer and wider at 1.0% by wt. of alcohol for the short and long CO_x (Figure 5.24 a-b). The diameter distribution shows that both solutions used give similar nanoparticle dimensions c. a. 13 nm diameter and 54.5 nm long for the long CO_x and c. a. 10.5 nm diameter and 24 nm long for short CO_x (Figure 5.25). In general for the CO_x we observe that

the encapsulated nanowires in short CO_x have lower diameter and length compared with the long CO_x.

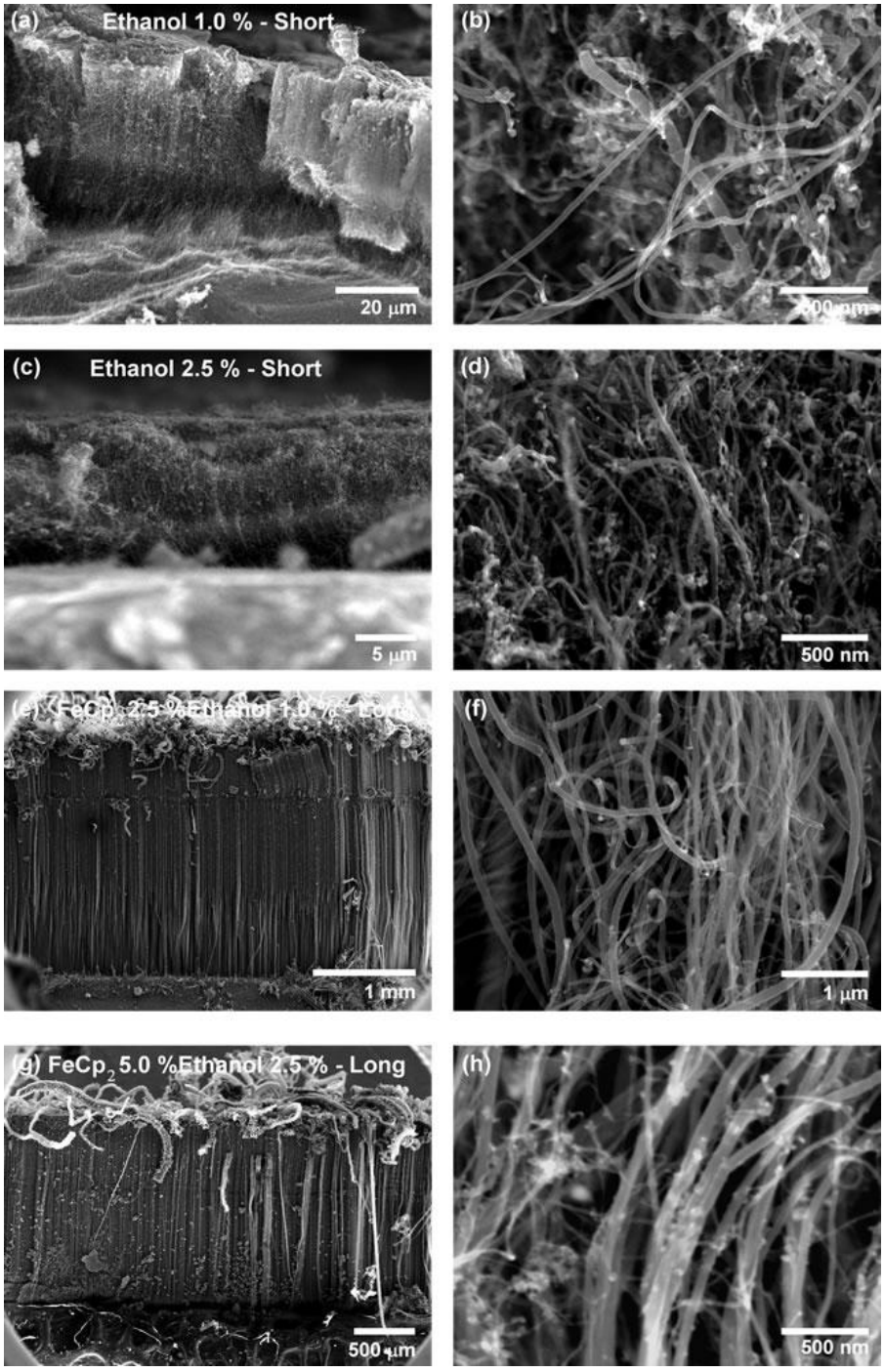

Figure 5.23: Scanning electron microscopy (SEM) images for ferromagnetic nanowires (Fe) inside multiwall carbon nanotubes functionalized with oxygen groups (CO_x) synthesized during 15 minutes and 3 hours. Samples synthesized during 15 minutes with **(a, b)** 1.0% by wt. ethanol and in **(c, d)** with 2.5% by wt. ethanol. Lower images were synthesized during 3 hours with in **(e, f)** $FeCp_2$ 2.5% and Ethanol 1.0 % by wt., and in **(g, h)** $FeCp_2$ 5.0% and Ethanol 2.5 % by wt.

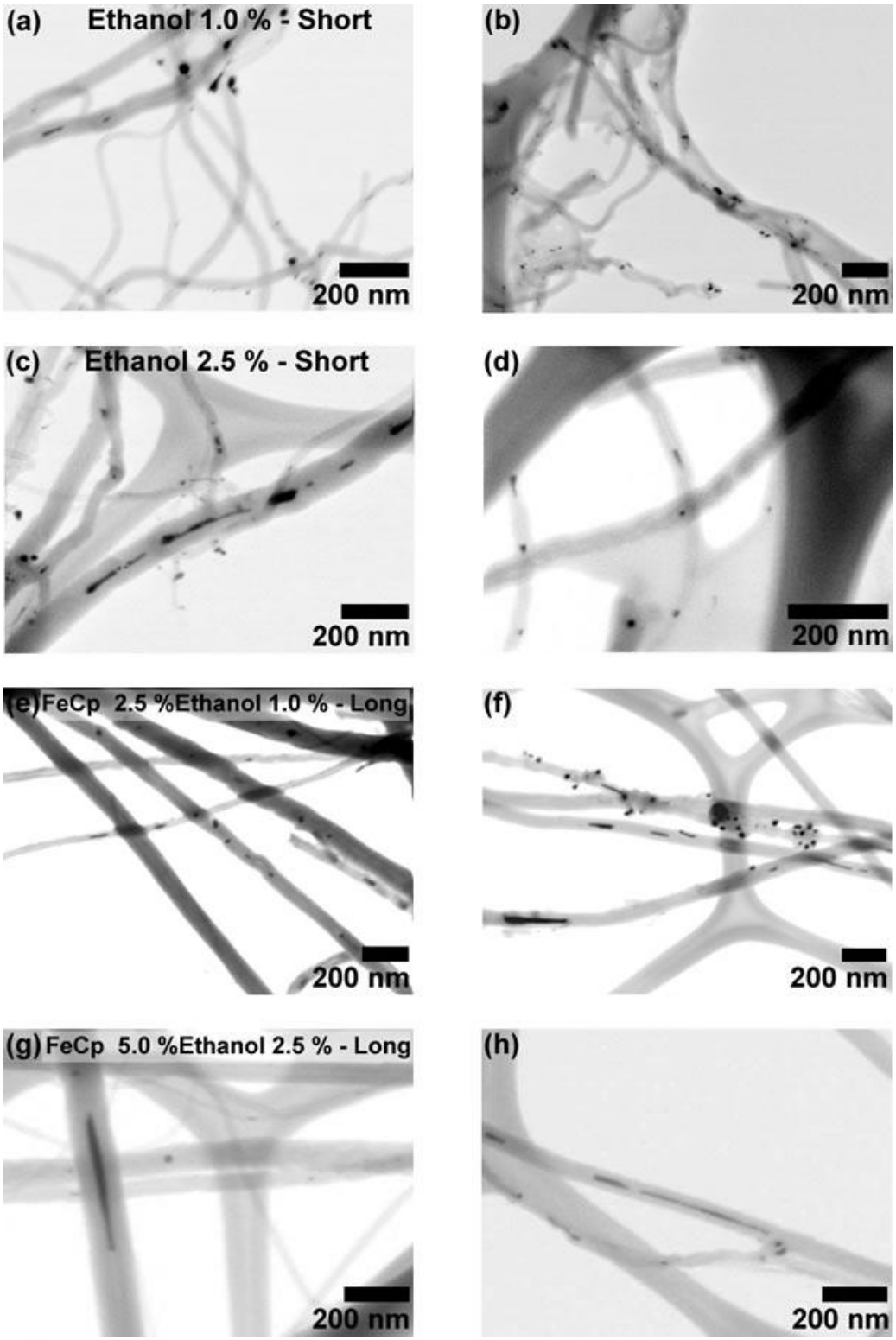

Figure 5.24: Scanning transmission electron microscopy images of the Fe nanopartices encapsulated in CO_x synthesized during 15 minutes and 3 hours. Samples synthesized during 15 minutes with **(a, b)** 1.0% by wt. ethanol and in **(c, d)** with 2.5% by wt. ethanol. Lower images were synthesized during 3 hours with **(e, f)** $FeCp_2$ 2.5% and Ethanol 1.0 % by wt., and in **(g, h)** with $FeCp_2$ 5.0% and Ethanol 2.5 % by wt.

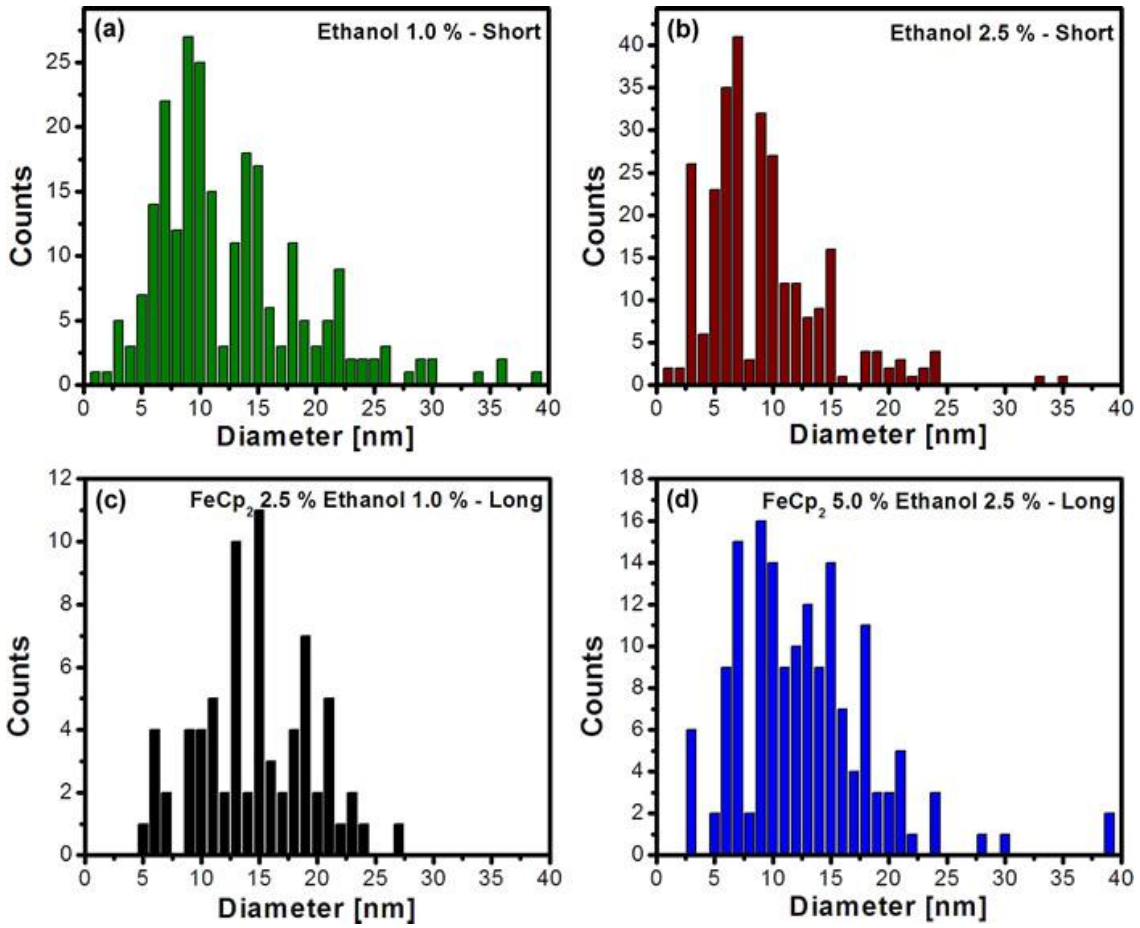

Figure 5.25: Diameter distribution of the CO_x synthesized during 15 minutes and 3 hours. Under different synthesis conditions: during 15 minutes with **(a)** 1.0% and **(b)** 2.5% by wt. of Ethanol and during 3 hours with **(c)** $FeCp_2$ 2.5% and Ethanol 1.0 % by wt., and in **(d)** $FeCp_2$ 5.0% and Ethanol 2.5 % by wt.

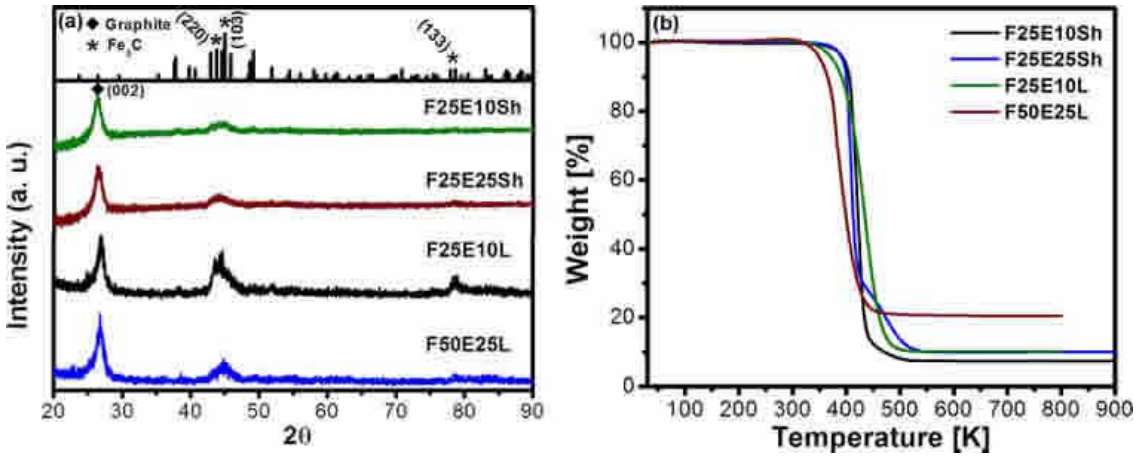

Figure 5.26: (a) X-ray powder diffraction patterns and **(b)** thermogravimetric analysis of ferromagnetic nanowires inside CO_x synthesized during 15 minutes (Sh) with 1.0% and 2.5% by wt. of ethanol and 3 hours (L) with $FeCp_2$ 2.5% and ethanol 1.0 % by wt. and $FeCp_2$ 5.0% and ethanol 2.5 % by wt.

From the XRD patterns we find that the short (F25E**Sh) and the long (F25E**L) CO_x samples have the characteristic (002) plane for carbon nanotubes and there is a presence of Fe_3C particles (Figure 5.26 a), this is more clear for the long CO_x with 2.5% by wt. of $FeCp_2$ (F25E10L). For the long CO_x F25E10L there is a characteristic peak for Fe_3C which is the plane (133) around 78 2θ. TGA results tell us that the short CO_x have an iron content of 5.14 and 6.98 % by wt. for ethanol at 1.0 and 2.5 % by wt. respectively, due to the height of the F25E25Sh forest we can think that they have a greater filling factor of Fe (Fe %/forest height) inside the carbon nanotubes. On the other hand, the long CO_x have 7.12 and 14.32 % by wt. of Fe inside F25E10 and F50E25 (Figure 5.26 b), respectively, this tendency is in accordance with the amount of ferrocene used, where a higher amount of ferrocene gives a greater content of Fe in the CNT sample. Surprisingly the long F25E10L has a greater content of Fe than the short F25E10Sh, this may be explained by a higher content of byproducts in the long CO_x, here we observed in SEM that the section of the nanotube on the top side of the forest has a greater amount of byproducts anchored on the wall of the CNTs.

The magnetic properties of powder samples of CO_x were measured, here they have a slightly larger coercivity, magnetic saturation and more square like (M_r/M_s) hysteresis curve at ethanol 1.0% by wt. (Figure 5.27 a, c and d) (H_c = 0.25 and M_r/M_s = .51), here the nanoparticle aspect ratio (length/diameter) 2.11 is slightly higher than with 2.5% by wt. of ethanol 2.08, explaining a slighter enhancement of the magnetic properties. The long CO_x coercivities do not change significantly between synthesis conditions (Figure 5.27 b) since the Fe nanowire dimensions are similar, however they present high values of coercivity c. a. 0.26 T, this might be explained by the combination of the low diameter and high content of nanowires. We also observe that the magnetic saturation is larger for the concentration $FeCp_2$ 5.0% by wt. where this a greater content of Fe in the sample as observed by TGA. The dimensions and magnetic properties of the studied samples are presented in the table 5.4.

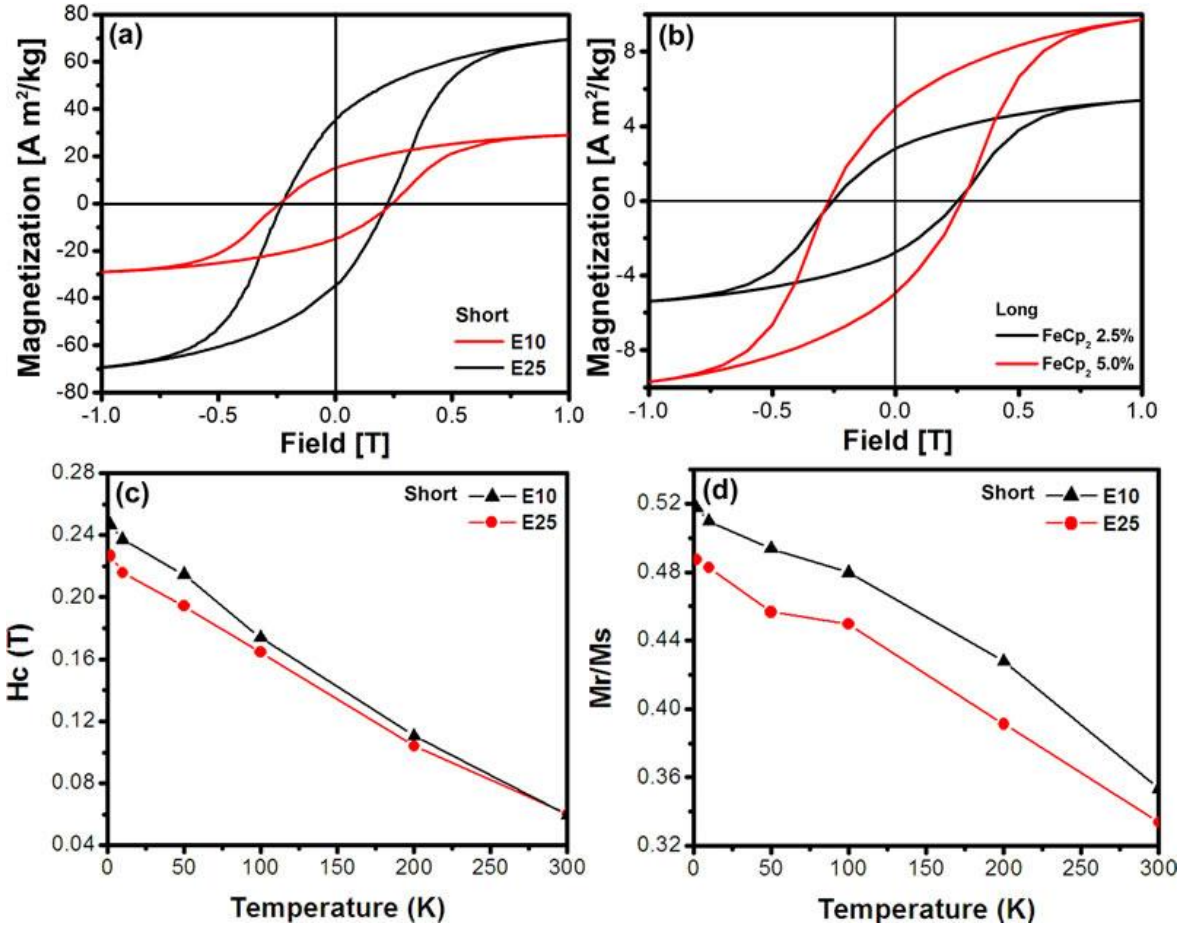

Figure 5.27: (a) Hysteresis curves for Fe_3C encapsulated in **(a)** short 1.0 and 2.5 % by wt. of ethanol, E10 and E25 respectively measured at 2 K, and **(b)** long CO_x (2.5 and 5.0 5 by wt. of ferrocene) measured at 5 K. Coercive fields (H_c) in **(c)** and normalized remanence magnetization (M_r/M_s) in **(d)** as a function of the temperature for short CO_x. Measurements were made with powder sample.

Table 5.4: Fe nanowires encapsulated in CO_x; average dimensions and magnetic properties. All values shown here were measured at 2 K.

	Temp (^oC)	Diameter (nm)	Length (nm)	H_c (T)	M_r/M_s
Short	E10	11.9	29.1	0.25	0.51
	E25	8.9	18.6	0.23	0.48
Long	F25	14.4	68	0.26	0.47
	F50	12.5	53.8	0.26	0.46

5.3.2.4 FeCo@MWNT

The SEM images of the MWNT forest morphology with FeCo nanowires show that when synthesized at 750 ^oC the CNTs are shorter (77 μm) and they are less aligned (Figure 5.28 a,b), all of these forests do not show any impurity layer on the surface of the CNTs, showing that all the magnetic material is encapsulated

inside the CNTs. The STEM images show that the particles are elongated (Figure 5.29) with different size distribution depending upon the synthesis temperature, our statistical analysis shows that for 800 ^{o}C the distribution is narrower and located at a smaller size (8.89 nm) (Figure 5.30 a).

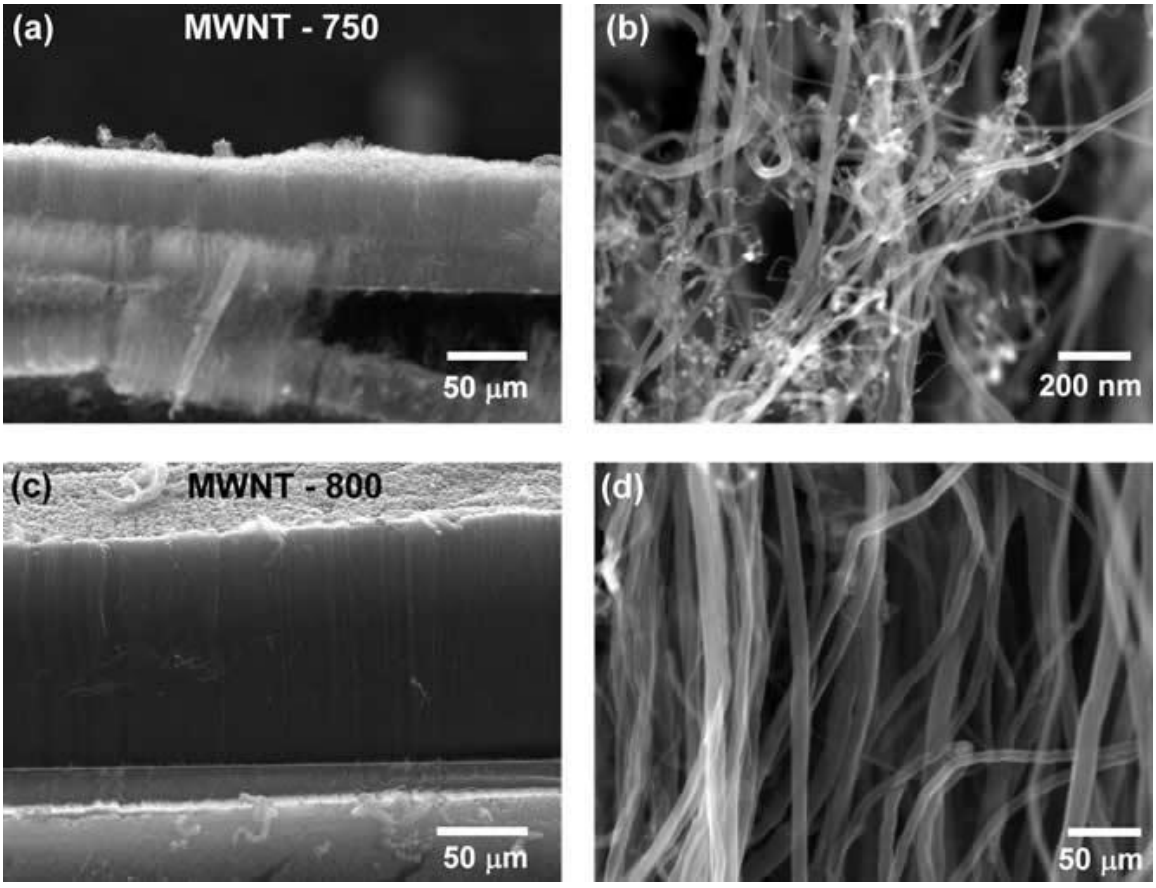

Figure 5.28: Scanning electron microscopy (SEM) images for ferromagnetic (FeCo) nanowires encapsulated inside multiwall carbon nanotubes, synthesized at **(a)** and **(b)** 750 and **(c)** and **(d)** 850 ^{o}C .

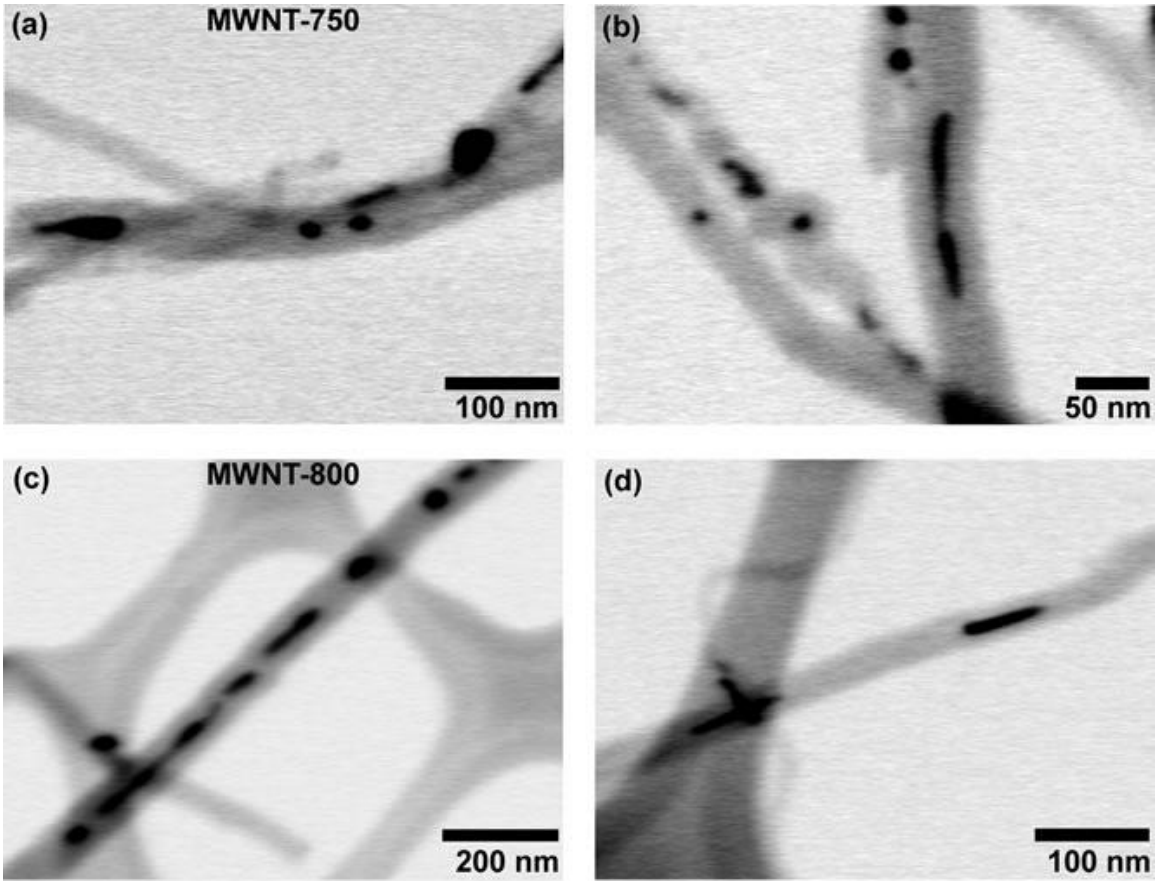

Figure 5.29: Scanning transmission electron microscopy images of the FeCo nanopartices encapsulated in MWNT synthesized at **(a,b)** 750 and **(c,d)** 800 ^{o}C.

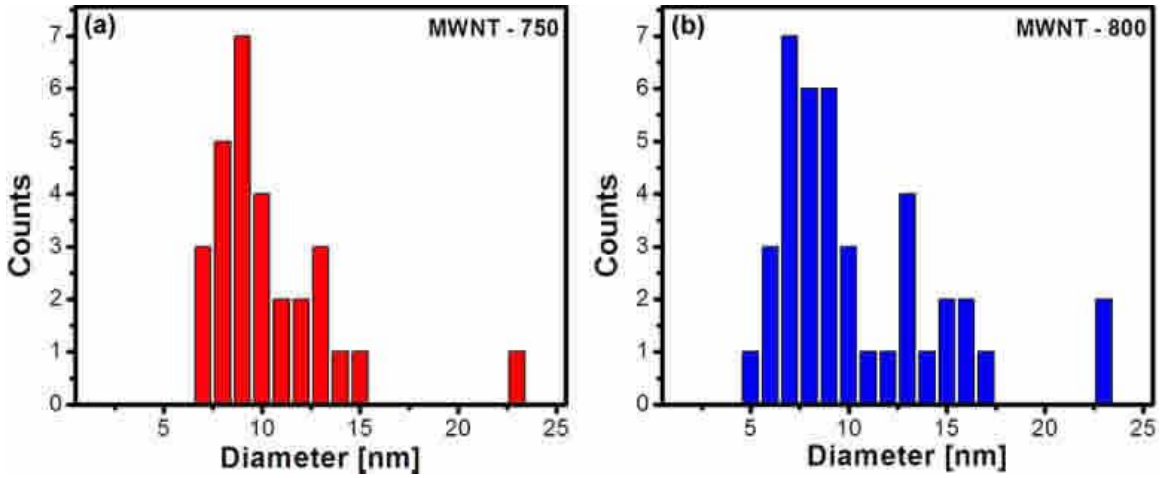

Figure 5.30: Diameter distribution of FeCo nanowires encapsulated in MWNT's. Under different synthesis temperatures: **(a)** 750 and **(b)** 800 ^{o}C. Notice that at 800 ^{o}C the diameter distribution is wider.

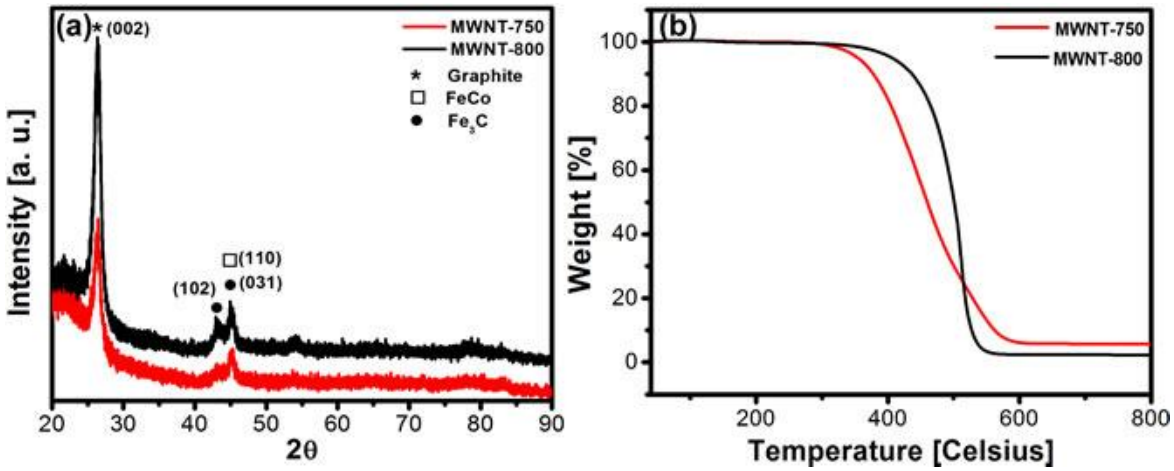

Figure 5.31: (a) X-ray powder diffraction patterns and **(b)** thermogravimetric analysis of ferromagnetic nanowires (FeCo) inside multiwall carbon nanotubes synthesized at 750 and 800 ^{o}C.

The XRD patterns of these samples show the characteristic (002) plane of carbon nanotubes along with two characteristic planes (102) and (031) for Fe_3C, however around 45 2θ the peak could also be associated to the plane (110) of FeCo (Figure 5.31 a). The plane (102) for Fe_3C is more intense for MWNT-800. The XRD shows the possibility of a mixture of Fe and FeCo nanowires in the samples. The TGA results clearly show that MWNT-750 suffers decomposition at a lower temperature than MWNT-800 and it has a higher content of metal inside the entire sample (Figure 5.31 b).

The magnetometry measurements give smooth hysteresis curves where MWNT-800 has a higher magnetic moment (Figure 5.32), perhaps due to a higher content of Fe_3C according to the XRD pattern (Figure 5.31 a) with more elongated nanowires (Table 5.5), although both samples present similar coercivities (0.12 T) and a slight difference in the squareness (M_r/M_s between 0.41 and 0.44), the measured values of the coercivity (0.12 T) are similar than those reported by A. L. Elías et al. [8], at room temperature it is larger (H_c = 0.09 T) than bulk FeCo (H_c = 0.07 T).

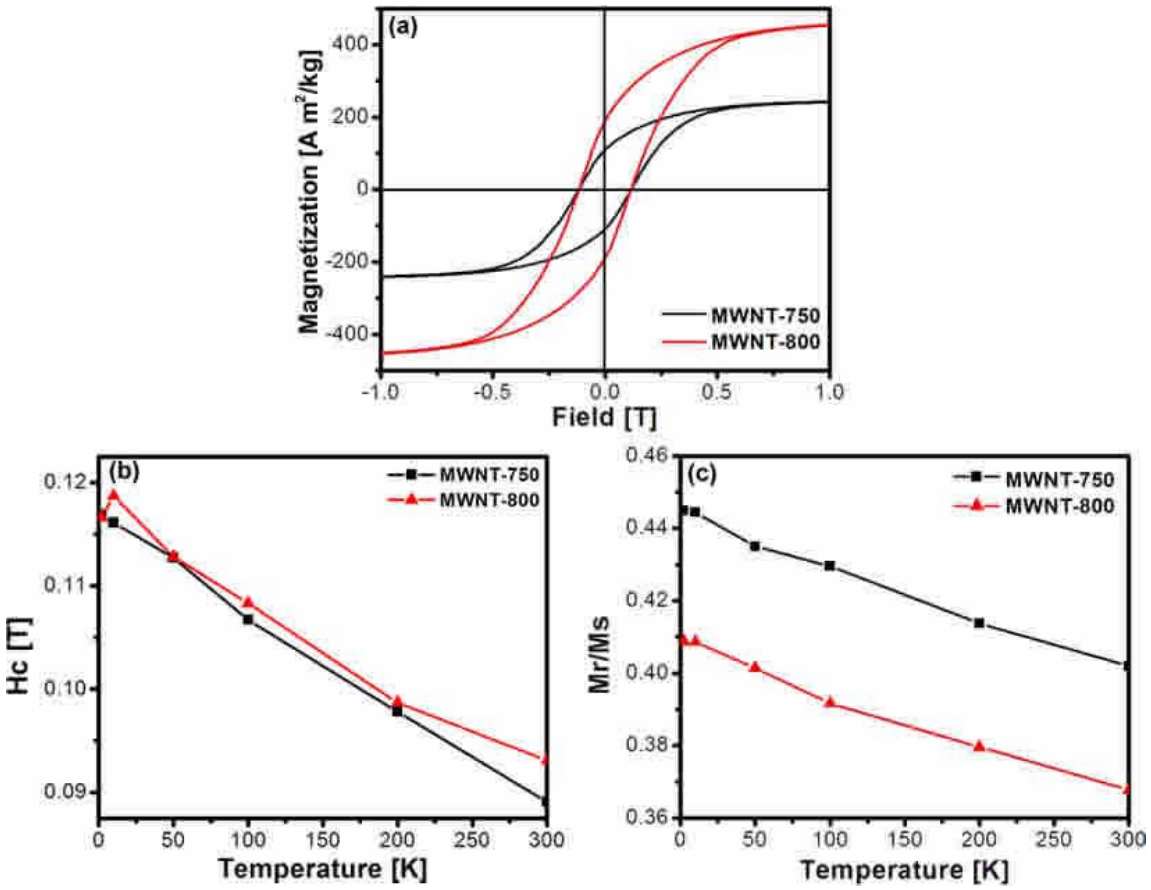

Figure 5.32: (a) Hysteresis curves for FeCo encapsulated in MWNT synthesized at 750 and 800 ^{o}C, measured at 2 K. Coercive fields (H_c) in **(b)** and normalized remanence magnetization (M_r/M_s) in **(c)** as a function of the temperature for all samples synthesized at 750 and 800 ^{o}C. Measurements were made with powder sample.

Table 5.5: FeCo nanowires encapsulated in MWNT; average dimensions and magnetic properties. All values shown here were measured at 2 K.

Temp (^{o}C)	Diameter (nm)	Length (nm)	H_c (T)	M_r/M_s
750	9.8	72.1	0.12	0.44
800	8.9	106.0	0.12	0.41

5.3.2.5 FeCo-CN_x

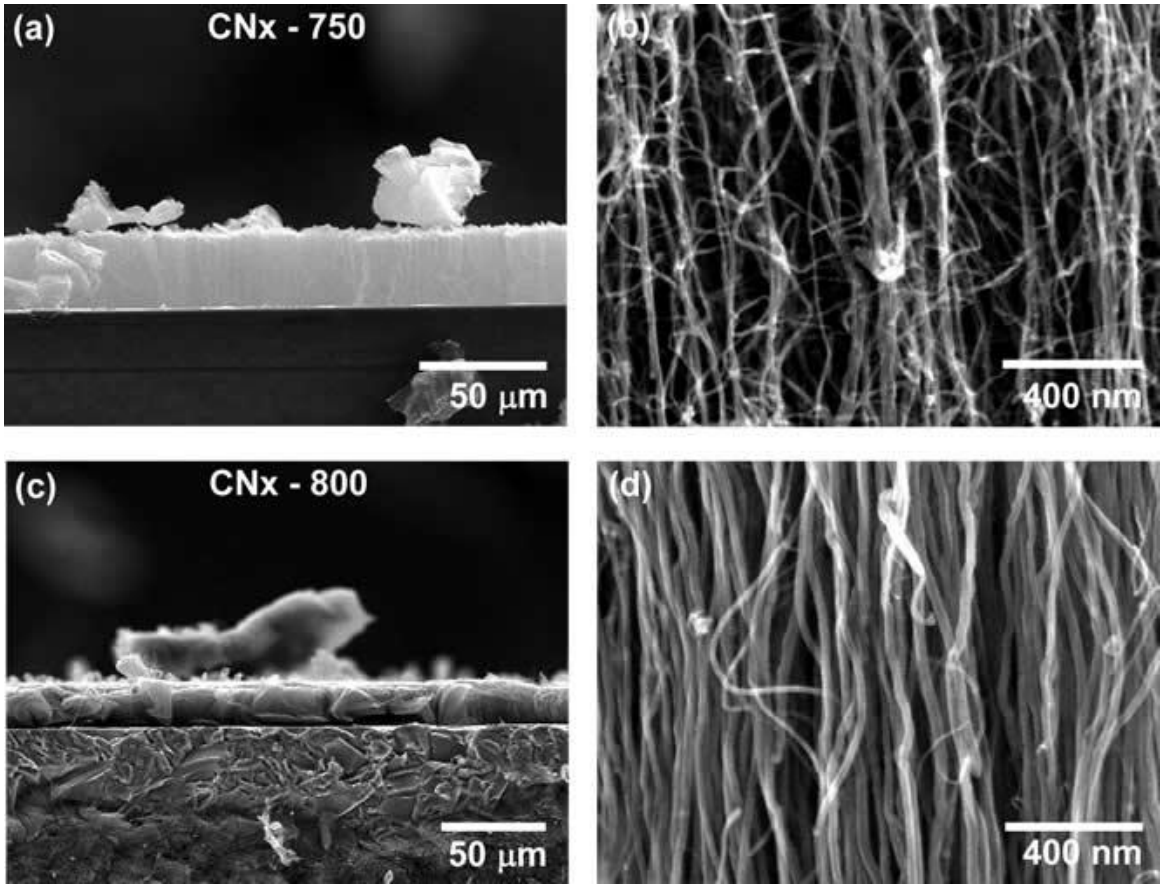

Figure 5.33: Scanning electron microscopy (SEM) images for ferromagnetic (FeCo) nanowires inside multiwall carbon nanotubes doped with nitrogen synthesized at **(a)** and **(b)** 750 and **(c)** and **(d)** 850 ^{o}C .

We observe from the SEM images that the CN_x forests have similar heights (c. a. 24 μm), although CN_x-750 is slightly taller (Figure 5.33), however this forest qualitatively shows a higher spacing between carbon nanotubes. The STEM images (Figure 5.34) along with the statistical analysis show that the nanowires have similar diameter (7.145 nm) and length (24.2 nm), (see Figure 5.35).

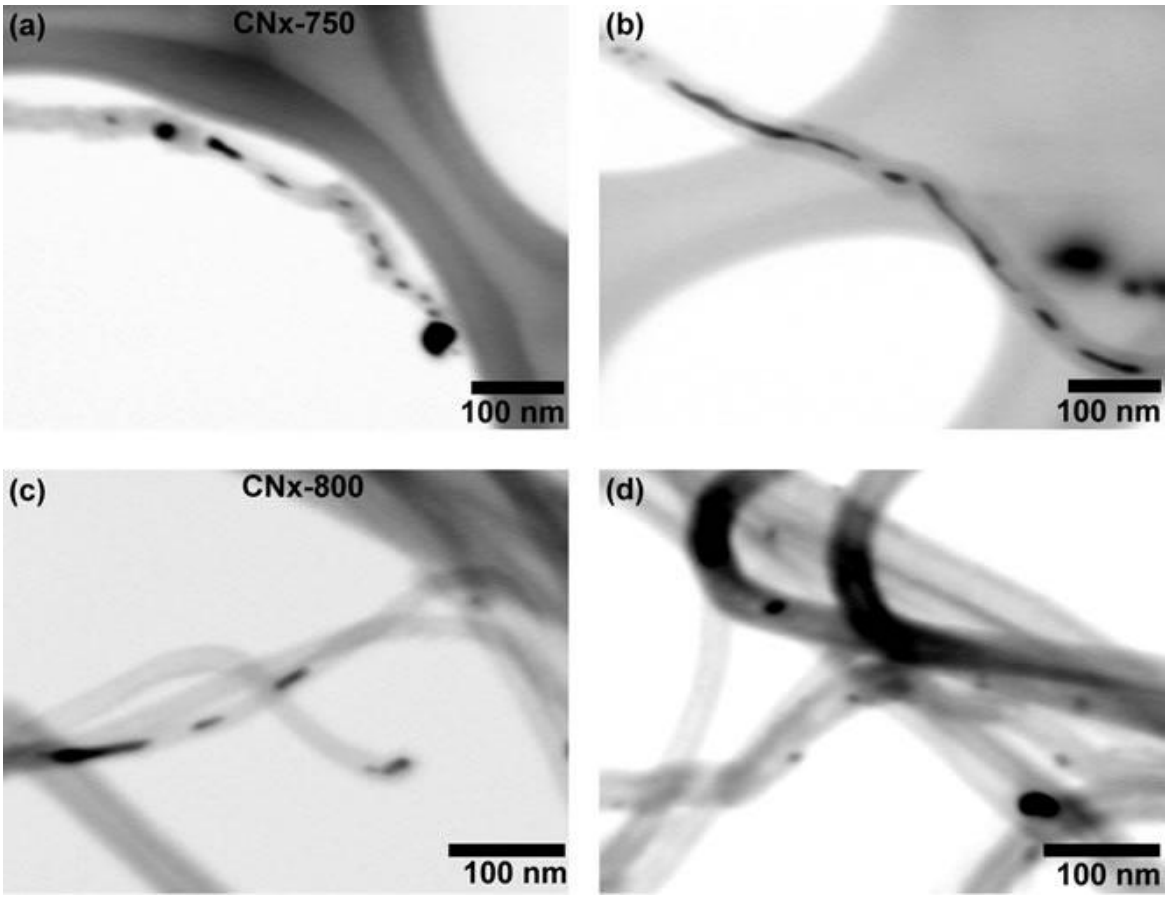

Figure 5.34: Scanning transmission electron microscopy images of the FeCo nanopartices encapsulated in CN_x synthesized at **(a,b)** 750 and **(c,d)** 800 ^{o}C.

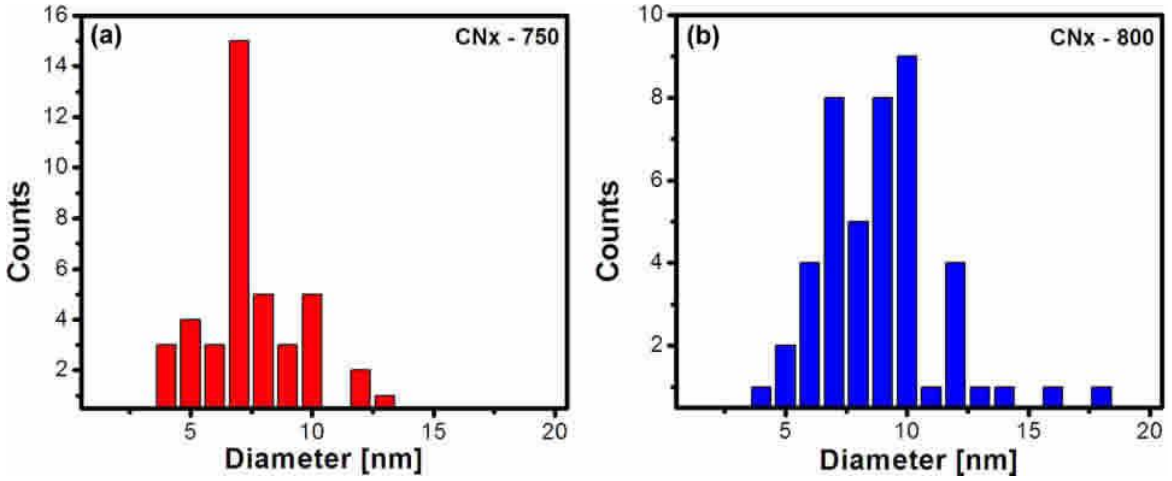

Figure 5.35: Diameter distribution of FeCo nanowires encapsulated in MWNT's under different synthesis temperatures: **(a)** 750 and **(b)** 800 ^{o}C.

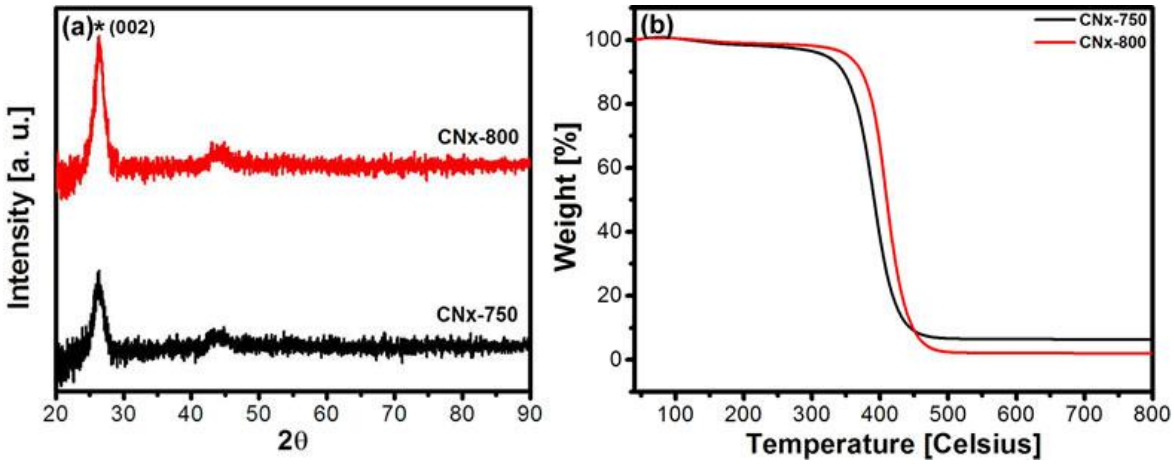

Figure 5.36: (a) X-ray powder diffraction patterns and **(b)** thermogravimetric analysis of ferromagnetic nanowires (FeCo) inside multiwall carbon nanotubes doped with nitrogen synthesized at 750 and 800 ^{o}C.

The XRD analysis shows the presence of a metallic material with a peak around 44 2θ that may be attributed to Fe_3C or FeCo, and it has the characteristic (002) plane for carbon nanotubes (Figure 5.36 a). From the TGA we observe that CN_x-800 has lower decomposition temperature and it has a higher content of metal inside the CNTs (Figure 5.36 b).

The magnetic properties measured by VSM show smooth hysteresis curves for both samples (Figure 5.37 a), were the samples synthesized at 800 ^{o}C have a greater magnetic moment, which may be explained by a higher content of ferromagnetic material. The coercivity is similar for both samples (0.095 T) (Table 5.6 and Figure 5.37 b), regarding the squareness there is a non linear behavior having a maximum at 50 K (Figure 5.37 c). The similarity of the magnetic properties is due to the similar nanoparticle dimensions.

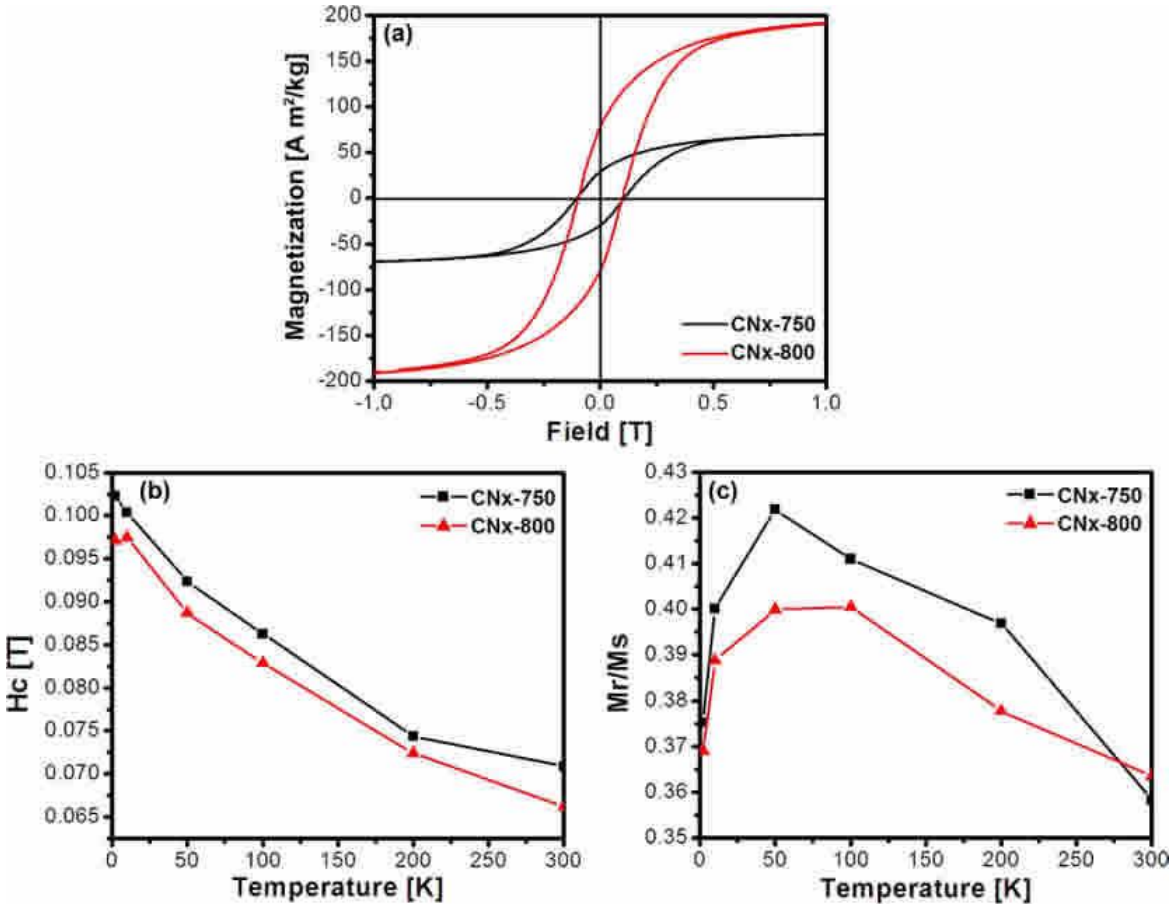

Figure 5.37: (a) Hysteresis curves for FeCo encapsulated in CN_x synthesized at 750 and 800 ^oC, measured at 2 K. Coercive fields (H_c) in **(b)** and normalized remanence magnetization (M_r/M_s) in **(c)** as a function of the temperature for all samples synthesized at 750 and 800 ^oC. Measurements were made with powder sample.

Table 5.6: FeCo nanowires encapsulated in CN_x; average dimensions and magnetic properties. All values shown here were measured at 2 K.

Temp (^oC)	Diameter (nm)	Length (nm)	H_c (T)	M_r/M_s
750	7.1	24.2	0.10	0.37
800	7.1	24.2	0.09	0.37

5.4 Conclusions

We have synthesized MWNT, CN_x and CO_x encapsulating ferromagnetic nanowires (Fe and FeCo) using chemical vapor deposition. In the case of Fe-MWNT, the chemical composition of ferromagnetic nanowires was controlled by monitoring the toluene in the pyrolysis process. We have obtained that when only ferrocene is used in the CVD method, the nanowires exhibit a coexistence of the α-Fe and Fe_3C phase and when toluene and ferrocene are used the ferromagnetic nanowires present the Fe_3C crystal structure. The measurements of magnetic

properties revealed large coercivities at low temperature, even larger than the corresponding to the bulk of the iron. These coercivities strongly depend on the Fe particles diameter, and are not affected by the length of the particles as shown by micromagnetic simulations and experimental magnetometry measurements. We also observed that at low synthesis temperature, the purity of the carbon nanotube is low (there is a lower coercive field and magnetic remanence).

Regarding the Fe-CN_x the nanowires also present a Fe_3C structure, here the measured magnetic properties show similar coercivity values as Fe-MWNT, which might be caused by the similarity in the diameter of the nanoparticle, however the length is significantly shorter for Fe-CN_x.

The Fe-CO_x samples present the highest coercivity among all the studied samples, specially the long CO_x, however the nanowires do not have the smallest diameter although these samples have the highest content of iron.

For the synthesis of FeCo-MWNT and FeCo-CN_x there is a possible mixture of Fe_3C and FeCo nanowires. We found that the magnetic properties of FeCo-MWNT are lower than Fe-MWNT, this same comparison happens for Fe-CN_x and FeCo-CN_x. However, for bulk Fe and FeCo, the alloy has a higher coercive field. When comparing the FeCo-MWNT and FeCo-CN_x they present similar magnetic properties, given that the diameters of the nanowires are alike, however their lengths are not.

The experimental results may present lower values than our simulations due to dipole interactions occurring between large aspect ratio magnetic particles, miss alignment of carbon nanotubes (i. e. tilted or curved CNTs). Although the importance of the nanoparticle dimensions is predominant in experimental and simulation results, in both cases when having lower diameter nanowires the coercive field increased. Therefore, the length of the particles may have a significant effect, although our results indicate it has a small value almost negligible upon the magnetic properties of magnetic nanowires. However, in the case of very elongated nanowires in CO_x (length > 50 nm), there are high coercivities. Other factors such as aspect ratio, magnetic material content, chemical composition of the magnetic nanowires and degree of alignment of the carbon nanotubes may also influence the magnetic properties.

These findings suggest that in order to produce a magnetic recording device short and well aligned carbon nanotubes with thin nanowires (i. e. 5 nm diameter and 25 nm long) would be a good candidate for these applications.

5.5 References

1. *Synthesis of carbon nanotubes containing metal oxides and metals of the d-block and f-block transition metals and related studies.* **Y. K. Chen, A. Chu, J. Cook, M. L. H. Green, P. J. F. Harris, R. Heesom, M. Humphries, J. Sloan, S. C. Tsang, J. F. C. Turner.** 1997, J. Mater. Chem., Vol. 7, pp. 545-550.

2. *Opening carbon nanotubes with oxygen and implications for filling.* **P. M. Ajayan, T. W. Ebbesen, . Ichihashi, S. Ijima, K. Tanigaki, H. Hiura.** 1993, Nature, Vol. 362, pp. 522-525.

3. *Nickel nanowires of 4 nm diameter in the cavity of carbon nanotubes.* **B. K. Pradhan, T. Kyotani, A. Tomita.** 1999, Chem. Commun., pp. 1317-1318.

4. *Enhanced magnetic coercivities in Fe nanowires.* **N. Grobert, W. K. Hsu, Y. Q. Zhu, J. P. Hare, H. W. Kroto, D. R. M. Walton, M. Terrones H. Terrones, Ph. Redlich, M. Rühle, R. Escudero, F. Morales.** 1999, Appl. Phys. Lett., Vol. 75, pp. 3363-3365.

5. *Magnetic properties of aligned Fe-filled carbon nanotubes.* **T. Mül, D. Elefant, A. Graff, R. Kozhuharova, A. Leonhardt, I. Mönch, M. Ritschel, P. Simon, S. Groudeva-Zotova, C. M. Schneider.** 2003, J. Appl. Phys. 93, pp. 7894-7896.

6. *Preparation and characteristics of carbon nanotubes filled with cobalt.* **S. Liu, J. Zhu, Y. Mastai, I. Felner, A. Gedanken.** 2000, Chem. Mater., Vol. 12, pp. 2205-2211.

7. *Cu-filled carbon nanotubes by simultaneous plasma-assisted copper incorporation.* **G. Y. Zhang, E. G. Wang.** 2003, Appl. Phys. Lett., Vol. 82, pp. 1926-1928.

8. *Production and characterization of single-crystal FeCo nanowires inside carbon nanotubes.* **A. L. Elías, J. A. Rodríguez-Manzo, M. R. McCartney, D. Golberg, A. Zamudio, S. E.Baltazar, F. López-Urías, E. Muñoz-Sandoval, L. Gu, C. C. Tang, D. J. Smith, Y. Bando, H. Terrones, M. Terrones.** 2005, Nano Lett., Vol. 5, pp. 467-472.

9. *Carbon nanotube synthesis in supercritical toluene.* **D. C. Lee, F. V. Mikulec, B. A. Korgel.** 2004, J. Am. Chem. Soc., Vol. 126, pp. 4951-4957.

10. *Alloy nanowires: Invar inside carbon nanotubes.* **N. Grobert, M. Mayne, M. Terrones, J. Sloan, R.E. Dunin-Borkowski, R. Kamalakaran, T. Seeger, H. Terrones, M. Rühle, D.R.M. Walton, H.W. Kroto, J.L. Hutchison.** 2001, Chem. Commun., Vol. 5, pp. 471-472.

11. *Thinning and opening of carbon nanotubes by oxidation using carbon dioxide.* **S. C. Tsang, P. J. F. Harris, M. L. H. Green.** 1993, Nature, Vol. 362, pp. 520-522.

12. *Self-organized Fe nanowire arrays prepared by shadow deposition on NaCl(110) templates.* **A. Sugawara, T. Coyle, G. G. Hembree, M. R. Scheinfein.** 1997, Appl. Phys. Lett., Vol. 70, pp. 1043-1045.

13. *Magnetic properties and magnetization reversal of -Fe nanowires deposited in alumina film.* **Y. Peng, H.-L. Zhang, S.-L. Pan, H.-L. Li.** 2000, J. Appl. Phys., Vol. 87, pp. 7405-7408.

14. *Preparation and magnetic property of Fe nanowire array.* **S. Yang, H. Zhu, D. Yu, Z. Jin, S. Tang, Y. Du.** 2000, J. Mag Mag. Mater. , Vol. 222, pp. 97-100.

15. *Magnetic texture in iron nanowire arrays.* **J. B. Wang, X. Z. Zhou, Q. F. Liu, D. S. Xue, F. S. Li, B. Li, H. P. Kunkel, G. Williams.** 2004, Nanotech. 15 (2004) 485, Vol. 15, pp. 485-489.

16. *Fabrication and magnetic properties of ultrathin Fe nanowire arrays.* **X. Y. Zhang, G. H. Wen, Y. F. Chan, R. K. Zheng, X. X. Zhang, N. Wang.** 2003, Appl. Phys. Lett., Vol. 83, pp. 3341-3343.

17. *Enhanced magnetism in Fe-filled carbon nanotubes produced by pyrolysis of ferrocene.* **A. Leonhardt, M. Ritschel, D. Elefant, N. Mattern, K. Biedermann, S. Hampel, Ch. Müller, T. Gemming, B. Büchner.** 2005, J. Appl. Phys. , Vol. 98, p. 074315.

18. *Synthesis, properties, and applications of ferromagnetic-filled carbon nanotubes.* **A. Leonhardt, S. Hampel, C. Müller, I. Mönch, R. Koseva, M. Ritschel, D. Elefant, K. Biedermann, B. Büchner.** 2006, Chem. Vap. Deposition, Vol. 12, pp. 380-387.

19. *Magnetism in Fe-based and carbon nanostructures: Theory and applications.* **H. Terrones, F. López-Urías, E. Muñoz-Sandoval, J.A. Rodríguez-Manzo, A. Zamudio, A.L. Elías, M. Terrones.** 2006, Solid State Sciences, Vol. 8, pp. 303-320.

20. *Oxidation characteristics and magnetic properties of iron carbide and iron ultrafine particles.* **X. Q. Zhao, Y. Liang, Z. Q. Hu, B. X. Liu.** 1996, J. Appl. Phys., Vol. 80, pp. 5857-5860.

21. *Laser pyrolysis fabrication of ferromagnetic -Fe4N and FeC nanoparticles.* **C. A. Grimes, D. Qian and E. C. Dickey, J. L. Allen, P. C. Eklund.** 2000, J. Appl. Phys., Vol. 87, pp. 5642-5644.

22. *Magnetic properties of Fe deposited into anodic alumina oxide pores as a function of particle size.* **D. AlMawlawi, N. Coombs, M. Moskovits.** 1991, J. Appl. Phys., Vol. 70, pp. 4421 – 4425.

23. *Structure and magnetic properties of ferromagnetic nanowires in self-assembled arrays.* **H. Zeng, R. Skomski, L. Menon, Y. Liu, s. Bandyopadhyay, D. J. Sellmyer.** 2002, Phys. Rev. B, Vol. 65, p. 134426.

24. *Magnetic properties of self-assembled Co nanowires of varying length and diameter.* **H. Zeng, M. Zheng, R. Skomski, D. J. Sellmyer, Y. Liu, L. Menon, S. Bandyopadhyay.** 2000, J. Appl. Phys., Vol. 87, pp. 4718-4720.

25. *Modelling hysteresis of interacting nanowires arrays.* **M. Vázquez, K. Nielsch, P. Vargasc, J. Velázquez, D. Navasa, K. Pirota, M. Hernández-Vélez, E. Vogel, J. Cartes, R.B. Wehrspohn, U. Gosele.** 2004, Physica B 343, Vol. 343, pp. 395–402.

26. *Patterned magnetic nanostructures and quantized magnetic disks.* **Chou., S. Y.** 1997, Proc. IEEE , Vol. 85, pp. 652-671.

27. *Single-domain magnetic pillar array of 35 nm diameter and 65 Gbits/in.2 density for ultrahigh density quantum magnetic storage.* **S. Y Chou, M. S. Wei, P. R. Krauss, P. B. Fischer.** 1997, J. Appl. Phys., Vol. 76, pp. 6673-6675.

28. *Applications of magnetic nanoparticles in biomedicine.* **Q. A. Pankhurst, J. Connolly, S. K. Jones J. Dobson.** 2003, J. Phys. D: Appl. Phys. , Vol. 36, pp. 167-181.

29. *A novel polyacrylamide magnetic nanoparticle contrast agent.* **B. A. Moffat, G. R. Reddy, P. McConville, D. E. Hall.** 2003, Molecular Imaging ., Vol. 2, pp. 324-332.

30. *Carbon nanotubes produced by aerosol pyrolysis: growth mechanisms and post-annealing effects.* **M. Pinault, H. Mayne-L'Hermite, C. Reynaud, O. Beyssac, J.N. Rouzaud, C. Clinard.** 2004, Diamond Relat. Mater., Vol. 13, pp. 1266-1269.

31. *Growth of multiwalled carbon nanotubes during the initial stages of aerosol-assisted CCVD.* **M. Pinault, H. Mayne-L'Hermite, C. Reynaud, C. Pichot, P. Launois, D. Ballutad.** 2005, Carbon, Vol. 43, pp. 2968-2976.

32. *Novel nanoscale gas containers: encapsulation of N2 in CNx nanotubes.* **M. Terrones, R. Kamalakaran, T. Seeger, M. Rühle.** 2000, Chem. Commun., pp. 2335–2336.

33. *Controlling the dimensions, reactivity and crystallinity of multiwalled carbon nanotubes using low ethanol concentrations.* **A. Botello-Méndez, J. Campos-Delgado, A. Morelos-Gómez, J. M. Romo-Herrera, A. G. Rodríguez, H. Navarro, M. A. Vidal, H. Terrones, M. Terrones.** 2008, Chem. Phys. Lett., Vol. 453, pp. 55–61.

34. *OOMMF User'Guide, version 1.0, Interagency Report NISTIR 6376, Gaithersburg, MD (2004).* **M. J. Donahue, D. G. Porter.**

35. *Reversal modes in arrays of interacting magnetic Ni nanowires: Monte Carlo simulations and scaling technique.* **M. Bahiana, F. S. Amaral, S. Allende, D. Altbir.** 2006, Phys. Rev. B, Vol. 74, p. 174412.

36. *Magnetization reversal process and magnetic relaxation of self-assembled Fe3Pt nanowire arrays with different diameters: Experiment and micromagnetic simulations.* **J. -H. Gao, D. -L. Sun, Q. -F. Zhan, W. He, Z. -H. Cheng.** 2007, Phys. Rev. B, Vol. 75, p. 064421.

37. *Magnetic behavior of iron-filled multiwalled carbon nanotubes.* **S. Karmakar, S. M. Sharma, M. D. Mukadam, S. M. Yusuf, A. K. Sood.** 2005, J. Appl. Phys. , p. 054306.

38. *Incremental analysis of the magnetization behavior in iron-filled carbon nanotube arrays.* **C. Müller, D. Elefant, A. Leonhardt, B. Büchner.** 2008, J. Appl. Phys. , Vol. 103, p. 034302.

39. *Structure and magnetic properties of iron nanowires encased in multiwalled carbon nanotubes.* **A. Shpak, S. Kolesnik, G. Mogilny, Y. Petrov, V. Sokhatsky, L. Trophimova, B. Shanina, V. Gavriljuk.** 2007, Acta Materialia, Vol. 55, pp. 1769-1778.

40. *In situ synthesis and magnetic anisotropy of ferromagnetic buckypaper.* **R. Lv, S. Tsuge, X. Gui, K. Takai, F. Kang, T. Enoki, J. Wei, J. Gu, K. Wang, D. Wu.** 2009, Carbon, Vol. 47, pp. 1141-1145.

41. *Magnetism of Fe, Co and Ni nanowires.* **D. J. Sellmyer, M. Zheng, R. Skomski.** 2001, J. Phys.: Condens. Matter, Vol. 13, pp. 433-460.

42. *Hysteresis in magnetism for physicist, materials scientists and engineers.* **Bertotti, Giorgio.** Torino, Italy : Academic Press, 1998.

43. *Modern Magnetic Materials: Principles and Applications.* **Principles, R. C. O'Handley R C 2000 Modern Magnetic Materials:.** s.l. : Weinheim: Wiley-VCH, 2000.

44. **M. J. Donahue and D. G. Porter, OOMMF User'Guide, version 1.0, Interagency Report NISTIR 6376, Gaithersburg, MD (2004).**

45. *Approach to fabricating Co nanowire arrays with perpendicular anisotropy: Application of a magnetic field during deposition.* **S. Ge, C. Li, X. Ma, W. Li, L. Xi, C. X. Li.** 2001, J. Appl. Phys., Vol. 90, pp. 509-511.

46. *Electrodeposition and room temperature ferromagnetic anisotropy of Co and Ni-doped ZnO nanowire arrays.* **J. B. Cui, U. J. Gibson.** 2005, Appl. Phys. Lett., Vol. 87, p. 133108.

6. Conclusions and Perspectives

6.1 Contributions

One of the objectives of nanoscience and nanotechnology is the use of nanostructures as building blocks in order to create new materials. For this purpose, self-assembly is widely used by many researchers giving new materials with interesting properties. In this work we have studied two nanosystems: carbon inverse opal and carbon nanotube forests.

6.1.1 Carbon inverse opal

Carbon inverse opal (CIO) is of interest due to its high surface area and the ordering of the pores allows it to behave as a photonic crystal (see chapter 2 and 3). First, we synthesized and characterized carbon inverse opal via chemical vapor deposition (CVD) and solution based infiltration. All samples produced by CVD gave thin layers of carbon on the surface of the silica nanoparticles, these layers were thin enough in order to preserve certain optical transmission of the entire sample when immersed in chloroform. When the solution based infiltration was used we observed different levels of infiltration giving thin layers of carbon or a completely filled opal. Next, we doped the carbon inverse opal with different contents of nitrogen, here the pyrazine concentration was varied for synthesis in order to obtain different nitrogen concentrations in our carbon material. When using a higher content of pyrazine there was an increase of the carbon structural ordering reflected in the I_D/I_G for 10 and 100 nm pore size, however with 300 nm pore size there was a decrease of ordering; also the (002) interplanar distance decreases. Further on, the thermal decomposition temperature slightly increases when introducing pyrazine in the synthesis.

This doping was used for carbon inverse opal with pore sizes of 10, 100 and 300 nm. Regarding the materials with 300 nm, the fcc ordering of the pores allows is it to present a photonic band gap, at the same time the nitrogen doping of this material altered the photonic band gap blue-shifting it to certain maximum value (see chapter 3).

Further on, in order to have a better understanding of the effect of nitrogen doping we studied the physical properties of CIO doped with different contents of

nitrogen; here we studied resistivity, magnetoresistance, magnetization and we made preliminary measurements of field emission, along with this vapor sensing and photoconductivity tests were realized.

Our resistivity measurements show that the introduction of nitrogen in the CIO decreases its resistance from 0.30 to 0.02 Ω cm, however afterwards it increases up to 0.69 Ω cm, possibly due to a higher degree of structural disorder. It was clear that around 150 K, there is a change in the conduction mechanism of all studied samples (chapter 4). For temperatures below 150 K all the nitrogen doped samples exhibit variable range hopping (VRH) in 1-D, 2-D or 3-D, however the undoped carbon material did not exhibit any characteristic VRH this may be attributed to a higher structural disorder.

The magnetoresistance (MR) measurements also show a transition of the properties of the undoped and nitrogen doped carbon inverse opal, although around 50 K. At temperatures below 50 K all samples exhibit a positive MR, were the nitrogen doped samples exhibit higher values. This positive MR may be caused by electron-electron interactions, along with this we propose two mechanisms: 1) localization of electron at or around the nitrogen atoms that become more fixed at higher magnetic fields, 2) the electrons may also be trapped in ring currents around the periphery of the pores [1] thus increasing the resistivity at higher magnetic fields. For temperatures above 50 K we observed a less symmetric and negative MR, here the MR values of the nitrogen doped and doped materials are similar, the negative MR was attributed to weak localization.

When measuring the magnetic properties of CIO, we observed a transition in its properties around 100 K, below this temperature all nitrogen doped and undoped samples exhibit a paramagnetic response and above mentioned temperature there is a gradual transition towards a diamagnetic behavior. The paramagnetic behavior at low temperature was attributed to the formation of ring currents and localization of electrons at higher order carbon rings (these rings induce curvature in the structure). The pore size heavily defines the magnetic transition (paramagnetic/diamagnetic) temperature, with a smaller pore size this temperature is higher, and along with this the magnetization is higher. The introduction of nitrogen in the system gave lower magnetization values, possibly due to a higher content of electrons in the system allowing a higher interaction between the magnetic moments. We found that the magnetic transition temperature is more sensitive to the pore size than the introduction of nitrogen in the system.

The physical properties (resistance and magnetic) of the studied carbon inverse opal change around 50 K. When held at low temperatures (below 50 K), we believe that the material tends to localize electrons near the curvature sites thus increasing resistivity and magnetization. We observed that the resistivity increases with the introduction of nitrogen, however the magnetization of the material decreases. We conclude that the degree of order in the structure significantly determines the electrical and magnetic properties of mesoporous carbon materials.

Vapor gas sensing experiments reveal that nitrogen doped carbon inverse opals have a greater response compared with the undoped counterparts, this was more pronounced in the case of chloroform. Surprisingly, some tests with highest content of nitrogen exhibited an opposite response, for example a decrease in resistivity was observed instead of an increase (as shown for the other samples). It was clear that the carbon inverse opal with 300 nm pore size exhibited a greater response than the 100 nm pore size materials. On the other hand, the photoconductivity measurements reveal that the porous carbons with 100 nm pore size exhibit a higher decrease in its resistivity when exposed to a flash of light, compared with the 300 nm pore size samples.

6.1.2 Encapsulated magnetic nanowires inside carbon nanotubes

We have studied the magnetic properties of MWNT, CN_x and CO_x encapsulating ferromagnetic nanoparticles (Fe and FeCo). Overall, our simulations and experimental studies reveal that the dimensions of the nanowires is important in order to determine the magnetic properties, specifically we found that with lower diameter the coercivity is increased, despite the length of the nanowires. We also observed that the misalignment of the carbon nanotubes (i. e. tilted or curved CNTs), dipole interaction between the magnetic nanowires, magnetic material content, chemical composition of the nanowires may influence the magnetic properties.

Particularly, in the case of Fe-MWNT we observed that the thermolysis with only ferrocene may favor the coexistence of α-Fe and Fe_3C, where possibly the Fe_3C is a thin layer surrounding the α-Fe, however when toluene and ferrocene are used in the CVD method the nanowires exhibit an Fe_3C phase. The experimental magnetic measurements reveal the coercivities strongly depend on the Fe nanowire's diameter, and do not exhibit strong length dependency.

For the Fe-CN_x system the magnetic properties exhibit coercive field values similar as the Fe-MWNT, this can be due to the similarity of the nanowire diameter, however the length of the nanowires are shorter. When analyzing Fe-CO_x, these present the highest coercivities among all the studied sample, this can be due to the greater content of iron in the sample, however the nanowires do not exhibit the lowest diameter.

The FeCo nanowires encapsulated in MWNT and CN_x exhibit a mixture between Fe_3C and FeCo nanowires. The obtained magnetic properties for FeCo-CNT are lower than Fe-CNT, this is for both cases of MWNT and CN_x, this is surprising since in the bulk FeCo has a greater coercivity than Fe. Due to the similarity between the dimensions of the nanowires in FeCo-MWNT and FeCo-CN_x, the observed magnetic properties are alike.

6.2 Future work

6.2.1 Carbon inverse opal

Preliminary experiments of carbon shells shown in chapter 2 are of interest and they may be studied due to following possibilities:

1) Synthesis of boron doped carbon inverse opal may also be of interest because it may introduce a p-type doping, thus modifying its structural and therefore electrical properties [2; 3].
2) A higher surface area, since the interstitial spaces between the initial silica particles are not filled, and it resembles a bicontinuos surface in which one region can be filled with material A and the other region with a material B, where both materials will never be in contact. These shells may also be doped with nitrogen, boron or other elements in order to provide interesting properties.
3) The possibility of encapsulating other nanostructures inside of these shells may be of interest. For example, metallic or semiconductor nanoparticles may be anchored on the carbon walls in order to be applied in energy storage or solar cells.

If larger pores are used, then these materials may be used as a 3D bio-scaffold, this may be enhanced by nitrogen doping along with the anchoring of specific biomolecules that enhance cell growth.

In order to have a better understanding of the studied material theoretical studies may be pursued in order to elucidate the origin of the changes in the optical properties due to doping of carbon. In a similar manner the magnetic properties may also be studied, however in order to have a better understanding, closer to experimental characterization, the studied system may present co-defect, meaning that it may be doped (for example with nitrogen) and at the same time the introduction of carbon rings different than six member, the latter may be a Stone–Wales transformation or the introduction of curvature. The study of ring currents in porous carbon may be of interest in order to understand better how to obtain a more paramagnetic or even ferromagnetic carbon material, this could be seen in the concept of pore size, to elucidate at what pore size will there be a more ferromagnetic or paramagnetic behavior.

Sensors are of great interest in order to detect the presence of toxic or explosive molecules that may be present in a determined environment; therefore the use of materials with high surface area may give a better response. Therefore further experimental and theoretical studies of mesoporous carbons as sensors could lead to more reliable sensors, perhaps the introduction of specific molecules or nanoparticles on the surface of the carbon walls may enhance the sensing application [4; 5; 6]. The theoretical study of co-defects (doping and carbon rings different than six member) may also be studied to pursue an enhancement of reactivity or molecule sensing.

The higher degree of conductivity of the carbon inverse opal may be exploited as an electrode for photovoltaic devices, the pores may be used as reservoirs for photosensitive molecules or nanoparticles, thus having a greater surface area to harvest solar radiation.

6.2.2 Encapsulated magnetic nanowires inside carbon nanotubes

Since there is a better understanding of the magnetic properties of iron nanoparticles encapsulated in carbon nanotubes, an approximation of a magnetic recording device based on a pattern of this nanostructured system may be tested. In average, if we consider each CNT as a bit with 62 nm diameter, each magnetic nanowire to have 14.6 diameter and the CNT will be separate between each other with a distance of 83 nm (these numbers were obtained by averaging obtained results in chapter 5), therefore a density of 39 Tb/m^2 (25 $Gb/inch^2$) can be obtained, if we consider a compact array of CNT with no separation between them

we may obtain 170 Tb/m^2 (110 Gb/$inch^2$), however current research with magnetic granular media can obtain 10 nm grains with 1.5 Pb/m^2 (~1 Tb/$inch^2$) [7; 8].

Interestingly nanostructured FePt and CoPt may present higher coercivities than nanostructured Fe, obtaining values around 0.9 T - 2 T for FePt [9; 10; 11] and 0.8 T for CoPt [12]. Therefore, a better study of these alloys encapsulated in carbon nanotubes is of interest in order to search for a system with the best magnetic properties for determined applications.

The studied magnetic systems (Fe@CNT) are of interest in medicine for biotargeting, other studies of biocompatibility [13], chemistry [14; 15] and pharmacology [16] of carbon nanotubes may be joined with Fe@CNT for applications in drug delivery, magnetic resonance imaging contrast agents among other applications in medicine [17].

Regarding a simulation point of view, a more detailed study of the optimum diameter and length of magnetic nanowires with different composition may be useful in order to have an idea of a goal system for a determined application that may require ferromagnetic or paramagnetic materials. Along with this, a better understanding of 3D arrays of magnetic nanowires may be of interest to obtain more knowledge of the system obtained in the laboratory.

6.3 References

1. *Magnetism in corrugated carbon nanotori: the importance of symmetry, defects, and negative curvature.* **J. A. Rodríguez-Manzo, F. López-Urías, M. Terrones, H. Terrones.** 2004, Nano Lett., Vol. 4, pp. 2179-2183.

2. *Boron-doping effects in carbon nanotubes.* **W. K. Hsu, S. Firth, P. Redlich, M. Terrones, H. Terrones, Y. Q. Zhu, N. Grobert, A. Schilder, R. J. H. Clark, H. W. Kroto, D. R. M. Walton.** 2000, J. Mater. Chem., Vol. 10, pp. 1425-1429.

3. *Electrical transport in pure and boron-doped carbon nanotubes.* **B. Wei, R. Spolenak, P. Kohler-Redlich, M. Rühle, E. Arzt.** 1999, Appl. Phys. Lett., Vol. 74, pp. 3149-3151.

4. *Carbon nanotube gas and vapor sensors.* **D. R. Kauffman, A. Star.** 2008, Angew. Chem. Int. Ed., Vol. 47, pp. 6550–6570.

5. *Functionalized carbon nanotubes for molecular hydrogen sensors.* **J. Kong, M. G. Chapline, H. Dai.** 2001, Adv. Mater., Vol. 13, pp. 1384-1386.

6. *Understanding the sensor response of metal-decorated carbon nanotubes.* **D. R. Kauffman, D. C. Sorescu, D. P. Schofield, B. L. Allen, K. D. Jordan, A. Star.** 2010, Nano Lett., Vol. 10, pp. 958–963.

7. *Direct magnetic patterning due to the generation of ferromagnetism by selective ion irradiation of paramagnetic FeAl alloys.* **E. Menéndez, M. O. Liedke, J. Fassbender, T. Gemming, A. Weber, L. J. Heyderman, K. V. Rao, S. C. Deevi, S. Suriñach, M. D. Baró, J. Sort, J. Nogués.** 2009, Small, Vol. 5, pp. 229-234.

8. *Magnetic recording at 1.5 Pb m−2 using an integrated plasmonic antenna.* **B. C. Stipe, T. C. Strand, C. C. Poon, H. Balamane, T. D. Boone, J. A. Katine, J.-L. Li, V. Rawat, H. Nemoto, A. Hirotsune, O. Hellwig, R. Ruiz, E. Dobisz, D. S. Kercher, N. Robertson, Tho.** 2010, Nature Photonics, Vol. 4, pp. 484-488.

9. *Intrinsic and hysteresis properties of FePt nanoparticles.* **J. A. Christodoulides, M. J. Bonder, Y. Huang, Y. Zhang, S. Stoyanov, G. C. Hadjipanayis, A. Simopoulos, D. Weller.** 2003, Phys. Rev. B, Vol. 68, p. 054428.

10. *Compositionally controlled FePt nanoparticle materials.* **Shouheng Sun, Eric E. Fullerton, Dieter Weller, C. B. Murray.** 2001, IEEE Trans. Magn, Vol. 37, pp. 1239-1243.

11. *Ferromagnetic FePt nanowires: solvothermal reduction synthesis and characterization.* **Y. Hou, H. Kondoh, R. Che, M. Takeguchi, T. Ohta.** 2006, Small, Vol. 2, pp. 235–238.

12. *High-yield solvothermal formation of magnetic CoPt alloy nanowires.* **Z. Zhang, D. A. Blom, Z. Gai, J. R. Thompson, J. Shen, S. Dai.** 2003, J. Am. Chem. Soc., Vol. 125, pp. 7528-7529.

13. *Viability studies of pure carbon- and nitrogen-doped nanotubes with entamoeba histolytica: from amoebicidal to biocompatible structures.* **A. L. Elias, J. C. Carrero-Sanchez, H. Terrones, M. Endo, J. P. Laclette, M. Terrones.** 2007, Small, Vol. 3, pp. 1723-1729.

14. *Bioelectrochemistry and enzymatic activity of glucose oxidase immobilized onto the bamboo-shaped CNx nanotubes.* **N. Jia, L. Liu, Q. Zhoua, L. Wang, M. Yan, Z. Jiang.** 2005, Electrochimica Acta, Vol. 51, pp. 611–618.

15. *Bamboo-like CNx nanotubes for the immobilization of hemoglobin and its bioelectrochemistry.* **N. Jia, L. Wang, L. Liu, Q. Zhou, Z. Jiang.** 2005, Electrochem. Commun., Vol. 7, pp. 349-354.

16. *Functionalized carbon nanotubes in drug design and discovery.* **M. Prato, K. Kostarelos, A. Bianco.** 2008, Acc. Chem. Res, Vol. 41, pp. 60-68.

17. *Applications of magnetic nanoparticles in biomedicine.* **Q. A. Pankhurst, J. Connolly, S. K. Jones, J. Dobson.** 2006, J. Phys. D: Appl. Phys., Vol. 36, pp. R167–R181.

Appendix A

Synthesis of Carbon Nanotubes Ensapsulating Fe Nanowires

Introduction

Among the synthesis methods for carbon nanotubes three of them are mainly used, which are arc discharge, laser ablation and chemical vapor deposition. Highly crystalline carbon nanotubes can be produce by arc-discharge as identified by Ijima [1], this method consists of the passage of current (80-100 A) between two electrodes in an inert atmosphere (helium). During the process the anode is consumed and in there is a deposit on the cathode, this deposit contains carbon nanotubes and nested polyhedral graphene particles.

Experimental

The method used in this work to grow carbon nanotubes (CNT) is by chemical vapor deposition (CVD) by aerosol pyrolysis [7; 8] (see Figure A1). The experiment consists of a glass container with a solution of a carbon precursor solvent and an organometallic molecule. First the furnace is heated up to a determined temperature while a flow of inert gas passes by. Once the temperature is achieved the solution is sonicated and creates a cloud with the carbon precursor and the catalyst, an argon flow is used to carry this aerosol through the quartz tube that is inside a cylindrical furnace. When this aerosol reaches temperatures above 700 ^{o}C it starts to react, during this reaction the organometallic molecule is broken down and the metal atoms aggregate forming a nanoparticle on the surface of the quartz tube [8], this growth can be selective since it has been observed that CNTs only grow on SiO_2 regions and not on Si [9; 10]. Now the carbon atoms start to diffuse into the nanoparticle and reach a point of saturation, in this moment the carbon atoms leave and at the surface of the nanoparticle they start to create a rolled hexagonal lattice which is the carbon nanotube, in this method all the carbon nanotubes grow vertically aligned upward from the substrate. Depending on the diameter of the nanoparticle it can determine the resulting diameter [11; 12; 13; 14; 15; 16; 17] (see Figure A2) and even the number of walls. Now during the synthesis the iron nanoparticles also travel along

the carbon nanotube growth axis, thus being encapsulated [18; 19; 20]. The resulting material consists of an aligned array of carbon nanotubes.

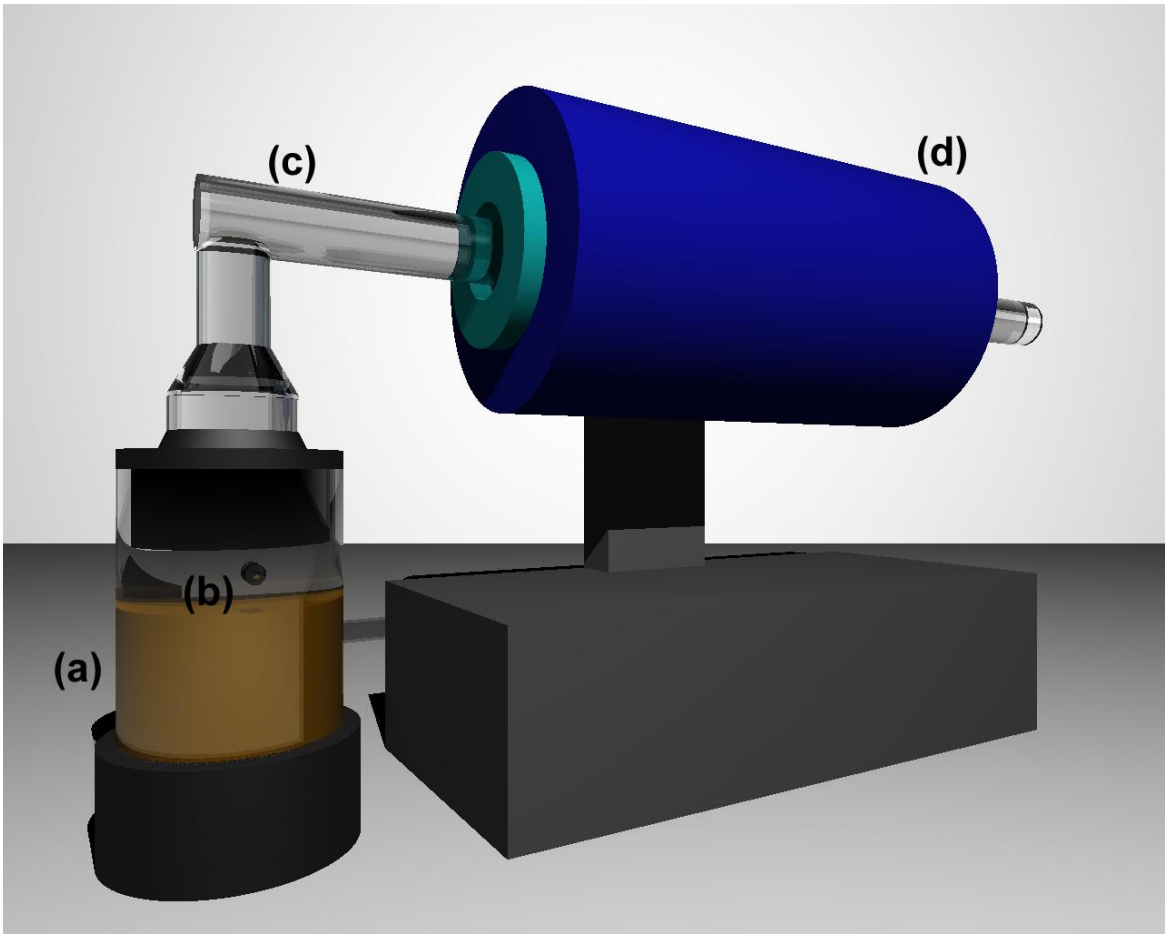

Figure A1. Experimental chemical vapor deposition setup. (a) Glass container with solution of carbon precursor and metal catalyst. **(b)** Inlet for inert gas. **(c)** Quartz tube. **(d)** Cylndrical furnace.

Depending upon the solution content and synthesis conditions SWNT and MWNT can be produced. Different catalyst have been used to grow CNTs such as Fe, Ni, Co, Au, Ag, Pt, Pd, Cu, if other elements are in the solution these carbon nanotubes can be doped with N [21], N-P [22] or contain oxygen functional groups on their walls [23], or other elements may be introduced in carbon nanotubes such as B [24; 25; 26], Si [27] and S [28] . Even other carbon structures may be produced such is the case of carbon nanoribbons [29].

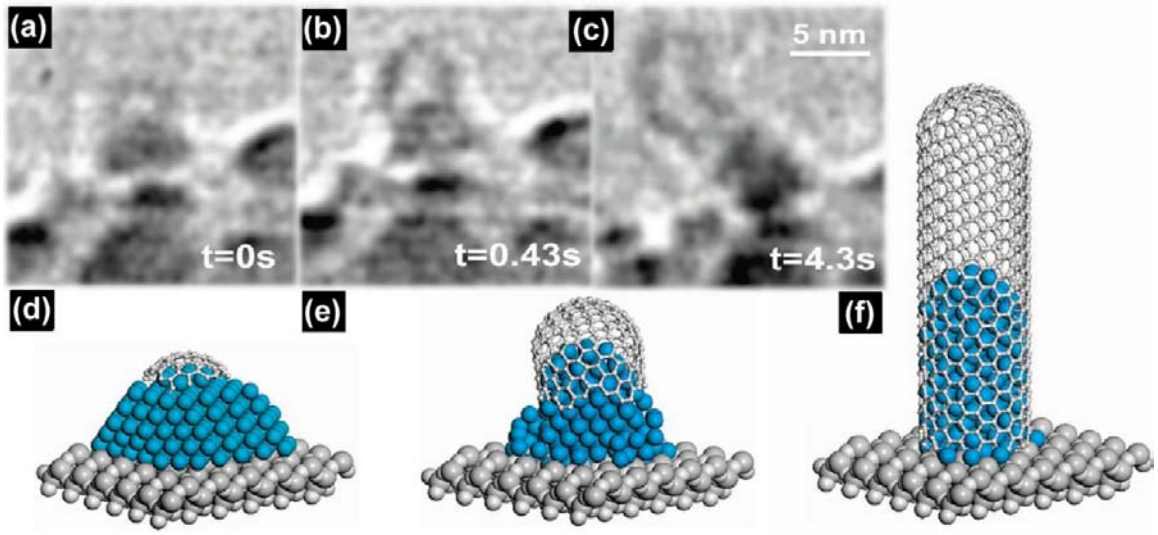

Figure A2. Root growth of a SWNT. (a-c) ETEM image sequence of Ni-catalyzed CNT root growth. **(d-f)** Schematic ball-and-stick model of different SWNT growth stages. (Image from ref **[17]**).

Simulations

The growth of carbon nanotubes has been studied in a theoretical manner showing that the metal catalyst nanoparticle is converted in to a carbide and due to the heating between 800 – 1400 K process the carbon atoms are segregated to the surface of the nanoparticle [30; 31], if these carbide particles are heated below 600 K these particles are covered by graphene sheets and in the case of temperatures above 1600 K three-dimensional soot-like structure is formed. In the beginning stage the carbon atoms are dissolved in to the catalytic nanoparticle, due to the constant intake of carbon the nanoparticle reaches a supersaturation point. At the surface of the nanoparticles carbon atoms tend to create linear chains and aromatic rings, if more carbon atoms are introduced in to the catalyst these tend to move towards the aromatic rings and form different scenarios depending upon the heating temperature as mentioned previously. During the ring formation process five-, six-, seven-, and eight-membered rings are created and broken repeatedly by the constant intake and out take of the C atoms [32] (Figure A3). The hexagonal ring unit remains rather stable and form graphitic islands. The number of graphitic islands depends on the carbide cluster size. The larger islands usually grow faster than smaller ones, and the smaller islands may also dissolve back into the FeC cluster. If two or more islands are close enough these can coalesce. Once that a large island is formed this may lift of and form the cap of the single wall carbon nanotube. The size of the catalytic nanoparticle can also determine the diameter of the carbon nanotube; this has been studied theoretically showing small variations of the CNT/nanoparticle diameter for clusters between 20 and 200 atoms of Fe [33].

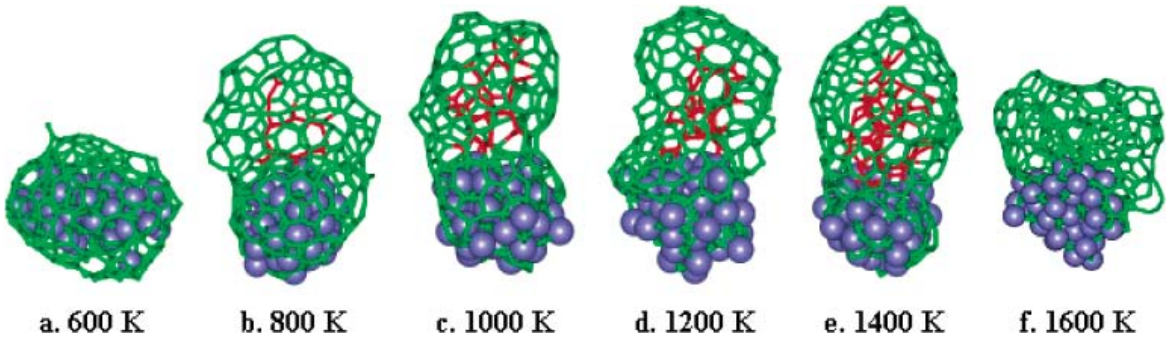

Figure A3. $Fe_{50}C$ at different temperature simutlations. (a) Graphene, **(b-e)** SWNT and **(f)** soot structures obtained between 600 and 1600 K. (Image from ref **[32]**)

References

1. *Helical microtubules of graphitic carbon.* **Ijima, S.** Nature, Vol. 354, pp. 56-58.

2. *Self-assembly of tubular fullerenes.* **T. Guo, P. Nikoleav, A. G. Rinzler, D. Tománek, D. T. Colbert, R. E. Smalley.** 1995, J. Phys. Chem., Vol. 99, pp. 10694–10697.

3. *Crystalline Ropes of Metallic Carbon Nanotubes .* **A. Thess, R. Lee, P. Nikolaev, H. Dai, P. Petit, J. Robert, C. Xu, Y. Hee Lee, S. Gon Kim, A. G. Rinzler, D. T. Colbert, G. E. Scuseria, D. Tománek, J. E. Fischer.** 1996, Science, Vol. 273, pp. 483–487.

4. *Nucleation and growth of carbon deposits from the nickel catalyzed decomposition of acetylene.* **R. T. K. Baker, M. A. Braber, P. S. Harris.** 1972, J. Catal., Vol. 26, pp. 51–64.

5. *In situ observations of catalyst dynamics during surface-bound carbon nanotube nucleation.* **S. Hofmann, R. Sharma, C. Ducati, G. Du, C. Mattevi, C. Cepek, M. Cantoro, S. Pisana, A. Parvez, F. Cervantes-Sodi, A. C. Ferrari, R. Dunin-Borkowski, S. Lizzit, L. Petaccia, A. Goldoni, J. Robertson.** 2007, Nano Lett., Vol. 7, pp. 602-608.

6. *Formation of filamentous carbon from iron, cobalt and chromium catalyzed decomposition of acetylene.* **R. T. K. Baker, P. S. Harris, R. B. Thomas, R. J. Waite.** 1973, J. Catal., Vol. 30, pp. 86–92.

7. *Carbon nanotubes produced by aerosol pyrolysis: growth mechanisms and post-annealing effects.* **M. Pinaulta, M. Mayne-L'Hermite, C. Reynaud, O. Beyssac, J.N. Rouzaud, C. Clinard.** 2004, Diamond and Related Materials, Vol. 13, pp. 1266-1269.

8. *Growth of multiwalled carbon nanotubes during the initial stages of aerosol-assisted CCVD.* **M. Pinault, M. Mayne-L'Hermite , C. Reynaud , V. Pichot.** 2005, Carbon , Vol. 43, pp. 2968-2976.

9. *Mechanism of selective growth of carbon nanotubes on SiO2/Si patterns.* **Y. J. Jung, B. Wei, R. Vajtai, P. M. Ajayan.** 2003, Nano Lett., Vol. 3, pp. 561-564.

10. *Assembly of Highly Organized Carbon Nanotube Architectures by Chemical Vapor Deposition.* **B. Q. Wei, R. Vajtai, Y. Jung, J. Ward, R. Zhang, G. Ramanath, P. M. Ajayan.** 2003, Chem. Mater. , Vol. 15, pp. 1598-1606.

11. *Model of carbon nanotube growth through chemical vapor deposition.* **S.B. Sinnott, R. Andrews, D. Qian, A.M. Rao, Z. Mao , E.C. Dickey, F. Derbyshire.** 1999, Chem. Phys. Lett. , Vol. 315, pp. 25-30.

12. *Correlation between catalyst particle and single-walled carbon nanotube diameters.* **A. G. Nasibulin, P. V. Pikhitsa, H. Jiang, E. I. Kauppinen.** 2005, Carbon, Vol. 43, pp. 251-2257.

13. *Growth of single-walled carbon nanotubes from discrete catalytic nanoparticles of various sizes.* **Y. Li, W. Kim, Y. Zhang, M. Rolandi, D. Wang, H. Dai.** 2001, J. Phys. Chem. B, Vol. 105, pp. 11424-11431.

14. *Imaging as-grown single-walled carbon nanotubes originated from isolated catalytic nanoparticles.* **Y. Zhang, Y. Li, W. Kim, D. Wang, H. Dai.** 2001, Appl. Phys. A , Vol. 74, pp. 325–328.

15. *Synthesis of ultralong and high percentage of semiconducting single-walled carbon nanotubes.* **W. Kim, H. C. Choi, M. Shim, Y. Li, D. Wang, H. Dai.** 2002, Nano Lett. , Vol. 2, pp. 703-708.

16. *Monodisperse multiwall carbon nanotubes obtained with ferritin as catalyst.* **J.-M. Bonard, P. Chauvin, C. Klinke.** 2002, Nano Lett. , Vol. 2, pp. 665-667.

17. *In situ Observations of Catalyst Dynamics during Surface-Bound Carbon Nanotube Nucleation.* **S. Hofmann, R. Sharma, C. Ducati, G. Du, C. Mattevi, C. Cepek, M. Cantoro, S. Pisana, A. Parvez, F. Cervantes-Sodi, A. C. Ferrari, R. Dunin-Borkowski, S. Lizzit, L. Petaccia, A. Goldoni, J. Robertson.** 2007, Nano Lett., Vol. 7, pp. 602-608.

18. *Enhanced magnetism in Fe-filled carbon nanotubes produced by pyrolysis of ferrocene.* **A. Leonhardt, M. Ritschel, D. Elefant, N. Mattern, K. Biedermann, S. Hampel, Ch. Müller, T. Gemming, B. Büchner.** 2005, J. Appl. Phys. 98 (2005) 074315, Vol. 98, p. 074315.

19. *Synthesis, properties, and applications of ferromagnetic-filled carbon nanotubes.* **A. Leonhardt, S. Hampel, C. Müller, I. Mönch, R. Koseva, M. Ritschel, D. Elefant, K. Biedermann, B. Büchner.** 2006, Chem. Vap. Deposition 12 (2006) 380, Vol. 12, p. 380.

20. *Magnetism in Fe-based and carbon nanostructures: Theory and applications .* **H. Terrones, F. López-Urías, E. Muñoz-Sandoval, J.A. Rodríguez-Manzo, A. Zamudio, A.L. Elías, M. Terrones.** 2006, Solid State Sciences 8 (2006) 303, Vol. 8, p. 303.

21. *Novel nanoscale gas containers: encapsulation of N2 in CNx nanotubes.* **M. Terrones, R. Kamalakaran, T. Seegera, M. Rühlea.** 2000, Chem. Commun., pp. 2335-2336.

22. *Heterodoped nanotubes: theory, synthesis, and characterization of phosphorus - nitrogen doped multiwalled carbon nanotubes.* **E. Cruz-Silva, D. A. Cullen, L. Gu, J. M. Romo-Herrera, E. Muñoz-Sandoval, F. López-Urías, B. G. Sumpter, V. Meunier, J.-C. Charlier, D. J. Smith, H. Terrones, M. Terrones.** 2008, ACS Nano, Vol. 2, pp. 441-448.

23. *Controlling the dimensions, reactivity and crystallinity of multiwalled carbon nanotubes using low ethanol concentrations.* **A. Botello-Méndez, J. Campos-Delgado, A. Morelos-Gómez, J. M. Romo-Herrera, Á. G. Rodríguez, H. Navarro, M. A. Vidal, H. Terrones, M. Terrones.** 2008, Chemical Physics Letters, Vol. 453, pp. 55-61.

24. *Doping graphitic and carbon nanotube structures with boron and nitrogen.* **O. Stephan, P. M. Ajayan, C. Colliex, P. Redlich, J. M. Lambert, P. Bernier, P. Lefin.** 1994, Science, Vol. 266, pp. 1683-1685.

25. *Boron-doping effects in carbon nanotubes.* **W. K. Hsu, S. Firth, P. Redlich, M. Terrones, H. Terrones, Y. Q. Zhu, N. Grobert, A. Schilder, R. J. H. Clark, H. W. Kroto, D. R. M. Walton.** 2000, J. Mater. Chem., Vol. 10, pp. 1425-1429.

26. *Boron-doped carbon nanotubes prepared through a substitution reaction.* **W. Han, Y. Bando, K. Kurashima, T. Sato.** 1999, Chem. Phys. Lett., Vol. 299, pp. 368–373.

27. *Substitutional Si doping in deformed carbon nanotubes.* **S. B. Fagan, R. Mota, Antonio J. R. da Silva, A. Fazzio.** 2004, Nano Lett., Vol. 4, pp. 975-977.

28. *An atomistic branching mechanism for carbon nanotubes: sulfur as the triggering agent.* **J. M. Romo-Herrera, B. G. Sumpter, D. A. Cullen, H. Terrones, E. Cruz-Silva, D. J. Smith, V. Meunier, M. Terrones.** 2008, Angew. Chem. Int. Ed., Vol. 47, pp. 2948 –2953.

29. *Bulk production of a new form of sp2 carbon: crystalline graphene nanoribbons.* **J. Campos-Delgado, J. M. Romo-Herrera, X. Jia, D. A. Cullen, H.i Muramatsu, Y. A. Kim, T. Hayashi, Z. Ren, D. J. Smith, Y. Okuno, T. Ohba, H. Kanoh, K.i Kaneko, M. Endo, H. Terrones, M. Dresselhaus, M. Terrones.** 2008, Nano Lett. , Vol. 8, pp. 2773-2778.

30. *Root-growth mechanism for single-wall carbon nanotubes.* **J. Gavillet, A. Loiseau, C. Journet, F. Willaime, F. Ducastelle, J.-C. Charlier.** 2001, Phys. Rev. Lett., Vol. 87, p. 275504.

31. *Nucleation and growth of single-walled carbon nanotubes: a molecular dynamics study.* **F. Ding, K. Bolton, A. Rosrén.** 2004, J. Phys. Chem. B, Vol. 108, pp. 17369-17377.

32. *Rapid growth of a single-walled carbon nanotube on an iron cluster: density-functional tight-binding molecular dynamics simulations.* **Y. Ohta, Y. Okamoto, S. Irle, K. Morokuma.** 2008, ACS Nano, Vol. 2, pp. 1437–1444.

33. *Molecular dynamics study of the catalyst particle size dependence on carbon nanotube growth.* **F. Ding, A. Rosén, K. Bolton.** 2004, J. Chem. Phys., Vol. 121, No. 6, 8 August 2004, Vol. 121, pp. 2775-2779.

34. *A Novel Polyacrylamide Magnetic Nanoparticle Contrast Agent.* **Bradford A. Moffat, G. Ramachandra Reddy, Patrick McConville, Daniel E. Hall.** 2003, Molecular Imaging ., Vol. 2, pp. 324-332.

35. *Large-scale synthesis of aligned carbon nanotubes.* **W. Z. Li, S. S. Xie, L. X. Qian, B. H. Chang, B. S. Zou, W. Y. Zhou, R. A. Zhao, G. Wang.** 1996, Science, Vol. 274, pp. 1701–1703.

Appendix B

Long multiwall carbon nanotubes with oxygen functional groups

We were interested in synthesizing tall forests of carbon nanotubes by CVD, as a result of this interest an article titled “Controlling the dimensions, reactivity and crystallinity of multiwall carbon nanotubes using low ethanol concentrations” was published. Here were able to control the diameter, reactivity, crystallinity and the height of the carbon nanotube forests, by the introduction of a low concentration of ethanol in the solution of toluene/ferrocene used for the CVD synthesis. In general, when increasing the amount of ethanol the diameter of the MWCNTs was decreased. The crystallinity was analyzed by the I_D/I_G Raman ratio, here the minimum values by ethanol concentration varies according to the amount of ferrocene used for the synthesis. Further on, the infrared spectroscopy measurements reveal that the MWCNT synthesized with ethanol exhibit a higher degree of oxygen functionalization than when synthesized only with toluene and ferrocene, therefore we named these MWCNT as CO_x. Interestingly, we found optimum ethanol concentrations for the solutions, at specific ferrocene contents, to grow higher MWCNT forests. In order to search for a growth limit several hour synthesis were carried out with 2.5% by wt. of ferrocene, and 1 % by wt. of ethanol in toluene, the forests grew 0.64, 1.27, 5 and ~ 7 mm for reaction times of 0.5, 1, 3 and 7 hours (see Figure B1). We found that the growth rate is equivalent to 1 mm/hour. For synthesis time of 3 hours we find that our forests exhibit fibers of MWCNTs on the surface, below, these fibers the MWCNTs exhibit impurities, such as particles, on the walls of the MWCNTs, when observing the forest downwards the amount of impurities decrease. We attribute the gradient of impurities along the height of the forest due to the exposure time of the MWCNTs grown in the initial stage, these are continuously exposed to the CVD therefore it is more likely that impurities are somehow anchored on the walls, on the contrary the final stage or “newer” section of the forest has a lower amount of time exposed to the CVD. For further detail about this work the published article is attached in the following pages.

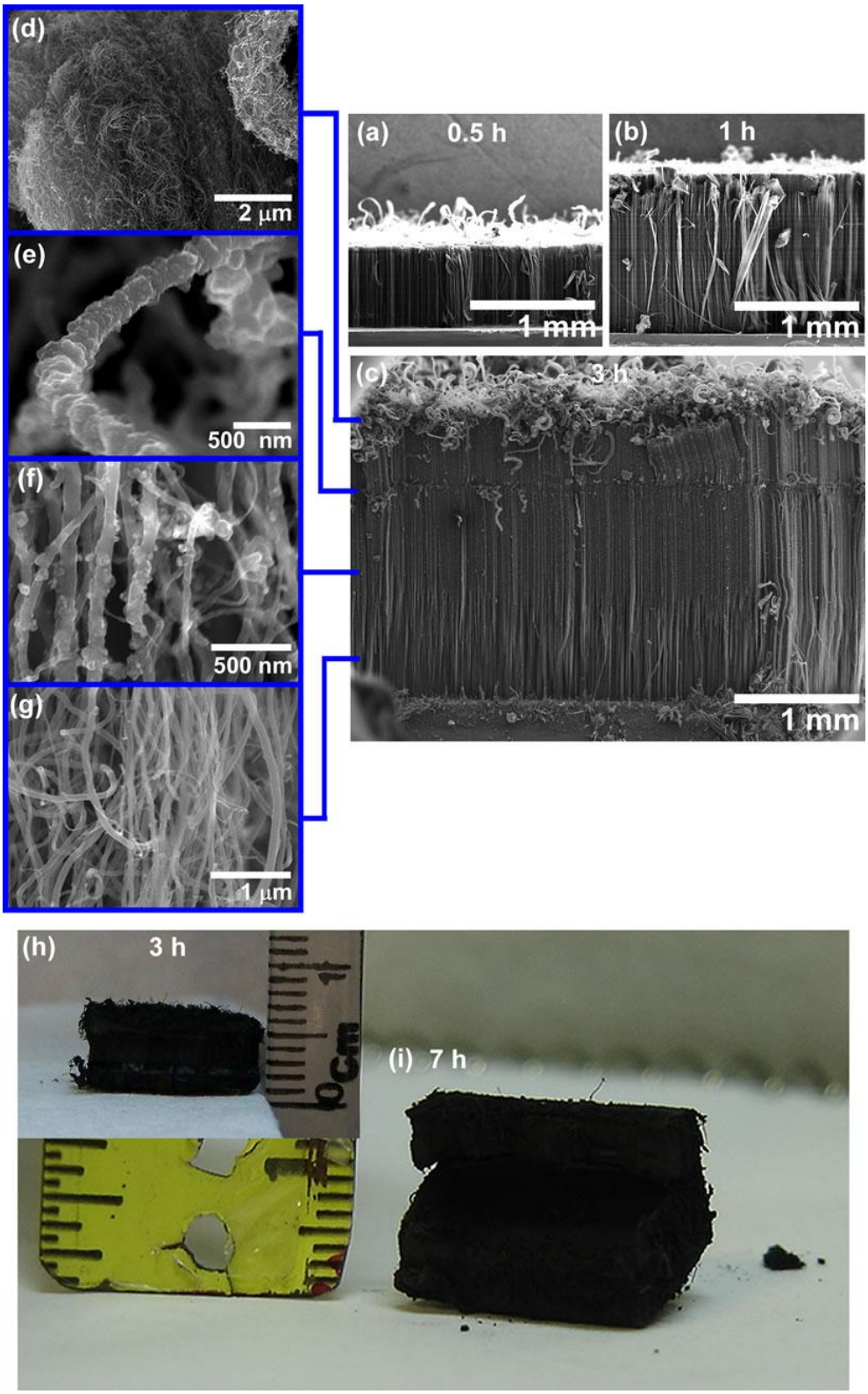

Figure B1: Long CO_x. These CO_x were synthesized during **(a)** 0.5 hours, **(b)** 1 hours, **(c)** and **(h)** 3 hours and **(i)** 7 hours. **(d-g)** SEM images of the surface and lower of the 3 hour synthesis, it is clear that the higher section exhibits more impurities and the lower section is more pure.

Available online at www.sciencedirect.com
ScienceDirect
Chemical Physics Letters 453 (2008) 55–61
CHEMICAL PHYSICS LETTERS
www.elsevier.com/locate/cplett

Controlling the dimensions, reactivity and crystallinity of multiwalled carbon nanotubes using low ethanol concentrations

Andrés Botello-Méndez [a], Jessica Campos-Delgado [a], Aarón Morelos-Gómez [a], José M. Romo-Herrera [a], Ángel G. Rodríguez [b], Hugo Navarro [b], Miguel A. Vidal [b], Humberto Terrones [a], Mauricio Terrones [a,*]

[a] *Advanced Materials Department, IPICYT, Camino a la Presa San José 2055, Col. Lomas 4a Sección, San Luis Potosí 78216, Mexico*
[b] *Optoelectronic Materials, IICO, Av. Karakorum 1470, San Luis Potosí 78210, Mexico*

Received 6 November 2007; in final form 27 December 2007
Available online 5 January 2008

Abstract

We study the role of ethanol in the thermolytic synthesis of multiwalled carbon nanotubes. We show that low concentrations of ethanol control the length and diameter, as well as the crystalline quality of the produced nanotubes. We statistically evaluated the dimensions of the tubes as the concentration of ethanol is increased. The quality of the samples results in more crystalline products when low concentrations of ethanol (~1–2%) are used in the experiments. In addition, the introduction of ethanol during the synthesis seems to incorporate coordination groups on the surface of nanotubes that cause an enhanced reactivity and a better solubility.
© 2008 Elsevier B.V. All rights reserved.

1. Introduction

The unique and fascinating properties of carbon nanotubes (CNTs) [1] have motivated intensive research in the fabrication of nanocomposites (as reinforcement fillers), electronic components (interconnects) [2], field emission sources [3] and hydrogen storage devices [4]. It is noteworthy that certain CNT applications require specific dimensions and different levels of homogeneity (e.g. diameter, length, reactivity, crystallinity and purity). In this context, various researchers have developed different CNT synthesis methods followed by purification techniques. Unfortunately, the current CNT production methods usually yield products with a wide distribution of diameters, lengths and other characteristics. As a consequence, one of the most important challenges in the CNT field consists in the ability to achieve real control in the CNT dimensions, reactivity and crystallinity so that real devices based on these structures are produced.

The chemical vapor deposition (CVD) method based on the pyrolysis of hydrocarbons over metal catalysts, has shown advantages when compared to other synthesis methods because aligned CNTs bundles can be produced in a single step process, without further purification treatments, at a relatively low cost and without prior preparation of substrates [5,6]. Various attempts aimed to control the CNT dimensions by varying the metal concentration in the hydrocarbon precursors have been reported [7,8]. Alternatively, the deposition of sputtered catalyst film of different thicknesses has also proven size-selective growth of CNTs [9]. Other studies related to the effects of temperature on the CNT growth (diameter and crystallinity) have also been carried out [10].

More recently, Hata et al. demonstrated that it is possible to improve the CNT purity when extremely small concentrations of water (e.g. ppm) were added during the CVD process. These experiments resulted in clean single-walled carbon nanotube (SWCNT) forests free from amorphous carbon [11]. Other authors have also used pure ethanol (EtOH) to produce SWCNTs [12,13]. However, and to the best of our knowledge, the effect of EtOH during the

* Corresponding author. Fax: +52 444 834 2010.
E-mail address: mterrones@ipicyt.edu.mx (M. Terrones).

0009-2614/$ - see front matter © 2008 Elsevier B.V. All rights reserved.
doi:10.1016/j.cplett.2007.12.073

Appendix C

Characterization tools

Scanning electron microscopy

Here, electrons from a thermionic or field-emission cathode are accelerated by a voltage. The beam cross-section may have a diameter of 10-50 μm for thermoionic and 10-100 nm for field-emission guns, further on it may be reduced to an electron probe of 1-10 aided by a two- or three-stage electron lens system. Usually the final probe-forming lends operates at relatively long working distances (i. e. 5 mm).

Here an electron beam irradiates a sample where the same or different electrons leave the sample. The image formation is made by the electron-specimen interaction. The most important interactions are secondary electrons (SE), backscattered electrons (BSE) and Auger electrons (AE). The SE are formed when there is an inelastic excitation, when the electrons have an energy higher than the work function before they are decelerated to the Fermi level. Here the electron-specimen interactions provide voltage contrasts, “negatively biased areas appearing bright and positively biased regions are dark”.

The backscattered electrons are generated by the deceleration of electrons “that have suffered multiple energy losses and undergone multiple scattering through large angles”. Therefore, they depend upon the surface topography, exhibiting a better shadow effect than the SE, since the BSE move on straight trajectories. The backscattering coefficient depends upon the mean atomic number *Z*, this may allow the observation of the difference among phases in the sample. [1]

Transmission electron microscopy

A transmission electron microscope mainly consists of an electron gun and magnetic lenses. The electron gun consists of a filament cathode and an anode with a hole to define the optic axis. The magnetic lenses are made of coils with a current centered on the optic axis; this configuration provides a magnetic field distribution. If the electrons are closer to the optic axis, they will suffer no

deflection. Once the electrons travel through the sample they are diffracted in several directions depending on the crystal orientation. To see the diffraction pattern, the intermediate lens is adjusted to focus on the back focal plane of the objective lens. Now, to obtain the image the intermediate lens is adjusted so that its object plane coincides with the image plane of the objective lens. The contrast may be caused by thickness variation or composition variation. [2]

In a TEM the small wavelength of the electrons gives a very large radius of the corresponding Ewald sphere, even larger when compared with the spacing between reciprocal lattice points. The electrons that are transmitted through the sample produce reciprocal lattice points which are elongated along the thin axis of the sample. The reciprocal lattice image produced by the TEM is known as diffraction pattern and is obtained by the direction of incidence of the electrons. [2]

Energy Dispersive X-ray analysis

The chemical analysis of materials may be done by a quantitative x-ray microanalysis, were each element has characteristic energies were an electron from an inner shell is excited to a higher level, leaving an electron hole. Then, an electron from a higher energy shell fills the electron hole, here the difference in energy between the shells is released in the form of an X-ray. These characteristic energies of each element allows us to determine the chemical composition of a certain material. [1; 3]

X-Ray diffraction

X-rays of a known wavelength are irradiated on a sample, varying the angle of irradiation in order to obtain an x-ray diffraction spectrum. Particularly, we used the powder method. Here, each particle of the powder has a random orientation with respect to the incident beam; therefore every set of lattice planes will be diffracted. The diffraction arises from the periodic arrangement of atoms, here determined directions will satisfy Bragg's law thus scattering the incident beam. These directions have a distance between scattering centers that are the same order of magnitude as the wavelength of the wave motion. From the diffraction spectrum we can determine the spacing d of various planes in a crystal, with a known wavelength source. Experimentally the measured angle is 2θ which is between the diffracted beam and the transmitted beam. [2]

X-ray photoelectron spectroscopy

Here the sample is irradiated with highly monochromatic x-rays photons, the sample absorbs the photons and there is an emission of photoelectrons from the electronic core with a kinetic energy equal to the energy of the incident photon minus the binding energy of the electron in the material; other electrons will collide with other electrons from topper layers of the sample, they will have a lower energy and be part of the noise signal of the spectrum. Typically the electrons that are emitted come from the layer near the surface c. a. 10 - 100 Å in depth. [4] The instrument is under high vacuum in order to eliminate excessive surface contamination. The obtained spectrum will have peak, with a characteristic binding energy for each element, and for each element there can be several peaks corresponding to the binding of two elements, these sub-peaks can be correlated with chemical bonds.

The quantification of the chemical composition may be obtained according with the area and kinetic energy of the peak with the following equation:

$$W = \frac{E_k A}{\sigma \lambda}$$

W is the number of "counts", E_k is the kinetic energy of the peak, A is the area, σ is the electron elastic-scattering cross section and λ is the electron attenuation length. This equation is applied to each deconvoluted peak for a determined element, later all the W values are summed. This is repeated for all the identified elements in the sample, further on the sums for all the elements are normalized in order to obtain an atomic percent for the analyzed area.

Raman spectroscopy

This technique is used to study vibrational, rotational or other low frequency modes in a system. The Raman effect is the inelastic scattering of a photon by a crystal, where a phonon or magnon is created or annihilated. In the first-order Raman effect there is one phonon involved and in the second-order Raman effect there are two phonons involved in the scattering of the photon. The photon emission may be caused by the absorption (anti-Stokes) or emission (Stokes) of phonon, here the emitted photon may have; the frequency incident photon frequency (w) plus the frequency of the adsorbed phonon (W) (anti-Stokes), or it

may be w – W for Stokes scattering. [4] The shift in energy gives information about the phonon modes in the studied system.

PPMS (resistivity, magnetoresistance, magnetometry)

The physical properties measurement system (PPMS) used is a tool that allows the measurement of heat capacity, resistivity and vibrating sample magnetometry.

In the case of resistivity, the sample was mounted with a four wire configuration, this allows a great certainty for the current and the voltage drop across the sample and thus calculate the resistance with Ohm's law. [5] The PPMS has a sample holder (known as puck) with the possibility to mount three different samples with the four wire configuration. The system has the capability to vary the temperature and even apply a determined external magnetic field; this gives the possibility to measure resistivity versus temperature and resistivity versus magnetic field (magnetoresistance) at different temperatures. In order to obtain values that are comparable, the geometry of measured samples is taken in to account as follows:

$$\rho_{spec} = \rho \frac{l}{A}$$

Here ρ_{spec} is the electrical resistance; ρ is the electrical resistivity; l is the distance between the middle wires from the four wire configuration; and A is the cross section area of the current flow.

To measure the magnetization the vibrating sample measurement mode was used, here the sample is attached to the end of a sample rod. The sample is vibrated near a detection coil, where the center of oscillation is located at the center of a gradiometer. The voltage induced is synchronously detected and amplified with the pickup coil. This mode is capable to detect magnetization of less than 10^{-6} emu at a data rate of 1 Hz. [6]

The principle of operation is that the changing magnetic flux will induce a voltage in a pickup coil, according to the following equation:

$$V_{coil} = \frac{d\Phi}{dt} = \left(\frac{d\Phi}{dz}\right)\left(\frac{dz}{dt}\right)$$

Φ is the magnetic flux, *z* is the vertical position of the sample with respect to the coil, and *t* is time. In case of a sinusoidal oscillation the voltage follows this equation:

$$V_{coil} = 2\pi f C m A sin(2\pi f t)$$

C is a coupling constant, *m* is the DC magnetic moment of the sample, *A* is the amplitude of oscillation, and *f* is the frequency of oscillation.

References

1. *Scanning Electron Microscopy.* **Reimer, Ludwig.** s.l. : Springer-Verlag, 1985.

2. *Elements of x-ray diffraction.* **B. D. Cullity, S. R. Stock.** s.l. : Prentice Hall, 2001.

3. **Wikipedia contributors. Self-assembly. Wikipedia, The Free Encyclopedia (2010) at http://en.wikipedia.org/wiki/Energy-dispersive_X-ray_spectroscopy, Retrieved on July 13, 2010.**

4. *Introduction to solid state physics, 8th edition.* **Kittel, Charles.** s.l. : John Wiley and Sons, Inc, 2005.

5. *Resistivity Option User's Manual, Physical Property, Quantum Design.*

6. *Vibrating sample magnetometer, Quantum Design, Brochure.*

Appendix D

Micromagnetic simulations

In a micromagnetic model the total energy of the system is the sum of the exchange energy, anisotropic energy, Zeeman energy and demagnetization energy. There are short and long-range interactions between magnetic moments; the short range interactions are related with exchange interaction and anistropic energy, and the long range interactions are the Zeeman energy and the demagnetization energy.

The exchange interaction tends to align neighbor spins; this will tend to produce small magnetic uniform regions known as magnetic domains. The expression for the interaction energy is given by $E_{int}= -2J_{int}S_A \cdot S_B$ J_{int} is the exchange integral for the two electronic wave functions of each atom, and S_A and S_B are the total spins of each atom. From this equation it is clear that if neighbor magnetization vectors exhibit an angle between them there will be an increase in energy.

The Heisenberg exchange energy is invariant with respect to the choice of coordinate system. It has been observed experimentally that due to the structure of a material there can be a favored direction called the easy direction, this direction make the alignment of the magnetization easier, this effect is known as crystalline anisotropy. The crystalline anisotropy energy is the work required to make the magnetization lie at a certain angle compared with the easy direction, this energy is usually expressed as a power series of trigonometric functions of the angles the magnetization makes with the principal axis of the system $E_{ani} = K_1\sin^2\theta + K_2\sin^4\theta + ...$ For example, Iron has a cubic structure; however the cube edges are the easy directions. This anisotropy energy usually is temperature sensitive. For small particles there may be shape anisotropy (also known as dipolar anisotropy), here the favored magnetization direction is determined by the geometry of the particle.

The magnetostatic or demagnetization energy is derived from Maxwell's equations considering the absence of electric fields and free currents. This energy tends to divide a magnetic material in to uniform magnetic domains. This division is harder to produce in nanostructures, to a point where they may exist as monodomain. Sometimes these structures may exhibit different spin configurations

resembling figures such as onions, whirlwinds, flowers, vortexes, etc. These configurations are mainly ruled by the geometry of the structure.

The Zeeman energy is the interaction of the magnetization of a material with the external magnetic field and it reaches a minimum when the magnetization vectors are parallel with the applied magnetic field.

For our micromagnetic simulations we used the Object Oriented Micromagnetic Framework (OOMMF) [1], this may be download from the website: http://math.nist.gov/oommf/ .

The energy terms that are used in the code are the following:

$$E_{exch} = \int (A_{exch}[\nabla \vec{m}(\vec{r})]^2) d^3r$$

$$E_{anis} = \int \left((K_1) \frac{(\vec{n} \cdot \vec{M})^2}{M_s^2} \right) d^3r$$

$$E_{zeem} = \int \left(-\frac{\mu_0}{2} (\vec{M} \cdot \overrightarrow{H_m}) \right) d^3r$$

$$E_{demag} = \frac{\mu_0}{2} \vec{M}(r) \cdot \left(\int \frac{\nabla \cdot \vec{M}\left(\overrightarrow{r'}\right)\left(\vec{r} - \overrightarrow{r'}\right) d^3r}{\left|\vec{r} - \overrightarrow{r'}\right|^3} + \frac{1}{4\pi} \int \frac{\vec{n} \cdot \vec{M}\left(\overrightarrow{r'}\right)\left(\vec{r} - \overrightarrow{r'}\right) da'}{\left|\vec{r} - \overrightarrow{r'}\right|} \right)$$

The exchange energy is obtained by the point product of eight neighbors [2]. The magnetostatic energy is calculated with the Fast Fourier Transformations of a scalar potential. The magnetization of the nanosystem is obtained as a solution of the dynamic equation of Landau-Lifshitz-Gilbert, this is because ferromagnetic materials do not have a linear magnetization and this equation may describe the magnetization on the microscale:

$$\frac{\partial \vec{M}}{\partial t} = -\frac{\omega}{(1+\lambda^2)} \vec{M} \times \overrightarrow{H_{eff}} - \frac{\lambda\omega}{(1+\lambda^2)M_s} \left(\vec{M} \times \vec{M} \times \overrightarrow{H_{eff}}\right)$$

Where the effective field is:

$$\overrightarrow{H_{eff}} = -\frac{1}{\mu_0}\frac{\partial E_{total}}{\partial \vec{M}}$$

ω is the gyromangetic ratio and λ is the damping constant.

The OOMMF code is capable to obtain the behavior of the magnetization when an external magnetic field is applied and therefore obtain hysteresis curves. The code has the versatility to use black and white figures in GIF or PPM format, these are used as masks in order to simulate a desired system, due to the study of nanostructures the choice of the unit cell size that divides the nanomagnet is important in order to obtain reliable results, in our case we chase a unit cell size of 2 nm.

References

1. *OOMMF User'Guide, version 1.0, Interagency Report NISTIR 6376, Gaithersburg, MD (2004).* **M. J. Donahue, D. G. Porter.**

2. *Exchange energy representations in computational micromagnetics.* **McMichael, M. J. Donahue and R. D.** 1997, Physica B, Vol. 233, pp. 272-278.

3. Home page of Massimiliano d'Aquino at *http://wpage.unina.it/mdaquino/PhD_thesis/main/node1.html, Retrieved on July 13, 2010*

4. *The physical principles of magnetism.* **Morrish, A. H.** s.l. : IEEE Press, 2001.

Journal of Materials Chemistry

www.rsc.org/materials

Volume 20 | Number 28 | 28 July 2010 | Pages 5765–5968

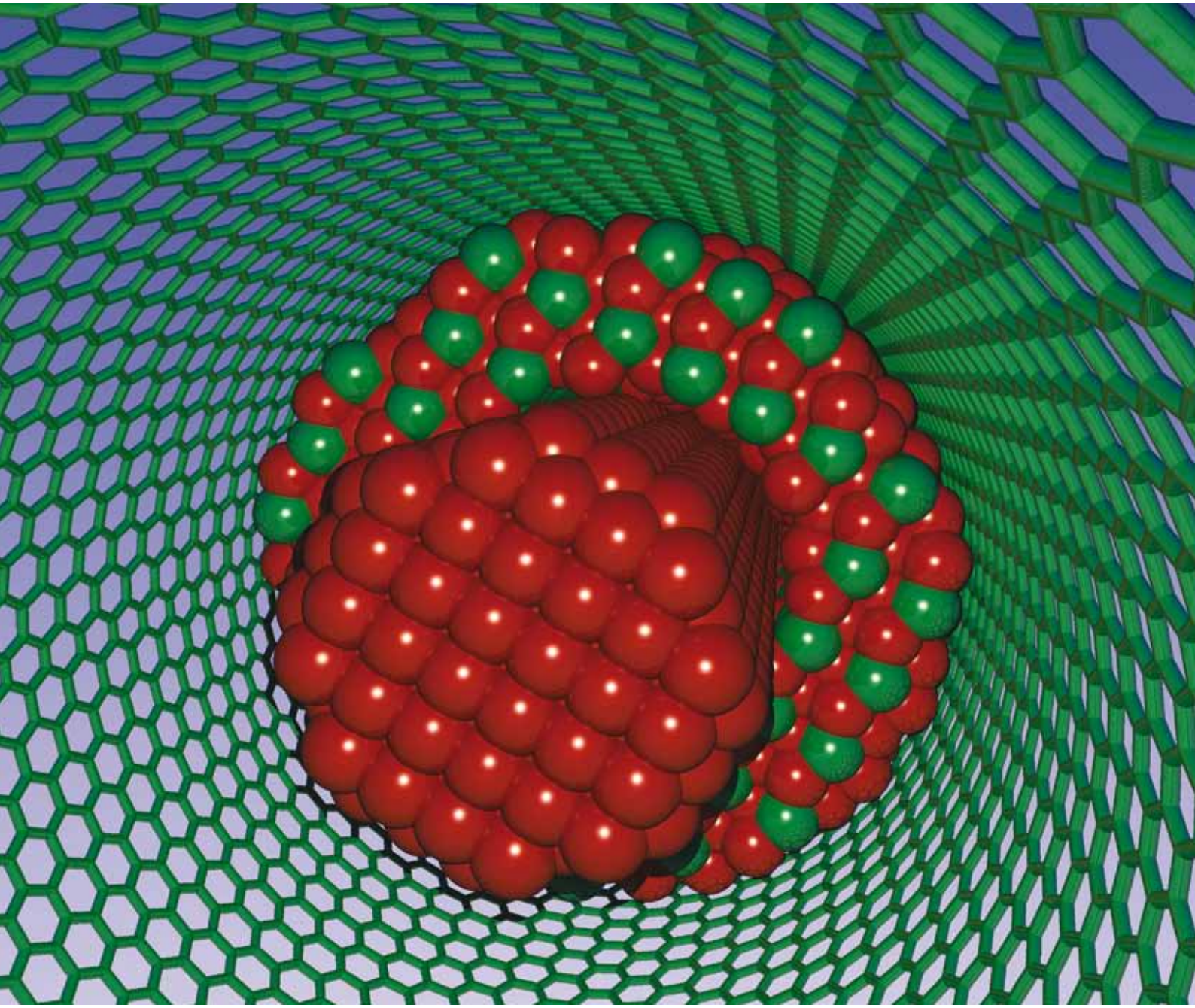

ISSN 0959-9428

RSC Publishing

0959-9428(2010)20:28;1-J

Controlling high coercivities of ferromagnetic nanowires encapsulated in carbon nanotubes†

Aarón Morelos-Gómez,[ab] Florentino López-Urías,[a] Emilio Muñoz-Sandoval,[a] Cindi L. Dennis,[a] Robert D. Shull,[a] Humberto Terrones[c] and Mauricio Terrones*[d]

Received 10th March 2010, Accepted 10th May 2010
First published as an Advance Article on the web 15th June 2010
DOI: 10.1039/c0jm00660b

Cylindrical ferromagnetic nanowires encapsulated inside multiwalled carbon nanotubes (MWNTs) are synthesized by pyrolyzing either ferrocene powder or ferrocene–toluene mixtures. By changing the way the precursor is thermolyzed, we have been able to control the composition of the ferromagnetic byproducts. In particular, we noted the coexistence of α-Fe and Fe_3C phases when only powder ferrocene is theromolyzed in an inert atmosphere. However, when toluene–ferrocene solutions are sprayed and thermolyzed, only Fe_3C nanocrystals are produced. Magnetic measurements of the aligned nanotubes containing these cylindrical nanowires revealed large coercive fields as high as 0.22 T at 2 K. Interestingly, these magnetic coercivities strongly depend on the Fe particles' diameter, and are not affected by the length of the particles, which was also confirmed using micromagnetic simulations. Our experimental and theoretical results indicate that short and well aligned carbon nanotubes containing narrow ferromagnetic nanowires (*i.e.* 5 nm diameter and 25 nm long) would be suitable for producing prototypes of magnetic recording devices.

Introduction

Magnetic nanomaterials are attracting the attention of numerous scientists due to their fascinating physico-chemical properties and possible applications. Some of these applications include magnetic recording,[1,2] separation of biological species,[3] targeted transportation of drugs,[4] contrast improvement in magnetic resonance imaging,[5] *etc.* In order to apply ferromagnetic nanowire arrays in magnetic recording, the fabrication of patterned nanostructures and perpendicular magnetic recording have been proposed.[1,2] However, magnetic materials have the disadvantage of facile oxidation. Therefore, one alternative is to use small magnetic nanowires encapsulated in carbon nanotubes. Using different synthetic methods, different metals have been encapsulated inside multiwalled carbon nanotubes (MWNTs) such as Fe, Ni, Co, FeCo, FePt, FeNi and Fe_3C.[6–19] In particular, the chemical vapor deposition (CVD) method is one of most successful methods able to encapsulate these ferromagnetic materials. These magnetic nanoparticles and nanowires encapsulated inside carbon nanotubes have exhibited large coercive fields and a coherent reversal magnetization process.[9,10] Furthermore, the magnetic properties remain stable even at high temperatures.[10]

Fe nanowires have also been synthesized using a templating method,[20–24] in which the template is generally porous anodic aluminium oxide. The Fe nanowires obtained using this method are polycrystalline with large aspect ratios (length of the order of microns).[20,21] These materials display large coercive fields (0.22–0.42 T)[20–24] at low temperatures (<10 K), and it is likely that an iron oxide layer is also formed thus changing the magnetic response. An alternative method is the pyrolysis of organometallic precursors; with this method it is possible to encapsulate ferromagnetic (such as Fe) nanowires inside carbon nanotubes; no oxide layers are formed in the process. In addition, high coercivities have been obtained by this method (H_c = 0.13–0.23 T).[25–28] Using the laser pyrolysis method, Fe_3C spherical nanowires with diameters of *ca.* 20 nm have been synthesized, showing a small coercivity of 0.056 T, and a saturation magnetization of around 120 A m^2/kg (emu g^{-1}).[29,30]

In this work, we have investigated the magnetic properties of ferromagnetic nanowires of different dimensions and compositions, encapsulated inside MWNTs. Ferrocene and ferrocene–toluene mixture precursors were used in our CVD process. By changing the toluene concentration in the synthesis process, it is possible to vary the chemical composition of the ferromagnetic nanowires, and therefore their magnetic properties. By varying the synthesis temperature, we could also control the magnetic properties because their morphology is being modified.

Experimental

The MWNTs containing cylindrical encapsulated nanowires were synthesized by pyrolyzing toluene/ferrocene solutions (2.5% of ferrocene by weight in toluene) at 700 °C, 800 °C and 850 °C

[a]*Advanced Materials Department, IPICYT, Camino a la Presa San José 2055, Col. Lomas 4ª sección, San Luis Potosí S.L.P., 78216, México*
[b]*Metallurgy Division, NIST, Gaithersburg, Maryland, 20899-8443, USA*
[c]*Université Catholique de Louvain (UCL), Institute of Condensed Matter and Nanosciences (IMCN), Place Croix du Sud 1 (PCPM-Boltzmann), 1348 Louvain-la-Neuve, Belgium*
[d]*Department of Materials Science and Engineering & Chemical Engineering, Polytechnic School, Carlos III University of Madrid, Avenida Universidad 30, 28911 Leganés, Madrid, Spain. E-mail: mtterrones@gmail.com*

† Electronic supplementary information (ESI) available: Hysteresis curves and the vector representations of a linear array of Fe nanowires inside carbon nanotubes. The external magnetic field was applied in three different directions (0°, 45° and 90°). See DOI: 10.1039/c0jm00660b

 This journal is © The Royal Society of Chemistry 2010